# Synthesis and Properties of 2D Layered Semiconductors and Heterostructures

---

Yang Lu

Supervised by Professor Jamie H. Warner & Professor Harish Bhaskaran




St. Peter's College

Department of Materials

University of Oxford

*Submitted in conformity with the requirements*

*for the degree of DPhil in Materials Science*

Oct 2021

Copyright © 2021 by Yang Lu

# Declaration

The material contained within this thesis has not previously been submitted for a degree at the University of Oxford or any other university. The research reported within this thesis has been conducted by the author unless indicated otherwise.

# Copyright Notice

The copyright of this thesis rests with the author. No quotation from it should be published without the prior written consent of the author, and any information derived from it should be acknowledged.

# Abstract

## Synthesis and Properties of 2D Layered Semiconductors and Heterostructures

*by Yang Lu*

*St Peter's College*

*In pursuit of DPhil degree, Trinity Term, 2021*

More than a decade after the successful isolation of the first monolayer two-dimensional (2D) layered materials in 2004, a major focus in contemporary material science research is to expand the 2D family with novel layered materials or vertical layered heterostructures (VLHs) presenting extraordinary properties. Especially, 2D layered semiconductors with various bandgaps are considered as promising candidates for versatile applications in nanoelectronics, optoelectronics, sensors, etc. This DPhil project aims to contribute to the field by developing fundamental knowledge in the synthesis of 2D layered semiconductors and their VLHs via vapour phase deposition, and also in subsequent characterisation of their material properties for optoelectronic applications.

Simple direct sulfurization process was first developed for 2D semiconductor $MoS_2$ which employs glass as a precursor-soluble substrate. This approach enables low cost and large-area uniformity as well as self-limiting crystal thickness and small nucleation density. Understanding of the diffusion-controlled dissolution and interface-limited precipitation processes facilitated morphological tuning of the $MoS_2$ single crystals. Then, thickness- and stoichiometric-controlled growth of 2D GaS, a wide bandgap semiconductor, was achieved by chemical vapour deposition (CVD). A detailed investigation was performed into the stoichiometry- and thickness-dependent stability, optical and optoelectronic properties of GaS.

Both layer-by-layer growth and stacking assembly are commonly used for fabrication of 2D VLHs. Based on the Frenkel-Kontorova model, a general framework was proposed for understanding the origin of small twist angles in high-mismatch epitaxially-grown VLHs. Experimentally, the framework was tested on CVD-grown epitaxial GaS/$MoS_2$ and GaS/graphene by scanning transmission electron microscopy. Finally, the non-stoichiometric $GaS_{0.87}$ was stacked with $WS_2$ to investigate optoelectronic behaviour of the bilayer VLH. The band alignment and charge transfer behaviour of the isotype type-II heterojunction were probed by various spectroscopic characterisation techniques. In addition, both large linear dynamic range and large photoresponsivity across the visible light spectrum were observed for $GaS_{0.87}/WS_2$ photodetectors.

# Acknowledgements

The DPhil study during my last four years and this thesis cannot be completed without tremendous guidance and support from my supervisors, colleagues, family and friends. First and foremost, I would like to thank profoundly my supervisor, Professor Jamie Warner, for providing me with meticulous guidance about materials science and invaluable mentorship throughout the four years. His vigorous passion towards science and insightful wisdom have deeply influenced my transformation from a fresh graduate to an independent researcher. I am also grateful to Professor Harish Bhaskaran, who as my co-supervisor, supported me with encouragement and wisdom, especially in the difficult times of national lockdown.

I would like to express my deepest gratitude to all my colleagues at Nanostructured Materials Group who contributed their specialist expertise and knowledge in this work. Dr. Tongxin Chen contributed enormously through selfless training me on various lab skills and thinkings, as well as constant brainstorming, collaboration and criticising to shape my work. Dr. Jun Chen conducted STEM imaging of GaS and heterostructures and generously supported my image simulation and analysis even after graduation. Dr. Xiaochen Wang initiated the research on the CVD growth of gallium sulfide which laid a solid foundation for my research. Dr. Yuewen Sheng and Dr. Ren-Jie Chang provided deep insights and support about CVD growth and setup and other knowledge without reservation, which greatly aided in developing novel synthesis routes. Additionally, I would like to thank Dr. Viktoryia Shautsova for help and advice with AFM characterisation and Dr. Gyeonghee Ryu for STEM imaging of $MoS_2$. I am thankful to my peers, Ms. Linlin Hou, Ms. Yi Wen and Ms. Qianyang Zhang for helpful discussions, company and encouragement during the many out-of-hours lab sessions. I also

appreciate Mr. Matthew Coupin and Dr. Hyoju Park from Prof. Jamie Warner's group at University of Texas, Austin for their support in image processing. The rest of my colleagues, Dr. Wenshuo Xu, Dr. Yingqiu Zhou, Dr. Sha Li, Dr. Hefu Huang, Dr. Sapna Sinha, Dr. Martin Tweedie, Mr. Peng Tang and others provided constructive advices during discussions, which broadened my horizon and improved the research.

I would also like to show my earnest appreciation for collaborators in Professor Harish Bhaskaran's group. The expertise and extensive support of Ms. Yu Shu on the use of AFM was greatly appreciated. I acknowledge Dr. Nhlakanipho Mkhize for performing KPFM analysis and Dr. Xuan Li for sharing her knowledge on nanofabrication techniques. In addition, I would like to thank Dr. Philip Holdway for conducting XPS analysis and Mr. Paul Pattinson for successful maintaining of the amazing cleanroom facilities. I am also thankful to Dr. Yutian Wen, Dr. Xinya Bian, Ms. Ross Luo, Mr. Jiangrui Qian for enriching my knowledge of a broad field in materials science.

Lastly, I would like to devote my sincere gratitude to my parents for their unconditional love and financial support during the four-year period, and my beloved girlfriend Yu Shu for her understanding and inspiration behind my every achievement.

# Publications

Here presents a list of work that is published or is in the process of being published during the course of this project. In this thesis, Chapter 2 uses some writing from Ref. 3. Chapter 4 is based on Ref. 1. Chapter 5 is based on Ref. 2. Chapter 6 is based on Ref. 5 and Chapter 7 is based on Ref. 4.

**First-Author:**

1. **Lu, Y.**; Chen, T.; Ryu, G. H.; Huang, H.; Sheng, Y.; Chang, R.-J.; Warner, J. H., Self-Limiting Growth of High-Quality 2D Monolayer $MoS_2$ by Direct Sulfurization Using Precursor-Soluble Substrates for Advanced Field-Effect Transistors and Photodetectors. *ACS Applied Nano Materials* **2018**, *2* (1), 369-378.
2. **Lu, Y.**; Chen, J.; Chen, T.; Shu, Y.; Chang, R.-J.; Sheng, Y.; Shautsova, V.; Mkhize, N.; Holdway, P.; Bhaskaran, H.; Warner, J. H., Controlling Defects in Continuous 2D GaS Films for High-Performance Wavelength-Tunable UV-Discriminating Photodetectors. *Advanced Materials* **2020**, *32* (7), 1906958.
3. **Lu, Y.** and Warner, J. H., Synthesis and Applications of Wide Bandgap 2D Layered Semiconductors Reaching the Green and Blue Wavelengths. *ACS Applied Electron Materials* **2020**, *2* (7), 1777-1814.
4. **Lu, Y.**; Chen, T.; Mkhize, N.; Chang, R.-J.; Sheng, Y.; Holdway, P.; Bhaskaran, H.; Warner, J. H., GaS:$WS_2$ Heterojunctions for Ultrathin Two-Dimensional Photodetectors with Large Linear Dynamic Range across Broad-Wavelengths. *ACS Nano* **2021**, *15* (12), 19570-19580.
5. **Lu, Y.;** Chen, J.; Coupin, M. J.; Sinha, S.; Warner, J. H., Lattice Mismatch Driven Small Angle Moiré Twists in Epitaxial 2D Vertical Layered Heterostructures. **2021**, *Under review.*

**Co-Author:**

6. Chen, J.; Zhou, S.; Wen, Y.; Ryu, G. H.; Allen, C.; **Lu, Y.**; Kirkland, A. I.; Warner, J. H., In situ high temperature atomic level dynamics of large inversion domain formations in monolayer $MoS_2$. *Nanoscale* **2019**, *11* (4), 1901-1913.
7. Sheng, Y.; Chen, T.; **Lu, Y.**; Chang, R.-J.; Sinha, S.; Warner, J. H., High-performance $WS_2$ monolayer light-emitting tunneling devices using 2D materials grown by chemical vapour deposition. *ACS Nano* **2019**, *13* (4), 4530-4537.
8. Chang, R.-J.; Sheng, Y.; Chen, T.; Mkhize, N.; **Lu, Y.**; Bhaskaran, H.; Warner, J. H., Morphology Control of Two-Dimensional Tin Disulfide on Transition Metal Dichalcogenides Using Chemical Vapour Deposition for Nanoelectronic

Applications. *ACS Applied Nano Materials* **2019**, *2* (7), 4222-4231.

9. Chang, R.-J.; Sheng, Y.; Ryu, G. H.; Mkhize, N.; Chen, T.; **Lu, Y.**; Chen, J.; Lee, J. K.; Bhaskaran, H.; Warner, J. H., Postgrowth Substitutional Tin Doping of 2D $WS_2$ Crystals Using Chemical Vapour Deposition. *ACS Applied Materials & Interfaces* **2019**, *11* (27), 24279-24288.
10. Chen, J.; Ryu, G. H.; Zhang, Q.; Wen, Y.; Tai, K.-L.; **Lu, Y.**; Warner, J. H., Spatially Controlled Fabrication and Mechanisms of Atomically Thin Nanowell Patterns in Bilayer $WS_2$ Using in Situ High Temperature Electron Microscopy. *ACS Nano* **2019**, *13* (12), 14486-14499.
11. Chen, T.; **Lu, Y.**; Sheng, Y.; Shu, Y.; Li, X.; Chang, R.-J.; Bhaskaran, H.; Warner, J. H., Ultrathin All-2D Lateral Graphene/GaS/Graphene UV Photodetectors by Direct CVD Growth. *ACS Applied Materials & Interfaces* **2019**, *11* (51), 48172-48178.
12. Shautsova, V.; Sinha, S.; Hou, L.; Zhang, Q.; Tweedie, M.; **Lu, Y.**; Sheng, Y.; Porter, B. F.; Bhaskaran, H.; Warner, J. H., Direct Laser Patterning and Phase Transformation of 2D $PdSe_2$ Films for On-Demand Device Fabrication. *ACS Nano* **2019**, *13* (12), 14162-14171.
13. Gerkman, M. A.; Lee, J. K.; Li, X.; Zhang, Q.; Windley, M.; Fonseca, M. V.; **Lu, Y.**; Warner, J. H.; Han, G. G., Direct Imaging of Individual Molecular Binding to Clean Nanopore Edges in 2D Monolayer $MoS_2$. *ACS Nano* **2020,** *14* (1), 153-165.
14. Li, X.; Lee, J. K.; **Lu, Y**; Gerkman, M. A.; Kengmana, E. S.; Fonseca, M. V.; Warner, J. H.; Han, G. G., Precursor Design for High Density Single Pt Atom Sites on $MoS_2$: Enhanced Stability at Elevated Temperatures and Reduced 3D Clustering. *Chemistry of Materials* **2020**, *32* (6), 2541-2551.
15. Tai, K.-L.; Chen, J.; Wen, Y.; Park, H.; Zhang, Q.; **Lu, Y**; Chang, R.-J.; Tang P.; Allen, C. S.; Wu W.-W.; Warner, J. H., Phase Variations and Layer Epitaxy of 2D $PdSe_2$ Grown on 2D Monolayers by Direct Selenization of Molecular Pd Precursors. *ACS Nano* **2020**, *14* (9), 11677-11690.
16. Shu, Y.; Porter, B. F.; Soh, E. J. H.; Farmakidis, N.; Lim, S.; **Lu, Y**; Warner, J. H.; Bhaskaran, H., Nanoscale Bilayer Mechanical Lithography Using Water as Developer. *Nano Letters* **2021**, *21* (9), 3827-3834.
17. Zhang, Q.; Hou, L.; **Lu, Y**; Chen, J.; Zhou, Y.; Shautsova, V.; Warner, J. H., Large-Scale Uniform-Patterned Arrays of Ultrathin All-2D Vertical Stacked Photodetector Devices. *ACS Applied Materials & Interfaces* **2021**, 13 (29), 34696-34704.

# Table of Contents

**Chapter 1 Introduction** ..... **1**
1.1 Project Aims ..... 1
1.2 The Scope of this Thesis ..... 1
**Chapter 2 Literature Review** ..... **4**
2.1 Introduction ..... 4
2.1.1 What Are 2D Layered Semiconductors and VLHs? ..... 4
2.1.2 Why Are 2D Layered Semiconductors and VLHs Important? ..... 6
2.2 Properties of 2D Layered Semiconductors ..... 7
2.2.1 Crystal Structure ..... 7
2.2.2 Electronic Properties ..... 11
2.2.3 Optical Properties ..... 18
2.2.4 Stability ..... 23
2.3 Synthesis of 2D Layered Semiconductors ..... 25
2.3.1 Mechanical Exfoliation ..... 26
2.3.2 Liquid Phase Exfoliation ..... 27
2.3.3 Vapour Phase Deposition ..... 29
2.4 Fabrication and Properties of VLHs ..... 51
2.4.1 Manual Assembly ..... 51
2.4.2 Layer-by-Layer Growth ..... 53
2.4.3 Energy Band Alignment ..... 56
2.4.4 Twistronics ..... 58
2.5 Ultrathin Optoelectronics Based on 2D Layered Semiconductors ..... 60
2.5.1 Photoconductors ..... 61
2.5.2 Photodiodes ..... 67
2.5.3 Light Emitting Diodes ..... 71
2.6 Conclusion and Future Outlook ..... 76
2.7 References ..... 77
**Chapter 3 Methodology** ..... **97**
3.1 Introduction ..... 97
3.2 Vapour Phase Deposition Synthesis of 2D Materials ..... 97

3.2.1 Synthesis of $MoS_2$ ..... 97
3.2.2 Synthesis of GaS ..... 99
3.2.3 Synthesis of Graphene ..... 99
3.2.4 Synthesis of $WS_2$ ..... 100
3.2.5 Synthesis of GaS-Based VLHs ..... 101
3.3 Transfer of 2D Materials ..... 102
3.3.1 Transfer of 2D Materials on Glass Substrates ..... 102
3.3.2 Transfer of 2D Materials on $SiO_2$/Si Substrates ..... 102
3.3.3 Transfer of 2D Materials on Cu Substrates ..... 103
3.4 Microscopy Characterisation ..... 103
3.4.1 Optical Microscopy ..... 103
3.4.2 Scanning Electron Microscopy ..... 104
3.4.3 Annular Dark Field Scanning Transmission Electron Microscopy ..... 105
3.4.4 Atomic Force Microscopy ..... 107
3.5 Spectroscopic Characterisation ..... 107
3.5.1 Raman Spectroscopy ..... 107
3.5.2 Photoluminescence Spectroscopy ..... 110
3.5.3 X-Ray Photoelectron Spectroscopy ..... 111
3.5.4 Energy-Dispersive X-Ray Spectroscopy ..... 112
3.5.5 Cathodoluminescence ..... 113
3.6 Device Measurement ..... 114
3.6.1 Device Fabrication ..... 114
3.6.2 Electrical and Optoelectrical Measurement ..... 115
3.7 References ..... 117
**Chapter 4 Facile, Uniform and Low-Cost Growth of Large Monolayer $MoS_2$ Single Crystals ..... 119**
4.1 Introduction ..... 119
4.2 Results and Discussion ..... 121
4.2.1 Self-Limiting Sulfurization at Vapour-Solid Interface ..... 121
4.2.2 Morphological Control of $MoS_2$ Crystals ..... 129
4.2.3 Characterisation and Properties of $MoS_2$ Crystals ..... 134
4.3 Conclusion ..... 139
4.4 References ..... 140
**Chapter 5 Synthesis of High-Quality Continuous 2D GaS Films ..... 144**

5.1 Introduction ..... 144
5.2 Results and Discussion ..... 146
5.2.1 Controlling Stoichiometry in Continuous 2D GaS Films ..... 146
5.2.2 Thickness- and Stoichiometry-Dependent Properties of GaS ..... 153
5.2.3 Degradation Mechanism of 2D GaS ..... 162
5.3 Conclusion ..... 168
5.4 References ..... 169
**Chapter 6 Commensurability of van der Waals Epitaxy in High-Mismatched Systems ..... 172**
6.1 Introduction ..... 172
6.2 Results and Discussion ..... 173
6.2.1 Commensurate Multilevel Maps ..... 173
6.2.2 Growth and Characterisation of High-Mismatched Epitaxial Systems ..... 183
6.2.3 Visualisation of Moiré Patterns ..... 188
6.3 Conclusion ..... 190
6.4 References ..... 190
**Chapter 7 Understanding Interfacial Coupling in $GaS_{0.87}/WS_2$ VLH for High Performance Photodetectors ..... 194**
7.1 Introduction ..... 194
7.2 Results and Discussion ..... 198
7.2.1 Band Alignment of Bilayer $GaS_{0.87}/WS_2$ VLH ..... 198
7.2.2 Characterisation of Charge Transfer Under Visible Light Excitation ..... 201
7.2.3 Mechanism for Achieving Large Linear Dynamic Range ..... 207
7.3 Conclusion ..... 215
7.4 References ..... 216
**Chapter 8 Conclusions ..... 221**
8.1 Thesis summary ..... 221
8.2 Outlook ..... 224

# Chapter 1

# Introduction

## 1.1 Project Aims

This doctorate project aims to develop and optimise vapour phase deposition (VPD) techniques for the growth of two-dimensional (2D) layered semiconductors and vertical layered heterostructures (VLHs) mainly based on molybdenum disulfide ($MoS_2$) and gallium sulfide (GaS), to investigate the properties of these semiconductors via a variety of characterisation techniques, and to explore and understand new phenomena in the VLHs systems due to strong structural and electronic coupling between layers.

## 1.2 The Scope of this Thesis

This thesis covers research that I have undertaken over the time span of four years of UK DPhil degree at Department of Materials, University of Oxford. It begins with a literature review in Chapter 2 that summarises the recent advances on the synthesis and properties of 2D layered semiconductors and VLHs, as well as their applications in optoelectronics. This is followed by methodology in Chapter 3 which briefly provides the experimental details on VPD setup and synthesis of 2D materials, various characterisation and nanofabrication techniques, as well as measurements of 2D devices.

The first task, summarised in Chapter 4, is to develop a simple, low-cost and large-scale growth route for the well-studied 2D semiconductor $MoS_2$. The concept of 'precursor-

soluble substrate' is introduced in 2D semiconductor synthesis for the first time, which guarantees uniform crystal thickness and small nucleation density using the direct sulfurization procedure. The diffusion-controlled dissolution and interface-limited precipitation processes are further confirmed under X-ray photoemission spectroscopy (XPS), which guides morphological tuning of nucleation density, crystal size and coverage. This method shows tremendous advantages in large-scale production of $MoS_2$ single crystals, and has already facilitated several new research projects conducted by collaborators in many fields including electron microscopic imaging, catalysis and optoelectronics.

Subsequently, the study turned to the synthesis of wide bandgap 2D semiconductors, which are essential for applications regarding wavelengths in the visible or UV range. In Chapter 5, a thickness- and stoichiometric-controlled growth method for 2D GaS films by chemical vapour deposition (CVD) is established. A detailed investigation into the stoichiometry- and thickness-dependent optical properties, stability and optoelectronic properties of GaS is conducted. These characterisations help to unveil possible degradation mechanisms of GaS. Owing to its large bandgap, defect-free 2D GaS shows UV-discriminating photoresponse.

Subsequent to the synthesis of high-quality 2D layered semiconductors, this thesis shifts its focus to potential applications of 2D VLHs in next-generation optoelectronics. Layer-by-layer overgrowth is considered as one potential route for large-scale fabrication of 2D VLHs. In Chapter 6, the concept of van der Waals (vdWs) epitaxial growth is revisited in VLHs with high lattice mismatch. The weak vdWs interactions allow great tolerance for lattice mismatch and misalignment, which leads to different manifestation of epitaxy from conventional semiconductors. Based on the Frenkel-Kontorova model, a general framework is proposed where epitaxy in high-mismatched

vdWs systems is governed by commensurability, and a commensurate multilevel map is introduced. Experimentally, GaS/$MoS_2$ and GaS/graphene vdWs heterostructures with large lattice mismatch are obtained by CVD and characterised under scanning transmission electron microscopy. The observed mismatch-twist angle relation suggests good accordance with the theory, indicating the requirement of a more comprehensive description of epitaxy.

Besides layer-by-layer growth, assembling 2D layered materials is another popular method to fabricate 2 D VLHs for the exploration and demonstration of novel properties. Chapter 7 reports novel optoelectronic behaviours in stacked bilayer $GaS_{0.87}/WS_2$ VLH where both large linear dynamic range and large photoresponsivity are achieved across the visible light spectrum. The band alignment information is probed by XPS, photoluminescence and cathodoluminescence. Subsequently, charge transfer behaviour is evidenced via photoluminescence and Kelvin probe force microscopy. Further device measurements suggest increased mobility in the dual channel under the visible light. This work proposes a novel design route for improving performance of 2D photodetectors, and provides deep insights into how coupled behaviour between 2D layered semiconductors could offer heterostructures with desired properties and functions.

The last chapter summarises and concludes the whole thesis. Several potential aspects of future works as the extension to this thesis are also envisioned

# Chapter 2

# Literature Review

## 2.1 Introduction

### 2.1.1 What Are 2D Layered Semiconductors and VLHs?

As the name of 2D suggests, their properties are different from bulk materials in one of the three dimensions, resembling a large but very thin piece of paper. 2D layered materials, also called vdWs layered materials, are featured for their high bonding anisotropicity. These materials have a layered structure where complete chemical bonding is formed within one layer but the adjacent layers are bonded by vdWs interactions. Non-layered materials present tremendous dangling bonds on the surface when being thinned down, leading to unwanted surface states with high reactivity. In comparison, layered materials are regarded as the flattest surface which is relatively stable and could reveal the intrinsic nanoscale properties or quantum phenomena in such systems. The layered structure also enables easy isolation of the materials down to one single layer of few-atom-thickness, which makes these systems among the thinnest platforms.

So far, theoretical calculations have predicted over 1,800 layered crystals that are potentially easily exfoliable.[1] Among the vast family, many of them have exhibited semiconductor properties that are especially promising for a wide range of applications in transistors, energy harvesting and light emitting.[2-4] 2D layered semiconductors have been demonstrated with very different behaviours than their 3D counterparts, such as the variation of bandgap, strong light-matter interactions and efficient gate

modulation.[5-6] A wide variety of 2D layered semiconductors have been successfully isolated and studied in recent years, and some examples that have attracted particular interests include black phosphorus, transition metal dichalcogenides (TMDs), post-transition metal monochalcogenides (MX compounds) and so on.[7]

VLHs, or vdWs heterostructures are artificial materials made by stacking different 2D layered materials on top of one another. The word vertical is to differentiate with lateral heterostructures formed by in-plane bondings that are not in the scope of this study.[8] The facile assembly of 2D building blocks one-by-one is analogous to 'Lego' blocks (Fig. 2.1),[9] but these blocks are even fancier: owing to the weak, non-directional and unsaturated vdWs interactions, even crystals with different crystal structures and lattice parameters can be put together without suffering from local strain or dangling bonds. Thus the intrinsic properties of each material are largely preserved while interesting properties from the interface can be observed as well. In addition, the orientation between different layers can also be manually controlled to form a twist, which have spurred a novel research field of twistronics.[10] Thus, artificial structures of VLHs with almost no restriction on components or orientation represent another novel and versatile platform, allowing further modification of properties and functionalities of 2D materials.

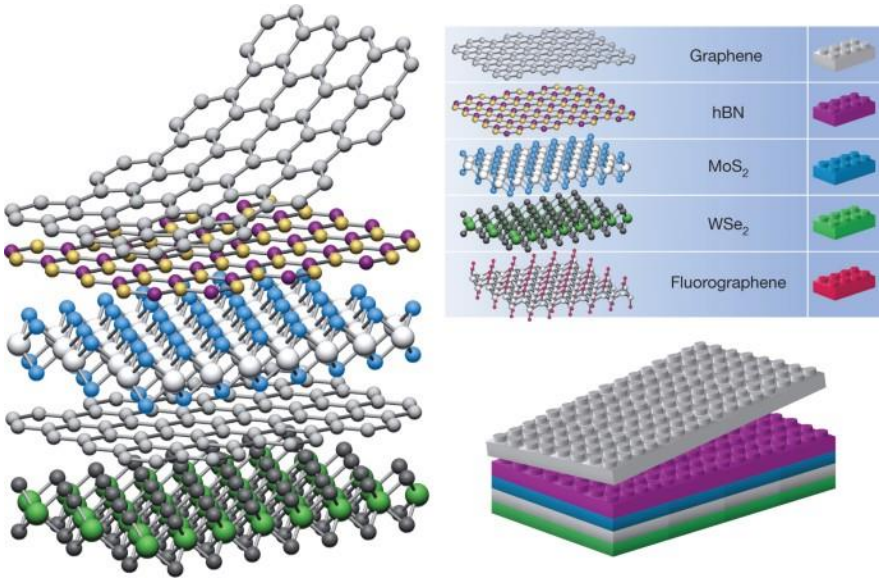



**Figure 2.1. Construction of a huge variety of layered structures analogous to Lego blocks (right panel).** Reproduced with permission from ref. 9. Copyright 2013 Springer.

### 2.1.2 Why Are 2D Layered Semiconductors and VLHs Important?

Similar to graphene and other 2D layered materials, one critical advantage of 2D layered semiconductors over other nanomaterials is the capability to be incorporated into the extensively-used planar device manufacturing technology in silicon-based microelectronics. But 2D layered semiconductors have many other unique characteristics that render themselves a heated research field.

The energy bandgap in 2D layered semiconductor presents another critical advantage for many applications in electronics and optoelectronics. Unlike graphene or other metallic 2D layered materials, 2D layered semiconductors have been demonstrated with high on-off ratio of $10^8$ for building transistors to extend the Moore's law or making memory devices.[11-13] Also differing from insulators such as h-BN, 2D layered semiconductors show enhanced excitonic effects due to the reduced dielectric screening effect.[14] As semiconductor-based heterostructures are cornerstones of contemporary

transistors and light emitting diodes (LEDs), these 2D layered semiconductors are highly promising in fabricating high-performance optical sensors, emitters, solar cells, hydrogen generation centres for next-generation nano-devices.[15-17] In addition, 2D layered semiconductor based heterostructures are regarded as the host of many novel and intriguing interlayer coupling behaviours where crystals with different properties are confined within atomic scale.[18-19]

In this chapter, a brief introduction of properties of 2D layered semiconductors and heterostructures is presented in section 2.2, with further detailed discussion on the case of the two main materials studied in this thesis, $MoS_2$ and GaS. Section 2.3 focuses on recent advances in synthesis of 2D layered semiconductors. Section 2.4 outlines current techniques in designing and fabricating 2D layered semiconductor based VLHs. In section 2.5, common optoelectronics applications based on 2D layered semiconductors and VLHs are highlighted. Finally, a brief discussion in section 2.6 concludes the review on synthesis and properties of 2D layered semiconductors and heterostructures, and their implications on the development of these scientific knowledge and technology from laboratory to industrial applications.

## 2.2 Properties of 2D Layered Semiconductors

### 2.2.1 Crystal Structure

In general, 2D layered semiconductors have chemical bonds within one layer and weak vdWs force between layers. The in-plane crystal structure affects many properties. For example, a lack of inversion symmetry in monolayer TMDs has led to valley polarisation and nonlinear optics such as second harmonic generation. In addition,

many 2D materials possess multiple polymorphs or stacking orders, which affect the crystal's properties.

In TMDs such as $MoS_2$, each layer is composed of three X-M-X (X for chalcogenide and M for metal) atomic planes with a layer thickness of around 0.65-0.8 nm from previous reports (Fig. 2.2).[20-21] For monolayer $MoS_2$, two polymorphs exist according to the location of the coordinating six S atoms around each Mo atom. The trigonal prismatic coordination (point group $D_{3h}$) is referred as 1H which has in-plane mirror symmetry, and the octahedral coordination (point group $D_{3d}$) is referred as 1T which has inversion symmetry. For multilayer $MoS_2$ with trigonal prismatic coordination, two further polytypes are commonly found dependent on the stacking order. One is the 2H phase where the S or Mo atom of the second layer is right on top of the Mo or S atom of the first layer. From the top view, the void hexagonal centres are aligned and the two layers have 60°-orientation. The other one is the 3R phase, where all layers have 0°-orientation to each other with staggering overlapping of S atom, Mo atom and the void hexagonal centres. The number in the polymorph symbol indicates the number of layers in the unit cell, and the letter corresponds to the crystal symmetry (T for trigonal, H for hexagonal and R for rhombohedral). Among the IT, 2H and 3R phases, the 2H and 3R phases (and 1H in monolayer) are more energetically favourable compared with the metastable 1T phase. In addition, the 2H and 3R phases are semiconductors while the 1T phase is a metal.

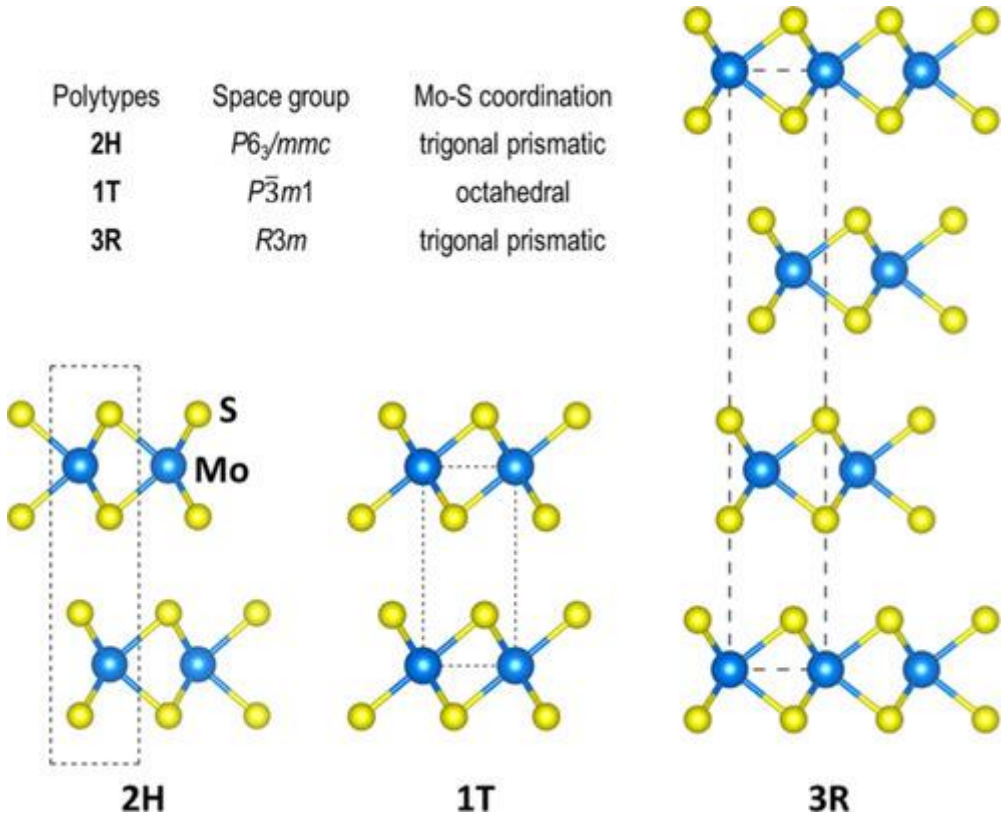



**Figure 2.2. Crystal structure of $MoS_2$.** Reproduced with permission from ref. 22. Copyright 2018 Wiley-VCH.

In group III-VI MX compounds such as GaS, each layer of the crystal consists of quaternary planar layers of close-packed X-M-M-X atoms connected by covalent bonds and also shows a 3-fold honeycomb symmetry similar to those of graphene and the 1H TMD monolayers (Fig. 2.3a). Based on various reports, the measured thicknesses of individual monolayer GaS, GaSe and InSe are similar to each other and are in the range of 0.8–1.0 nm.[23] These layers are stacked together with weak vdW bonds, which makes themselves easy to be exfoliated. Differences in stacking order are categorised into four main polymorphs, as shown in Figure 2.3b. The most thermodynamically stable polytype under ambient conditions is the β-GaS, where both Ga or S atoms from the second layer are aligned with S or Ga in the first layer.

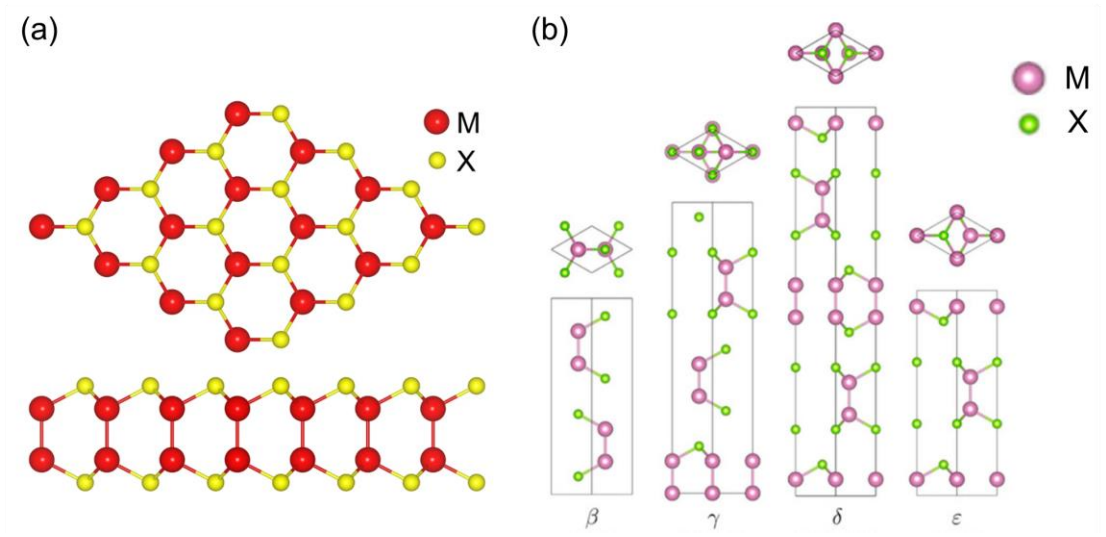



**Figure 2.3. Atomic structure of group III−VI MX compounds.** (a) Side and top view of honeycomb structure of monolayer group III−VI MX compounds. Reproduced with permission from ref. 24. Copyright 2019 Springer. (b) Top view and side view of unit cells of four polytypes, β, γ, δ and ε of multilayer group III-VI MX compounds. Reproduced with permission from ref. 25. Copyright 2018 AIP Publishing.

The structural diversity of 2D crystals offers vast opportunities as well as challenges in synthesis to obtain crystals with the desired phases. As an example, Lee et al.[26] used atomic resolution cross-sectional ADF-STEM to show that most regions of GaSe exhibit the most stable 0°-orientation ε-GaSe stacking polytype, while at certain regions a 60° rotation can be observed, corresponding to the β-GaSe polytype. These results are in accordance with Li et al.'s calculations of rotational energy barriers in bilayer triangular GaSe domains from 0° (ε-GaSe) to 60° (β-GaSe).[27] The results show that 60°-orientation is another local energy minimum, which explains why β-GaSe presents but is not dominant. In addition, they noted that the rotational energy barriers are also size dependent; therefore β-GaSe is more likely to form at a nanoscale nucleation site during the initial stage of growth. Besides structural characterisation tools such as

atomic resolution ADF-STEM or Raman spectroscopy, the polymorphs can also be easily distinguished based on their electronic or optical properties such as absorption or photoluminescence spectroscopies.[20, 23]

### 2.2.2 Electronic Properties

(1) Band Structures

For studying electronic properties of 2D layered semiconductors, it is a prerequisite to understand their electronic band structures and the values of their bandgaps. The bandgap of a semiconductor can be divided into electronic bandgap ($E_{eg}$) and optical bandgap ($E_{og}$). The optical bandgap corresponds to the minimum energy a photon has to be absorbed with the formation of an exciton, while the electronic bandgap is the minimum energy to excite the electron in the valence band (VB) into the conduction band (CB) without the formation of bound electron–hole pairs. In other words, $E_{eg} = E_{og} + E_b$, where $E_b$ is the exciton binding energy. In 3D semiconductors, the strong electric field screening leads to a weak Coulomb interaction between the electron and hole, and the exciton binding energy is very small; therefore the difference of the two bandgap values can be ignored. In 2D layered semiconductors, however, the quantum confinement results in a large $E_b$ (usually about the order of hundreds of meV in a single layer). Therefore, optical bandgap values are frequently used in phenomena associated with the strong light–matter interactions and excitonic effects.

Currently, many characterisation techniques for experimentally determining the optical bandgap of 2D semiconductors have been reported, including UV–vis absorption spectroscopy, photoluminescence (PL) spectroscopy, cathodoluminescence (CL) spectroscopy, angle-resolved photoemission spectroscopy (ARPES), etc. In the UV–

vis absorption spectrum, the onset of absorption gives the bandgap value because a transition in the middle of the gap is forbidden. The onset can be determined using the equation $(\alpha h\nu)^n = A(h\nu - E_g)$, where n = 2 for a direct allowed transition and n = 0.5 for an indirect allowed transition. PL spectroscopy gives the emission spectrum of the material, which is very important for lighting applications. And under high excitation energy, more-complex quasi-particle systems, such as trions or biexcitons, have been observed in 2D materials that generate emission with energy smaller than that of the exciton peak. Both methods involve higher energy photon excitation of electrons in the VB into the CB. The absorption and excitation of photons in indirect bandgap semiconductors is forbidden without the spontaneous absorption or emission of a phonon; hence the signals in indirect bandgap semiconductors are usually weak. CL spectroscopy uses a high-energy electron beam to excite the VB electrons, where electrons can provide momentum, therefore allowing an indirect band transition, although due to the ultrathin thickness it might be challenging to detect the CL signal, as the electron–hole creation cross section is extremely small. Still, monolayer GaS and GaSe have shown good CL signals that could be further enhanced by h-BN encapsulation.[28-29] Finally, ARPES provides direct observation of the distribution of electrons in reciprocal space and can offer much detailed information about electronic band structure.[30-31]

The band structures of 2D layered semiconductors are significantly dependent on the number of layers due to interlayer interactions as well as quantum confinement effects. For example, 2H-$MoS_2$ undergoes indirect-to-direct bandgap transition from bulk to monolayer (Fig. 2.4a). In bulk $MoS_2$ with an indirect bandgap of 1.2−1.3 eV, the valence band maximum (VBM) is located at the Γ point in the Brillouin zone and the conduction band minimum (CBM) is positioned in the middle between the Γ and K

points.[20, 32] With decreasing number of layers down to a few layers, the change in interlayer interactions exhibits different effects on band states at different the points in the Brillouin zone. The VB states at the Γ point shift downwards and the CB states at the Γ point shift upwards, while the band states at the K point hardly moves. At monolayer thickness, the VBM and CBM both shift to the K point in the Brillouin zone, leading to a direct bandgap of 1.8−1.9 eV. The direct band-to-band transition process without involvement of phonons leads to the high efficiency in monolayer $MoS_2$ PL signals.[32] Many other TMDs like $MoSe_2$ and $WS_2$ also exhibits indirect-to-direct bandgap transition from bulk to monolayer. In contrast, many members of the group III−VI MX compounds show direct-to-indirect bandgap transition from bulk to atomically thin layers.

In bulk GaS, experimental results suggest the smallest bandgap is indirect at ~2.5 eV while the second smallest bandgap is direct at ~3.0 eV.[33-34] The CBM is located at the M point in the Brillouin zone and the VBM is situated at the Γ point. Bilayer GaS was measured with an indirect bandgap of 3.02 eV and monolayer GaS with an indirect bandgap of 3.325 eV.[28, 35] These results indicate similar increase in bandgap due to quantum confinement effects. In addition, many atomically thin group III-VI MX compounds such as GaSe and InSe have experimentally shown a Mexican-hat-shape dispersion by ARPES, where two split VBM positions are observed around the Γ point.[31, 36-37] This unique band structure results in van Hove singularity in the density of states near the VBM, which could give rise to excellent thermoelectric properties[38], tunable magnetism via hole-doping, half-metallicity and so on.[39]

Various calculation results have predicted similar features in atomically thin GaS where the CBM remains at the M point while the VBM is split into two around the Γ point.[40-

[41] The split of VBM is more prominent for crystals with number of layers below four (Fig. 2.4b), although further experimental evidence is required, as these calculation results have shown underestimation of the bandgap value compared with experiments.

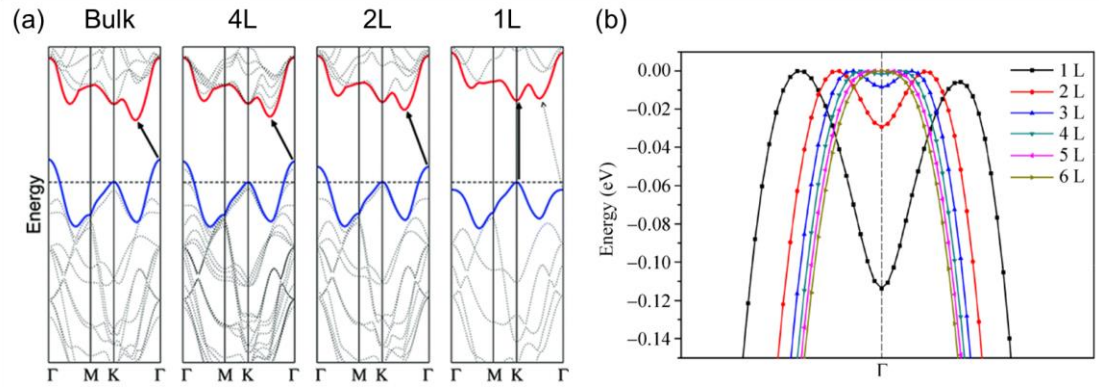



**Figure 2.4. Band structure evolution of 2D layered semiconductors with number of layers.** (a) Calculated band structures of bulk, 4L, 2L and 1L $MoS_2$. The black solid arrows indicate the lowest energy transitions. Reproduced with permission from ref. 32. Copyright 2010 American Chemistry Society. (b) First principles calculation results of Mexican-hat-shape dispersion around VBM in 2D β-GaS with layers from 1L to 6L. The valence band structure is computed along K→Γ→M with the dashed line indicating the position of the Γ point. Reproduced with permission from ref. 41. Copyright 2015 Springer.

GaS and some other group III-VI MX compounds are among the first developed 2D semiconductors with large bandgap. To date, many of the studies concentrate on narrow bandgap semiconductors (bandgap $E_g$ < 2 eV) such as $MoS_2$, $WSe_2$ and black phosphorus (Fig. 2.5a).[1, 5, 11, 42] Wide bandgap semiconductors ($E_g$ > 2 eV) have become very important for the electronics, optoelectronics and power industries as well.[43-45] They are also essential for applications relating to visible light such as imaging and lighting, as photons with energy within this range include almost all colours from orange to purple, except red. From both scientific and industrial points of view, the

development of wide bandgap 2D semiconductors shares equal importance with narrow bandgap 2D semiconductors in order to push forward the next revolution in nanodevices. Still, only a few wide bandgap 2D semiconductors have been confirmed today, with the experimentally measured bandgap values summarised in Figure 2.5b.

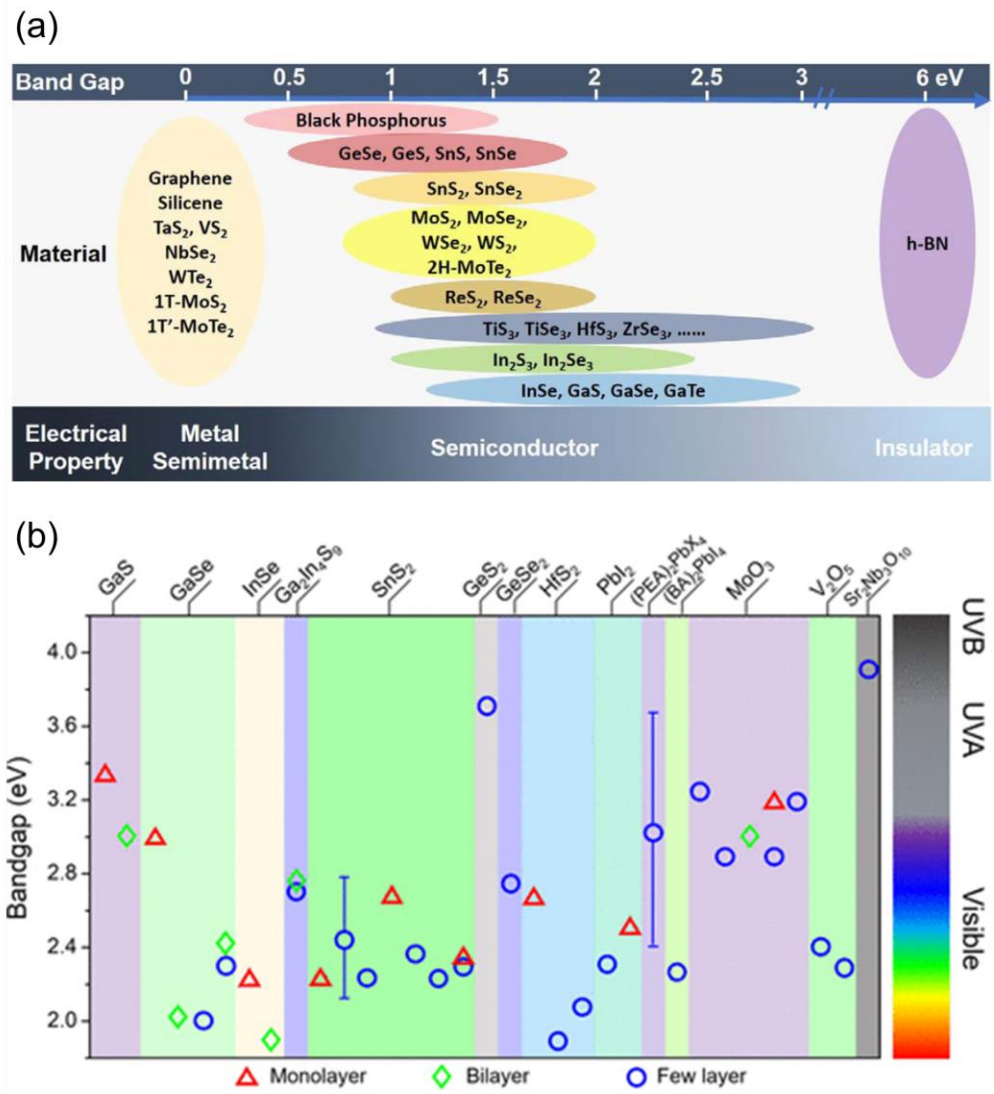



**Figure 2.5. Bandgap of 2D layered semiconductors.** (a) Summary of bandgaps of various 2D materials. Reproduced with permission from ref. 46. Copyright 2018 IEEE. (b) Experimentally obtained optical bandgap of wide bandgap 2D materials. GaS: 3.325 eV (M),[28] 3.02 eV (B).[35] GaSe: 3.001 eV (M),[28] 2.02 eV (B),[47] 2.0 eV (F),[48] 2.42 eV (B),[49] 2.27 eV (F).[49] InSe: 2.2 eV (M),[50] 1.88 eV (B).[49] $Ga_2In_4S_9$: 2.76 eV (B), 2.7 eV (F).[51] $SnS_2$: 2.23 eV (M),[52] 2.1–2.77 eV (F),[53] 2.23 eV (F),[54] 2.6 eV (M),[55] 2.35 eV (F),[56] 2.21 eV (F),[57] 2.34 eV (M),[58] 2.29 eV (F).[58]

$GeS_2$: 3.71 eV (F).[59] $GeSe_2$: 2.74 eV (F).[60] $HfS_2$: 2.64 eV (M),[61] 1.87 eV (F),[62] 2.07 eV (F).63 $PbI_2$: 2.3 eV (F),[64] 2.47 eV (M).[65] $(PEA)_2PbX_4$ (X = Cl, Br, I): 2.4–3.7 eV.[66] $(BA)_2PbI_4$: 2.24 eV.[67] $MoO_3$: 3.25 eV (F),[68] 2.9 eV (F),[69] 3.0 eV (B),[70] 3.2 eV (M),[71] 2.9 eV (F),[71] 3.2 eV (F).[72] $V_2O_5$: 2.4 eV (F),[73] 2.27 eV (F).[74] $Sr_2Nb_3O_{10}$: 3.9 eV (F).[75] (M for monolayer, B for bilayer, and F for few-layer.)

(2) Mobility

Extraction of the mobility value from field effect transistors (FETs) could be done by two methods. The effective mobility $\mu_{eff}$ is obtained from the linear region of the source-drain I−V curve (under $V_G > V_{th}$):

$$\mu_{eff} = \frac{g_d}{C_{ox}(V_G - V_{th})}\frac{L}{W} \tag{2.1}$$

where $g_d$ is the drain conductance ($g_d \equiv \partial I_{ds}/\partial V_{ds}$), $C_{ox}$ is the capacitance of the dielectric layer, $V_G$ is the gate voltage, $V_{th}$ is the threshold voltage, and $L$, $W$ are the geometric parameter (length and width) of the channel. The field-effect mobility $\mu_{FE}$ is obtained from the linear region ($V_G > V_{th}$) of the gate transfer curve:

$$\mu_{FE} = \frac{g_m}{C_{ox} \cdot V_{ds}}\frac{L}{W} \tag{2.2}$$

where $g_m$ is the transconductance ($g_d \equiv \partial I_{ds}/\partial V_{ds}$), $V_{ds}$ is the source-drain voltage.

Mobility in 2D semiconductors is restricted by a number of scattering effects including electron-phonon interactions (acoustic and optical), Coulomb effects from charged impurities, surface roughness and so on.[5] First principles calculations on monolayer $MoS_2$ suggest the carrier mobility is mainly limited by acoustic phonon scattering at low temperature (< 100K) and by optical phonon scattering at around room

temperature.[76] A room temperature limit of ~410 $cm^2V^{-1}s^{-1}$ is estimated for monolayer $MoS_2$ mobility. However, experimental demonstrations of 2D semiconductor devices report mobility values of 10−60 $cm^2V^{-1}s^{-1}$ for high-performance transistors.[11, 77-78] The deviation from theoretical value is found largely due to interfacial Coulomb scattering possibly from lattice defects, impurities or absorbates, which can be suppressed by optimising the fabrication process and screening with high-k dielectric materials such as $Al_2O_3$ or $HfO_2$. For example, early studies applying 30 nm thickness high-k $HfO_2$ top gates improved channel mobility of monolayer $MoS_2$ from ~1 to ~10 $cm^2V^{-1}s^{-1}$, with other extraordinary transistor figure of merits such as on-off ratio of $10^8$ and low SS slope of 70–75 mV $dec^{-1}$.[11, 77, 79]

The moderate mobility of monolayer $MoS_2$ at room temperature limits its application in the FET transport channel. This is partly related to the ultrathin thickness.[80] Li et al.[81] showed an increase in mobility from 20 in monolayer $MoS_2$ to 180 $cm^2V^{-1}s^{-1}$ in multilayer $MoS_2$, which is mainly attributed to the thickness-dependent Coulomb charge impurity scattering effect. It should be noted that the ultraflat surface and absence of dangling bonds in atomically thin 2D layered semiconductors make it more advantageous in short-channel devices compared to Si with comparable thickness.[82] Still, a higher mobility is needed in 2D layered semiconductors. Few-layer black phosphorus (10 nm) has exhibited room temperature mobility of 1,000 $cm^2V^{-1}s^{-1}$ with on-off ratio of $10^5$ and SS value of 4.6 V $dec^{-1}$.[42] Few-layer InSe (Eg ≈ 1.2 eV) has been demonstrated with the highest mobility (exceeding 1,000 $cm^2V^{-1}s^{-1}$) ever reported in 2D semiconductors due to a combination of weak electron–phonon scattering and a light electron effective mass ($m^*=0.145m_0$).[83-84]

Certain 2D layered semiconductors with reduced symmetry have also shown anisotropic in-plane mobility. For example, black phosphorous was reported with

mobilities with a ratio of 1.8 in the high conductance and low conductance directions.[85] Gu et al.[86] measured a ratio of 1.1 in anisotropic in-plane mobility for few layer $PdSe_2$ with high mobility of ~290 $cm^2V^{-1}s^{-1}$. Unlike the anisotropic out-of-plane mobility in 2D materials that originates from the vdWs gap, in-plane anisotropy is often related to differences in electron effective mass in different directions and could also result in anisotropic absorption, photoconductivity, thermal conductivity and so on. These materials are intriguing for fabrication of devices with anisotropic properties.

### 2.2.3 Optical Properties

(1) Excitonic Effects

Due to the quantum confinement effect and the reduced dielectric screening effect, the exciton binding energy in 2D semiconductors reaches several hundreds of meV which makes the bound state stable at room temperature. The strong Coulomb interaction in the tightly bound excitons promotes exciton recombination and photon emission in monolayer TMDs, which facilitates their application as light emitters.[87] For example, monolayer $MoS_2$ is measured with an exciton binding energy of 200−400 meV, and monolayer $WS_2$ has shown exciton binding energy of 300−700 meV.[14, 88-89]

Another important feature of the strong excitonic effect is the tunability of related quasiparticles. Excitons could further bind to another free carrier to form trions. While the trion binding energy is very small in quantum wells, in monolayer TMDs this value is 20−30 meV.[90-91] This results in the emergence of a trion emission peak even at room temperature. The trion peak with slightly smaller energy than the exciton emission peak can be separated by fitting the emission spectrum. In addition, the exciton and trion emission can be facially tuned either by electrostatic gating or molecular doping. Ross

et al.[92] demonstrated electrostatic gating control of excitons and trions in mechanically exfoliated $MoSe_2$. The colour map of PL spectra changing with gating voltage under low temperature shows an exciton emission peak of ~1.65 eV at intrinsic doping state (Fig. 2.6a), while showing a trion-dominated emission peak of ~1.63 eV at positive and negative gating voltages, which corresponds to electron-bounded trions and hole-bounded trions, respectively (Fig. 2.6b). The similar trion binding energy for electron and hole originates from their similar effective mass. They also studied the temperature dependence of PL emission and found more prominent trion emission at low temperature, as the thermal energy at high temperature assists dissociation of bound trions. Similar studies have also been done on monolayer $MoS_2$ and $WS_2$.[91, 93] Shang et al.[93] reported electrical doping effect on monolayer $WS_2$ at room temperature. At gate voltage higher than 25 V, they observed nearly disappeared exciton peak but nearly unchanged trion peak intensity, corresponding to the heavily doped case as the $WS_2$ is n-doped at 0 V gate voltage. In addition, the observed red-shift in trion peak position is influenced by the increase of Fermi level, leading to an increase in trion binding energy. Apparently the free carrier concentration is also affected by incident light, thus the trion to exciton ratio also increases with excitation power. Molecular doping has also been used to control the free carrier concentration in TMDs to tune their trion and exciton emission behaviour.[94-96] It was further shown that such doping can also enhance the PL quantum yield (QY). While 0.01-6% PLQY was often demonstrated in monolayer $MoS_2$, Amani et al.[97] observed near-unity PLQY in TSFI-treated samples at low excitation power. A long recombination lifetime of ~10 ns was measured, which is an order higher than untreated samples. The strong suppression of non-radiative decay was speculated to be from the removal of absorbed water, hydroxyl groups and other contaminants on the surface. The exposed surface allows sulfur vacancies to rearrange

with sulfur adatoms under the presence of TSFI, to approach stoichiometric $MoS_2$. Similar strategy has been applied in other 2D semiconductors such as InSe to improve optical properties and device performance.[98] Other more complex quasiparticle systems such as biexcitons or charged biexcitons have also been observed under high excitation power, which are usually significant at very low temperatures.[93, 99-101]

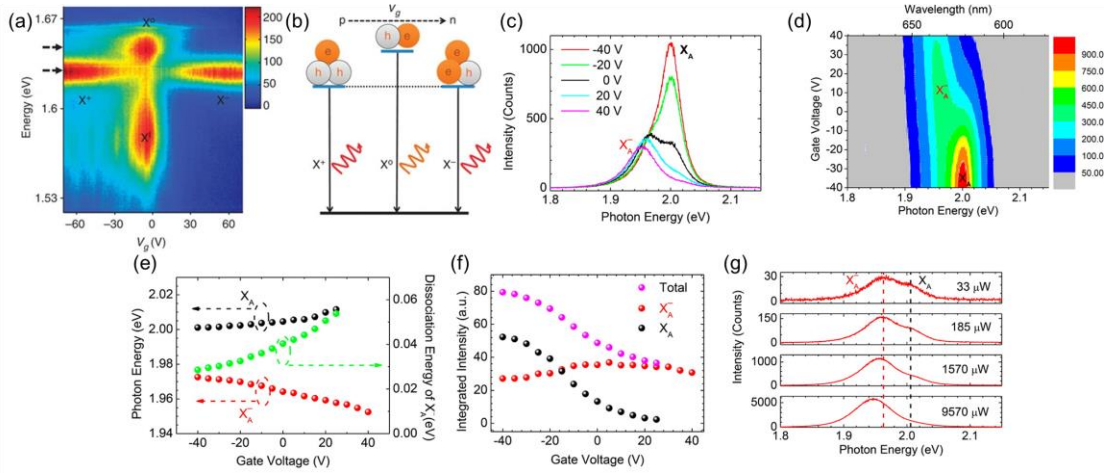



**Figure 2.6. Exciton and trion emission in TMDs.** (a) Colour map of PL spectra under different gate voltages in monolayer $MoSe_2$ at 30 K. (b) Schematic illustration of evolution of electron and hole bounded trion with changing gate voltages. Reproduced with permission from ref. 92. Copyright 2013 Springer. (c) PL spectra of monolayer $WS_2$ with different gate voltages at room temperature. (d) Colour map of PL spectra under different gate voltages in monolayer $WS_2$. (e) Exciton, trion peak position (left axis) and trion binding energy (right axis) versus the gate voltage. (f) Exciton, trion emission intensity and total intensity versus the gate voltage. (g) PL spectra of monolayer $WS_2$ under different illumination powers. Reproduced with permission from ref. 93. Copyright 2015 American Chemistry Society.

(2) Interlayer excitons in 2D heterostructures

Charge transfer and separation are commonly expected for type-II heterojunctions, which is beneficial for reducing charge recombination from photo-excited carriers.

Interestingly, owing to the strong interlayer coupling, transformation of intralayer excitons to interlayer excitons by charge transfer in type-II 2D heterojunctions is prominent even with the large exciton binding energy. In the $WSe_2/MoS_2$ heterostructure, Fang et al.[18] observed quenched PL emission from individual layers and a new peak arising at lower energy, which corresponds to emission from interlayer exciton emission (Fig. 2.7a-b). As the band structure in Figure 2.7c shows, electrons excited to the CB of $WSe_2$ transfer to the CB in $MoS_2$, while excited holes in $MoS_2$ transfer to VB in $WSe_2$. They also demonstrated that the interlayer coupling could be tuned by insertion of h-BN layers, where trilayer h-BN nearly restores the intralayer PL (Fig. 2.7d). Vacuum thermal annealing can tune the interlayer coupling as well.[102] Similar reports of interlayer exciton emission peak have also been studied on $MoS_2/WS_2$,[103] $MoS_2/WSe_2$,[104-105] $MoS_2/MoSe_2$,[106-107] $WSe_2/WS_2$,[108] etc. It has also been shown that the interlayer exciton can be tuned by the number of layers or twist angles[109] (and show Moiré exciton behaviour when the twist angle is small, which will be discussed in section 2.4.4)[110-113]. For example, Tan et al.[114] fabricated $MoS_2/WSe_2$ heterostructures where one component is monolayer and the other is multilayer. By increasing the number of layers, the interlayer exciton peak position redshifts due to increased dielectric screening and change in VB positions. Temperature measurements further show that the interlayer excitons are direct in 1L-$WSe_2$/mL-$MoS_2$ and 2L-$WSe_2$/1L-$MoS_2$, but is indirect for mL-$WSe_2$/1L-$MoS_2$ with $m>2$ and 2L-$WSe_2$/3L-$MoS_2$, dependent on the VBM point shift.

Another important question is about how fast the charge transfer process is and how it impacts the recombination lifetime. Hong et al.[19] observed ultrafast hole charge transfer of ~50 fs in $MoS_2/WS_2$ heterostructures by exciting the $MoS_2$ with a pump laser so that only holes are transferred (Fig. 2.7e-f). Such charge transfer process is much faster than

the exciton lifetime of TMDs, which implies that recombination lifetime should increase due to the ultrafast charge separation. This is partly explained by the close proximity between two layers, but further understanding is demanded. Ceballos et al.[115] obtained similar value of sub-picosecond electron and hole charge transfer rate in $MoS_2/MoSe_2$ heterostructures and found that the interlayer exciton lifetime is an order longer than that in individual layers. Rivera et al.[105] further observed long interlayer exciton lifetime of 1.8 ns at 20 K in $MoS_2/WSe_2$ heterostructures, which is two orders longer than intralayer exciton lifetimes. These studies confirm the advantage of 2D type-II heterojunctions for applications in photonic and optoelectronics.

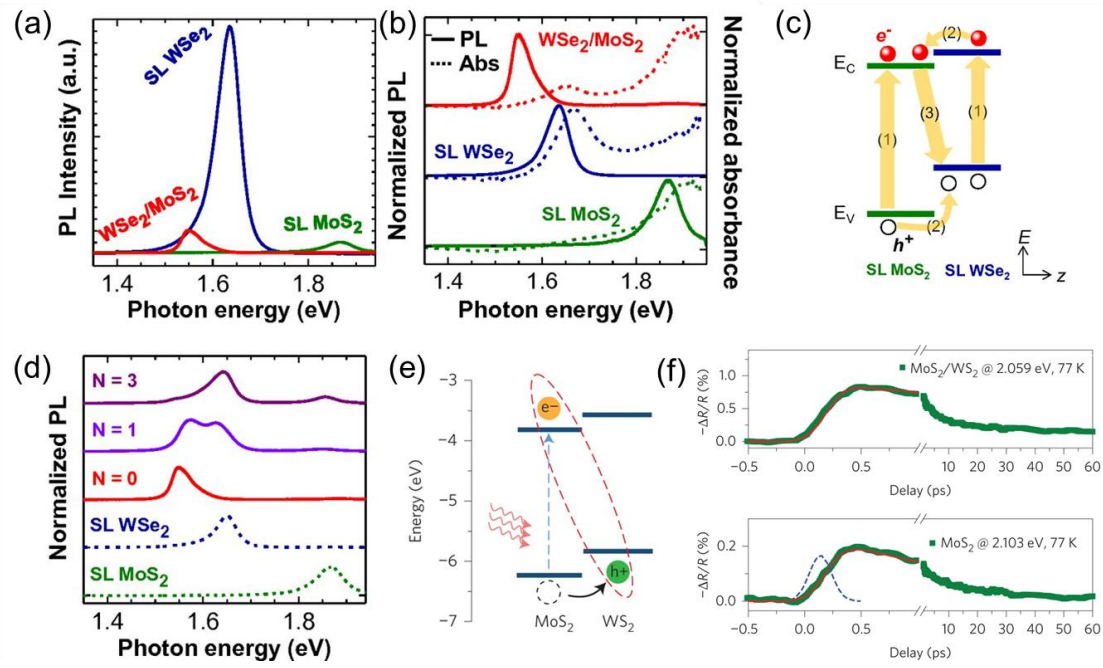



**Figure 2.7. Interlayer exciton in 2D VLHs.** (a) PL spectra of individual layers of $WSe_2$, $MoS_2$ and their heterostructure. (b) Normalised PL and absorption spectra of individual layers of $WSe_2$, $MoS_2$ and their heterostructure. (c) Schematic of band structure of $WSe_2/MoS_2$ heterostructure and transfer of photo-excited charges. (d) PL spectra of $WSe_2/MoS_2$ heterostructure with inserted h-BN layers (N for the number of layers of h-BN). Reproduced with permission from ref. 18. Copyright 2014 United States National Academy of Sciences. (e) Schematic of theoretically predicted $MoS_2/WS_2$ heterostructure energy levels with type-II band

alignment. (f) Ultrafast hole transport in $MoS_2/WS_2$ heterostructure. Up: Transient absorption signal at $WS_2$ A exciton resonance in $MoS_2/WS_2$ heterostructure. Bottom: Transient absorption signal at $MoS_2$ B exciton resonance in $MoS_2$. The blue dashed line indicates instrument response function. Reproduced with permission from ref. 19. Copyright 2014 Springer.

### 2.2.4 Stability

The stability of not just semiconductors but all 2D layered materials are of critical concern as many of the materials have been criticised for lack of it.[116-117] The stability of a material is not only the intrinsic crucial factor in applications that limits the device's working environment and lifetime, but should also be preliminary knowledge for further scientific study to avoid misinterpretation of results. Here the discussion highlights the most basic and fundamental aspect of stability: the chemical stability in ambient conditions. Studies concerning this topic have been focused on several well-developed 2D materials, and they can be generally categorised into the following three groups:

(1) Stable (graphene, h-BN, $MoS_2$, $WS_2$, etc.). Owing to the absence of dangling bonds, these surfaces are considered as immune to oxidation, but the defects and grain boundaries are more reactive as they can provide reactive bonding sites and may reduce the kinetic barrier for $O_2$ dissociation.[79, 118-120] For example, Rong et al.[121] showed that grain boundaries in the air-stable monolayer $WS_2$ are more susceptible to oxidation than the basal plane, which is obvious enough to be revealed under the optical microscope. The difference in oxidation process could be further enhanced under high temperature of 250 °C, which provides an approach for rapid assessment of grain size in continuous films. DFT-based calculations on kinetic barriers also confirmed that the oxygen dissociative adsorption barrier on pristine $MoS_2$ surfaces is quite large to hinder the

thermodynamically favourable adsorption process, while the kinetic barrier is significantly lower on S deficient surfaces, leading to differences in their stability in ambient environments.[122]

(2) Reactive to air (silicene, germanene, $MoTe_2$, etc.). The reaction mechanism and by-products of different materials have been reported. DFT calculations show that the oxidation kinetic barrier is zero for silicene surface and the process for oxygen molecules to dissociate into single O atoms should be spontaneous.[123-125] Jannatul et al.[126] used Raman spectroscopy to show that both Te metals and tellurium oxides form on the surface of layered GaTe crystals due to rapid oxidation. In addition, Zhao et al.[127] demonstrated that GaSe begins to degrade within hours on exposure to air into amorphous selenium, $Ga_2Se_3$ and $Ga_2O_3$. Preservation and characterisation of these unstable materials, are often conducted in inert atmosphere protection, and encapsulation process is required for further applications.

(3) Photo-induced oxidation (black phosphorus, $CrI_3$, etc.). These 2D materials usually degrade slowly in air but the process can be greatly accelerated by light.[128-129] For example, although the half-filled $t_{2g}$ $d^3$ ligand field of $Cr^{3+}$ ions in the ferromagnetic semiconductor $CrI_3$ suggests high stability, the crystal degrades under illumination due to photoactivated $Cr^{3+}$ d-d transitions and subsequent fast ligand substitution into $Cr(H_2O)_6^{3+}$.[130] Oxygen and water molecules absorbed on the surface are frequently involved in this process, which is also reported for photo-induced oxidation of black phosphorus into $PO_x$.[131]

Still, as the degradation chemistry for each material is different, current studies are still concentrated on several easily obtained materials,[116] and more studies are required for elucidating the stability of the increasing new members in the 2D family.

## 2.3 Synthesis of 2D Layered Semiconductors

The strategies for obtaining 2D materials can be generally divided into the top-down approach and the bottom-up approach. The top-down approach, including mechanical or liquid phase exfoliation, utilises the weak vdW interactions between layers for cleavage into atomically thin monolayers. Mechanical exfoliation is generally regarded as being able to produce materials with the highest quality; thus it is often used for the fundamental study of novel physical phenomena and demonstration of novel devices. However, it suffers from low throughput, and the exfoliated crystals are usually small in size. Liquid phase exfoliation is another top-down method where materials are exfoliated either by sonication[132] or by chemical intercalation[133]. It is suitable for low-cost and large-scale production and especially for printed electronics, but the wet chemical process may inevitably introduce defects or undesired dopants into the lattice,[134] and the number of layers and size often lack controllability. To overcome these limitations, bottom-up synthetic routes have shown great promise to generate clean and high-quality 2D materials with controlled thickness, scalable size, and good repeatability. Vapour phase deposition (VPD) generally involves vapour phase transport of precursors to the desired substrates followed by absorption, nucleation and growth in a carefully controlled way, and 2D materials grown by VPD have shown wafer-scale uniformity with well-controlled thickness and electronic and optoelectronic properties comparable to those of mechanically exfoliated materials.[135] The recent advances in successful production of 2D layered semiconductors, especially TMDs and MX compounds, are presented in the following sections for evaluation of their merits.

### 2.3.1 Mechanical Exfoliation

Mechanical exfoliation was first used in the isolation of monolayer graphene[136] and has been proved effective for many other 2D materials. It was used in many of the early studies on 2D layered semiconductors.[32, 137-138] The exfoliated monolayer crystal is usually only several micrometers in length. Recently, a gold-assisted mechanical exfoliation method has been introduced by Velicky et al.[139] for extraordinarily large monolayer TMDs and GaSe (Fig. 2.8a). The large-area exfoliation is enabled by an enhanced vdW interaction attributed to the ultraclean and ultrasmooth surface of freshly grown thin gold films. The edge length of the exfoliated monolayer crystal has increased to several hundreds of micrometres (Fig. 2.8b-c), which could facilitate many research areas such as electrochemistry and photocatalysis.

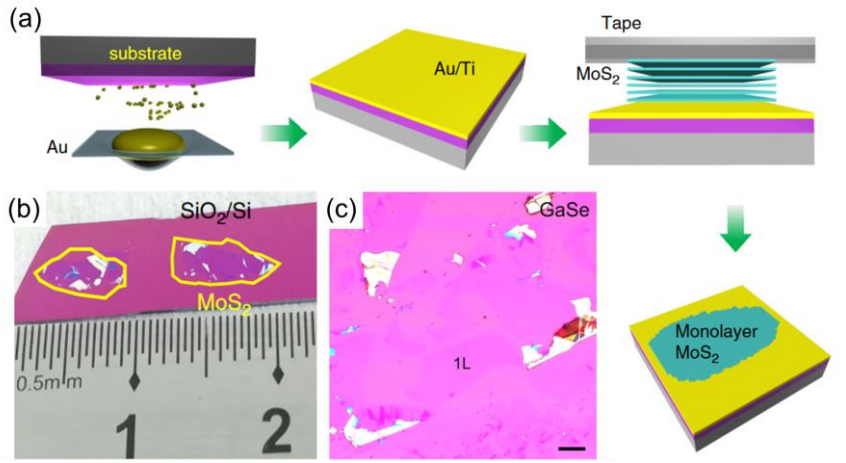



**Figure 2.8. Gold-assisted mechanical exfoliation of monolayer materials with macroscopic size.** (a) Schematic of the gold-assisted exfoliation process. (b) Optical image of exfoliated $MoS_2$ on $SiO_2$/Si. (c) GaSe monolayer crystal prepared by gold-assisted mechanical exfoliation. Scale bar: 100 μm. Reproduced with permission from ref 139. Copyright 2018 American Chemical Society.

### 2.3.2 Liquid Phase Exfoliation

Liquid phase exfoliation solves the low-yield problem of mechanical exfoliation by sonicating solid powder in the presence of suitable solvents followed by centrifugation to control size and thickness distribution (Fig. 2.9a). For example, Harvey et al.[140] performed liquid phase exfoliation of GaS in 15 different solvents (Fig. 2.10a-b). By analysing the concentration of the obtained dispersion after removal of unexfoliated materials, it was found that the breaking of vdWs forces and the stabilisation of exfoliated nanosheets is closely related to the solvent's surface energies, with a surface tension close to 40 mJ $m^{-2}$ for successful solvents. The exfoliated GaS nanosheets are pristine and defect-free except for a higher oxygen content in the vicinity of the edges. By using controlled centrifugation with increasing centrifugation velocity in consecutive steps, different nanosheets with a mean thickness ranging from 10 to 40 layers can be separated, which is beneficial for study of thickness-related properties (Fig. 2.10c).

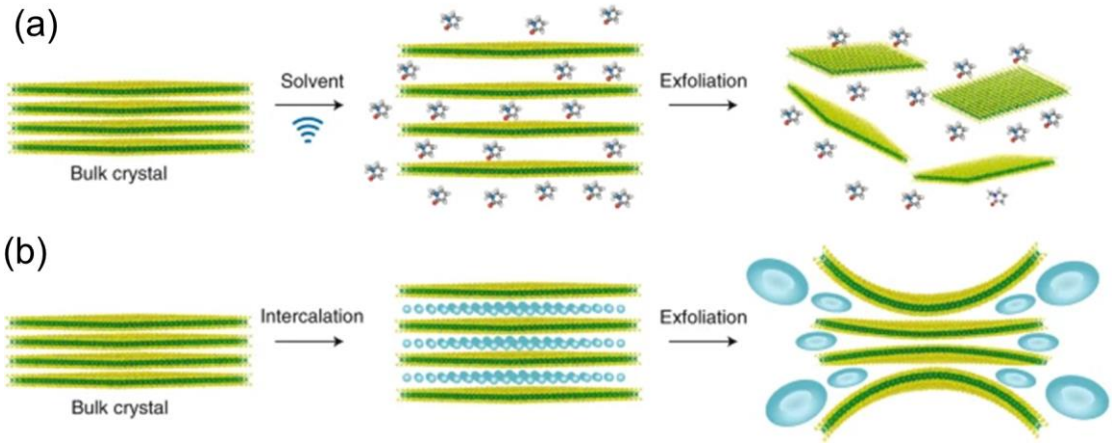



**Figure 2.9. Two approaches in liquid phase exfoliation.** (a) Direct liquid phase exfoliation by intense sonication of bulk layered crystals in suitable solvents. (b) Intercalant-based exfoliation, where intercalation of additional ions or molecules is employed to assist the exfoliation. Reproduced with permission from ref. 141. Copyright 2019 Springer.

Direct liquid-phase exfoliation method using solvents often results in a relatively broad thickness distribution that demands additional precipitation selection process of the 2D nanosheets prior to further applications. In comparison, intercalation-based exfoliation offers more uniform thickness distribution using foreign ions or molecules as intercalants (Fig. 2.9b). Alkali metal ions ($Li^+$, $Na^+$ and $K^+$) have been frequently used in liquid intercalation exfoliation of $MoS_2$, with phase transformation into the metallic 1T structure (Fig. 2.10d) as the absorbed alkali metal ions on the surface changes the relative phase stability between 1T and 2H phase.[142-145] Another important group of intercalants that have been reported are quaternary ammonium molecules. In the reports by Lin et al.,[146] the electrochemical intercalation of the tetraheptylammonium bromide (THAB) molecules and subsequent mild sonication process results in pure 2H-$MoS_2$ few-layer nanosheets with narrow thickness distribution and high crystallinity. This enables scalable fabrication of $MoS_2$ thin-film transistors with on-off ratio exceeding $10^6$, which enables successful demonstration of various logic gates and computational circuits (Fig. 2.10e).

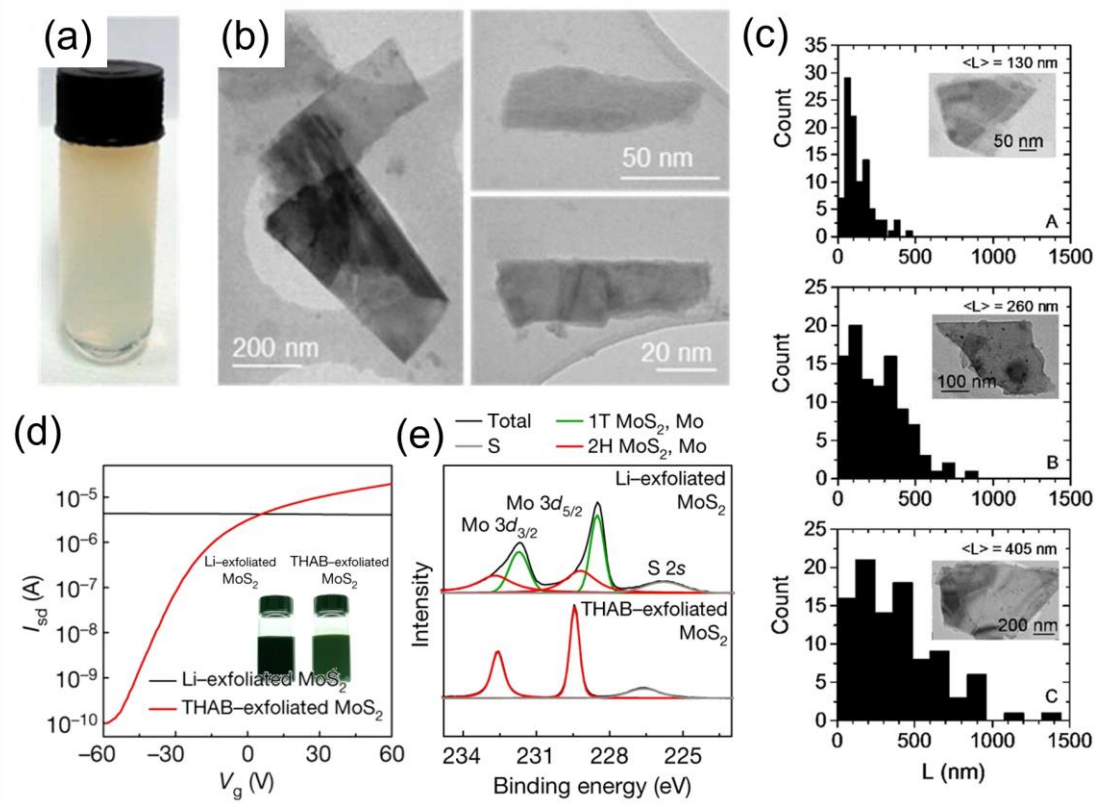



**Figure 2.10. Liquid phase exfoliation of MX compounds and TMDs.** (a) Photograph of a typical dispersion of GaS in iso-propanol. (b) Low-resolution bright-field TEM images of GaS nanosheets exfoliated in IPA. (c) Length histograms and representative images of size-selected GaS in IPA as insets. (A) Smallest-size GaS, (B) medium-sized GaS, (C) large GaS. Reproduced with permission from ref 140. Copyright 2015 American Chemical Society. (d) Photograph of THAB–exfoliated $MoS_2$ nanosheets in isopropanol and Li–exfoliated $MoS_2$ nanosheets in water. (e) Comparison of XPS spectra of THAB–exfoliated 2H-phase $MoS_2$ and Li–exfoliated mostly 1T-phase $MoS_2$. Reproduced with permission from ref. 146. Copyright 2018 Springer.

### 2.3.3 Vapour Phase Deposition

VPD for thin-film deposition has been extensively used to grow various 2D materials owing to the extraordinarily controllability over morphology (thickness, grain size, and

orientation) and crystal quality. In addition, the planar surface for growth matches well with that of the 2D crystal, and the obtained materials can be directly applied in fabrication of electronic or optoelectronic devices. The most basic and commonly used VPD methods are physical vapour deposition (PVD) and chemical vapour deposition (CVD), and these growth systems of 2D materials have been reviewed in detail over the past decade.[147-150] In PVD, the precursor is the same as the product. The precursor is evaporated in a well-controlled manner, often under low pressure conditions, and then transported to the target substrate followed by deposition process. While the approach is suitable for large-scale film deposition, the grain size is usually small and additional annealing is often required to enhance the crystallinity. In CVD the vapour phase precursors are transported to the substrate to undergo chemical reactions. A high temperature is usually needed to initiate the reaction. By fine tuning of the nucleation and growth conditions, CVD has been demonstrated with great controllability over crystal thickness and morphology, showing high-crystallinity with device performance comparable to mechanically exfoliated materials.

(1) Precursor Engineering

Versatile precursors have been developed in CVD or PVD synthesis of GaX (X = S, Se), including GaSe, $Ga_2Se_3$,[151-152] $Ga_2S_3$,[153] etc. Li et al.[151] used the PVD method to grow 2D GaSe single crystals with thickness down to monolayer. Rounded flakes were obtained with the use of GaSe powders as sole precursor, while triangular flakes would form upon adding a small amount of $Ga_2Se_3$ (1:50) (Fig. 2.11a-b). This difference in edge structure is explained by differences in the concentration of vapour phase reactant species in the growth region. During the vapour transport, bulk GaSe would decompose

into vapour phase $Ga_2Se$ and $Se_2$, which would then diffuse to the substrate with different mean free paths. Therefore, similar to the case in $MoS_2$,[154] an increase in the $Se_2$ concentration results in regularly-shaped triangular flakes. Larger amounts of $Ga_2Se_3$ result in the formation of $Ga_2Se_3$ crystals. The authors further explored the edge stabilities and evolution of monolayer GaSe crystals under growth and etching dynamics.[152] Experimental results showed that the morphology evolution follows the Kinetic Wuff Construction theory and is governed by different chemical potentials of Ga and Se. A similar case of Ga(III)–Ga(II) transition is further demonstrated on GaS synthesis. For example, Wang et al.[153] used $Ga_2S_3$ as a single precursor under a reductive $H_2$ atmosphere to achieve large-scale synthesis of monolayer GaS. Another approach has been proposed by Carey et al.[35] which utilised the 3 nm native oxide skin of metal Ga for the synthesis of GaS at pre-defined locations (Fig. 2.11c). First, non-wettable regions are patterned by photolithography followed by selective treatment with 1h-1h-2h-2h-perfluorodecyltriethoxysilane (FDTES). Then liquid Ga with a thin native oxide layer is dropped onto it, where the oxide layer can adhere strongly to $SiO_2$ but not to the treated areas. By further removal of residual Ga liquid, the oxide layer is first reacted with HCl to form $GaCl_3$ and then sulfurized in S vapour to form patterned GaS with bilayer thickness.

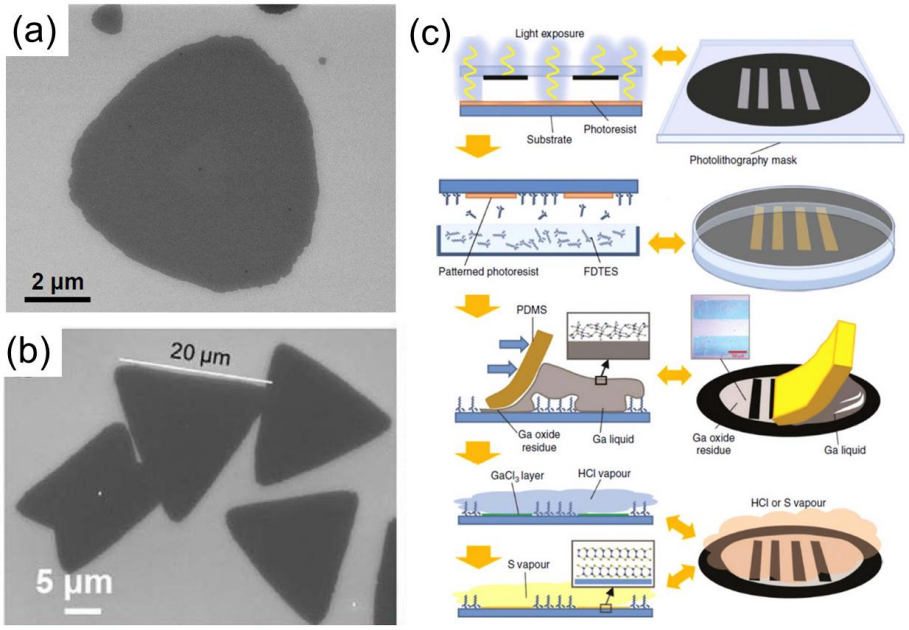



**Figure 2.11. Morphological control in 2D GaS synthesis.** (a-b) PVD growth of atomic layer GaSe without and with the addition of $Ga_2Se_3$. Reproduced with permission from ref. 151. Copyright 2014 Springer. (c) Synthesis of GaS at pre-defined locations with Ga-oxide layer as precursors. Reproduced with permission from ref. 35. Copyright 2017 Springer.

So far, the most prevalent precursors for growing $MoS_2$ in the laboratory are $MoO_3$ and sulfur, which are known for the production of pure phase high-quality crystals with a large grain size. In addition, with the help of seeding promoters such as reduced graphene oxide or other large aromatic systems, growth of monolayer $MoS_2$ has been demonstrated on various insulating substrates including sapphire, amorphous silicon dioxide, quartz, $TiO_2$, etc.[155] Two possible growth routes are expected for the reaction and deposition where both start from the formation of volatile species $MoO_{3-x}$ after partial sulfurization of $MoO_3$.[156] In Figure 2.12a, the volatile $MoO_{3-x}$ and S would either adsorb and diffuse on the substrate and then undergo surface reaction to form $MoS_2$, or the reaction would occur in the gas phase and then the gas phase $MoS_2$ clusters undergo adsorption, nucleation and growth on the substrate. It is expected that controlling of

growth conditions such as temperature, pressure and so on could adjust the two competitive processes and influence the morphology, nucleation rate or domain size. In addition, pioneering work by Najmaei et al.[157] and Wang et al.[154] found that the relative ratio of the metal and chalcogen species in the vapour phase is also significant in morphology control of the 2D crystal. By intentionally introducing a Mo-precursor concentration gradient in the synthesis (Fig. 2.12b), the shape evolution of monolayer $MoS_2$ single crystals was observed where the morphology develops from triangular (Mo-rich) to hexagonal (stoichiometric) and then back to triangular (S-rich) due to different growth speeds of Mo-terminated and S-terminated edges (Fig. 2.12c).[154] Xu et al.[158] further synthesised large-area monolayer $MoS_2$ from branched triangular to highly dendritic structures with quaternary arms by further decreasing the Mo to S ratio. The side branches always form a 60° angle with the backbones (Fig. 2.12d-f), which cannot be explained solely by the classical diffusion limited aggregation (DLA) model.[159] The same evolution from triangular to dendrites was also observed by Chen et al.[160] in the growth of second layer on top of monolayer $MoS_2$ under lower sulfur chemical potentials. Besides $MoO_3$, other Mo-based precursors such as $MoCl_5$ and $MoO_2$ have been reported.[161-162] For example, Yu et al.[161] utilised $MoCl_5$ and S as precursors to synthesise uniform monolayer and bilayer $MoS_2$ films under low chamber pressure of ~2 Torr. The authors contributed the uniform thickness to the self-limiting growth behaviour with the equilibrium gaseous phase precursor partial pressure, which was tested by controlling the number of layers through the $MoCl_5$ amount, the chamber pressure and the substrate temperature. In addition to these precursors, in the following section on variants of CVD techniques, some other special precursors will be introduced.

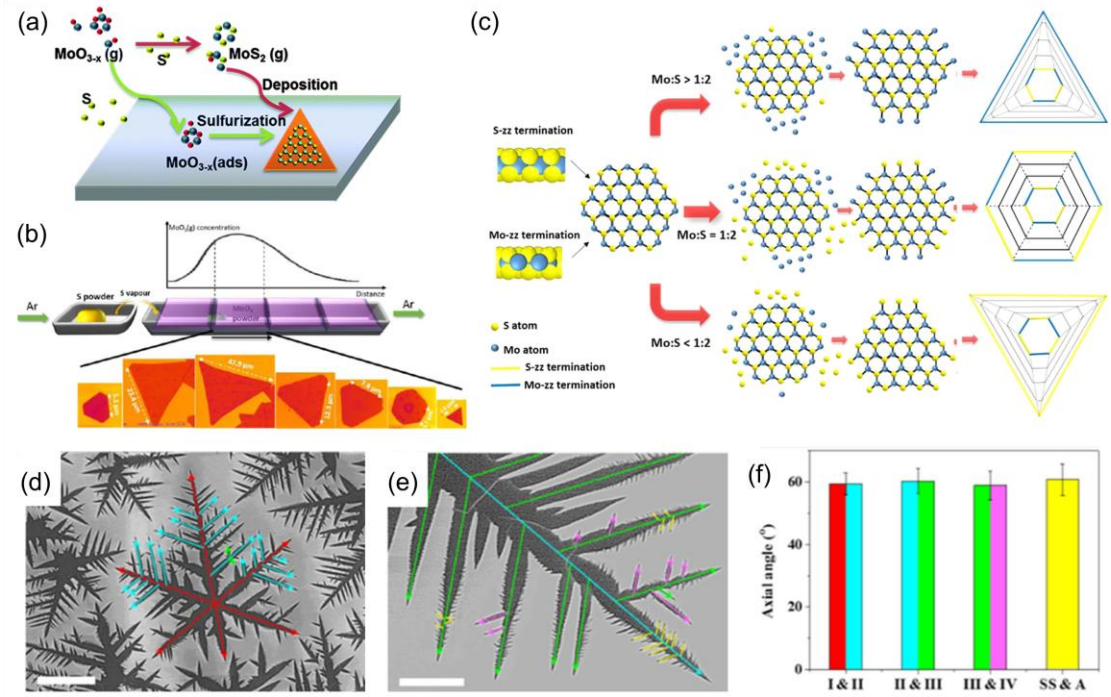



**Figure 2.12. Morphological control in 2D $MoS_2$ synthesis.** (a) Schematic diagram of two growth routes for $MoS_2$ using $MoO_3$ and S as precursors. Reproduced with permission from ref. 156. Copyright 2015 Royal Society of Chemistry. (b) Schematic showing $MoS_2$ grown on different section of substrates with various $MoO_3$ vapour concentrations. (c) Schematic illustration of the domain shape evolution of $MoS_2$ crystals with different Mo:S atom ratios and different edge growth speeds. Reproduced with permission from ref. 154. Copyright 2014 American Chemistry Society. (d-e) CVD-grown monolayer $MoS_2$ dendrites. The hierarchical structures are marked by arrows, i.e., red for the primary (I) backbone, cyan, green, and pink for the secondary (II), tertiary (III), and quaternary (IV) arms. The side sprouts (SS) are marked by yellow lines. Scale bars: (d) 100 μm; (e) 20 μm. (f) Histogram of the axial angle between different hierarchical arms (I and II, II and III, and III and IV) and between the arms and their side sprouts (A and SS). Reproduced with permission from ref. 158. Copyright 2018 American Chemistry Society.

The carrier gas in CVD functions as vapour transport agent. Inert gases such as argon or nitrogen are often used for protecting the chemical reaction from air, while in other

cases the carrier gas could also participate in the rection. Hydrogen is frequently employed as additional reducing agent as discussed previously in the reduction of $Ga_2S_3$ into GaS. It is also used in the synthesis of selenides and tellurides to further reduce metal oxides.[163-164] It has also been reported that hydrogen can result in higher nucleation density and smaller grains, where high concentration of hydrogen shows etching effect on the synthesised chalcogenides, leading to perfect triangular-shaped crystals.[165-166] Sheng et al.[167] reported the addition of hydrogen for growing continuous monolayer $WS_2$ films under ambient pressure by the suppression of multilayer nuclei, and the obtained $WS_2$ films showed better electrical properties as hydrogen helped in removing impurities. On the contrary, small amounts of oxygen can be used for metal elements when the corresponding metal oxides are more volatile.[135]

Although the growth of most 2D layered semiconductors is non-catalytic, certain catalysts have been developed to promote growth. Alkali metal halides have been reported in growing larger Mo- and W- dichalcogenide crystals under lower temperature, where multiple catalytic pathways have been identified. Li et al.[168] demonstrated halide-assisted synthesis of $WS_2$ and $WSe_2$ large domains at lower temperature using alkali metal halides as additives. They attributed this effect to the reaction between $WO_3$ and alkali metal halides mixed together at high temperature with the following reaction routes:

$$WO_3(s) + NaCl(s) \rightarrow NaWO_3(s) + WOCl_4(g) + WO_2Cl_2(g) + WO_2(s) + W(s) \quad (1)$$

$$WOCl_4(g) + WO_2Cl_2\,(g) + Se(g) + H_2(g) \rightarrow WSe_2(s) + HCl(g) + H_2O(g) \quad (2)$$

Therefore, the role of alkali metal halides here is mainly to facilitate the vaporisation of transition metal precursor by forming volatile oxyhalide intermediates. Similar results were reported on the synthesis of 1T' $MoTe_2$ and $WTe_2$.[169] The molten-salt-

assisted method has further been extended to the synthesis of a library of 2D transition metals (including Ti, Zr, Hf, V, Nb, Ta, Re, Pt, Pd and Fe) chalcogenides including some newly-synthesised 2D semiconductors (Fig. 2.13a-b), demonstrating that the catalytic effect of alkali metal halides are applicable to a wide range of metal precursors.[170] It is worth mentioning that the alkali metal halides can be removed during the transfer process, thus the quality of the material is maintained. Monolayer $MoS_2$ nanoribbons have also been synthesised directly on NaCl single crystals (Fig. 2.14a-b).[171] It was discovered that the reaction between NaCl and $MoO_3$ could form $Na_2Mo_2O_7$, which is liquid at high temperature. The Na-Mo-O droplets therefore can crawl on the NaCl surface and form trails of monolayer $MoS_2$ nanoribbon when encountering sulfur vapour (Fig. 2.14c-d). Similarly, Yang et al.[135] demonstrated that NaCl and NaOH can facilitate the growth of uniform monolayer $MoS_2$ on quartz substrates, while $CaCl_2$ cannot. DFT calculations further suggest that the underlying catalytic mechanism is by reduction of the energy barrier of S-terminated edges with sodium ions (Fig. 2.14e).

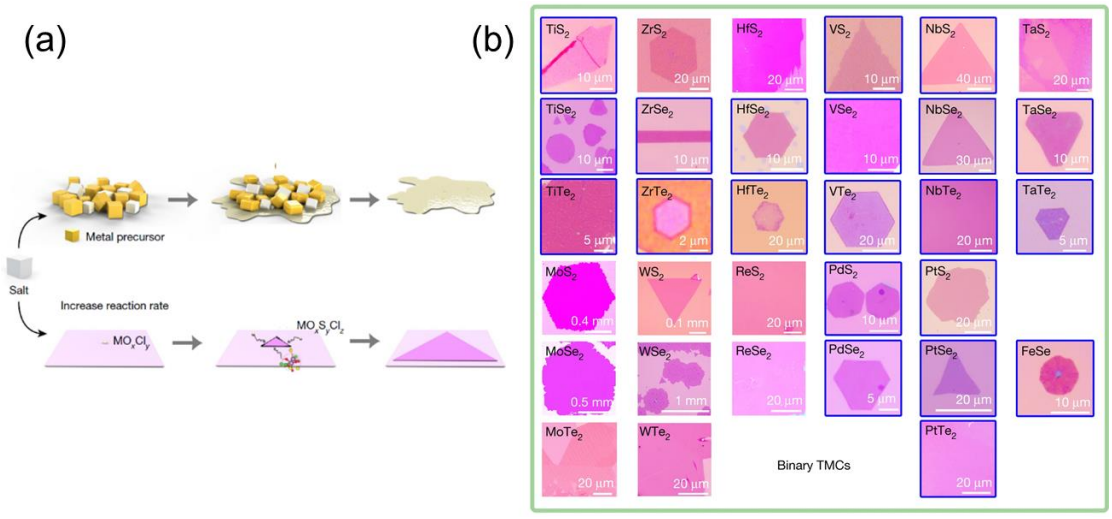



**Figure 2.13. Catalytic growth of a library of TMDs using alkali metal halides.** (a) Schematic of molten-salt-assisted CVD where metal oxychlorides are formed to promote the

reactions. (b) Optical image of 32 different binary TMDs synthesised by the molten-salt-assisted CVD. Reproduced with permission from ref. 170. Copyright 2018 Springer.

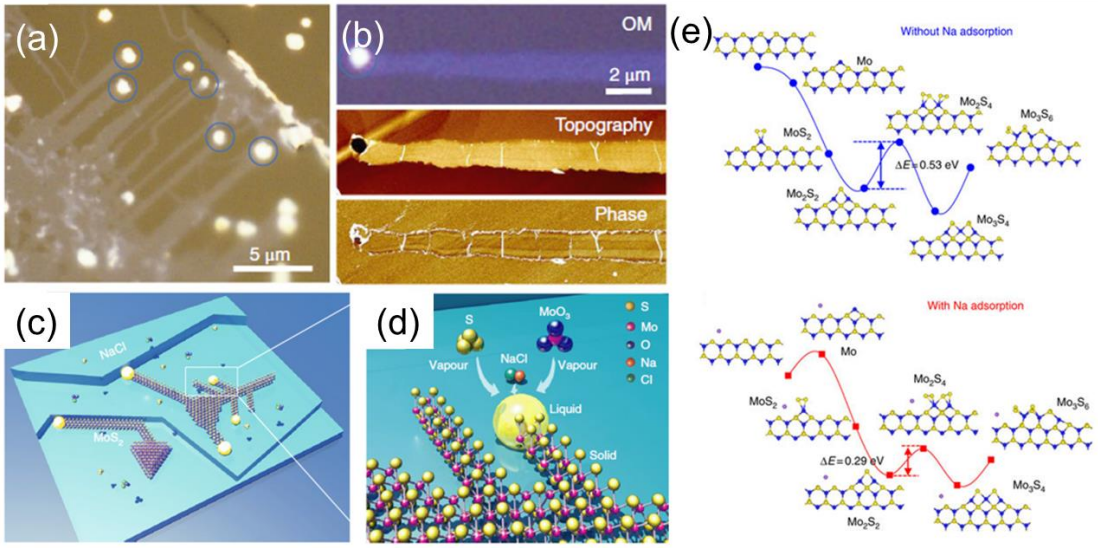



**Figure 2.14. The role of sodium in catalytic growth of $MoS_2$.** (a) Optical image of $MoS_2$ ribbons grown on a NaCl crystal. (b) Optical image and corresponding AFM topography and phase images of a $MoS_2$ ribbon. (c-d) Schematics of the growth of $MoS_2$ ribbons on a NaCl crystal surface. Reproduced with permission from ref. 171. Copyright 2018 Springer. (e) DFT-calculated energy diagrams for $MoS_2$ growth along the S-terminated edges, (top) without and (bottom) with Na adsorption. Reproduced with permission from ref. 135. Copyright 2018 Springer.

(2) Substrate Effect

Highly oriented growth on epitaxial substrates has also attracted much attention, as it can reduce disordered grain boundaries and help study phenomena related to Moiré patterns. Single-crystal substrates such as c-plane sapphire, mica, and quartz with hexagonal symmetry have been frequently used in epitaxial growth of 2D

semiconductors. Dong et al.[172] elucidated that the oriented epitaxial growth is by aligning the high symmetry directions of the 2D material and the substrate due to the preferential propagation of crystal edge, thus a preferred orientation of 0° or 60° is usually observed for the above hexagonal substrates. For example, Zhou et al.[173] synthesised GaSe with aligned orientation via PVD on thin fluorophlogopite mica substrates (Fig. 2.15a-b). The thin mica substrate provides an atomically smooth and chemically inert surface, which allows epitaxial growth despite a significant lattice mismatch of 35% between GaSe and mica. The as-synthesised triangular-shaped single crystals exhibit identical orientations with each other at multiples of 60°, indicating strong evidence of epitaxial growth. Position-controlled synthesis is also achieved by selective oxygen plasma etching of the mica surface. Further investigation into the alignment kinetics suggests that the orientation is determined at the early stage of growth. Epitaxial growth of monolayer $MoS_2$ has been demonstrated on c-plane sapphire with 0°- or 60°-orientation (Fig. 2.15c).[174] Aljarb et al.[175] demonstrated that small and monolayer $MoS_2$ seeds are easier to rotate to energy minimum positions compared to larger and thicker seeds. By using a two-step heating profile that first grows small-sized seeds and then promotes lateral growth, an improved alignment is achieved. In contrast, due to the weaker interaction between $WS_2$ and sapphire substrate, the orientation is usually random. Ji et al.[176] successfully achieved epitaxial growth of $WS_2$ on sapphire by hydrogen-assisted CVD (Fig. 2.15d). The introduction of hydrogen changes the surface from O-terminated to Al-terminated, which greatly enhances the interaction between $WS_2$ and substrate, resulting in the observed epitaxial growth. Such aligned growth is beneficial for electronic applications as the 0°-oriented grain boundary maintains similar conductance compared with single crystal channel, while the misoriented grains show defective grain boundaries with impaired conductivity (Fig.

2.15e-f). 2D materials can also be used as substrates for direct epitaxial growth of wide bandgap 2D semiconductors to fabricate vdW heterostructures. Li et al.[152, 177] demonstrated epitaxial growth of GaSe on graphene and $MoSe_2$. HADDF-STEM characterisation was used to track the epitaxial growth of GaSe on 2D materials with identical crystal symmetry. On one hand, GaSe single crystals show well-aligned stacking on $MoSe_2$ crystals without any rotations, and a periodic superlattice caused by lattice mismatch of 13% can be seen (Fig. 2.16a-b). The binding energy between the two layers is calculated as 117 meV/GaSe, confirming a relatively strong vdW interaction within the atomically thin p–n junction. Interestingly, it is also shown that for GaSe growing at the $MoSe_2$ monolayer–bilayer boundaries, the GaSe layer prefers to buckle up and overlap the second $MoSe_2$ layer rather than forming an atomically sharp lateral boundary (Fig. 2.16c-e). On the other hand, GaSe crystals grown on graphene were observed with a favoured stacking angle of 10.5° in 50% of cases, which is in agreement with the calculation that a rotation angle of 10.9° results in the smallest supercell size and smallest strain (Fig. 2.17a-c). A significantly larger binding energy of 47 meV/GaSe is also calculated compared with a lower (~25–36 meV/GaSe) binding energy at other rotation angles (Fig. 2.17d). It is suggested that the lattice orientation is determined at the nucleation stage when the small crystal size enables the crystal to diffuse and rotate to the most stable configuration. As the flake grows larger, the difference in binding energies between different rotation angles becomes larger; therefore the crystal is pinned in a particular orientation. In summary, a competition between growth rate and diffusion rate determines whether a large-scale highly aligned crystal can be obtained. Such highly aligned growth has also been observed in GaSe/$MoS_2$ and for $PbI_2$ on graphene and $WS_2$.[178-180]

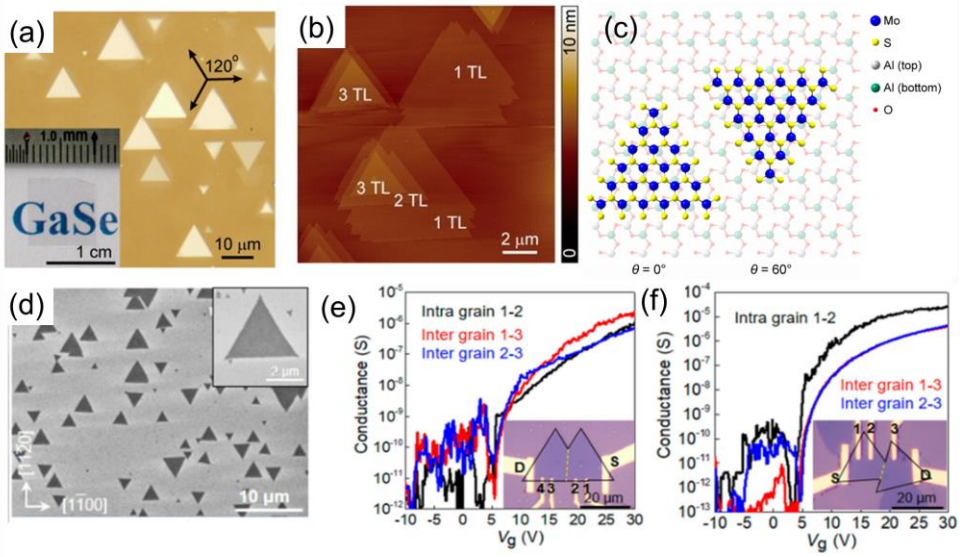



**Figure 2.15. Oriented growth of 2D layered semiconductors on single-crystal substrates.** (a) Optical image of ultrathin GaSe nanoplates grown epitaxially on a mica substrate. Inset shows a photograph of 2D GaSe nanoplate arrays grown on the mica substrate. (b) AFM image of GaSe nanoplate array with identical orientations and terrace structures. Reproduced with permission from ref. 173. Copyright 2014 American Chemical Society. (c) Schematic of the top view of relative lattice orientations between monolayer $MoS_2$ and c-plane sapphire. Reproduced with permission from ref. 174. Copyright 2015 American Chemical Society. (d) SEM image of aligned $WS_2$ grown on sapphire with hydrogen addition. (e-f) Transport properties of merged $WS_2$ crystals synthesised with hydrogen and $WS_2$ crystals with grains synthesised without hydrogen. Reproduced with permission from ref. 176. Copyright 2018 American Chemical Society.

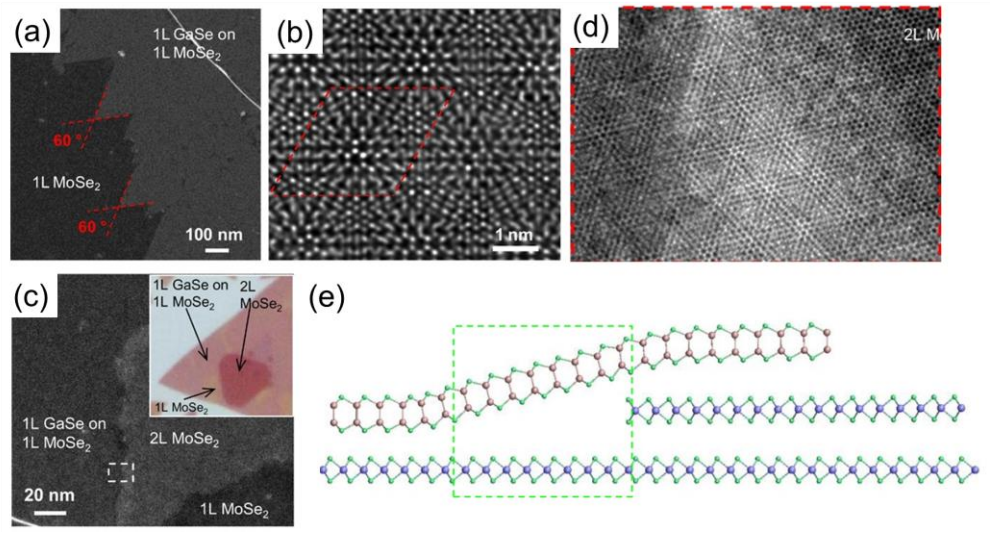



**Figure 2.16. Oriented growth of GaSe on $MoSe_2$.** (a) Low-magnification ADF-STEM image showing the edge area of the 1L GaSe domain grown on 1L $MoSe_2$. (b) Atomic-resolution ADF-STEM image showing the atomic structure of the periodic superlattice where 1L GaSe stacks on top of 1L $MoSe_2$. The red dashed rhombuses indicate the unit cell of the GaSe/$MoSe_2$ heterostructure (supercell), with a lattice constant of l = 2.63 nm. (c) Low-magnification STEM image showing how a 1L GaSe domain connects laterally to a 1L $MoSe_2$ domain where both sit on top of another 1L $MoSe_2$ and follow its lattice orientation. Inset: Optical micrograph showing a similar structure on a large scale (the red triangle is the 2L $MoSe_2$ region). (d) Atomic-resolution ADF-STEM image of the area highlighted in the white dashed rectangle in (c), showing an overlapping region between the 1L GaSe domain and the bilayer $MoSe_2$ in the lateral connection region. (e) Schematic of the overlapping structure in the lateral connection region that shows the buckling of 1L GaSe (on 1L $MoSe_2$) stacks on top of the second $MoSe_2$ layer. Reproduced with permission from ref. 177. Copyright 2016 American Association for the Advancement of Science.

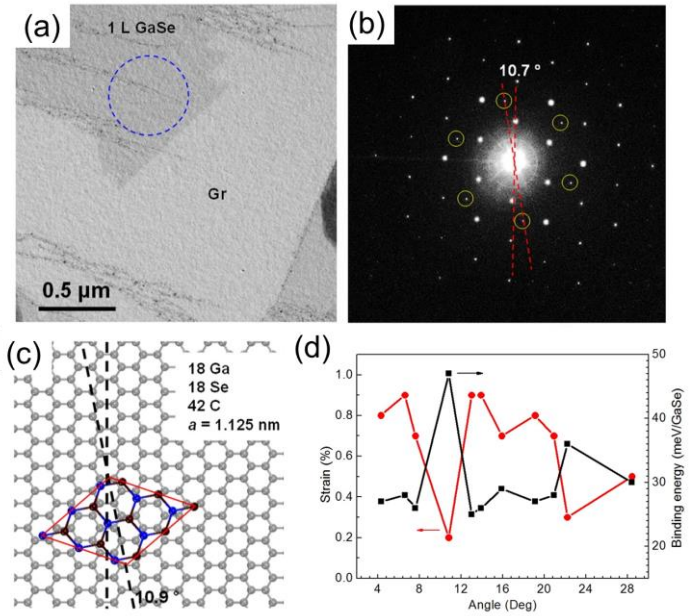



**Figure 2.17. Oriented growth of GaSe on graphene.** (a) TEM image of a 1L GaSe grown on CVD-grown 1L graphene. (b) SAED pattern obtained from the region included by dashed circles in (a). The brighter, hexagonally arranged set of diffraction spots is from the GaSe, while the spots with much lower intensity, indicated by yellow circles, are from the underlying graphene. The two sets of spots show a rotation angle of ~10°. (c) Schematic illustrations of vdW heterostructure unit cells (supercells) constructed by 1L GaSe epitaxy on 1L graphene with interlayer lattice rotations of 10.9°. (d) Residue interlayer strains (red dots) and binding energies (black squares) between 1L graphene and 1L GaSe epitaxial layers as a function of interlayer lattice rotation angles. Reproduced with permission from ref. 152. Copyright 2015 American Chemical Society.

Inspired by the growth of graphene on liquid substrates such as molten copper,[181] different liquid substrates have been developed for the preparation of 2D layered semiconductors with large grain size. As the nucleation takes place preferentially at impurities or defect sites, the formation of a homogenous interface on the liquid substrate would greatly reduce the nucleation density. In addition, the interactions

between the adatom and the liquid substrate is weaker, allowing the adatoms or clusters to migrate easily on the substrate until they reach binding sites. Low nucleation density and low migration barrier for adatoms contribute to the formation of millimetre sized $MoSe_2$ and $MoS_2$ on molten glass (Fig. 2.18a-c).[160] A high mobility of 95 $cm^2V^{-1}s^{-1}$ and on/off current ratio of $10^7$ for $MoSe_2$ is achieved, owing to the high-quality large crystals. Monolayer films and highly organised secondary layer patterns of $MoS_2$ have also been reported on molten glass.[135, 182]

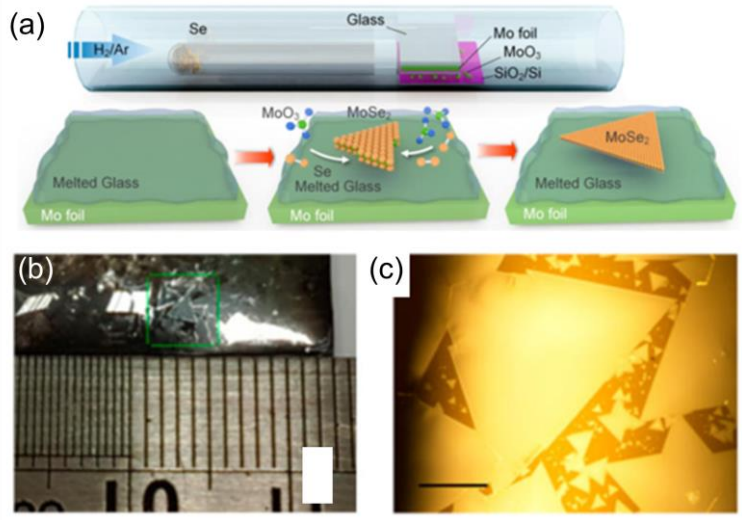



**Figure 2.18. Liquid substrates for the growth of 2D layered semiconductors with large grain size.** (a) Schematic illustration for synthesis of $MoSe_2$ on molten glass. (b-c) Photo and optical images of the $MoSe_2$ crystal on glass. Scale bar: 0.5 mm. Reproduced with permission from ref. 160. Copyright 2017 American Chemical Society.

Liquid substrates can also serve as a source of the metal precursor. Unlike the use of pre-deposited metal precursors where thick layers are almost inevitable, the thickness of 2D materials here is more uniform owing to the homogeneous distribution of precursors across the surface. For example, Zhang et al.[183] reported the growth of $WS_2$ on re-solidified Au substrate (Fig. 2.19a). Under annealing at 1100 °C, the tungsten foil

placed under the Au foil gradually diffused into the Au foil and formed $WS_2$ when encountering $H_2S$ at 900 °C. $WS_2/ReS_2$ heterostructures were also synthesised by using W/Re alloys. A low-temperature synthesis of atomically thin GaSe and $Ga_xIn_{1-x}Se$ on liquid metals at about 100–150 °C has been reported by Zhou et al.[184] Liquid Ga or Ga–In alloys are supported by W foil or a polyimide film at a low temperature, while the $Ga_2Se_3$ source is heated at a higher temperature (Fig. 2.19b-c). Stoichiometric GaSe with a thickness of ~5L is formed on the liquid Ga surface, as GaSe is the only stable compound in a Ga-rich melt. A regular facet angle of ~120° can be found on the film that matches well with the hexagonal phase of GaSe, and a nearly identical crystalline orientation is achieved on the liquid surface (Fig. 2.19d-e). These two examples demonstrate that one great advantage of using liquid substrates is the facile synthesis of uniform metal alloyed 2D crystals. Although current reports on liquid substrates are rare, the simplicity of the process and the potential to obtain various alloyed 2D semiconductors make these substrates promising in production of large-area uniform 2D materials in industry.

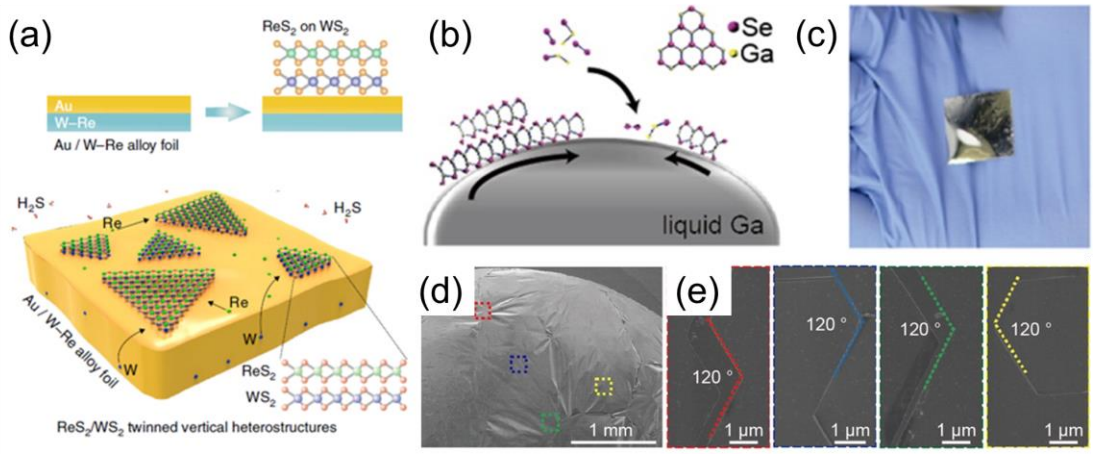



**Figure 2.19. Metallic liquid substrates as sources for the growth of 2D layered semiconductors and heterostructures.** (a) Schematic for twined growth of $ReS_2/WS_2$

heterostructures with W-Re alloy foil as precursor and molten Au foil as substrate. Reproduced with permission from ref. 183. Copyright 2016 Springer. (b) Schematic of low-temperature growth of 2D GaSe crystals on liquid metal Ga. (c) Photographs of liquid gallium on tungsten foil held in hand. (d) SEM image of 2D GaSe crystal on liquid Ga after growth. (e) Corresponding high-magnification SEM images recorded at four different positions indicated as four boxes in (d). Reproduced with permission from ref. 184. Copyright 2016 American Chemical Society.

(3) Variants of Vapour Phase Deposition Techniques

Several variants of PVD and CVD techniques developed for high-quality 2D material growth are discussed here. In the simplest form of PVD, the precursor is vapourised by thermal heating, which is inefficient and difficult to control in practice. In pulsed laser deposition (PLD), the precursor material (target) is vapourised by a pulsed laser under high or ultrahigh vacuum conditions and then forms a complex plume before depositing onto the substrate. By controlling the laser energy or deposition pressure, the growth kinetics can be tuned to obtain crystal films with desired thickness. One key issue is maintaining stoichiometry during deposition without unwanted defects. Serna et al.[185] introduced extra sulfur (S:$MoS_2$ 1:1) and optimised $MoS_2$ particle size in the target to successfully achieve large-area deposition of stoichiometric $MoS_2$ with controlled number of layers from 1−10 L. The addition of excess sulfur helps to remove defects and results in improved device performance. Yang et al.[50] used PLD for the growth of monolayer to few-layer InSe films with precise control of the number of layers. A post-growth annealing process is further carried out in a Se environment to improve crystallinity and stoichiometry of the large-area uniform InSe films. Mahjouri-Samani et al.[186] reported the growth of 1–3L GaSe nanosheets by PLD which would eventually

form 2D films of ~20 nm with increasing pulses (Fig. 2.20a-c). Molecular beam epitaxy (MBE) is another PVD approach for growing high-quality crystal films with well-controlled thickness benefiting from the layer-by-layer growth mode. Yuan et al.[187] synthesised 2–8L GaSe by MBE on both n-Si and transparent mica substrates. GaSe shows vdW epitaxy on the substrate with layer-by-layer growth behaviour, which facilitates the study of layer-dependent properties. Similarly, 1–3L GaSe was deposited by MBE on graphene for ARPES characterisation of its electronic band structure (Fig. 2.20d).[30]

Compared to conventional CVD, metal-organic chemical vapour deposition (MOCVD) applies all gaseous precursors, thus the partial pressures of reactive species are much more controllable and repeatable, and the uniformity and quality of synthesised product can be greatly improved. Kang et al.[188] achieved synthesis of monolayer $MoS_2$ films on 4-inch wafer with an average grain size of ~1 μm by using $Mo(CO)_6$ and $(C_2H_5)_2S$ as gaseous precursors (Fig. 2.20e-f). It was found that the partial pressure of Mo-species ($P_{Mo}$) due to thermal decomposition of $Mo(CO)_6$ could effectively tune the growth mode. Low $P_{Mo}$ in the excess of $(C_2H_5)_2S$ atmosphere leads to layer-by-layer growth where monolayer islands gradually stitch into continuous films (Fig. 2.20g), while high $P_{Mo}$ results in non-uniform and multilayer growth. The growth on entire 4-inch wafer enables the fabrication of over 8100 transistor devices with high mobility of 30 $cm^2V^{-1}s^{-1}$, which is attributed to the high-quality intergrain stitching (Fig. 2.20h). Atomic layer deposition (ALD) is similar to MOCVD in using gaseous precursors. In ALD, two precursors are transported to the growth surface in an alternate, sequential manner, so that each precursor only reacts with the previous surface in a self-limiting way. This special transport of precursors results in well-controlled number of layers. ALD has been frequently reported with a low growth temperature as it uses highly

reactive precursors. For example, by using hexakis(dimethylamido)digallium and hydrogen sulfide, Meng et al.[189] observed the self-limiting growth of $GaS_x$ films with a thickness of 20–30 nm in the temperature range of 125–225 °C. Kuhs et al.[190] also achieved the self-limiting growth of $GaS_x$ films using trimethylgallium and $H_2S$/Ar plasma with a temperature range from 70 to 350 °C. However, a low growth temperature is unfavourable for the formation of thermodynamically stable products, and disorder is common in low-temperature growth, which can degrade their electrical properties. The precursors used in MOCVD or ALD are usually highly flammable and harmful to humans and environment. Alternatives for less toxicity or improving crystal quality have been developed in recent years, especially many Mo-sources such as $MoOCl_4$,[191] $[Mo(thd)_3]$,[192] $[Mo(NMe_2)_4]$,[193] $[Mo(N^tBu)_2(^tBu_2DAD)]$,[194] etc.

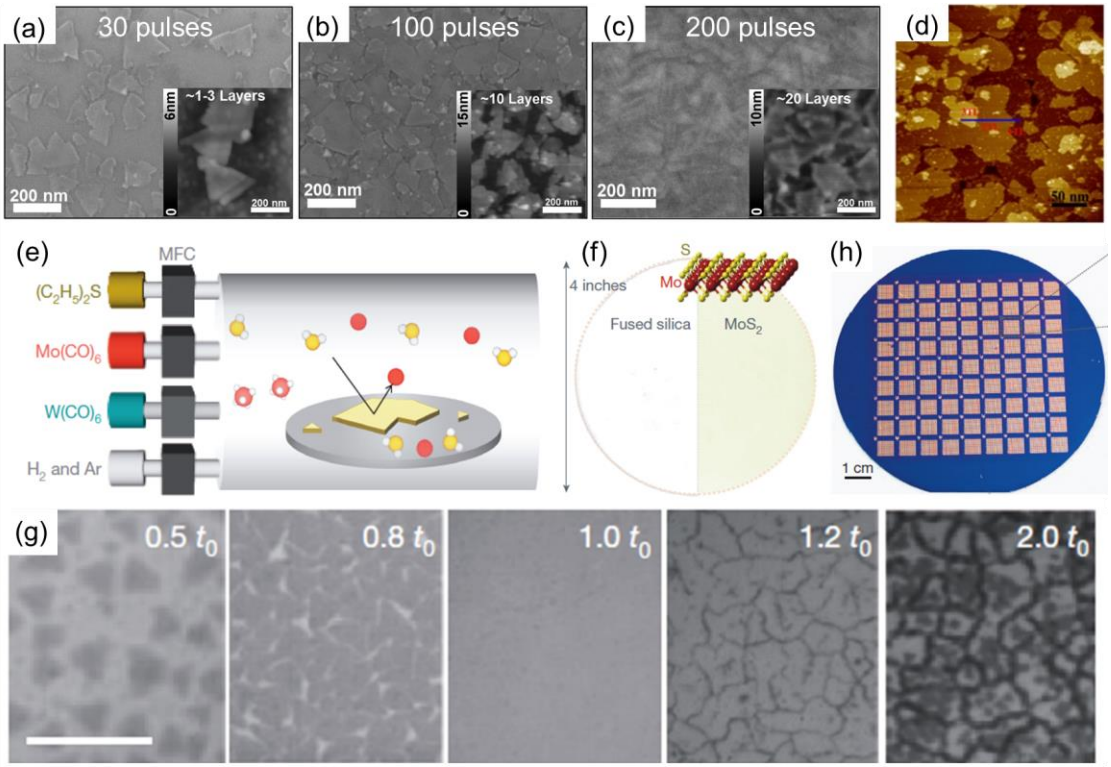



**Figure 2.20. Other VPD techniques for 2D layered semiconductor growth.** (a-c) SEM and AFM (insets) images of GaSe nanosheets deposited onto $SiO_2$/Si substrate at 30, 100, and 200 laser pulses. Reproduced with permission from ref. 186. Copyright 2014 Wiley-VCH. (d)

Large-scale (300 nm × 300 nm) scanning tunnelling microscopy image showing a GaSe flake containing monolayer, bilayer, and trilayer thickness. Reproduced with permission from ref. 30. Copyright 2017 American Physcial Society. (e) Schematic illustration of the MOCVD system and the gaseous precursors. (f) Photograph showing $MoS_2$ monolayers on 4-inch fused silica substrates (the left halves show the bare substrate for comparison). (g) Optical images of $MoS_2$ films at different growth times ($t_0$ is the optimal growth time for full monolayer coverage) (scale bar: 10 μm). (h) Mass production of ~8100 FET devices on the substrate. Reproduced with permission from ref. 188. Copyright 2015 Springer.

Direct sulfurization/selenization is a special CVD variant commonly used in 2D layered semiconductor growth. For example, as early as 2012, Zhan et al.[195] used a thin layer of pre-deposited Mo on $SiO_2$/Si wafer to react with S vapour at 750 °C to grow $MoS_2$ films (Fig. 2.21a-b). The thickness of the $MoS_2$ film is roughly controlled by the thickness of the deposited Mo film. However, due to the difficulty in depositing a uniform metal film, the $MoS_2$ after reaction consisted of both monolayer and few-layers (Fig. 2.21c). In addition, the mobility of the obtained $MoS_2$ layers is two orders of magnitude lower than mechanically exfoliated $MoS_2$, as a result of the nanoscale sized grains, defects and possibly unreacted metal precursor. As an improvement, Wang et al.[196] synthesised $MoS_2$ with controlled layers and high crystallinity by layer-by-layer sulfurization of $MoO_2$ microcrystals formed prior to sulfurization by reduction and thermal evaporation of $MoO_3$ (Fig. 2.21d). The sulfurization only takes place at the outmost $MoO_3$, and the $MoS_2$ flakes can be completely separated from $MoO_2$ by PMMA-assisted transfer. As the sulfurization of $MoO_2$ microplates is slow, layer-by-layer sulfurization can be accomplished and the layer thickness can be fine controlled from 1L to 3−4 L. Although the domain size is still limited by the $MoO_2$ microcrystal

template (generally 10 μm), the $MoS_2$ with high crystallinity shows mobility comparable with that of mechanically exfoliated $MoS_2$. Song et al.[197] synthesised ultrathin $WS_2$ films with controlled number of layers due to precise thickness control of the $WO_3$ precursor film deposited by ALD (Fig. 2.22a). With increasing ALD cycles from 20 to 50 in $WO_3$ growth, $WS_2$ with different number of layers from 1L to 3L can be uniformly grown on the substrate (Fig. 2.22b). Besides using metal and metal oxides, Liu et al.[155] demonstrated synthesis of mostly trilayer $MoS_2$ films on insulating substrates. First the substrate is dip-coated with diluted $(NH4)_2MoS_4$ solution, then the $(NH4)_2MoS_4$ underwent thermolysis under hydrogen protection ($(NH_4)_2MoS_4 + H_2 \rightarrow 2NH_3 + 2H_2S + MoS_2$) which is further annealed under sulfur vapour at 1000 °C (Fig. 2.21e). Although the $(NH4)_2MoS_4$ can directly decompose into $MoS_2$ at high temperature, the addition of sulfur significantly increased the crystal quality, PL signal intensity and electrical performance, with a high mobility of 4.7 $cm^2V^{-1}s^{-1}$. While these methods have obtained high-quality continuous films, one significant issue in all the above PVD or CVD variant techniques is the limited grain size under 1 μm due to the difficulty in controlling the nucleation process.

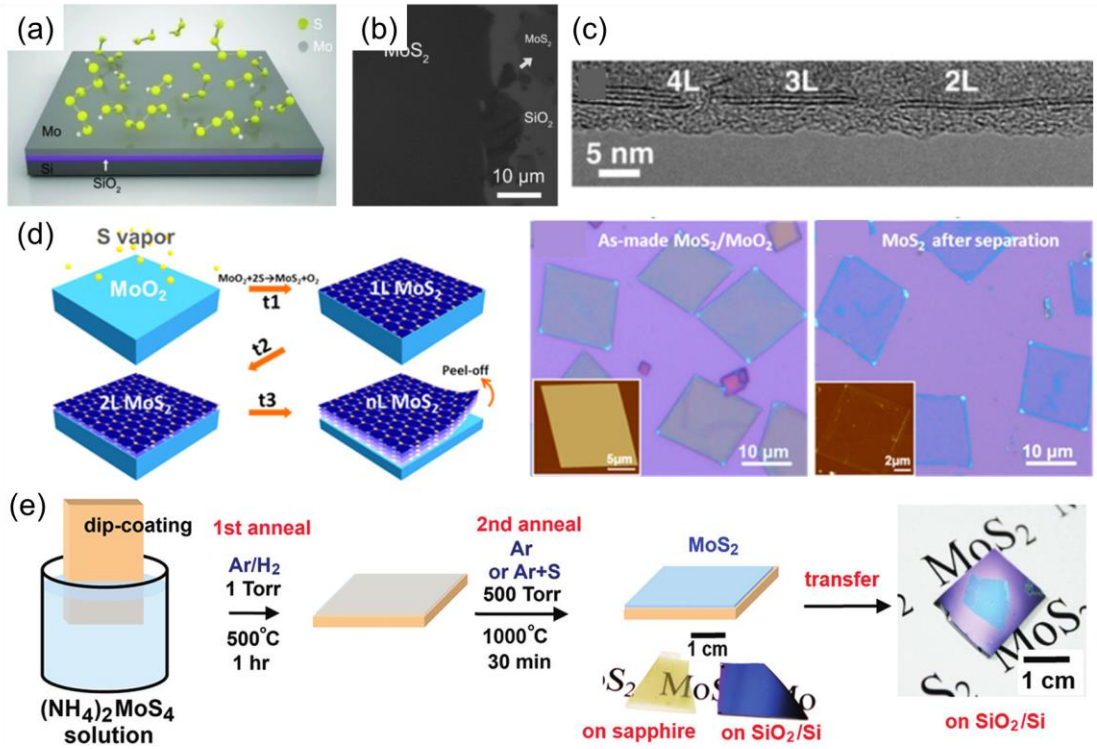



**Figure 2.21. Direct sulfurization of $MoS_2$ growth.** (a) Schematic illustration of sulfurization of Mo film on $SiO_2$/Si substrate. (b) SEM image of synthesised $MoS_2$ crystals. (c) TEM image of typical edge structure of as-grown $MoS_2$ showing varying thickness. Reproduced with permission from ref. 195. Copyright 2012 Wiley-VCH. (d) Schematics for the synthesis and cleavage of $MoS_2$ on $MoO_2$ templates. Below are optical and AFM (insets) images of as-made $MoS_2/MoO_2$ plates and the transferred $MoS_2$ flakes, respectively. Reproduced with permission from ref. 196. Copyright 2013 American Chemistry Society. (e) Schematic illustration of the two-step thermolysis process for synthesis of $MoS_2$ thin layers on insulating substrates using $(NH_4)_2MoS_4$ precursor. Reproduced with permission from ref. 155. Copyright 2012 American Chemistry Society.

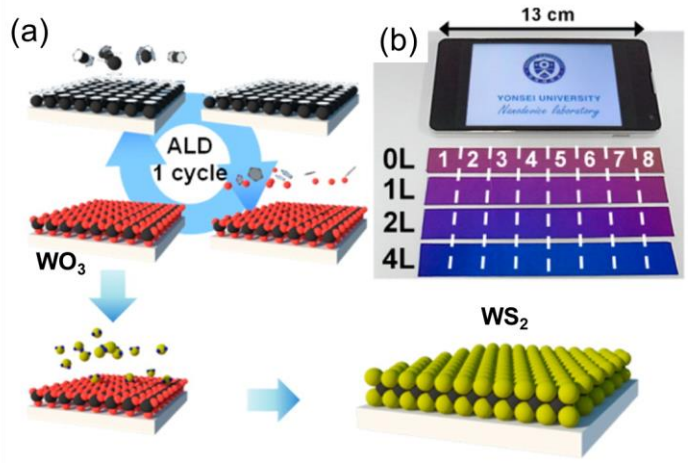



**Figure 2.22. Direct sulfurization of $WS_2$ growth.** (a) Schematic illustration of $WO_3$ films prepared by ALD and followed by sulfurization into $WS_2$ films. (b) Optical image of atomic thin $WS_2$ films with increasing number of layers. Reproduced with permission from ref. 197. Copyright 2013 American Chemistry Society.

## 2.4 Fabrication and Properties of VLHs

VLHs are artificial materials enabled by the weak vdWs interactions to easily bring different layered materials together at the nanometre scale with no restriction on lattice mismatch. Tuning the coupling between various 2D layered semiconductors in VLHs opens novel physical phenomena. In this section, two main fabrication methods: manual assembly and layer-by-layer growth are introduced. Then the energy band alignment between semiconductors in VLHs is discussed. The last part turns to a relatively new but heated research topic of twistronics which reveals the effect of twist angle on VLHs.

### 2.4.1 Manual Assembly

As artificial materials, fabrication of VLHs is built on successfully obtaining individual 2D layered semiconductors. In manual assembly, the building blocks are mostly

synthesised by mechanical exfoliation or VPD so that the number of layer or crystal orientation is uniform and known. The bottom building component is first transferred onto the target substrate, and then the next building component is transferred on top of it with the assistance from a supporting agent. Two issues are of main concern here. The first one is the accurate positioning of the two building components. This is achieved by using transparent supporting agents that allow tuning of position and also crystal orientation under optical microscope before the two layers make contact. Initially, scotch tapes are used for both mechanical exfoliation and stacking, but they are more difficult to manipulate mechanically, and thus are replaced by the transparent poly(dimethylsiloxane) (PDMS) stamps. The process is also applicable for wet transfer of 2D layered semiconductors synthesised from VPD. The other issue relates to the unwanted polymer residue between the layers that degrades the interfacial coupling. Removal of these stamps by solvents often left significant residues. An additional polymer film such as PMMA or PVA has been proposed to reduce the surface residue. Alternatively, Kang et al.[198] proposed a layer-by-layer assembly approach for fabricating high-quality interfaces at the wafer-scale (Fig. 2.23a-c). The building blocks are uniform 2D films on wafer grown by VPD. A thermal release tape was applied to peel the top layer, then the top layer was stamped onto the second top layer in vacuum to avoid air and water absorbates. The peel-stamp process was repeated until the designed structure is formed, with the top thermal release tape removed by heating. This method enables probing the intrinsic properties of the interface in VLHs without polymer residue or absorbates.

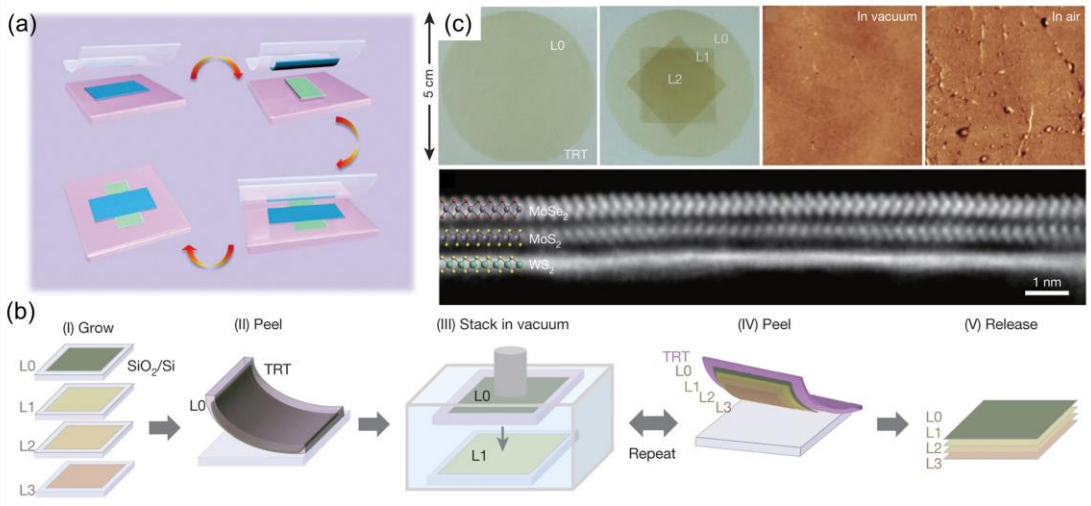



**Figure 2.23. Assembly of 2D layered semiconductors.** (a) Schematic illustration of transfer of 2D layered semiconductors by PDMS stamp and fabrication of VLHs from bottom to top. Reproduced with permission from ref. 199. Copyright 2018 Wiley-VCH. (b) Workflow for layer-by-layer assembly of 2D layered semiconductors using thermal release tape (TRT) and fabrication of VLHs from top to bottom. (c) Up left: Photo of wafer-scale 2D VLHs fabricated by layer-by-layer assembly approach. Up right: comparison of interface cleanliness under AFM. Bottom: cross-section TEM characterisation of the heterostructure interface. Reproduced with permission from ref. 198. Copyright 2017 Springer.

### 2.4.2 Layer-by-Layer Growth

The interface quality of VLHs fabricated by manual stacking is very sensitive to the fabrication environment and procedures, where it is difficult to completely remove polymer residues or surface absorbates. With the advancement in VPD techniques, layer-by-layer growth of 2D building blocks on top of another has been developed for fabrication of VLHs due to the clean interface under high temperature and the ability to scale-up. A number of examples are already discussed in section 2.3.3 of epitaxial growth where 2D materials as growth substrate leads to direct growth of VLHs

including GaSe/$MoSe_2$, GaSe/$MoS_2$, $PbI_2$/$WS_2$. Many other VLHs such as $SnS_2$/$WSe_2$,[200] $SnSe_2$/$MoS_2$,[201] $WS_2$/$MoS_2$,[202] $MoS_2$/$WSe_2$,[203] etc. have also been reported. In general, fabrication of VLH by layer-by-layer growth is considered as a two-step process and the bottom layer is required to have higher thermal stability. In addition, it is found that the growth temperature could alter the morphology of products. Chang et al.[204] demonstrated the growth of $SnS_2$ on monolayer $WS_2$ (Fig. 2.24a). Under lower growth temperature the $SnS_2$ growth occurs only at the $WS_2$ crystal edge, while a higher growth temperature enables the growth of $SnS_2$ on the $WS_2$ surface. This is explained by the diffusion barrier of Sn-species. As the $WS_2$ basal plane is considered as defect-free, the reactive species are more prone to attach to dangling bonds at edge structure (Fig. 2.24b) or grain boundaries (Fig. 2.24c). At higher temperature the diffusion barrier of Sn-species could be overcome thus leading to nucleation and growth on the $WS_2$ surface. Similar controllability of morphology has been reported by Gong et al.[202] in growth competition between vertical stacking and lateral stitching (Fig. 2.25c). It was found that the thermodynamic product (the vertical heterostructure) is formed at higher temperature of 850 °C while the kinetic product (the lateral heterostructure) grows preferably at 650 °C (Fig. 2.25a-b). As the nucleation barrier of $WS_2$ is high, attaching to the $MoS_2$ edge with strong chemical bonding results in smaller nucleation energy at lower temperature. At higher temperature, the large thermal energy allows nucleation at the $MoS_2$ surface, thus leading to the growth of thermodynamic product of $WS_2$/$MoS_2$ VLHs.

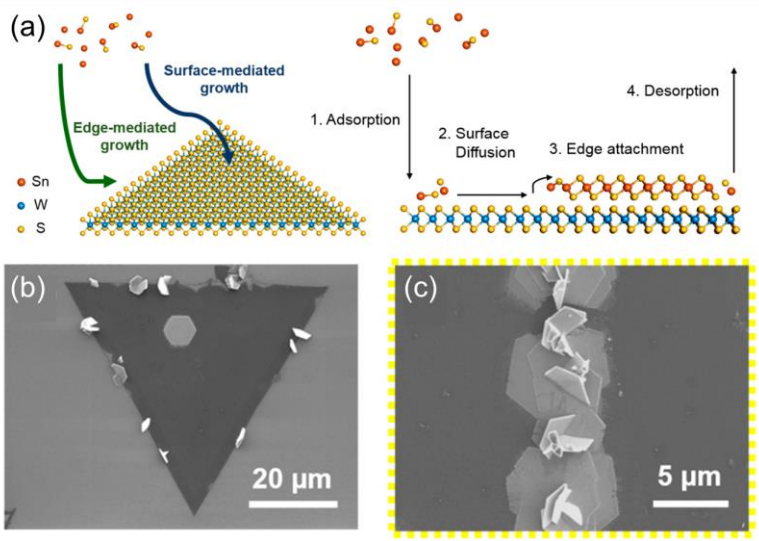



**Figure 2.24. Layer-by-layer growth of $SnS_2/WS_2$ VLHs.** (a) Schematic illustration showing the growth of $SnS_2$ on $WS_2$. The growth can be mediated by edge or surface where the surface-mediated growth is kinetically favoured. (b) SEM image of $SnS_2/WS_2$ VLHs showing edge and surface-mediated growth. (c) SEM image of $SnS_2/WS_2$ VLHs showing preferential growth on grain boundaries. Reproduced with permission from ref. 204. Copyright 2019 American Chemistry Society.

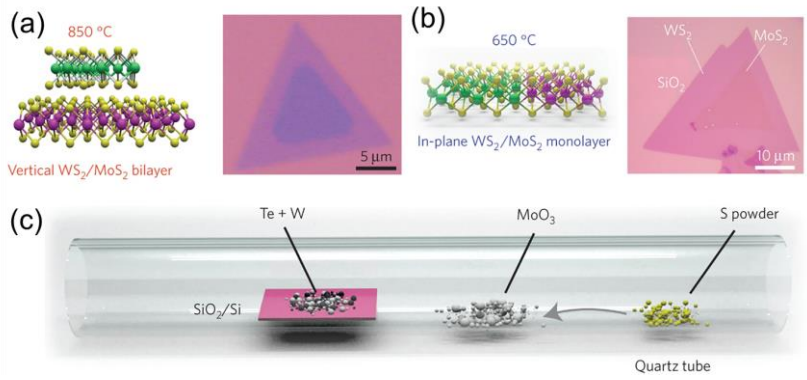



**Figure 2.25. Layer-by-layer growth of $WS_2/MoS_2$ VLHs.** (a) Atomic model and optical image of vertical $WS_2/MoS_2$ heterostructure synthesised at 850 °C. (b) Atomic model and optical image of in-plane $WS_2/MoS_2$ heterostructure synthesised at 650 °C. (c) Schematic illustration of one-furnace synthesis of $WS_2/MoS_2$ vertical/lateral heterostructures, where $MoS_2$ is found to grow first. Reproduced with permission from ref. 202. Copyright 2014 Springer.

### 2.4.3 Energy Band Alignment

In conventional semiconductor heterojunctions, the energy band alignment can be categorised into the following three types. Illustrated in Figure 2.26a, in type-I (straddling) heterojunctions, the CB of the left side is higher than that of the right side while the VB of the left side is lower than the other. Both electrons and holes tend to jump from the energy band from left to right, thus the confinement of both types of carriers is suitable for applications such as LEDs. In type-II (staggering) heterojunctions, both the CB and VB on one side is higher/lower than the other. Such a structure results in efficient charge separation, and is very beneficial for the photovoltaic effect in photodiode detectors or solar cells. As for the last one, the type-III (broken) heterojunction, the CB of the semiconductor on one side is lower than the VB of the other one. The bandgap of the two semiconductors do not overlap, which is suitable for applications in tunnelling FETs for achieving sub 60 mV/dec subthreshold swing. While theoretical calculations of band structure offer predictions of potential heterojunction formed between any two 2D layered semiconductors (Fig. 2.26b),[205] the actual band offset often is affected by charge doping, interfacial states or external fields,[206-208] thus additional characterisation of band structure is sometimes required to understand the heterojunction.

All three types of heterojunctions can be achieved in VLHs constituted of 2D layered semiconductors. The type-II heterojunction is explored most since they are attractive for many optoelectronic applications. The properties of interlayer excitons have been introduced in section 2.2.3 and application of these heterojunction in photodiodes will be discussed in detail in section 2.5.2. Here the attention is focused on differences

between conventional and atomically sharp type-II heterojunctions. In conventional p–n type-II heterojunctions, the built-in field is formed by carrier diffusion and the depletion region. In atomically thin VLHs without depletion region, the heterojunction properties are determined by interlayer tunnelling recombination across the vdWs gap. Charge separation is mediated through exciton dissociation under the large CB and VB offset, while charge recombination is mainly through two possible tunnelling mechanisms: Shockley–Read–Hall recombination assisted by trap states in the gap or Langevin recombination by Coulomb interactions (Fig. 2.26c-d).[209] Unlike conventional heterojunctions, the built-in field could be effectively tuned by external electric fields including electric gating and charge impurities to modify the electrical and optoelectronic behaviours.

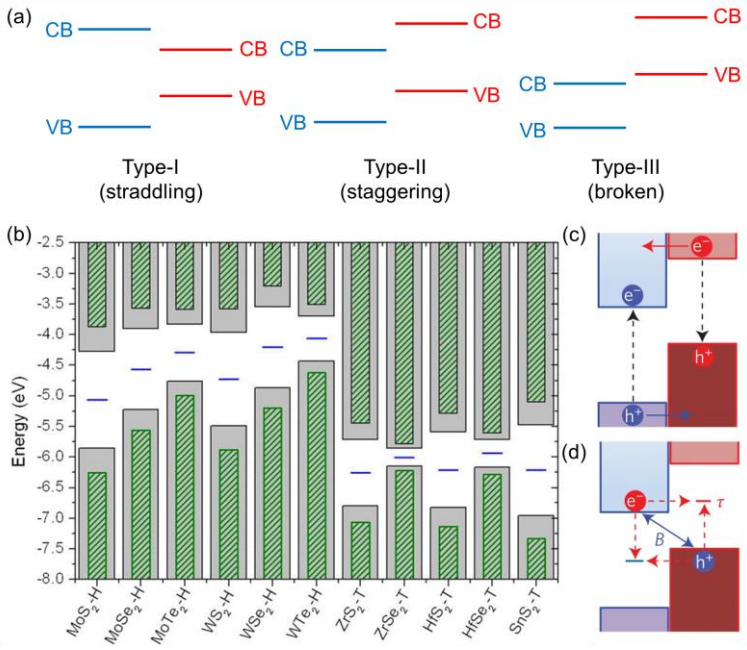



**Figure 2.26. Band alignment in 2D VLHs.** (a) Three types of band alignments in semiconductor VLHs. (b) Calculated CB and VB of several 2D layered semiconductors. Reproduced with permission from ref. 205. Copyright 2013 American Institute of Physics. (c) Exciton dissociation in atomically sharp 2D type-II VLHs. (d) Interlayer tunnelling

recombination in atomically sharp 2D type-II VLHs via SRH recombination or Langevin recombination. Reproduced with permission from ref. 209. Copyright 2014 Springer.

### 2.4.4 Twistronics

As the weak vdWs interaction releases restrictions on lattice mismatch and orientation, Moiré superlattices can be constructed from stacking of heterojunctions with lattice mismatch or misorientation. Especially, recent studies on small twist angle systems where the Moiré superlattice cell is larger than 10 nm has revealed significant quantum phenomena such as strong correlated electronic phases or Moiré excitons.[110-113, 210] This allows fine control of emerging properties in vdWs heterostructure by precisely tuning the twist angle. As an example, Tran et al.[113] observed Moiré excitons in twisted bilayer $MoSe_2/WSe_2$ heterostructures. Owing to the existence of lattice mismatch and misorientation, the Moiré pattern results in Moiré potential predicted with an amplitude of 100-200 meV (Fig. 2.27a). The strong potential is thus expected to localise interlayer excitons and form quantised energy levels due to the lateral confinement effect. By measuring the interlayer exciton emission spectrum at low temperature (15 K), quadrapeaks can be resolved in 1°-twisted $MoSe_2/WSe_2$ heterostructure across an energy range of ~70 meV, in accordance with the amplitude of the Moiré potential (Fig. 2.27b-c). Other studies have also demonstrated the effect of Moiré potential on valley exciton emission,[110] Moiré trions[211] and intralayer excitons,[111-112] and very recently the observation of Moiré excitons in trilayer systems.[212]

Quantum correlated phases have also been studied in TMD VLHs. Regan et al.[213] used optically detected resistance and capacitance to detect Mott states in nearly-0° twisted $WSe_2/WS_2$ heterostructure with 8 nm superlattice cell due to ~4% lattice mismatch.

Insulating states were observed at one hole per superlattice as well as 2/3 and 1/3 fillings (Fig. 2.27d). The unusual insulating states at 2/3 and 1/3 filling are considered as the generalised Wigner crystallisation of holes under highly correlated electrons (Fig. 2.27e). It was also shown that the Mott insulator state leads to enhancement of spin excitation lifetime. Very recently, metal-insulator transitions (MIT) have also been reported in twisted bilayer $WSe_2$ and $MoTe_2/WSe_2$ heterostructures.[214-215] The correlated insulating phase at fixed filling can continuously be transformed into the metallic phase by both gate modulation or vertical displacement field, which allows further investigation of quantum spin liquids. These studies demonstrated the excellency of TMD VLHs as novel platforms for the discovery of excited correlated phases due to both strong light-matter interactions and large spin-orbit coupling.

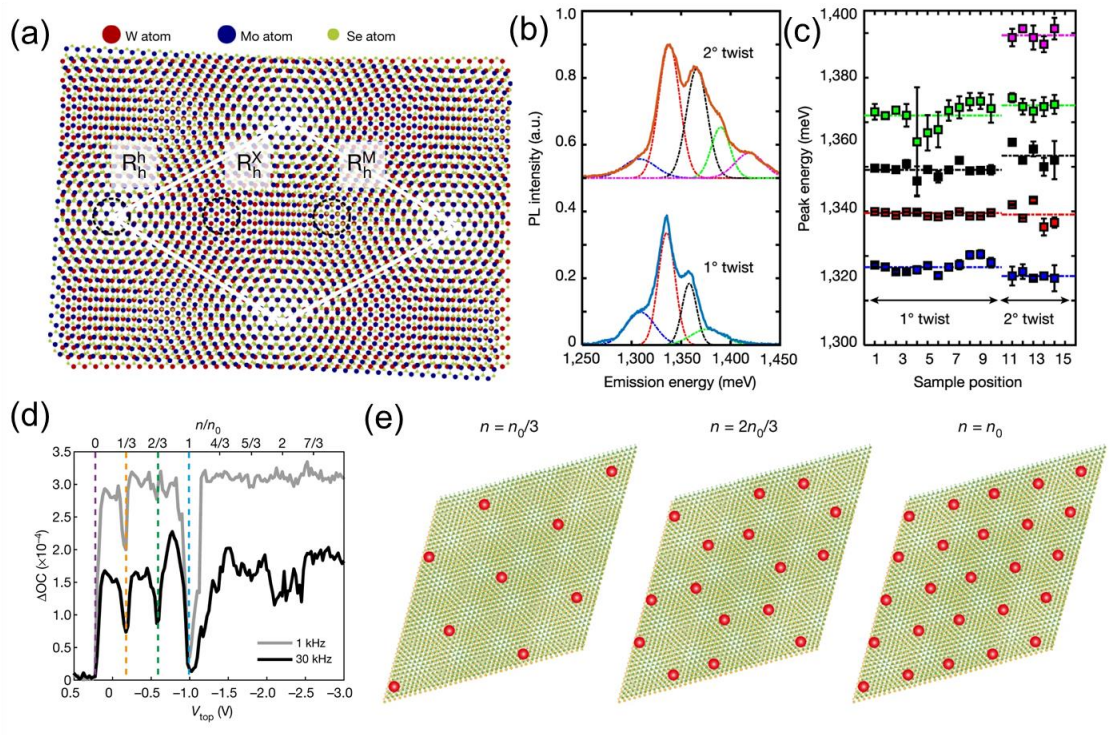



**Figure 2.27. Twistronics in TMD VLHs.** (a) Schematic showing local variation of Moiré potential in a small-angle twisted $MoSe_2/WSe_2$ VLH. The three highlighted points correspond to three points in the superlattice cell with three-fold rotational symmetry. (b) Interlayer PL

emission spectra in twisted $MoSe_2/WSe_2$ VLHs with 1° and 2° twist angles. (c) Peak positions of multiple peaks fitted from spectra in (b). Reproduced with permission from ref. 113. Copyright 2019 Springer. (d) ODRC signal at 1 kHz and 30 kHz under different hole doping conditions. (e) Schematic illustration of generalised Wigner crystal structure (left and middle) and Mott insulator states (right) in $WSe_2/WS_2$ VLHs. Reproduced with permission from ref. 213. Copyright 2021 Springer.

## 2.5 Ultrathin Optoelectronics Based on 2D Layered Semiconductors

In this section, the applications of 2D layered semiconductors in optoelectronics are introduced, especially as photodetectors or LEDs. The most prevalent photo sensing mechanism in 2D channels are photoconducting effect and photovoltaic effect, while photo thermoelectric effect and bolometric effect are less reported.[216-217] In photoconducting effect, the device operates under a bias voltage. Photoexcited carriers form free carriers and then contribute to the photocurrent. The photogain (G), which is defined as the number of collected carriers in the photocurrent for every excited electron by incident light, can be expressed as:

$$G = \frac{\tau \mu E}{L}, \tag{2.3}$$

where τ is the excess carrier lifetime, μ is the carrier (electron and hole) mobility, E is the electric field provided by bias voltage and L is the channel length.[218] For G values larger than 1, the physical interpretation can be understood as when the majority carrier reaches the drain electrode, another majority carrier enters from the source electrode to continue contribute to the photocurrent until it is recombined with a minority carrier. In atomically thin 2D layered semiconductors, the large exciton binding energy hinders dissociation of bound excitons into free carriers. However, the channel is sensitive to

surface or interfacial trap states, thus the dominant photocurrent is from a photogating effect, a special case of the photoconducting effect. In photogating, minority carriers in the exciton are localised at trap states and act as local gates to enhance the channel conductivity. Thus, ultrathin photodetectors could show ultrahigh photogain due to large surface ratio and strong light-matter interactions. The photovoltaic effect utilises the built-in field to enable efficient charge separation and collection, and could operate at zero bias voltage for low-power optoelectronics. The mechanism is the same as in solar cell devices. Note that photogain for photovoltaic devices operating at zero bias cannot exceed 1. Below, 2D photodetectors based on the two different mechanisms are introduced separately in sections 2.5.1 and 2.5.2.

### 2.5.1 Photoconductors

In 2D photoconductors, usually both the photoconducting and photogating effects exist, dependent on the layer thickness and surface electronic states. Furchi et al.[219] separated the two mechanisms in monolayer $MoS_2$ by differentiating the response time (Fig. 2.28a). The $MoS_2$ device shows strong photorepsonse (~6 A/W) and long response time (~2 s) under illumination with white light, but shows relatively low photocurrent (0.06 A/W, measured by an oscilloscope) and short response time (<0.1 ms) when illuminated with laser pulses. The large photoresponse under the photogating effect mechanism is accompanied by slow response due to long-lived carriers in traps. In addition, the photocurrent under this mechanism is gate-dependent as the photogating effect embodies a shift of the transfer curve in the lateral direction, while any photocurrent induced by the photoconducting effect is gate-independent. As Figure 2.28b-c shows, the $In_2Se_3$ photodetector exhibits much higher photoresponse at elevated carrier doping.[220] In addition, under the photoconducting effect mechanism, the photocurrent

increases nearly linearly with illumination power, while under the photogating effect mechanism the photocurrent soon begins to saturate due to saturation of trap states. The photoresponsivity for photoconductors based on 2D layered semiconductors could reach up to $10^6$ A/W although at a cost of slow response time.

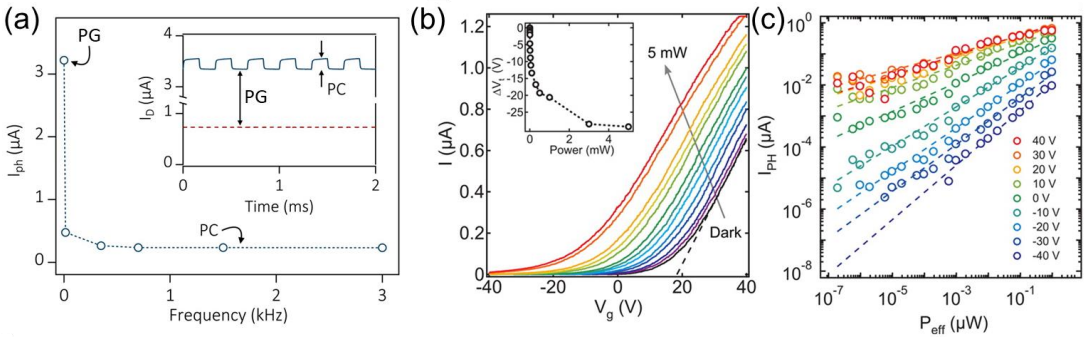



**Figure 2.28. Photoconductors based on 2D layered semiconductors.** (a) Photocurrent amplitude versus modulation frequency in $MoS_2$ devices. Inset: Source−drain current versus time under dark (dashed red line) and illumination (solid blue line). Reproduced with permission from ref. 219. Copyright 2014 American Chemistry Society. (b)Transfer curve evolution with increasing illumination power. Inset: Threshold voltage shift versus illumination power. (c) Photocurrent versus illumination power under different gate voltages in $In_2Se_3$ devices, showing dominantly photoconducting effect under negative gate voltage and dominantly photogating effect under positive gate voltage. Reproduced with permission from ref. 220. Copyright 2015 American Chemistry Society.

The photogating effect can also be used in VLHs where one type of carrier is trapped in one layer. Utilising the high mobility of graphene, Zhang et al.[221] fabricated graphene/$MoS_2$ heterostructures with ultrahigh photoresponsivity of $10^7$ A/W and photogain of $10^8$ (Fig. 2.29a-b). Due to the built-in field, photoexcited electrons are transferred from $MoS_2$ to graphene while the holes stay in the $MoS_2$. Note that while the charge transfer process and built-in field resembles the photovoltaic effect, there is

no charge collection here, thus it falls into the photogating effect mechanism. The photoresponsivity increases at a negative gate voltage, as a slightly p-doped graphene further facilitates the charge transfer process (Fig. 2.29c).

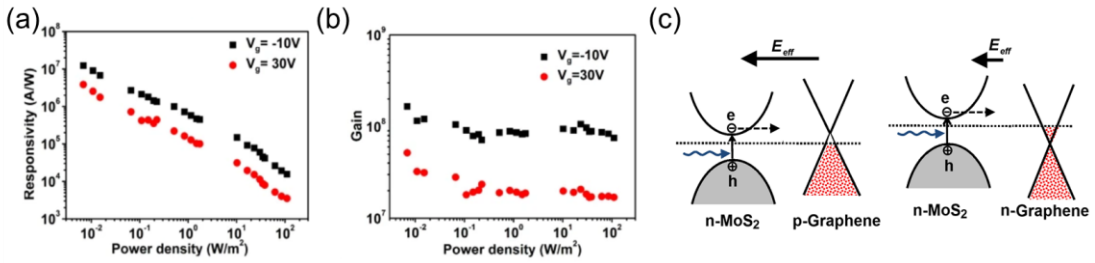



**Figure 2.29. Photogating in $MoS_2$/Gr heterostructures.** (a) Photoresponsivity versus illumination power under different gate voltages in graphene/$MoS_2$ heterostructures. (b) Photogain versus illumination power under different gate voltages in graphene/$MoS_2$ heterostructures. (c) Schematic illustration of charge transfer between graphene and $MoS_2$ under different gate voltages. Left: negative gating voltage. Right: positive gating voltage. Reproduced with permission from ref. 221. Copyright 2014 Springer.

As semiconductors only allow light absorption beyond their bandgap, 2D layered semiconductors with wide bandgap are ideal candidates for high-performance special wavelength photodetectors such as UV–vis or UV-discriminative photodetectors.[222-223] The first employment of wide bandgap 2D semiconductors in photodetectors was based on the MX III–VI family. Hu et al.[47] fabricated few-layer GaSe photodetectors by mechanical exfoliation with high sensitivity to UV–visible light (wavelength < 610 nm), in agreement with the GaSe bandgap. The device also showed a fast response time of 0.02 s and a high photoresponsivity of 2.8 A $W^{-1}$ at 254 nm, which values are superior to those of its bulk counterparts (Fig. 2.30a-b). Similarly, Lei et al.[48] showed that photodetectors prepared by 6–8L GaSe synthesised by vapour phase transport have a

photoresponse to excitations from 620 nm, and the low dark current, possibly originating from low impurity density, leads to a high on–off ratio of $10^3$ at 405 nm illumination, which makes it suitable for photodetector and sensor applications. In addition, the few-layer CVD-grown GaSe photodetectors fabricated by Li et al.[151] also showed a photoresponsivity of ∼1.7 A $W^{-1}$ under white light, comparable to that of mechanically exfoliated photodetectors.[224] GaS was introduced at the same time with larger bandgap but also extraordinary optoelectronic properties. An early report showed that GaS with unknown thickness exhibits a large on–off ratio with the illumination of white light.[225] Later, a 3L GaS photodetector prepared by mechanical exfoliation on $SiO_2$/Si substrate was further reported with a photoresponsivity of 4.2 A $W^{-1}$ at 254 nm and a high switching on–off ratio of $2.94 \times 10^4$, with an onset at 520 nm (Fig. 2.30c).[226] They also demonstrated that the photoresponsivity of a GaS photodetector could achieve 19.2 A $W^{-1}$ on a flexible substrate, and the performance was stable after repeated bending (Fig. 2.30d-e). Carey et al.[227] also prepared 2L GaS phototransistors with a responsivity of ∼6.4 A $W^{-1}$ under a solar simulator and an on/off ratio of ∼170. In addition to the MX family, other wide bandgap 2D semiconductors have also been used in photodetectors owing to the strong light–matter interactions. Zhou et al.[54] fabricated photodetectors based on CVD-grown 10 nm $SnS_2$ crystals. The photodetectors exhibited a cutoff wavelength at ∼560 nm (2.21 eV), which is close to the bandgap of 2.23 eV measured from the PL spectrum. The photodetectors possessed a very high photoresponsivity of 261 A $W^{-1}$ at 350 nm illumination, as well as a fast response time, with a rise time of 20 ms and a decay time of 16 ms. Ye et al.[55] fabricated photodetectors on monolayer $SnS_2$, which showed the strongest photoconductivity at 390 nm but with a tail extending to about 650 nm (Fig. 2.30f-g). The large rise in photocurrent at around 390 nm is understood as bandgap-related absorptions, while the

tail at lower photon energy is likely to originate from both the electron excitation at the metal–semiconductor interface with Schottky barrier and the charge carrier trap states within the bandgap. Many other studies have been reported on high-performance photodetectors based on 2D $SnS_2$,[228-230] $PbI_2$,[64] $HfS_2$,[61] etc.

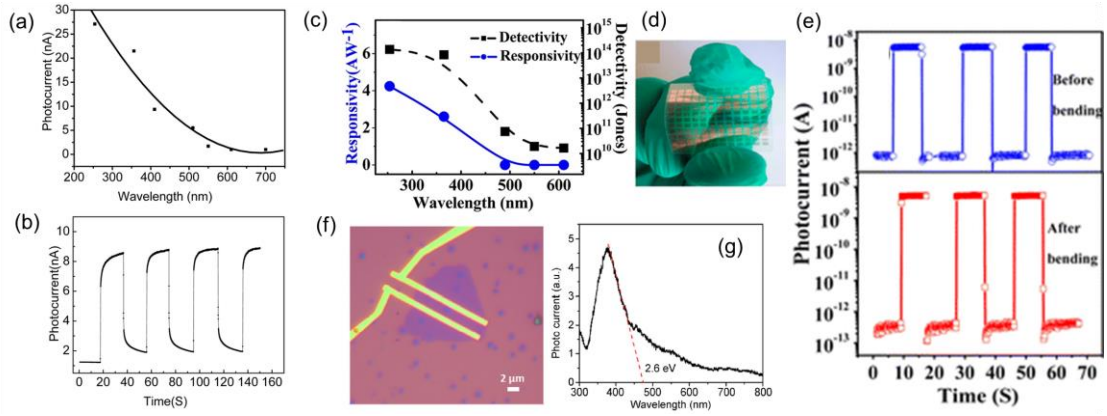



**Figure 2.30. Phototransistors based on wide bandgap 2D layered semiconductors.** (a) Wavelength-dependent photocurrent of a few-layer GaSe photodetector. (b) Photocurrent of a GaSe photodetector as a function of time at bias voltage of 1 V. Reproduced with permission from ref. 47. Copyright 2012 American Chemical Society. (c) Wavelength-dependent photoresponsivity and photodetectivity of a few-layer GaS photodetector. (d) Optical image of GaS nanosheet devices on a PET substrate. (e) Photocurrent as a function of time before or after bending the photodetector in (d) with the pulse illumination at a bias voltage of 2 V. Reproduced with permission from ref. 226. Copyright 2013 American Chemical Society. (f) Optical image of the $SnS_2$ device. (g) Photoconductivity spectrum of monolayer $SnS_2$ showing the strongest photoconductivity at about 390 nm with an estimated band gap of 2.6 eV. Reproduced with permission from ref. 55. Copyright 2017 Springer.

Devices for detecting UV light (or solar-blind detectors) have also been developed, which led to further expansion in the members of wide bandgap 2D semiconductors. The current commercial silicon-based UV detectors possess photoresponsivity of less

than 0.1 A $W^{-1}$ for $\lambda < 400$ nm.[231] Arash et al.[232] fabricated UV photodetectors based on 8 nm $MoO_{3-x}$ flakes grown by PVD and showed a high responsivity of 54.4 A $W^{-1}$. The deliberate introduction of oxygen vacancies in the crystal can lead to increasing carrier concentration, hence contributing to the high photoconductivity. The partially reduced cation sites are also regarded as electron traps which facilitate photogenerated charge separation. Interestingly, the device still shows a fast response time of 200 μs regardless of the defects. Zhong et al.[233] noted the anisotropic photoresponse in α-$MoO_3$ solar-blind photodetectors. The measured photoresponse along the [010] direction is 5.2 times larger than that along the [001] direction (Fig. 2.31a-b). Based on electronic measurements and theoretical modelling, this anisotropic behaviour is attributed to differences in electron effective mass-related carrier mobility along two axes, deriving from the intrinsic anisotropy in the crystal structure. Similar in-plane structural anisotropy in 2D $GeS_2$ and $GeSe_2$ has been employed for polarisation-sensitive UV detection. Polarisation-sensitive photodetection can be very helpful to navigation, high-contrast polarisers, and complex optical systems. As demonstrated by Yang et al.,[59-60] the crystals exhibit both anisotropic reflection and absorption with a two-lobe shape, showing an extinction ratio of 2.1 for $GeS_2$ and 3.4 for $GeSe_2$ (Fig. 2.31c-d).

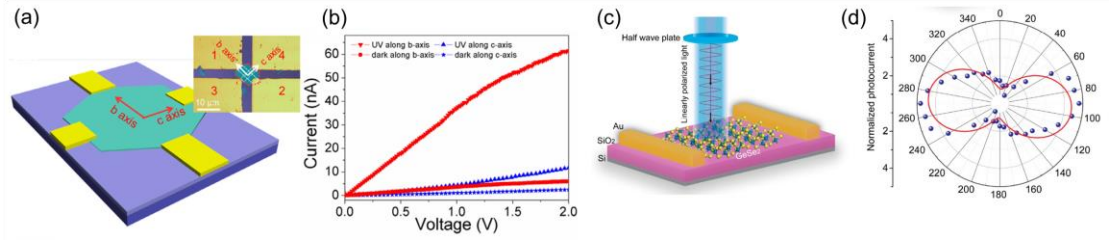



**Figure 2.31. Anisotropic photoresponse in wide bandgap 2D layered semiconductors.** (a) Schematic illustration of the anisotropic ultrathin α-$MoO_3$ device. Inset: optical image of the prepared device, with the effective area of the electrodes marked in the image. (b) I–V characteristics of the ultrathin α-$MoO_3$ device under dark and illumination conditions along

different axis. Reproduced with permission from ref. 233. Copyright 2018 Institute of Physics. (c) Schematic structure of the $GeSe_2$ photodetector. (d) Polar plot of the normalised angle-resolved photocurrent as a function of the polarisation angle. Reproduced with permission from ref. 59. Copyright 2018 American Chemical Society.

### 2.5.2 Photodiodes

The built-in field of photodiodes based on 2D VLHs can be realised either by graphene/semiconductor/graphene structure or p–n diode. In graphene/semiconductor/-graphene structures, a built-in field is formed across the two graphene layers due to differences in doping levels, which drives charge separation of excitons in the semiconductor layer and collection of free carriers at source and drain. Yu et al.[234] demonstrated a prominent photovoltaic effect on graphene/FL-$MoS_2$/graphene vertical structures (Fig. 2.32a). Under 80 μW illumination light, the photodiode exhibits an open-circuit voltage of 0.3 V and short-circuit current of 2 μA, which corresponds to a photoresponsivity of 0.025 A/W. In addition, the photo switching speed is lower than 50 μs, and photocurrent mapping suggests broad-area photocurrent generation (Fig. 2.32c). The VLH further shows efficient gate tunability due to changes in effective built-in field, which leads to a shift in open-circuit voltage and short-circuit current (Fig. 2.32b-c). A high external quantum efficiency (EQE: the ratio between optical input and electrical output) of 25% is observed under low illumination power but then decreases to 15% under high illumination power, which is attributed to the saturation in semiconductor absorption and the increased screening effect in the graphene channels. Similar results have also been reported in other TMDs, which demonstrates the efficient carrier separation and collection in graphene/semiconductor/graphene structures.[235]

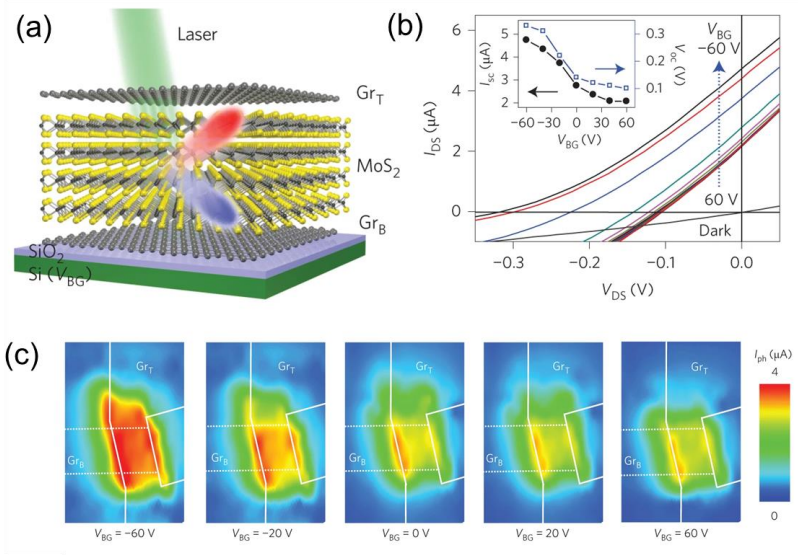



**Figure 2.32. 2D Graphene/TMD/Graphene photodiodes.** (a) Schematic illustration of graphene/-semiconductor/graphene vertical heterostructure and charge separation. (b) Source−drain current under dark and illumination light and various gating voltages. (c) Photocurrent spatial mapping of graphene/$MoS_2$/graphene under different gating voltages. Reproduced with permission from ref. 234. Copyright 2013 American Chemistry Society.

Alternatively, Lee et al.[209] demonstrated photodiodes built from atomically thin p–n heterojunctions of $MoS_2/WSe_2$ (Fig. 2.33a). Under zero gate voltage, the p–n junction exhibits a photoresponsivity of 2 mA/W under 532 nm laser illumination. While the 2D type-II heterojunction enables ultrafast charge separation, the author noted possible non-radiative interlayer recombination processes by two mechanisms: Shockley–Read–Hall recombination assisted by defect states and Langevin recombination under strong Coulomb interactions (Fig. 2.33b). Therefore, quick charge extraction can reduce non-radiative recombination and improve the photoresponsivity. In addition, it is believed that the charge collection process is inefficient across the low-conductivity semiconductor lateral channels, thus transparent graphene electrodes are used to assist charge separation and collection. As Figure 2.33c-d shows, the graphene-sandwiched

structure shows 5 times higher photoresponsivity than the vertical structure without graphene, with an EQE of ~2.4%. The EQE value can further be boosted up to 34% for multilayer p–n junctions due to increased absorption rate.

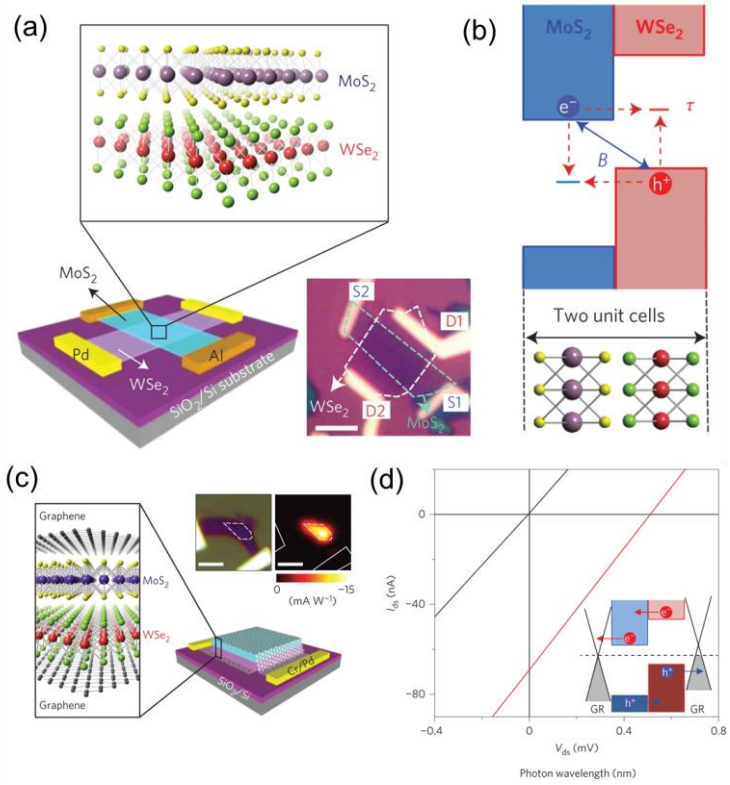



**Figure 2.33. 2D p-n junction photodiodes.** (a) Schematic, atomic model and optical image of $MoS_2/WSe_2$ p–n heterojunction. (b) Band diagram schematic illustration of Shockley–Read–Hall recombination process assisted by defect states and Langevin recombination process under strong Coulomb interactions. (c) Schematic illustration of graphene-sandwiched p–n photodiodes. Inset: Optical image and photocurrent spatial mapping of graphene-sandwiched p–n photodiodes. (d) Dark current and photocurrent of graphene-sandwiched p–n photodiodes. Reproduced with permission from ref. 209. Copyright 2014 Springer.

Photodiodes based on various TMD/TMD heterojunctions have been reported.[236-238] In addition, TMDs have been combined with other 2D layered semiconductors. Wei et al.[239] fabricated graphene-sandwiched $WSe_2$/GaSe p–n junctions with a high

photoresponsivity of 6.2±0.2 A $W^{-1}$ and an ultrafast response time down to ~30 μs, facilitated by the ultrafast charge separation between vdW heterostructures. After forming hybrid $MoS_2$ with 3L GaSe via direct CVD growth, Zhou et al.[178] noticed an improvement in response time by almost 3 orders of magnitude due to strong interlayer coupling. Islam et al.[240] also fabricated GaSe/$MoS_2$ photodetectors suitable for detecting ultra-low-level illumination with a very low noise equivalent power of ~$10^{-14}$ W/$Hz^{1/2}$ and a large linear dynamic range of 70 dB by manipulating the metal–semiconductor junction. A p−g−n device structure has been shown to exhibit broadband photodetector performance that is advantageous for many optoelectronic applications.[241] Li et al.[242] further fabricated h-BN/$MoTe_2$/graphene/$SnS_2$/h-BN vdW heterostructure photodetectors (Fig. 2.34a-c). The p−g−n junction exhibits a broadband photoresponsivity exceeding 2600 A $W^{-1}$ and an ultralow noise equivalent power of $10^{-17}$–$10^{-16}$ W/$Hz^{1/2}$ under low light illumination power (Fig. 2.34d-e). The large photocurrent from the built-in electric field originating from p-$MoTe_2$ and n-$SnS_2$ can significantly facilitate electron–hole separation along with the large mobility in both $MoTe_2$ and $SnS_2$. Meanwhile, the sandwiching graphene improves the interface quality and reduces interface charge traps, and the h-BN layers on both sides prevent the detrimental effect of charge impurities from either the substrate or environment. Instead of using a p–n junction, Zhou et al.[243] fabricated a tunnelling diode based on the $WSe_2$/$SnS_2$ heterostructure. The device shows an ultralow dark current at the depletion region and a high tunnelling current with photon illumination, therefore exhibiting an ultrahigh photodetectivity of 1.29 × $10^{13}$ jones and a photoresponsivity of 244 A $W^{-1}$ at reverse bias.

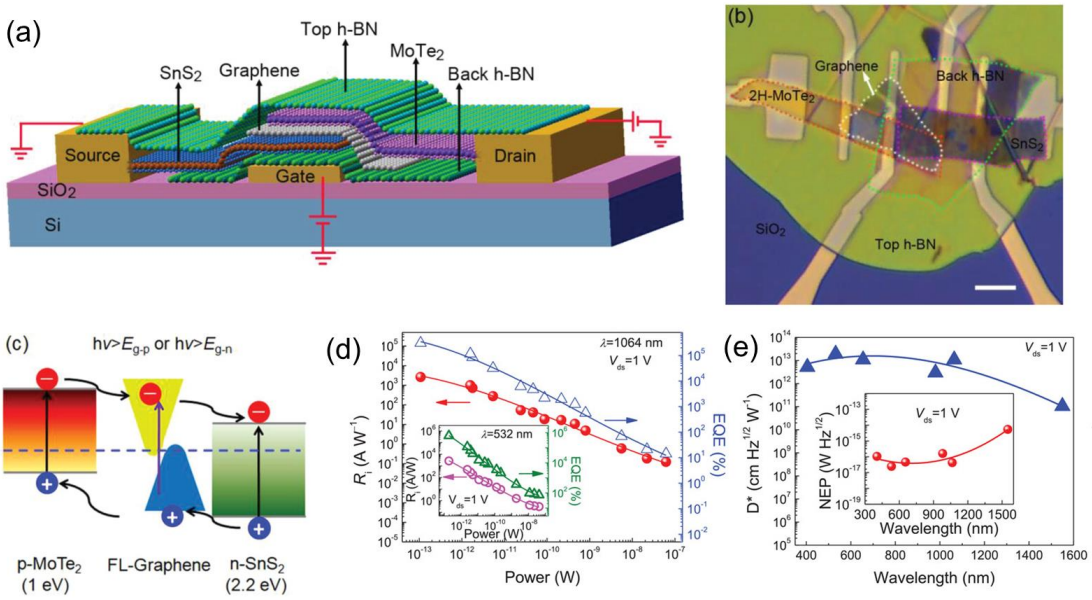



**Figure 2.34. 2D photodetectors based on VLHs for broadband photodetection.** (a) Schematic h-BN/$MoTe_2$/graphene/$SnS_2$/h-BN device configuration and the experimental setup. (b) Optical image of a typical fabricated device. Scale bar: 6 μm. (c) Schematic band diagram and photoexcited carriers transport of the $MoTe_2$/graphene/$SnS_2$ vdW heterostructures. (d) Responsivity (left axis) and EQE (right axis) versus light illumination power with excitation wavelength at 1064 nm, showing the high sensitivity of the devices, with direct measurement of 0.1 pW. Inset: Responsivity as functions of light power of the device at the excitation wavelength of 532 nm. (e) D* and noise equivalent power (NEP) at broadband ranging from 405 to 1550 nm at $V_g$ = 0 V and $V_{ds}$ = 1 V. Reproduced with permission from ref. 242. Copyright 2019 Wiley-VCH.

### 2.5.3 Light Emitting Diodes

Opposite to photodetectors or solar cells, in LEDs the energy is converted from electrical to light energy. The basic principle of LEDs is the injection of electrons and holes from separate electrodes and then the emission of light through radiative recombination. 2D semiconductors, especially 2D TMDs with direct bandgap at

monolayer thickness, possess the following advantages. The reduced dielectric screening in 2D semiconductors results in stronger electron–hole interactions and suppression of non-radiative recombination, which could improve the quantum efficiency. In addition, conventional quantum well structures are greatly restricted by lattice mismatch and interface engineering, where the self-passivating surface of 2D semiconductors presents great advantage. Finally, valley polarisation in 2D monolayer TMDs results in the demonstration of polarised LEDs.

Monolayer TMDs have been used in lateral p–n junction based LEDs.[244-246] Two gate electrodes are used to separately control the doping of an ambipolar semiconductor such as $WSe_2$ to create electron and hole transport regions in the same channel. The electrons and holes meet at the trench region to generate electroluminescent (EL) light (Fig. 2.35a-b). The characteristic EL peak is at 1.547 eV, which is 93 meV lower than its PL peak.[244] This is explained by the increased screening effect with carrier injection which changes the exciton binding energy as well as a photon emission contribution from trions with a lower energy. A relatively low EQE of 0.05−0.1% is typically observed. This is probably due to the large diffusion region (in μm scale) in lateral p–n junctions that reduces the recombination rate of minority carriers. In addition, vertical p–n junctions by stacking different 2D semiconductors to form type-II heterojunctions also show efficient EL emission. Cheng et al.[247] fabricated p-$WSe_2$/n-$MoS_2$ atomically sharp vertical heterojunctions (Fig. 2.35c-d). After the threshold voltage, the EL emission increases linearly with increasing bias, primarily showing emission characteristic of the monolayer $WSe_2$ with direct bandgap, while that from few-layer $MoS_2$ with indirect bandgap is weak (Fig. 2.35e-f).

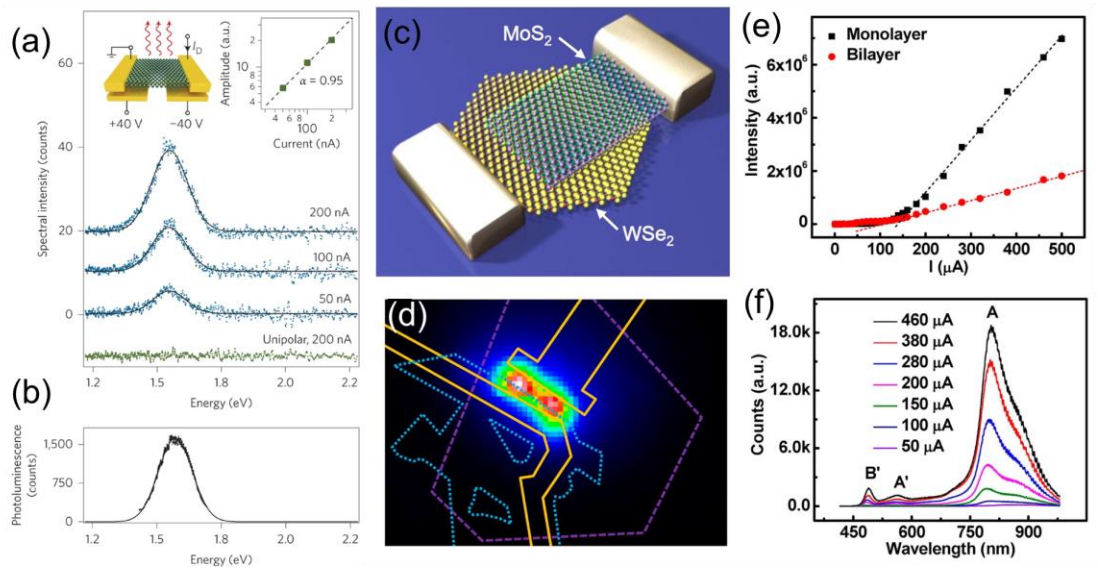



**Figure 2.35. 2D LEDs based on p–n diodes.** (a) EL emission spectra under different currents in the dual-gate monolayer $WSe_2$ LED. The inset shows emission amplitude with current. (b) PL emission spectra of the dual-gate monolayer $WSe_2$ LED. Reproduced with permission from ref. 244. Copyright 2014 Springer. (c) Schematic illustration of p-$WSe_2$/n-$MoS_2$ atomically sharp vertical heterojunction. (d) False-colour EL mapping of a working p-$WSe_2$/n-$MoS_2$ LED. (e) EL intensity versus injection current for both ML- and BL-$WSe_2$/$MoS_2$ heterojunction. (f) EL spectra of ML-$WSe_2$/$MoS_2$ heterojunction LED under various injection current. Reproduced with permission from ref. 247. Copyright 2014 American Chemistry Society.

Another strategy for obtaining EL in 2D semiconductor is based on vertical metal-insulator-semiconductor (MIS) tunnelling diodes based on graphene, h-BN and TMDs. In this type of structure, electron and holes are separately injected from two graphene electrodes into the TMD active layer through the h-BN tunnelling barriers, similar to a quantum well. The vertical Gr/h-BN/$WS_2$/h-BN/Gr structure allows improvement of LED performance with reduced contact resistance, high current flux and uniform illumination from whole overlapping area (Fig. 2.36a-b).[248] As the schematic in Figure 2.36c shows, under large bias between the top and bottom graphene electrodes, the

Fermi level of the top graphene is brought below the VB of TMD to allow hole injection. The structure shows high EQE of 1% for single quantum wells, and is further improved to 8.4% in multiple quantum wells where 3−4 layers of TMDs are separated by h-BN layers in the structure (Fig. 2.36d-e). Similar to the p–n diode based LEDs, the EL emission show lower energy than the PL emission due to enhanced screening effects (Fig. 2.36f-g). This may also allow incorporation of different 2D semiconductors as active layers in the multiple quantum wells to tune the emission spectrum. This kind of structure has also been used for generating single photon emission in quantum LEDs.[249] In addition, large-scale fabrication of MIS-type LEDs has been achieved using CVD-grown materials. Sheng et al.[250] fabricated over 110 LED devices on one chip with asymmetric vertical Au/h-BN/$WS_2$/h-BN/Gr structure with high EQE between 1−4% (Fig. 2.37a-b). The difference in the two Fermi levels of the electrodes results in different barrier to inject electrons into the $WS_2$, thus the EL show smaller onset at forward biasing (Fig. 2.37c-e). In summary, current studies on 2D-based LEDs have demonstrated great potential in future novel functioning light-emitting devices.

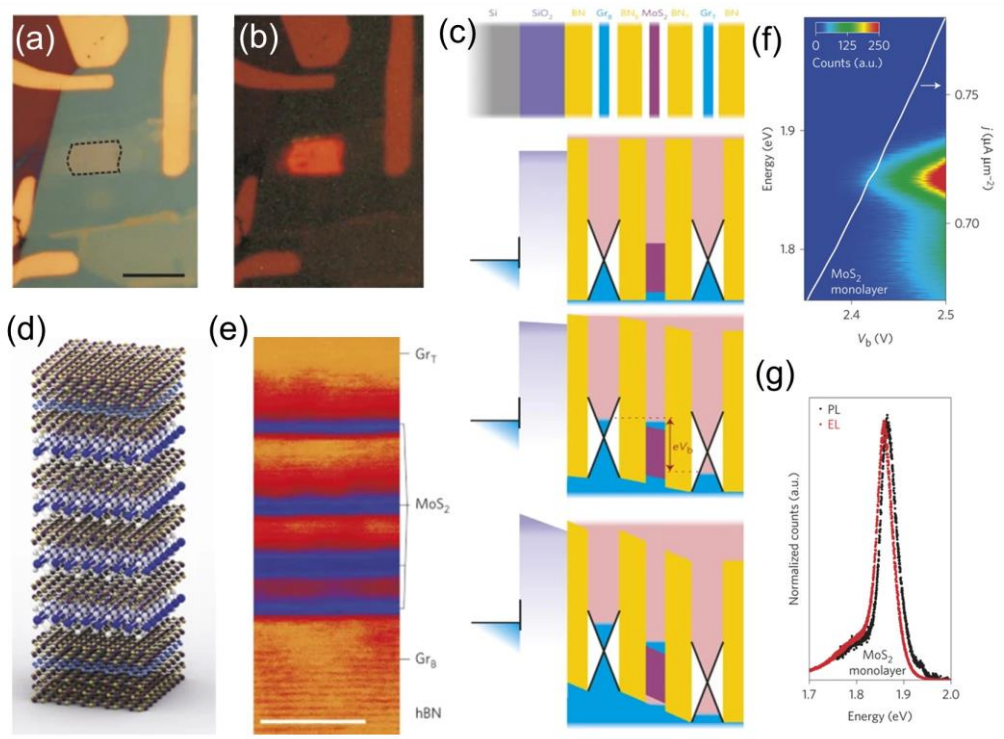



**Figure 2.36. 2D LEDs based on tunnelling diodes.** (a) Optical image of an operational device (Gr/h-BN/$MoS_2$/h-BN/Gr). The dashed lines outline the heterostructure region. Scale bar: 10 μm. (b) Optical image of EL from the same device. (c) Schematics and band diagrams for the heterostructure in (a) under zero applied bias, intermediate applied bias and high bias. (d)Schematic and (e) STEM image of multiple-quantum-well heterostructure consists of four $MoS_2$ quantum wells. (f) EL spectra as a function of bias voltage. White curve: I–V characteristic. (g) Comparison of PL and EL spectra for the same device. Reproduced with permission from ref. 248. Copyright 2015 Springer.

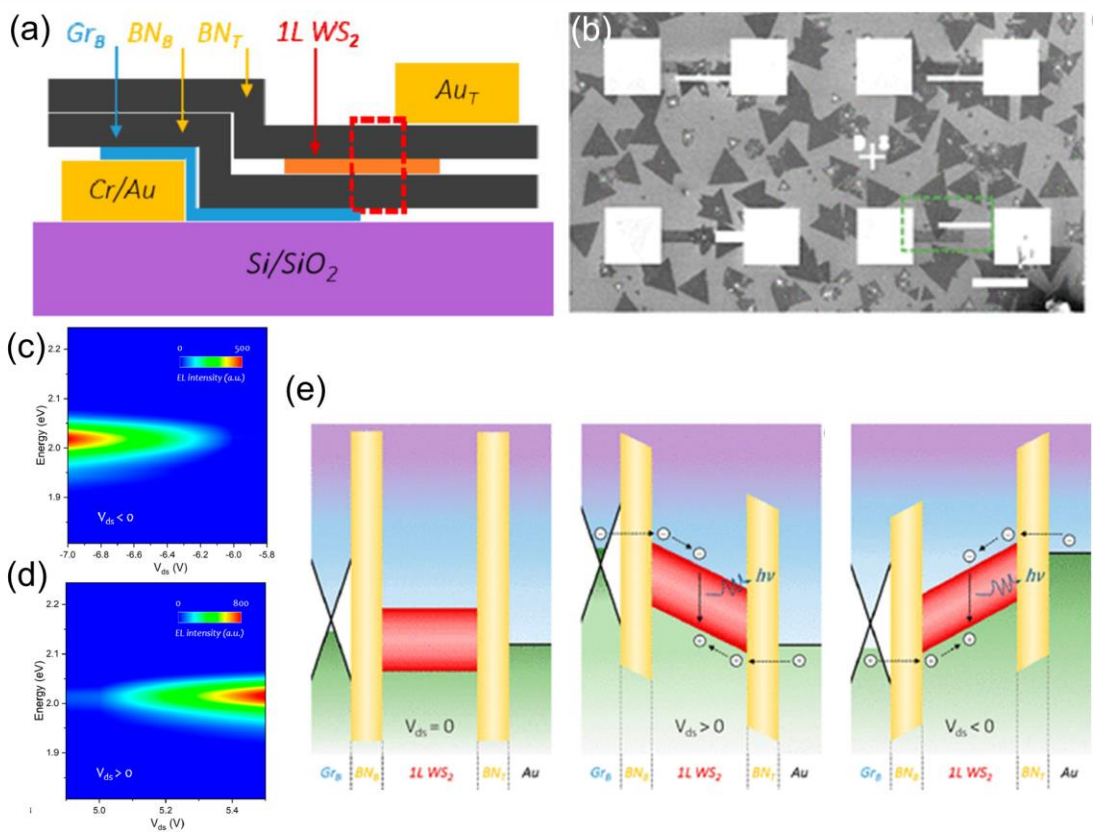



**Figure 2.37. 2D tunnelling LEDs fabricated by all-CVD grown materials.** (a) Side-view schematics of vertical Au/h-BN/$WS_2$/h-BN/Gr structure. (b) SEM image of large-area $WS_2$-based LEDs. Scale bar: 100 μm. (c) 2D mapping of the $WS_2$ LED EL spectra as a function of bias for the at negative bias. (d) 2D mapping of the $WS_2$ LED EL spectra at positive bias. (e) Band diagrams of the heterostructure under zero, positive and negative high bias conditions. Reproduced with permission from ref. 250. Copyright 2019 American Chemistry Society.

## 2.6 Conclusion and Future Outlook

Compared with early studied 2D materials such as graphene and h-BN, 2D layered semiconductors possess many intriguing properties such as strong light-matter interactions, strong interlayer coupling and versatility in band structure. 2D layered semiconductors are ideal building blocks for next generation nanoelectronics that are compatible with biological and chemical sensing purposes. Thus, it is desirable to

further expand the family and explore novel materials with unexpected properties. One relatively unexplored area is wide bandgap semiconductors for optoelectronic applications related to the visible and UV spectrum range. Various structural, optical and electronic characterisations are required to assess the potential of these candidates for optoelectronic applications. In addition, evaluation of material stability is important for both fundamental knowledge and practical applications. Recent progresses further prove that it is essential to develop and design novel 2D VLHs with unconventional functionalities owing to the unique vdWs interactions. Finally, the development of low-cost and scalable production methods for synthesising high-quality 2D layered semiconductors and VLHs is of significant importance for future commercialisation. While great advancements are witnessed for some 2D members, large-scale manufacturing and tailoring of these materials is still at an immature stage. Novel synthesis techniques based on VPD methods are required with thorough understanding of the mechanisms.

## 2.7 References

1. Mounet, N.; Gibertini, M.; Schwaller, P.; Campi, D.; Merkys, A.; Marrazzo, A.; Sohier, T.; Castelli, I. E.; Cepellotti, A.; Pizzi, G.; Marzari, N., Two-Dimensional Materials from High-Throughput Computational Exfoliation of Experimentally Known Compounds. *Nat. Nanotechnol.* **2018**, *13*, 246-252.

2. Li, X.; Tao, L.; Chen, Z.; Fang, H.; Li, X.; Wang, X.; Xu, J.-B.; Zhu, H., Graphene and Related Two-Dimensional Materials: Structure-Property Relationships for Electronics and Optoelectronics. *Appl. Phys. Rev.* **2017**, *4*, 021306.

3. Liu, Y.; Huang, Y.; Duan, X., Van der Waals Integration Before and Beyond Two-Dimensional Materials. *Nature* **2019**, *567*, 323-333.

4. Pu, J.; Takenobu, T., Monolayer Transition Metal Dichalcogenides as Light Sources. *Adv. Mater.* **2018**, *30*, 1707627.

5. Wang, Q. H.; Kalantar-Zadeh, K.; Kis, A.; Coleman, J. N.; Strano, M. S., Electronics and Optoelectronics of Two-Dimensional Transition Metal Dichalcogenides. *Nat. Nanotechnol.* **2012**, *7*, 699-712.

6. Gong, C.; Hu, K.; Wang, X.; Wangyang, P.; Yan, C.; Chu, J.; Liao, M.; Dai, L.; Zhai, T.; Wang, C.; Li, L.; Xiong, J., 2D Nanomaterial Arrays for Electronics and Optoelectronics. *Adv. Funct. Mater.* **2018**, *28*, 1706559.

7. Geng, D.; Yang, H. Y., Recent Advances in Growth of Novel 2D Materials: Beyond Graphene and Transition Metal Dichalcogenides. *Adv. Mater.* **2018**, *30*, 1800865.

8. Zhou, R. P.; Ostwal, V.; Appenzeller, J., Vertical versus Lateral Two-Dimensional Heterostructures: On the Topic of Atomically Abrupt p/n-Junctions. *Nano Lett.* **2017**, *17*, 4787-4792.

9. Geim, A. K.; Grigorieva, I. V., Van der Waals heterostructures. *Nature* **2013**, *499*, 419-425.

10. Tran, K.; Choi, J.; Singh, A., Moiré and Beyond in Transition Metal Dichalcogenide Twisted Bilayers. *2D Mater.* **2020**, *8*, 022002.

11. Radisavljevic, B.; Radenovic, A.; Brivio, J.; Giacometti, V.; Kis, A., Single-Layer $Mos_2$ Transistors. *Nat. Nanotechnol.* **2011**, *6*, 147-150.

12. Li, M. Y.; Su, S. K.; Wong, H. S. P.; Li, L. J., How 2D Semiconductors Could Extend Moore's Law. *Nature* **2019**, *567*, 169-170.

13. Ge, R.; Wu, X.; Kim, M.; Shi, J.; Sonde, S.; Tao, L.; Zhang, Y.; Lee, J. C.; Akinwande, D., Atomristor: Nonvolatile Resistance Switching in Atomic Sheets of Transition Metal Dichalcogenides. *Nano Lett.* **2018**, *18*, 434-441.

14. Wang, G.; Chernikov, A.; Glazov, M. M.; Heinz, T. F.; Marie, X.; Amand, T.; Urbaszek, B., Colloquium: Excitons in Atomically Thin Transition Metal Dichalcogenides. *Rev. Mod. Phys.* **2018**, *90*, 021001.

15. Huo, N. J.; Yang, Y. J.; Li, J. B., Optoelectronics Based on 2D TMDs and Heterostructures. *J. Semicond.* **2017**, *38*, 9.

16. Eda, G.; Maier, S. A., Two-Dimensional Crystals: Managing Light for Optoelectronics. *ACS Nano* **2013**, *7*, 5660-5665.

17. Briggs, N.; Subramanian, S.; Lin, Z.; Li, X.; Zhang, X.; Zhang, K.; Xiao, K.; Geohegan, D.; Wallace, R.; Chen, L.-Q.; Terrones, M.; Ebrahimi, A.; Das, S.; Redwing, J.; Hinkle, C.; Momeni, K.; van Duin, A.; Crespi, V.; Kar, S.; Robinson, J. A., A Roadmap for Electronic Grade 2D Materials. *2D Mater.* **2019**, *6*, 022001.

18. Fang, H.; Battaglia, C.; Carraro, C.; Nemsak, S.; Ozdol, B.; Kang, J. S.; Bechtel, H. A.; Desai, S. B.; Kronast, F.; Unal, A. A.; Conti, G.; Conlon, C.; Palsson, G. K.; Martin, M. C.; Minor, A. M.; Fadley, C. S.; Yablonovitch, E.; Maboudian, R.; Javey, A., Strong Interlayer Coupling in van der Waals Heterostructures Built from Single-Layer Chalcogenides. *PNAS* **2014**, *111*, 6198-6202.

19. Hong, X.; Kim, J.; Shi, S.-F.; Zhang, Y.; Jin, C.; Sun, Y.; Tongay, S.; Wu, J.; Zhang, Y.; Wang, F., Ultrafast Charge Transfer in Atomically Thin $Mos_2/WS_2$ Heterostructures. *Nat. Nanotechnol.* **2014**, *9*, 682-686.

20. Ganatra, R.; Zhang, Q., Few-Layer $MoS_2$: A Promising Layered Semiconductor. *ACS Nano* **2014**, *8*, 4074-4099.

21. Diware, M. S.; Park, K.; Mun, J.; Park, H. G.; Chegal, W.; Cho, Y. J.; Cho, H. M.; Park, J.; Kim, H.; Kang, S.-W.; Kim, Y. D., Characterization of Wafer-Scale $MoS_2$ and $WSe_2$ 2D Films by Spectroscopic Ellipsometry. *Curr. Appl. Phys.* **2017**, *17*, 1329-1334.

22. Zhao, W.; Pan, J.; Fang, Y.; Che, X.; Wang, D.; Bu, K.; Huang, F., Metastable $MoS_2$: Crystal Structure, Electronic Band Structure, Synthetic Approach and Intriguing Physical Properties. *Chem. Eur. J.* **2018**, *24*, 15942-15954.

23. Xu, K.; Yin, L.; Huang, Y.; Shifa, T. A.; Chu, J. W.; Wang, F.; Cheng, R. Q.; Wang, Z. X.; He, J., Synthesis, properties and applications of 2D layered (MXVI)-X-III (M = Ga, In; X = S, Se, Te) materials. *Nanoscale* **2016**, *8*, 16802-16818.

24. Ren, C.; Wang, S.; Tian, H.; Luo, Y.; Yu, J.; Xu, Y.; Sun, M., First-Principles Investigation on Electronic Properties and Band Alignment of Group III Monochalcogenides. *Sci. Rep.* **2019**, *9*, 13289.

25. Srour, J.; Badawi, M.; Hassan, F. E. H.; Postnikov, A., Comparative Study of Structural and Electronic Properties of GaSe and InSe polytypes. *J. Chem. Phys.* **2018**, *149*, 054106.

26. Lee, C. H.; Krishnamoorthy, S.; O'Hara, D. J.; Brenner, M. R.; Johnson, J. M.; Jamison, J. S.; Myers, R. C.; Kawakami, R. K.; Hwang, J.; Rajan, S., Molecular Beam Epitaxy of 2D-Layered Gallium Selenide on GaN Substrates. *J. Appl. Phys.* **2017**, *121*, 094302.

27. Li, X. F.; Basile, L.; Yoon, M.; Ma, C.; Puretzky, A. A.; Lee, J.; Idrobo, J. C.; Chi, M. F.; Rouleau, C. M.; Geohegan, D. B.; Xiao, K., Revealing the Preferred Interlayer Orientations and Stackings of Two-Dimensional Bilayer Gallium Selenide Crystals. *Angew. Chem. Int. Ed.* **2015**, *54*, 2712-2717.

28. Jung, C. S.; Shojaei, F.; Park, K.; Oh, J. Y.; Im, H. S.; Jang, D. M.; Park, J.; Kang, H. S., Red-to-Ultraviolet Emission Tuning of Two-Dimensional Gallium Sulfide/Selenide. *ACS Nano* **2015**, *9*, 9585-9593.

29. Zheng, S.; So, J.-K.; Liu, F.; Liu, Z.; Zheludev, N.; Fan, H. J., Giant Enhancement of Cathodoluminescence of Monolayer Transitional Metal Dichalcogenides Semiconductors. *Nano Lett.* **2017**, *17*, 6475-6480.

30. Ben Aziza, Z.; Pierucci, D.; Henck, H.; Silly, M. G.; David, C.; Yoon, M.; Sirotti, F.; Xiao, K.; Eddrief, M.; Girard, J. C.; Ouerghi, A., Tunable quasiparticle Band Gap in Few-Layer Gase/Graphene van der Waals Heterostructures. *Phys. Rev. B* **2017**, *96*, 035407.

31. Hamer, M. J.; Zultak, J.; Tyurnina, A. V.; Zolyomi, V.; Terry, D.; Barinov, A.; Garner, A.; Donoghue, J.; Rooney, A. P.; Kandyba, V.; Giampietri, A.; Graham, A.; Teutsch, N.; Xia, X.; Koperski, M.; Haigh, S. J.; Fal'ko, V. I.; Gorbachev, R. V.; Wilson, N. R., Indirect to Direct Gap Crossover in Two-Dimensional InSe Revealed by Angle-Resolved Photoemission Spectroscopy. *ACS Nano* **2019**, *13*, 2136-2142.

32. Splendiani, A.; Sun, L.; Zhang, Y.; Li, T.; Kim, J.; Chim, C.-Y.; Galli, G.; Wang, F., Emerging Photoluminescence in Monolayer $MoS_2$. *Nano Lett.* **2010**, *10*, 1271-1275.

33. Cingolani, A.; Minafra, A.; Tantalo, P.; Paorici, C., Edge Emission in GaSe and GaS. *Phys. Status Solidi. A* **1971**, *4*, K83-K85.

34. Aulich, E.; Brebner, J. L.; Mooser, E., Indirect Energy Gap in GaSe and GaS. *Phys. Status Solidi. B* **1969**, *31*, 129-131.

35. Carey, B. J.; Ou, J. Z.; Clark, R. M.; Berean, K. J.; Zavabeti, A.; Chesman, A. S. R.; Russo, S. P.; Lau, D. W. M.; Xu, Z.-Q.; Bao, Q.; Kavehei, O.; Gibson, B. C.; Dickey, M. D.; Kaner, R. B.; Daeneke, T.; Kalantar-Zadeh, K., Wafer-Scale Two-Dimensional Semiconductors from Printed Oxide Skin of Liquid Metals. *Nat. Comm.* **2017**, *8*, 14482.

36. Kibirev, I. A.; Matetskiy, A. V.; Zotov, A. V.; Saranin, A. A., Thickness-Dependent Transition of the Valence Band Shape from Parabolic to Mexican-Hat-Like in the MBE Grown InSe Ultrathin Films. *Appl. Phys. Lett.* **2018**, *112*, 191602.

37. Ben Aziza, Z.; Zólyomi, V.; Henck, H.; Pierucci, D.; Silly, M. G.; Avila, J.; Magorrian, S. J.; Chaste, J.; Chen, C.; Yoon, M.; Xiao, K.; Sirotti, F.; Asensio, M. C.; Lhuillier, E.; Eddrief, M.; Fal'ko, V. I.; Ouerghi, A., Valence Band Inversion and Spin-Orbit Effects in The Electronic Structure of Monolayer GaSe. *Phys. Rev. B* **2018**, *98*, 115405.

38. Özdamar, B.; Özbal, G.; Çınar, M. N.; Sevim, K.; Kurt, G.; Kaya, B.; Sevinçli, H., Structural, Vibrational, and Electronic Properties of Single-Layer Hexagonal Crystals of Group IV and V Elements. *Phys. Rev. B* **2018**, *98*, 045431.

39. Cao, T.; Li, Z.; Louie, S. G., Tunable Magnetism and Half-Metallicity in Hole-Doped Monolayer GaSe. *Phys. Rev. Lett.* **2015**, *114*, 236602.

40. Demirci, S.; Avazlı, N.; Durgun, E.; Cahangirov, S., Structural and Electronic Properties of Monolayer Group III Monochalcogenides. *Phys. Rev. B* **2017**, *95*, 115409.

41. Chen, Z.; Huang, L.; Xi, Y.; Li, R.; Li, W.; Xu, G.; Cheng, H., Geometrical Structures, and Electronic and Transport Properties of a Novel Two-Dimensional β-Gas Transparent Conductor. *Nano Res.* **2015**, *8*, 3177-3185.

42. Li, L.; Yu, Y.; Ye, G. J.; Ge, Q.; Ou, X.; Wu, H.; Feng, D.; Chen, X. H.; Zhang, Y., Black Phosphorus Field-Effect Transistors. *Nat. Nanotechnol.* **2014**, *9*, 372-377.

43. Fujita, S., Wide-Bandgap Semiconductor Materials: For Their Full Bloom. Japanese *J. Appl. Phys.* **2015**, *54*, 030101.

44. Yoder, M. N., Wide Bandgap Semiconductor Materials and Devices. *IEEE Trans. Electron Devices* **1996**, *43*, 1633-1636.

45. Neudeck, P. G.; Okojie, R. S.; Chen, L. Y., High-Temperature Electronics - A Role for Wide Bandgap Semiconductors? *Proc. IEEE* **2002**, *90*, 1065-1076.

46. Shen, P.; Lin, Y.; Wang, H.; Park, J.; Leong, W. S.; Lu, A.; Palacios, T.; Kong, J., CVD Technology for 2D Materials. *IEEE Trans. Electron Devices* **2018**, *65*, 4040-4052.

47. Hu, P. A.; Wen, Z. Z.; Wang, L. F.; Tan, P. H.; Xiao, K., Synthesis of Few-Layer GaSe Nanosheets for High Performance Photodetectors. *ACS Nano* **2012**, *6*, 5988-5994.

48. Lei, S.; Ge, L.; Liu, Z.; Najmaei, S.; Shi, G.; You, G.; Lou, J.; Vajtai, R.; Ajayan, P. M., Synthesis and Photoresponse of Large GaSe Atomic Layers. *Nano Lett.* **2013**, *13*, 2777-2781.

49. Terry, D. J.; Zolyomi, V.; Hamer, M.; Tyurnina, A. V.; Hopkinson, D. G.; Rakowski, A. M.; Magorrian, S. J.; Clark, N.; Andreev, Y. M.; Kazakova, O.; Novoselov, K.; Haigh, S. J.; Fal'ko, V. I.; Gorbachev, R., Infrared-To-Violet Tunable Optical Activity in Atomic Films of GaSe, InSe, and Their Heterostructures. *2D Mater.* **2018**, *5*, 041009.

50. Yang, Z. B.; Jie, W. J.; Mak, C. H.; Lin, S. H.; Lin, H. H.; Yang, X. F.; Yan, F.; Lau, S. P.; Hao, J. H., Wafer-Scale Synthesis of High-Quality Semiconducting Two-Dimensional Layered InSe with Broadband Photoresponse. *ACS Nano* **2017**, *11*, 4225-4236.

51. Wang, F.; Gao, T.; Zhang, Q.; Hu, Z. Y.; Jin, B.; Li, L.; Zhou, X.; Li, H.; Van Tendeloo, G.; Zhai, T., Liquid-Alloy-Assisted Growth of 2D Ternary $Ga_2In_4S_9$ Toward High-Performance UV Photodetection. *Adv. Mater.* **2019**, *31*, e1806306.

52. Sun, Y.; Cheng, H.; Gao, S.; Sun, Z.; Liu, Q.; Liu, Q.; Lei, F.; Yao, T.; He, J.; Wei, S.; Xie, Y., Freestanding Tin Disulfide Single-Layers Realizing Efficient Visible-Light Water Splitting. *Angew. Chem. Int. Ed.* **2012**, *51*, 8727-8731.

53. Ahn, J. H.; Lee, M. J.; Heo, H.; Sung, J. H.; Kim, K.; Hwang, H.; Jo, M. H., Deterministic Two-Dimensional Polymorphism Growth of Hexagonal N-Type $SnS_2$ and Orthorhombic P-Type SnS Crystals. *Nano Lett.* **2015**, *15*, 3703-3708.

54. Zhou, X.; Zhang, Q.; Gan, L.; Li, H. Q.; Zhai, T. Y., Large-Size Growth of Ultrathin $SnS_2$ Nanosheets and High Performance for Phototransistors. *Adv. Funct. Mater.* **2016**, *26*, 4405-4413.

55. Ye, G.; Gong, Y.; Lei, S.; He, Y.; Li, B.; Zhang, X.; Jin, Z.; Dong, L.; Lou, J.; Vajtai, R.; Zhou, W.; Ajayan, P. M., Synthesis of Large-Scale Atomic-Layer $SnS_2$ Through Chemical Vapor Deposition. *Nano Res.* **2017**, *10*, 2386-2394.

56. Mattinen, M.; King, P. J.; Khriachtchev, L.; Meinander, K.; Gibbon, J. T.; Dhanak, V. R.; Raisanen, J.; Ritala, M.; Leskela, M., Low-Temperature Wafer-Scale Deposition of Continuous 2D $SnS_2$ Films. *Small* **2018**, *14*, e1800547.

57. Zhao, E. L.; Gao, L. G.; Yang, S. Z.; Wang, L. K.; Cao, J. M.; Ma, T. L., In Situ Fabrication of 2D $SnS_2$ Nanosheets as a New Electron Transport Layer for Perovskite Solar Cells. Nano Research **2018**, *11*, 5913-5923.

58. Shao, G. L.; Xue, X. X.; Zhou, X. L.; Xu, J.; Jin, Y. Y.; Qi, S. Y.; Liu, N.; Duan, H. G.; Wang, S. S.; Li, S. S.; Ouzounian, M.; Hu, T. S.; Luo, J.; Liu, S.; Feng, Y. X., Shape-Engineered Synthesis of Atomically Thin 1T-$SnS_2$ Catalyzed by Potassium Halides. *ACS Nano* **2019**, *13*, 8265-8274.

59. Yang, Y.; Liu, S.-C.; Yang, W.; Li, Z.; Wang, Y.; Wang, X.; Zhang, S.; Zhang, Y.; Long, M.; Zhang, G.; Xue, D.-J.; Hu, J.-S.; Wan, L.-J., Air-Stable In-Plane Anisotropic $GeSe_2$ for Highly Polarization-Sensitive Photodetection in Short Wave Region. *JACS* **2018**, *140*, 4150-4156.

60. Yang, Y.; Liu, S.-C.; Wang, X.; Li, Z.; Zhang, Y.; Zhang, G.; Xue, D.-J.; Hu, J.-S., Polarization-Sensitive Ultraviolet Photodetection of Anisotropic 2D $GeS_2$. *Adv. Funct. Mater.* **2019**, *29*, 1900411.

61. Wang, D.; Meng, J.; Zhang, X.; Guo, G.; Yin, Z.; Liu, H.; Cheng, L.; Gao, M.; You, J.; Wang, R., Selective Direct Growth of Atomic Layered $HfS_2$ on Hexagonal Boron Nitride for High Performance Photodetectors. *Chem. Mater.* **2018**, *30*, 3819-3826.

62. Mattinen, M.; Popov, G.; Vehkamaki, M.; King, P. J.; Mizohata, K.; Jalkanen, P.; Raisanen, J.; Leskela, M.; Ritala, M., Atomic Layer Deposition of Emerging 2D Semiconductors, $HfS_2$ and $ZrS_2$, for Optoelectronics. *Chem. Mater.* **2019**, *31*, 5713-5724.

63. Yan, C.; Gan, L.; Zhou, X.; Guo, J.; Huang, W.; Huang, J.; Jin, B.; Xiong, J.; Zhai, T.; Li, Y., Space-Confined Chemical Vapor Deposition Synthesis of Ultrathin $HfS_2$ Flakes for Optoelectronic Application. *Adv. Funct. Mater.* **2017**, *27*, 1702918.

64. Tan, M.; Hu, C.; Lan, Y.; Khan, J.; Deng, H.; Yang, X.; Wang, P.; Yu, X.; Lai, J.; Song, H., 2D Lead Dihalides for High-Performance Ultraviolet Photodetectors and Their Detection Mechanism Investigation. *Small* **2017**, *13*, 1702024.

65. Zhong, M. Z.; Zhang, S.; Huang, L.; You, J. B.; Wei, Z. M.; Liu, X. F.; Li, J. B., Large-Scale 2D $PbI_2$ Monolayers: Experimental Realization and Their Indirect Band-Gap Related Properties. *Nanoscale* **2017**, *9*, 3736-3741.

66. Du, K.-Z; Tu, Q.; Zhang, X.; Han, Q.; Liu, J.; Zauscher, S.; Mitzi, D. B., Two-Dimensional Lead(II) Halide-Based Hybrid Perovskites Templated by Acene Alkylamines: Crystal Structures, Optical Properties, and Piezoelectricity. *Inorg. Chem.* **2017**, *56*, 9291-9302.

67. Cao, D. H.; Stoumpos, C. C.; Farha, O. K.; Hupp, J. T.; Kanatzidis, M. G., 2D Homologous Perovskites as Light-Absorbing Materials for Solar Cell Applications. *JACS* **2015**, *137*, 7843-7850.

68. Balendhran, S.; Deng, J. K.; Ou, J. Z.; Walia, S.; Scott, J.; Tang, J. S.; Wang, K. L.; Field, M. R.; Russo, S.; Zhuiykov, S.; Strano, M. S.; Medhekar, N.; Sriram, S.; Bhaskaran, M.; Kalantar-Zadeh, K., Enhanced Charge Carrier Mobility in Two-Dimensional High Dielectric Molybdenum Oxide. *Adv. Mater.* **2013**, *25*, 109-114.

69. Datta, R. S.; Haque, F.; Mohiuddin, M.; Carey, B. J.; Syed, N.; Zavabeti, A.; Zhang, B.; Khan, H.; Berean, K. J.; Ou, J. Z.; Mahmood, N.; Daeneke, T.; Kalantarzadeh, K., Highly Active Two Dimensional Alpha-$MoO_{3-X}$ for The Electrocatalytic Hydrogen Evolution Reaction. *J. Mater. Chem. A* **2017**, *5*, 24223-24231.

70. Ko, T. Y.; Jeong, A.; Kim, W.; Lee, J.; Kim, Y.; Lee, J. E.; Ryu, G. H.; Park, K.; Kim, D.; Lee, Z.; Lee, M. H.; Lee, C.; Ryu, S., On-Stack Two-Dimensional Conversion of $MoS_2$ into $MoO_3$. *2D Mater.* **2017**, *4*, 014003.

71. Kim, J. H.; Dash, J. K.; Kwon, J.; Hyun, C.; Kim, H.; Ji, E.; Lee, G. H., Van der Waals Epitaxial Growth of Single Crystal Alpha-$MoO_3$ Layers on Layered Materials Growth Templates. *2D Mater.* **2019**, *6*, 015016.

72. Hanson, E. D.; Lajaunie, L.; Hao, S. Q.; Myers, B. D.; Shi, F. Y.; Murthy, A. A.; Wolverton, C.; Arenal, R.; Dravid, V. P., Systematic Study of Oxygen Vacancy Tunable Transport Properties of Few-Layer $MoO_{3-x}$ Enabled by Vapor-Based Synthesis. *Adv. Funct. Mater.* **2017**, *27*, 1605380.

73. Yalagala, B. P.; Sahatiya, P.; Kolli, C. S. R.; Khandelwal, S.; Mattela, V.; Badhulika, S., $V_2O_5$ Nanosheets for Flexible Memristors and Broadband Photodetectors. *ACS Appl. Nano Mater.* **2019**, *2*, 937-947.

74. Wu, L.; Yu, Y.; Han, X.; Xu, T.; Zhang, Y.; Li, Y.; Zhi, J., Light-Assisted Oriented Attachment Process for Ultrathin Vanadium Pentoxide Nanosheets with Intensive Room-Temperature Photoluminescence Emission. *J. Mater. Chem. C* **2013**, *1*, 6703-6708.

75. Li, S.; Zhang, Y.; Yang, W.; Liu, H.; Fang, X., 2D Perovskite $Sr_2Nb_3O_{10}$ for High-Performance UV Photodetectors. *Adv. Mater.* **2019**, 32, e1905443.

76. Kaasbjerg, K.; Thygesen, K. S.; Jacobsen, K. W., Phonon-Limited Mobility in N-Type Single-Layer $MoS_2$ from First Principles. *Phys. Rev. B* **2012**, *85*, 115317.

77. Fuhrer, M. S.; Hone, J., Measurement of Mobility in Dual-Gated $MoS_2$ Transistors. *Nat. Nanotechnol.* **2013**, *8*, 146-147.

78. Jariwala, D.; Sangwan, V. K.; Late, D. J.; Johns, J. E.; Dravid, V. P.; Marks, T. J.; Lauhon, L. J.; Hersam, M. C., Band-Like Transport in High Mobility Unencapsulated Single-Layer $MoS_2$ Transistors. *Appl. Phys. Lett.* **2013**, *102*, 173107.

79. Novoselov, K. S.; Jiang, D.; Schedin, F.; Booth, T. J.; Khotkevich, V. V.; Morozov, S. V.; Geim, A. K., Two-Dimensional Atomic Crystals. *PNAS* **2005**, *102*, 10451-10453.

80. Bao, W.; Cai, X.; Kim, D.; Sridhara, K.; Fuhrer, M. S., High Mobility Ambipolar $MoS_2$ Field-Effect Transistors: Substrate and Dielectric Effects. *Appl. Phys. Lett.* **2013**, *102*, 042104.

81. Li, S.-L.; Wakabayashi, K.; Xu, Y.; Nakaharai, S.; Komatsu, K.; Li, W.-W.; Lin, Y.-F.; Aparecido-Ferreira, A.; Tsukagoshi, K., Thickness-Dependent Interfacial Coulomb Scattering in Atomically Thin Field-Effect Transistors. *Nano Lett.* **2013**, *13*, 3546-3552.

82. Gomez, L.; Aberg, I.; Hoyt, J. L., Electron Transport in Strained-Silicon Directly on Insulator Ultrathin-Body n-MOSFETs with Body Thickness Ranging from 2 to 25 nm. *IEEE Electron Device Lett.* **2007**, *28*, 285-287.

83. Sucharitakul, S.; Goble, N. J.; Kumar, U. R.; Sankar, R.; Bogorad, Z. A.; Chou, F.-C.; Chen, Y.-T.; Gao, X. P. A., Intrinsic Electron Mobility Exceeding $10^3$ $cm^2/(V\,S)$ in Multilayer InSe FETs. *Nano Lett.* **2015**, *15*, 3815-3819.

84. Bandurin, D. A.; Tyurnina, A. V.; Yu, G. L.; Mishchenko, A.; Zolyomi, V.; Morozov, S. V.; Kumar, R. K.; Gorbachev, R. V.; Kudrynskyi, Z. R.; Pezzini, S.; Kovalyuk, Z. D.; Zeitler, U.; Novoselov, K. S.; Patane, A.; Eaves, L.; Grigorieva, I. V.; Fal'ko, V. I.; Geim, A. K.; Cao, Y., High Electron Mobility, Quantum Hall Effect and Anomalous Optical Response in Atomically Thin InSe. *Nat. Nanotechnol.* **2017**, *12*, 223-227.

85. Xia, F.; Wang, H.; Jia, Y., Rediscovering Black Phosphorus as an Anisotropic Layered Material for Optoelectronics and Electronics. **2014**, *5*, 4458.

86. Gu, Y.; Cai, H.; Dong, J.; Yu, Y.; Hoffman, A. N.; Liu, C.; Oyedele, A. D.; Lin, Y.-C.; Ge, Z.; Puretzky, A. A.; Duscher, G.; Chisholm, M. F.; Rack, P. D.; Rouleau, C. M.; Gai, Z.; Meng, X.; Ding, F.; Geohegan, D. B.; Xiao, K., Two-Dimensional Palladium Diselenide with Strong In-Plane Optical Anisotropy and High Mobility Grown by Chemical Vapor Deposition. *Adv. Mater.* **2020**, *32*, 1906238.

87. Peimyoo, N.; Shang, J.; Cong, C.; Shen, X.; Wu, X.; Yeow, E. K. L.; Yu, T., Nonblinking, Intense Two-Dimensional Light Emitter: Mono Layer $WS_2$ Triangles. *ACS Nano* **2013**, *7*, 10985-10994.

88. Zhang, C.; Johnson, A.; Hsu, C.-L.; Li, L.-J.; Shih, C.-K., Direct Imaging of Band Profile in Single Layer $Mos_2$ on Graphite: Quasiparticle Energy Gap, Metallic Edge States, and Edge Band Bending. *Nano Lett.* **2014**, *14*, 2443-2447.

89. Cao, L., Two-Dimensional Transition-Metal Dichalcogenide Materials: Toward an Age of Atomic-Scale Photonics. *MRS Bulletin* **2015**, *40*, 592-599.

90. Wurstbauer, U.; Miller, B.; Parzinger, E.; Holleitner, A. W., Light–Matter Interaction in Transition Metal Dichalcogenides and Their Heterostructures. *J. Phys. D: Appl. Phys.* **2017**, *50*, 173001.

91. Mak, K. F.; He, K.; Lee, C.; Lee, G. H.; Hone, J.; Heinz, T. F.; Shan, J., Tightly Bound Trions in Monolayer $MoS_2$. *Nat. Mater.* **2013**, *12*, 207-211.

92. Ross, J. S.; Wu, S.; Yu, H.; Ghimire, N. J.; Jones, A. M.; Aivazian, G.; Yan, J.; Mandrus, D. G.; Xiao, D.; Yao, W.; Xu, X., Electrical Control of Neutral and Charged Excitons in a Monolayer Semiconductor. *Nat. Comm.* **2013**, *4*, 1474.

93. Shang, J.; Shen, X.; Cong, C.; Peimyoo, N.; Cao, B.; Eginligil, M.; Yu, T., Observation of Excitonic Fine Structure in a 2D Transition-Metal Dichalcogenide Semiconductor. *ACS Nano* **2015**, *9*, 647-655.

94. Peimyoo, N.; Yang, W.; Shang, J.; Shen, X.; Wang, Y.; Yu, T., Chemically Driven Tunable Light Emission of Charged and Neutral Excitons in Monolayer $WS_2$. *ACS Nano* **2014**, *8*, 11320-11329.

95. Pham, V. P.; Yeom, G. Y., Recent Advances in Doping of Molybdenum Disulfide: Industrial Applications and Future Prospects. *Adv. Mater.* **2016**, *28*, 9024-9059.

96. Hu, P.; Ye, J.; He, X.; Du, K.; Zhang, K. K.; Wang, X.; Xiong, Q.; Liu, Z.; Jiang, H.; Kloc, C., Control of Radiative Exciton Recombination by Charge Transfer Induced Surface Dipoles in $Mos_2$ and $WS_2$ Monolayers. *Sci. Rep.* **2016**, *6*, 24105.

97. Amani, M.; Lien, D.-H.; Kiriya, D.; Xiao, J.; Azcatl, A.; Noh, J.; Madhvapathy, S. R.; Addou, R.; KC, S.; Dubey, M.; Cho, K.; Wallace, R. M.; Lee, S.-C.; He, J.-H.; Ager, J. W.; Zhang, X.; Yablonovitch, E.; Javey, A., Near-Unity Photoluminescence Quantum Yield in $MoS_2$. *Science* **2015**, *350*, 1065-1068.

98. Wang, Y.; Wang, H.; Gali, S. M.; Turetta, N.; Yao, Y.; Wang, C.; Chen, Y.; Beljonne, D.; Samorì, P., Molecular Doping of 2D Indium Selenide for Ultrahigh Performance and Low-Power Consumption Broadband Photodetectors. *Adv. Funct. Mater.* **2021**, *31*, 2103353.

99. Barbone, M.; Montblanch, A. R. P.; Kara, D. M.; Palacios-Berraquero, C.; Cadore, A. R.; De Fazio, D.; Pingault, B.; Mostaani, E.; Li, H.; Chen, B.; Watanabe, K.; Taniguchi, T.; Tongay, S.; Wang, G.; Ferrari, A. C.; Atatüre, M., Charge-Tuneable Biexciton Complexes in Monolayer $WSe_2$. *Nat. Comm.* **2018**, *9*, 3721.

100. Zinkiewicz, M.; Woźniak, T.; Kazimierczuk, T.; Kapuscinski, P.; Oreszczuk, K.; Grzeszczyk, M.; Bartoš, M.; Nogajewski, K.; Watanabe, K.; Taniguchi, T.; Faugeras, C.; Kossacki, P.; Potemski, M.; Babiński, A.; Molas, M. R., Excitonic Complexes in N-Doped $WS_2$ Monolayer. *Nano Lett.* **2021**, *21*, 2519-2525.

101. Paradisanos, I.; Germanis, S.; Pelekanos, N. T.; Fotakis, C.; Kymakis, E.; Kioseoglou, G.; Stratakis, E., Room Temperature Observation of Biexcitons in Exfoliated $WS_2$ Monolayers. *Appl. Phys. Lett.* **2017**, *110*, 193102.

102. Tongay, S.; Fan, W.; Kang, J.; Park, J.; Koldemir, U.; Suh, J.; Narang, D. S.; Liu, K.; Ji, J.; Li, J.; Sinclair, R.; Wu, J., Tuning Interlayer Coupling in Large-Area Heterostructures with CVD-Grown $MoS_2$ and $WS_2$ Monolayers. *Nano Lett.* **2014**, *14*, 3185-3190.

103. Zhang, J.; Wang, J.; Chen, P.; Sun, Y.; Wu, S.; Jia, Z.; Lu, X.; Yu, H.; Chen, W.; Zhu, J.; Xie, G.; Yang, R.; Shi, D.; Xu, X.; Xiang, J.; Liu, K.; Zhang, G., Observation of Strong Interlayer Coupling in $MoS_2/WS_2$ Heterostructures. *Adv. Mater.* **2016**, *28*, 1950-1956.

104. Chiu, M.-H.; Li, M.-Y.; Zhang, W.; Hsu, W.-T.; Chang, W.-H.; Terrones, M.; Terrones, H.; Li, L.-J., Spectroscopic Signatures for Interlayer Coupling in $MoS_2$–$WSe_2$ van der Waals Stacking. *ACS Nano* **2014**, *8*, 9649-9656.

105. Rivera, P.; Schaibley, J. R.; Jones, A. M.; Ross, J. S.; Wu, S.; Aivazian, G.; Klement, P.; Seyler, K.; Clark, G.; Ghimire, N. J.; Yan, J.; Mandrus, D. G.; Yao, W.; Xu, X., Observation of Long-Lived Interlayer Excitons in Monolayer $MoSe_2$–$WSe_2$ Heterostructures. *Nat. Comm.* **2015**, *6*, 6242.

106. Long, R.; Prezhdo, O. V., Quantum Coherence Facilitates Efficient Charge Separation at a $MoS_2/MoSe_2$ van der Waals Junction. *Nano Lett.* **2016**, *16*, 1996-2003.

107. Kim, M. S.; Seo, C.; Kim, H.; Lee, J.; Luong, D. H.; Park, J.-H.; Han, G. H.; Kim, J., Simultaneous Hosting of Positive and Negative Trions and The Enhanced Direct Band Emission in $MoSe_2/MoS_2$ Heterostacked Multilayers. *ACS Nano* **2016**, *10*, 6211-6219.

108. Wang, K.; Huang, B.; Tian, M.; Ceballos, F.; Lin, M.-W.; Mahjouri-Samani, M.; Boulesbaa, A.; Puretzky, A. A.; Rouleau, C. M.; Yoon, M.; Zhao, H.; Xiao, K.; Duscher, G.; Geohegan, D. B., Interlayer Coupling in Twisted $WSe_2/WS_2$ Bilayer Heterostructures Revealed by Optical Spectroscopy. *ACS Nano* **2016**, *10*, 6612-6622.

109. Heo, H.; Sung, J. H.; Cha, S.; Jang, B.-G.; Kim, J.-Y.; Jin, G.; Lee, D.; Ahn, J.-H.; Lee, M.-J.; Shim, J. H.; Choi, H.; Jo, M.-H., Interlayer Orientation-Dependent Light Absorption and Emission in Monolayer Semiconductor Stacks. *Nat. Comm.* **2015**, *6*, 7372.

110. Seyler, K. L.; Rivera, P.; Yu, H.; Wilson, N. P.; Ray, E. L.; Mandrus, D. G.; Yan, J.; Yao, W.; Xu, X., Signatures of Moiré-Trapped Valley Excitons in $MoSe_2/WSe_2$ Heterobilayers. *Nature* **2019**, *567*, 66-70.

111. Alexeev, E. M.; Ruiz-Tijerina, D. A.; Danovich, M.; Hamer, M. J.; Terry, D. J.; Nayak, P. K.; Ahn, S.; Pak, S.; Lee, J.; Sohn, J. I.; Molas, M. R.; Koperski, M.; Watanabe, K.; Taniguchi, T.; Novoselov, K. S.; Gorbachev, R. V.; Shin, H. S.; Fal'ko, V. I.; Tartakovskii, A. I., Resonantly Hybridized Excitons in Moiré Superlattices in van der Waals Heterostructures. *Nature* **2019**, *567*, 81-86.

112. Jin, C.; Regan, E. C.; Yan, A.; Iqbal Bakti Utama, M.; Wang, D.; Zhao, S.; Qin, Y.; Yang, S.; Zheng, Z.; Shi, S.; Watanabe, K.; Taniguchi, T.; Tongay, S.; Zettl, A.; Wang, F., Observation of Moiré Excitons in $WSe_2/WS_2$ Heterostructure Superlattices. *Nature* **2019**, *567*, 76-80.

113. Tran, K.; Moody, G.; Wu, F.; Lu, X.; Choi, J.; Kim, K.; Rai, A.; Sanchez, D. A.; Quan, J.; Singh, A.; Embley, J.; Zepeda, A.; Campbell, M.; Autry, T.; Taniguchi, T.; Watanabe, K.; Lu, N.; Banerjee, S. K.; Silverman, K. L.; Kim, S.; Tutuc, E.; Yang, L.; Macdonald, A. H.; Li, X., Evidence for Moiré Excitons in van der Waals Heterostructures. *Nature* **2019**, *567*, 71-75.

114. Tan, Q.; Rasmita, A.; Li, S.; Liu, S.; Huang, Z.; Xiong, Q.; Yang, S. A.; Novoselov, K. S.; Gao, W.-B., Layer-Engineered Interlayer Excitons. *Sci. Adv.* **2021**, *7*, eabh0863.

115. Ceballos, F.; Bellus, M. Z.; Chiu, H.-Y.; Zhao, H., Ultrafast Charge Separation and Indirect Exciton Formation in a $MoS_2$–$MoSe_2$ van der Waals Heterostructure. *ACS Nano* **2014**, *8*, 12717-12724.

116. Wang, X.; Sun, Y.; Liu, K., Chemical and Structural Stability of 2D Layered Materials. *2D Mater.* **2019**, *6*, 042001.

117. Li, Q.; Zhou, Q.; Shi, L.; Chen, Q.; Wang, J., Recent Advances in Oxidation and Degradation Mechanisms of Ultrathin 2D Materials Under Ambient Conditions and Their Passivation Strategies. *J. Mater. Chem. A* **2019**, *7*, 4291-4312.

118. Gao, J.; Li, B.; Tan, J.; Chow, P.; Lu, T.-M.; Koratkar, N., Aging of Transition Metal Dichalcogenide Monolayers. *ACS Nano* **2016**, *10*, 2628-2635.

119. Longo, R. C.; Addou, R.; Kc, S.; Noh, J.-Y.; Smyth, C. M.; Barrera, D.; Zhang, C.; Hsu, J. W. P.; Wallace, R. M.; Cho, K., Intrinsic Air Stability Mechanisms of Two-Dimensional Transition Metal Dichalcogenide Surfaces: Basal Versus Edge Oxidation. *2D Mater.* **2017**, *4*, 025050.

120. Carlsson, J. M.; Hanke, F.; Linic, S.; Scheffler, M., Two-Step Mechanism for Low-Temperature Oxidation of Vacancies in Graphene. *Phys. Rev. Lett.* **2009**, *102*, 166104.

121. Rong, Y.; He, K.; Pacios, M.; Robertson, A. W.; Bhaskaran, H.; Warner, J. H., Controlled Preferential Oxidation of Grain Boundaries in Monolayer Tungsten Disulfide for Direct Optical Imaging. *ACS Nano* **2015**, *9*, 3695-3703.

122. KC, S.; Longo, R. C.; Wallace, R. M.; Cho, K., Surface Oxidation Energetics and Kinetics on $MoS_2$ Monolayer. *J. Appl. Phys.* **2015**, *117*, 135301.

123. Yang, S.; Cai, H.; Chen, B.; Ko, C.; Özçelik, V. O.; Ogletree, D. F.; White, C. E.; Shen, Y.; Tongay, S., Environmental Stability of 2D Anisotropic Tellurium Containing Nanomaterials: Anisotropic to Isotropic Transition. *Nanoscale* **2017**, *9*, 12288-12294.

124. Molle, A.; Grazianetti, C.; Chiappe, D.; Cinquanta, E.; Cianci, E.; Tallarida, G.; Fanciulli, M., Hindering the Oxidation of Silicene with Non-Reactive Encapsulation. *Adv. Funct. Mater.* **2013**, *23*, 4340-4344.

125. Xia, W.; Hu, W.; Li, Z.; Yang, J., A First-Principles Study of Gas Adsorption on Germanene. *Phys. Chem. Chem. Phys.* **2014**, *16*, 22495-22498.

126. Susoma, J.; Lahtinen, J.; Kim, M.; Riikonen, J.; Lipsanen, H., Crystal Quality of Two-Dimensional Gallium Telluride and Gallium Selenide Using Raman Fingerprint. *AIP Adv.* **2017**, *7*, 015014.

127. Zhao, Q.; Frisenda, R.; Gant, P.; Perez De Lara, D.; Munuera, C.; Garcia-Hernandez, M.; Niu, Y.; Wang, T.; Jie, W.; Castellanos-Gomez, A., Toward Air Stability of Thin GaSe Devices: Avoiding Environmental and Laser-Induced Degradation by Encapsulation. *Adv. Funct. Mater.* **2018**, *28*, 1805304.

128. Favron, A.; Gaufrès, E.; Fossard, F.; Phaneuf-L'Heureux, A.-L.; Tang, N. Y. W.; Lévesque, P. L.; Loiseau, A.; Leonelli, R.; Francoeur, S.; Martel, R., Photooxidation and Quantum Confinement Effects in Exfoliated Black Phosphorus. *Nat. Mater.* **2015**, *14*, 826.

129. Island, J. O.; Steele, G. A.; Zant, H. S. J. V. D.; Castellanos-Gomez, A., Environmental Instability of Few-Layer Black Phosphorus. *2D Mater.* **2015**, *2*, 011002.

130. Shcherbakov, D.; Stepanov, P.; Weber, D.; Wang, Y.; Hu, J.; Zhu, Y.; Watanabe, K.; Taniguchi, T.; Mao, Z.; Windl, W.; Goldberger, J.; Bockrath, M.; Lau, C. N., Raman Spectroscopy, Photocatalytic Degradation, and Stabilization of Atomically Thin Chromium Tri-Iodide. *Nano Lett.* **2018**, *18*, 4214-4219.

131. Wood, J. D.; Wells, S. A.; Jariwala, D.; Chen, K.-S.; Cho, E.; Sangwan, V. K.; Liu, X.; Lauhon, L. J.; Marks, T. J.; Hersam, M. C., Effective Passivation of Exfoliated Black Phosphorus Transistors Against Ambient Degradation. *Nano Lett.* **2014**, *14*, 6964-6970.

132. Coleman, J. N.; Lotya, M.; O'Neill, A.; Bergin, S. D.; King, P. J.; Khan, U.; Young, K.; Gaucher, A.; De, S.; Smith, R. J.; Shvets, I. V.; Arora, S. K.; Stanton, G.; Kim, H.-Y.; Lee, K.; Kim, G. T.; Duesberg, G. S.; Hallam, T.; Boland, J. J.; Wang, J. J.; Donegan, J. F.; Grunlan, J. C.; Moriarty, G.; Shmeliov, A.; Nicholls, R. J.; Perkins, J. M.; Grieveson, E. M.; Theuwissen, K.; Mccomb, D. W.; Nellist, P. D.; Nicolosi, V., Two-Dimensional Nanosheets Produced by Liquid Exfoliation of Layered Materials. *Science* **2011**, *331*, 568-571.

133. Eda, G.; Fujita, T.; Yamaguchi, H.; Voiry, D.; Chen, M.; Chhowalla, M., Coherent Atomic and Electronic Heterostructures of Single-Layer $MoS_2$. *ACS Nano* **2012**, *6*, 7311-7317.

134. Eda, G.; Yamaguchi, H.; Voiry, D.; Fujita, T.; Chen, M.; Chhowalla, M., Photoluminescence from Chemically Exfoliated $MoS_2$. *Nano Lett.* **2011**, *11*, 5111-5116.

135. Yang, P.; Zou, X.; Zhang, Z.; Hong, M.; Shi, J.; Chen, S.; Shu, J.; Zhao, L.; Jiang, S.; Zhou, X.; Huan, Y.; Xie, C.; Gao, P.; Chen, Q.; Zhang, Q.; Liu, Z.; Zhang, Y., Batch Production of 6-Inch Uniform Monolayer Molybdenum Disulfide Catalyzed by Sodium in Glass. *Nat. Comm.* **2018**, *9*, 979.

136. Novoselov, K. S.; Geim, A. K.; Morozov, S. V.; Jiang, D.; Zhang, Y.; Dubonos, S. V.; Grigorieva, I. V.; Firsov, A. A., Electric Field Effect in Atomically Thin Carbon Films. *Science* **2004**, *306*, 666-669.

137. Late, D. J.; Liu, B.; Matte, H.; Rao, C. N. R.; Dravid, V. P., Rapid Characterization of Ultrathin Layers of Chalcogenides on $SiO_2$/Si Substrates. *Adv. Funct. Mater.* **2012**, *22*, 1894-1905.

138. Yin, Z.; Li, H.; Li, H.; Jiang, L.; Shi, Y.; Sun, Y.; Lu, G.; Zhang, Q.; Chen, X.; Zhang, H., Single-Layer $MoS_2$ Phototransistors. *ACS Nano* **2012**, *6*, 74-80.

139. Velicky, M.; Donnelly, G. E.; Hendren, W. R.; Mcfarland, S.; Scullion, D.; Debenedetti, W. J. I.; Correa, G. C.; Han, Y. M.; Wain, A. J.; Hines, M. A.; Muller, D. A.; Novoselov, K. S.; Abruna, H. D.; Bowman, R. M.; Santos, E. J. G.; Huang, F. M., Mechanism of Gold-Assisted Exfoliation of Centimeter-Sized Transition-Metal Dichalcogenide Monolayers. *ACS Nano* **2018**, *12*, 10463-10472.

140. Harvey, A.; Backes, C.; Gholamvand, Z.; Hanlon, D.; Mcateer, D.; Nerl, H. C.; Mcguire, E.; Seral-Ascaso, A.; Ramasse, Q. M.; Mcevoy, N.; Winters, S.; Berner, N. C.; Mccloskey, D.; Donegan, J. F.; Duesberg, G. S.; Nicolosi, V.; Coleman, J. N., Preparation of Gallium Sulfide Nanosheets by Liquid Exfoliation and Their Application as Hydrogen Evolution Catalysts. *Chem. Mater.* **2015**, *27*, 3483-3493.

141. Lin, Z.; Huang, Y.; Duan, X., Van der Waals Thin-Film Electronics. *Nat. Electron.* **2019**, *2*, 378-388.

142. Acerce, M.; Voiry, D.; Chhowalla, M., Metallic 1T Phase $MoS_2$ Nanosheets as Supercapacitor Electrode Materials. *Nat. Nanotechnol.* **2015**, *10*, 313-318.

143. Zeng, Z.; Yin, Z.; Huang, X.; Li, H.; He, Q.; Lu, G.; Boey, F.; Zhang, H., Single-Layer Semiconducting Nanosheets: High-Yield Preparation and Device Fabrication. *Angew. Chem. Int. Ed.* **2011**, *50*, 11093-11097.

144. He, Q.; Zeng, Z.; Yin, Z.; Li, H.; Wu, S.; Huang, X.; Zhang, H., Fabrication of Flexible $MoS_2$ Thin-Film Transistor Arrays for Practical Gas-Sensing Applications. *Small* **2012**, *8*, 2994-2999.

145. Liu, L.; Wu, J.; Wu, L.; Ye, M.; Liu, X.; Wang, Q.; Hou, S.; Lu, P.; Sun, L.; Zheng, J.; Xing, L.; Gu, L.; Jiang, X.; Xie, L.; Jiao, L., Phase-Selective Synthesis of 1T′ $Mos_2$ Monolayers and Heterophase Bilayers. *Nat. Mater.* **2018**, *17*, 1108-1114.

146. Lin, Z.; Liu, Y.; Halim, U.; Ding, M.; Liu, Y.; Wang, Y.; Jia, C.; Chen, P.; Duan, X.; Wang, C.; Song, F.; Li, M.; Wan, C.; Huang, Y.; Duan, X., Solution-Processable 2D Semiconductors for High-Performance Large-Area Electronics. *Nature* **2018**, *562*, 254-258.

147. Shi, Y. M.; Li, H. N.; Li, L. J., Recent Advances in Controlled Synthesis of Two-Dimensional Transition Metal Dichalcogenides Via Vapour Deposition Techniques. *Chem. Soc. Rev.* **2015**, *44*, 2744-2756.

148. Tan, C.; Cao, X.; Wu, X.-J.; He, Q.; Yang, J.; Zhang, X.; Chen, J.; Zhao, W.; Han, S.; Nam, G.-H.; Sindoro, M.; Zhang, H., Recent Advances in Ultrathin Two-Dimensional Nanomaterials. *Chem. Rev.* **2017**, *117*, 6225-6331.

149. Cai, Z.; Liu, B.; Zou, X.; Cheng, H.-M., Chemical Vapor Deposition Growth and Applications of Two-Dimensional Materials and Their Heterostructures. *Chem. Rev.* **2018**, *118*, 6091-6133.

150. Cai, H.; Gu, Y.; Lin, Y.-C.; Yu, Y.; Geohegan, D. B.; Xiao, K., Synthesis and Emerging Properties of 2D Layered III–VI Metal Chalcogenides. *Appl. Phys. Rev.* **2019**, *6*, 041312.

151. Li, X. F.; Lin, M. W.; Puretzky, A. A.; Idrobo, J. C.; Ma, C.; Chi, M. F.; Yoon, M.; Rouleau, C. M.; Kravchenko, II; Geohegan, D. B.; Xiao, K., Controlled Vapor Phase Growth of Single Crystalline, Two-Dimensional GaSe Crystals with High Photoresponse. *Sci. Rep.* **2014**, *4*, 5497.

152. Li, X. F.; Basile, L.; Huang, B.; Ma, C.; Lee, J. W.; Vlassiouk, I. V.; Puretzky, A. A.; Lin, M. W.; Yoon, M.; Chi, M. F.; Idrobo, J. C.; Rouleau, C. M.; Sumpter, B. G.; Geohegan, D. B.; Xiao, K., Van der Waals Epitaxial Growth of Two-Dimensional Single-Crystalline GaSe Domains on Graphene. *ACS Nano* **2015**, *9*, 8078-8088.

153. Wang, X. C.; Sheng, Y. W.; Chang, R. J.; Lee, J. K.; Zhou, Y. Q.; Li, S.; Chen, T. X.; Huang, H. F.; Porter, B. F.; Bhaskaran, H.; Warner, J. H., Chemical Vapor Deposition Growth of Two-Dimensional Monolayer Gallium Sulfide Crystals Using Hydrogen Reduction of $Ga_2S_3$. *ACS Omega* **2018**, *3*, 7897-7903.

154. Wang, S.; Rong, Y.; Fan, Y.; Pacios, M.; Bhaskaran, H.; He, K.; Warner, J. H., Shape Evolution of Monolayer $MoS_2$ Crystals Grown by Chemical Vapor Deposition. *Chem. Mater.* **2014**, *26*, 6371-6379.

155. Liu, K.-K.; Zhang, W.; Lee, Y.-H.; Lin, Y.-C.; Chang, M.-T.; Su, C.; Chang, C.-S.; Li, H.; Shi, Y.; Zhang, H.; Lai, C.-S.; Li, L.-J., Growth of Large-Area and Highly Crystalline $MoS_2$ Thin Layers on Insulating Substrates. *Nano Lett.* **2012**, *12*, 1538-1544.

156. Ji, Q. Q.; Zhang, Y.; Zhang, Y. F.; Liu, Z. F., Chemical Vapour Deposition of Group-VIB Metal Dichalcogenide Monolayers: Engineered Substrates from Amorphous to Single Crystalline. *Chem. Soc. Rev.* **2015**, *44*, 2587-2602.

157. Najmaei, S.; Liu, Z.; Zhou, W.; Zou, X.; Shi, G.; Lei, S.; Yakobson, B. I.; Idrobo, J.-C.; Ajayan, P. M.; Lou, J., Vapour Phase Growth and Grain Boundary Structure of Molybdenum Disulphide Atomic Layers. *Nat. Mater.* **2013**, *12*, 754-759.

158. Xu, W.; Li, S.; Zhou, S.; Lee, J. K.; Wang, S.; Sarwat, S. G.; Wang, X.; Bhaskaran, H.; Pasta, M.; Warner, J. H., Large Dendritic Monolayer $MoS_2$ Grown by Atmospheric Pressure Chemical Vapor Deposition for Electrocatalysis. *ACS Appl. Mater. Interfaces* **2018**, *10*, 4630-4639.

159. Meakin, P., Diffusion-Limited Surface Deposition in The Limit of Large Anisotropy. *Phys. Rev. A, Gen. Phys.* **1986**, *33*, 1984-1989.

160. Chen, J. Y.; Zhao, X. X.; Tan, S. J. R.; Xu, H.; Wu, B.; Liu, B.; Fu, D. Y.; Fu, W.; Geng, D. C.; Liu, Y. P.; Liu, W.; Tang, W.; Li, L. J.; Zhou, W.; Sum, T. C.; Loh, K. P., Chemical Vapor Deposition of Large-Size Monolayer $MoSe_2$ Crystals on Molten Glass. *JACS* **2017**, *139*, 1073-1076.

161. Yu, Y.; Li, C.; Liu, Y.; Su, L.; Zhang, Y.; Cao, L., Controlled Scalable Synthesis of Uniform, High-Quality Monolayer and Few-Layer $MoS_2$ Films. *Sci. Rep.* **2013**, *3*, 1866.

162. Xie, Y.; Wang, Z.; Zhan, Y.; Zhang, P.; Wu, R.; Jiang, T.; Wu, S.; Wang, H.; Zhao, Y.; Nan, T.; Ma, X., Controllable Growth of Monolayer $MoS_2$ by Chemical Vapor Deposition Via Close $MoO_2$ Precursor for Electrical and Optical Applications. *Nanotechnology* **2017**, *28*, 084001.

163. Gong, Y.; Ye, G.; Lei, S.; Shi, G.; He, Y.; Lin, J.; Zhang, X.; Vajtai, R.; Pantelides, S. T.; Zhou, W.; Li, B.; Ajayan, P. M., Synthesis of Millimeter-Scale Transition Metal Dichalcogenides Single Crystals. *Adv. Funct. Mater.* **2016**, *26*, 2009-2015.

164. Li, Y.; Zhang, K.; Wang, F.; Feng, Y.; Li, Y.; Han, Y.; Tang, D.; Zhang, B., Scalable Synthesis of Highly Crystalline $MoSe_2$ and Its Ambipolar Behavior. *ACS Appl. Mater. Interfaces* **2017**, *9*, 36009-36016.

165. Zhang, Y.; Zhang, Y.; Ji, Q.; Ju, J.; Yuan, H.; Shi, J.; Gao, T.; Ma, D.; Liu, M.; Chen, Y.; Song, X.; Hwang, H. Y.; Cui, Y.; Liu, Z., Controlled Growth of High-Quality Monolayer $WS_2$ Layers on Sapphire and Imaging Its Grain Boundary. *ACS Nano* **2013**, *7*, 8963-8971.

166. Li, X. F.; Dong, J. C.; Idrobo, J. C.; Puretzky, A. A.; Rouleau, C. M.; Geohegan, D. B.; Ding, F.; Xiao, K., Edge-Controlled Growth and Etching of Two-Dimensional GaSe Monolayers. *JACS* **2017**, *139*, 482-491.

167. Sheng, Y. W.; Tan, H. J.; Wang, X. C.; Warner, J. H., Hydrogen Addition for Centimeter-Sized Monolayer Tungsten Disulfide Continuous Films by Ambient Pressure Chemical Vapor Deposition. *Chem. Mater.* **2017**, *29*, 4904-4911.

168. Li, S.; Wang, S.; Tang, D.-M.; Zhao, W.; Xu, H.; Chu, L.; Bando, Y.; Golberg, D.; Eda, G., Halide-Assisted Atmospheric Pressure Growth of Large $WSe_2$ and $WS_2$ Monolayer Crystals. *Appl. Mater. Today* **2015**, *1*, 60-66.

169. Chen, K.; Chen, Z.; Wan, X.; Zheng, Z.; Xie, F.; Chen, W.; Gui, X.; Chen, H.; Xie, W.; Xu, J., A Simple Method for Synthesis of High-Quality Millimeter-Scale 1T' Transition-Metal Telluride and Near-Field Nanooptical Properties. *Adv. Mater.* **2017**, *29*, 1700704.

170. Zhou, J.; Lin, J.; Huang, X.; Zhou, Y.; Chen, Y.; Xia, J.; Wang, H.; Xie, Y.; Yu, H.; Lei, J.; Wu, D.; Liu, F.; Fu, Q.; Zeng, Q.; Hsu, C.-H.; Yang, C.; Lu, L.; Yu, T.; Shen, Z.; Lin,

H.; Yakobson, B. I.; Liu, Q.; Suenaga, K.; Liu, G.; Liu, Z., A Library of Atomically Thin Metal Chalcogenides. *Nature* **2018**, *556*, 355-359.

171. Li, S.; Lin, Y.-C.; Zhao, W.; Wu, J.; Wang, Z.; Hu, Z.; Shen, Y.; Tang, D.-M.; Wang, J.; Zhang, Q.; Zhu, H.; Chu, L.; Zhao, W.; Liu, C.; Sun, Z.; Taniguchi, T.; Osada, M.; Chen, W.; Xu, Q.-H.; Wee, A. T. S.; Suenaga, K.; Ding, F.; Eda, G., Vapour–Liquid–Solid Growth of Monolayer $MoS_2$ Nanoribbons. *Nat. Mater.* **2018**, *17*, 535-542.

172. Dong, J.; Zhang, L.; Dai, X.; Ding, F., The Epitaxy of 2D Materials Growth. *Nat. Comm.* **2020**, *11*, 5862.

173. Zhou, Y.; Nie, Y.; Liu, Y.; Yan, K.; Hong, J.; Jin, C.; Zhou, Y.; Yin, J.; Liu, Z.; Peng, H., Epitaxy and Photoresponse of Two-Dimensional GaSe Crystals on Flexible Transparent Mica Sheets. *ACS Nano* **2014**, *8*, 1485-1490.

174. Dumcenco, D.; Ovchinnikov, D.; Marinov, K.; Lazić, P.; Gibertini, M.; Marzari, N.; Sanchez, O. L.; Kung, Y.-C.; Krasnozhon, D.; Chen, M.-W.; Bertolazzi, S.; Gillet, P.; Fontcuberta I Morral, A.; Radenovic, A.; Kis, A., Large-Area Epitaxial Monolayer $MoS_2$. *ACS Nano* **2015**, *9*, 4611-4620.

175. Aljarb, A.; Cao, Z.; Tang, H.-L.; Huang, J.-K.; Li, M.; Hu, W.; Cavallo, L.; Li, L.-J., Substrate Lattice-Guided Seed Formation Controls the Orientation of 2D Transition-Metal Dichalcogenides. *ACS Nano* **2017**, *11*, 9215-9222.

176. Ji, H. G.; Lin, Y.-C.; Nagashio, K.; Maruyama, M.; Solís-Fernández, P.; Sukma Aji, A.; Panchal, V.; Okada, S.; Suenaga, K.; Ago, H., Hydrogen-Assisted Epitaxial Growth of Monolayer Tungsten Disulfide and Seamless Grain Stitching. *Chem. Mater.* **2018**, *30*, 403-411.

177. Li, X. F.; Lin, M. W.; Lin, J. H.; Huang, B.; Puretzky, A. A.; Ma, C.; Wang, K.; Zhou, W.; Pantelides, S. T.; Chi, M. F.; Kravchenko, I.; Fowlkes, J.; Rouleau, C. M.; Geohegan, D. B.; Xiao, K., Two-Dimensional GaSe/$MoSe_2$ Misfit Bilayer Heterojunctions by Van der Waals Epitaxy. *Sci. Adv.* **2016**, *2*, e1501882.

178. Zhou, N.; Wang, R. Y.; Zhou, X.; Song, H. Y.; Xiong, X.; Ding, Y.; Lu, J. T.; Gan, L.; Zhai, T. Y., P-GaSe/N-$MoS_2$ Vertical Heterostructures Synthesized by Van der Waals Epitaxy for Photoresponse Modulation. *Small* **2018**, *14*, 1702731.

179. Zhang, J.; Huang, Y.; Tan, Z.; Li, T.; Zhang, Y.; Jia, K.; Lin, L.; Sun, L.; Chen, X.; Li, Z.; Tan, C.; Zhang, J.; Zheng, L.; Wu, Y.; Deng, B.; Chen, Z.; Liu, Z.; Peng, H., Low-Temperature Heteroepitaxy of 2D $PbI_2$/Graphene for Large-Area Flexible Photodetectors. *Adv. Mater.* **2018**, *30*, 1803194.

180. Zheng, W. H.; Zheng, B. Y.; Yan, C. L.; Liu, Y.; Sun, X. X.; Qi, Z. Y.; Yang, T. F.; Jiang, Y.; Huang, W.; Fan, P.; Jiang, F.; Ji, W.; Wang, X.; Pan, A. L., Direct Vapor Growth of 2D Vertical Heterostructures with Tunable Band Alignments and Interfacial Charge Transfer Behaviors. *Adv. Sci.* **2019**, *6*, 1802204.

181. Wu, Y. A.; Fan, Y.; Speller, S.; Creeth, G. L.; Sadowski, J. T.; He, K.; Robertson, A. W.; Allen, C. S.; Warner, J. H., Large Single Crystals of Graphene on Melted Copper Using Chemical Vapor Deposition. *ACS Nano* **2012**, *6*, 5010-5017.

182. Jianyi, C.; Xiaoxu, Z.; Gustavo, G.; Zhongxin, C.; R., T. S. J.; Wei, F.; Zijing, D.; Ibrahim, A.; Yi, L.; Dechao, G.; Yanpeng, L.; Kai, L.; Bo, L.; Wei, L.; Wei, T.; A., M. S.; John, P. S.; Ping, L. K., Homoepitaxial Growth of Large-Scale Highly Organized Transition Metal Dichalcogenide Patterns. *Adv. Mater.* **2018**, *30*, 1704674.

183. Zhang, T.; Jiang, B.; Xu, Z.; Mendes, R. G.; Xiao, Y.; Chen, L. F.; Fang, L. W.; Gemming, T.; Chen, S. L.; Rummeli, M. H.; Fu, L., Twinned Growth Behaviour of Two-Dimensional Materials. *Nat. Comm.* **2016**, *7*, 13911.

184. Zhou, Y. B.; Deng, B.; Zhou, Y.; Ren, X. B.; Yin, J. B.; Jin, C. H.; Liu, Z. F.; Peng, H. L., Low-Temperature Growth of Two-Dimensional Layered Chalcogenide Crystals on Liquid. *Nano Lett.* **2016**, *16*, 2103-2107.

185. Serna, M. I.; Yoo, S. H.; Moreno, S.; Xi, Y.; Oviedo, J. P.; Choi, H.; Alshareef, H. N.; Kim, M. J.; Minary-Jolandan, M.; Quevedo-Lopez, M. A., Large-Area Deposition of $Mos_2$ by Pulsed Laser Deposition with In Situ Thickness Control. *ACS Nano* **2016**, *10*, 6054-6061.

186. Mahjouri-Samani, M.; Gresback, R.; Tian, M. K.; Wang, K.; Puretzky, A. A.; Rouleau, C. M.; Eres, G.; Ivanov, I. N.; Xiao, K.; Mcguire, M. A.; Duscher, G.; Geohegan, D. B., Pulsed Laser Deposition of Photoresponsive Two-Dimensional GaSe Nanosheet Networks. *Adv. Funct. Mater.* **2014**, *24*, 6365-6371.

187. Yuan, X.; Tang, L.; Liu, S. S.; Wang, P.; Chen, Z. G.; Zhang, C.; Liu, Y. W.; Wang, W. Y.; Zou, Y. C.; Liu, C.; Guo, N.; Zou, J.; Zhou, P.; Hu, W. D.; Xiu, F. X., Arrayed Van der Waals Vertical Heterostructures Based on 2D GaSe Grown by Molecular Beam Epitaxy. *Nano Lett.* **2015**, *15*, 3571-3577.

188. Kang, K.; Xie, S.; Huang, L.; Han, Y.; Huang, P. Y.; Mak, K. F.; Kim, C.-J.; Muller, D.; Park, J., High-Mobility Three-Atom-Thick Semiconducting Films with Wafer-Scale Homogeneity. *Nature* **2015**, *520*, 656-660.

189. Meng, X.; Libera, J. A.; Fister, T. T.; Zhou, H.; Hedlund, J. K.; Fenter, P.; Elam, J. W., Atomic Layer Deposition of Gallium Sulfide Films Using Hexakis(Dimethylamido)Digallium and Hydrogen Sulfide. *Chem. Mater.* **2014**, *26*, 1029-1039.

190. Kuhs, J.; Hens, Z.; Detavernier, C., Plasma Enhanced Atomic Layer Deposition of Gallium Sulfide Thin Films. *J. Vac. Sci. Technol. A* **2019**, *37*, 020915.

191. Ahn, C.; Park, Y.; Shin, S.; Ahn, J.-G.; Song, I.; An, Y.; Jung, J.; Kim, C. S.; Kim, J. H.; Bang, J.; Kim, D.; Baik, J.; Lim, H., Growth of Monolayer and Multilayer $MoS_2$ Films by Selection of Growth Mode: Two Pathways Via Chemisorption and Physisorption of an Inorganic Molecular Precursor. *ACS Appl. Mater. Interfaces* **2021**, *13*, 6805-6812.

192. Mattinen, M.; Hatanpää, T.; Sarnet, T.; Mizohata, K.; Meinander, K.; King, P. J.; Khriachtchev, L.; Räisänen, J.; Ritala, M.; Leskelä, M., Atomic Layer Deposition of Crystalline $MoS_2$ Thin Films: New Molybdenum Precursor for Low-Temperature Film Growth. *Adv. Mater. Interface* **2017**, *4*, 1700123.

193. Jurca, T.; Moody, M. J.; Henning, A.; Emery, J. D.; Wang, B.; Tan, J. M.; Lohr, T. L.; Lauhon, L. J.; Marks, T. J., Low-Temperature Atomic Layer Deposition of $MoS_2$ Films. *Angew. Chem. Int. Ed.* **2017**, *56*, 4991-4995.

194. Wree, J.-L.; Ciftyurek, E.; Zanders, D.; Boysen, N.; Kostka, A.; Rogalla, D.; Kasischke, M.; Ostendorf, A.; Schierbaum, K.; Devi, A., A New Metalorganic Chemical Vapor Deposition Process for $MoS_2$ with a 1,4-Diazabutadienyl Stabilized Molybdenum Precursor and Elemental Sulfur. *Dalton Trans.* **2020**, *49*, 13462-13474.

195. Zhan, Y.; Liu, Z.; Najmaei, S.; Ajayan, P. M.; Lou, J., Large-Area Vapor-Phase Growth and Characterization of $MoS_2$ Atomic Layers on a $SiO_2$ Substrate. *Small* **2012**, *8*, 966-971.

196. Wang, X.; Feng, H.; Wu, Y.; Jiao, L., Controlled Synthesis of Highly Crystalline $MoS_2$ Flakes by Chemical Vapor Deposition. *JACS* **2013**, *135*, 5304-5307.

197. Song, J.-G.; Park, J.; Lee, W.; Choi, T.; Jung, H.; Lee, C. W.; Hwang, S.-H.; Myoung, J. M.; Jung, J.-H.; Kim, S.-H.; Lansalot-Matras, C.; Kim, H., Layer-Controlled, Wafer-Scale, and Conformal Synthesis of Tungsten Disulfide Nanosheets Using Atomic Layer Deposition. *ACS Nano* **2013**, *7*, 11333-11340.

198. Kang, K.; Lee, K.-H.; Han, Y.; Gao, H.; Xie, S.; Muller, D. A.; Park, J., Layer-By-Layer Assembly of Two-Dimensional Materials into Wafer-Scale Heterostructures. *Nature* **2017**, *550*, 229.

199. Zhou, X.; Hu, X. Z.; Yu, J.; Liu, S. Y.; Shu, Z. W.; Zhang, Q.; Li, H. Q.; Ma, Y.; Xu, H.; Zhai, T. Y., 2D Layered Material-Based van der Waals Heterostructures for Optoelectronics. *Adv. Funct. Mater.* **2018**, *28*, 1706587.

200. Yang, T. F.; Zheng, B. Y.; Wang, Z.; Xu, T.; Pan, C.; Zou, J.; Zhang, X. H.; Qi, Z. Y.; Liu, H. J.; Feng, Y. X.; Hu, W. D.; Miao, F.; Sun, L. T.; Duan, X. F.; Pan, A. L., Van der Waals Epitaxial Growth and Optoelectronics of Large-Scale $WSe_2/SnS_2$ Vertical Bilayer p-n Junctions. *Nat. Comm.* **2017**, *8*, 1906.

201. Zhou, X.; Zhou, N.; Li, C.; Song, H.; Zhang, Q.; Hu, X.; Gan, L.; Li, H.; Lü, J.; Luo, J.; Xiong, J.; Zhai, T., Vertical Heterostructures Based on $SnSe_2/MoS_2$ for High Performance Photodetectors. *2D Mater.* **2017**, *4*, 025048.

202. Gong, Y.; Lin, J.; Wang, X.; Shi, G.; Lei, S.; Lin, Z.; Zou, X.; Ye, G.; Vajtai, R.; Yakobson, B. I.; Terrones, H.; Terrones, M.; Tay, B. K.; Lou, J.; Pantelides, S. T.; Liu, Z.; Zhou, W.; Ajayan, P. M., Vertical and In-Plane Heterostructures from $WS_2/MoS_2$ Monolayers. *Nat. Mater.* **2014**, *13*, 1135-1142.

203. Lin, Y.-C.; Ghosh, R. K.; Addou, R.; Lu, N.; Eichfeld, S. M.; Zhu, H.; Li, M.-Y.; Peng, X.; Kim, M. J.; Li, L.-J.; Wallace, R. M.; Datta, S.; Robinson, J. A., Atomically Thin Resonant Tunnel Diodes Built from Synthetic van der Waals Heterostructures. *Nat. Comm.* **2015**, *6*, 7311.

204. Chang, R. J.; Sheng, Y. W.; Chen, T. X.; Mkhize, N.; Lu, Y.; Bhaskaran, H.; Warner, J. H., Morphology Control of Two-Dimensional Tin Disulfide on Transition Metal Dichalcogenides Using Chemical Vapor Deposition for Nanoelectronic Applications. *ACS Appl. Nano Mater.* **2019**, *2*, 4222-4231.

205. Gong, C.; Zhang, H.; Wang, W.; Colombo, L.; Wallace, R. M.; Cho, K., Band Alignment of Two-Dimensional Transition Metal Dichalcogenides: Application in Tunnel Field Effect Transistors. *Appl. Phys. Lett.* **2013**, *103*, 053513.

206. Yan, R.; Fathipour, S.; Han, Y.; Song, B.; Xiao, S.; Li, M.; Ma, N.; Protasenko, V.; Muller, D. A.; Jena, D.; Xing, H. G., Esaki Diodes in van der Waals Heterojunctions with Broken-Gap Energy Band Alignment. *Nano Lett.* **2015**, *15*, 5791-5798.

207. Wilson, N. R.; Nguyen, P. V.; Seyler, K.; Rivera, P.; Marsden, A. J.; Laker, Z. P. L.; Constantinescu, G. C.; Kandyba, V.; Barinov, A.; Hine, N. D. M.; Xu, X.; Cobden, D. H., Determination of Band Offsets, Hybridization, and Exciton Binding in 2D Semiconductor Heterostructures. *Sci. Adv.* **2017**, *3*, e1601832.

208. Chiu, M.-H.; Zhang, C.; Shiu, H.-W.; Chuu, C.-P.; Chen, C.-H.; Chang, C.-Y. S.; Chen, C.-H.; Chou, M.-Y.; Shih, C.-K.; Li, L.-J., Determination of Band Alignment in The Single-Layer $MoS_2/WSe_2$ Heterojunction. *Nat. Comm.* **2015**, *6*, 7666.

209. Lee, C.-H.; Lee, G.-H.; Van der Zande, A. M.; Chen, W.; Li, Y.; Han, M.; Cui, X.; Arefe, G.; Nuckolls, C.; Heinz, T. F.; Guo, J.; Hone, J.; Kim, P., Atomically Thin p–n Junctions with van der Waals Heterointerfaces. *Nat. Nanotechnol.* **2014**, *9*, 676-681.

210. Cao, Y.; Fatemi, V.; Fang, S.; Watanabe, K.; Taniguchi, T.; Kaxiras, E.; Jarillo-Herrero, P., Unconventional Superconductivity in Magic-Angle Graphene Superlattices. *Nature* **2018**, *556*, 43-50.

211. Liu, E.; Barré, E.; Van Baren, J.; Wilson, M.; Taniguchi, T.; Watanabe, K.; Cui, Y.-T.; Gabor, N. M.; Heinz, T. F.; Chang, Y.-C.; Lui, C. H., Signatures of Moiré Trions in $WSe_2/MoSe_2$ Heterobilayers. *Nature* **2021**, *594*, 46-50.

212. Förg, M.; Baimuratov, A. S.; Kruchinin, S. Y.; Vovk, I. A.; Scherzer, J.; Förste, J.; Funk, V.; Watanabe, K.; Taniguchi, T.; Högele, A., Moiré Excitons in $MoSe_2$-$WSe_2$ Heterobilayers and Heterotrilayers. *Nat. Comm.* **2021**, *12*, 1656.

213. Regan, E. C.; Wang, D.; Jin, C.; Bakti Utama, M. I.; Gao, B.; Wei, X.; Zhao, S.; Zhao, W.; Zhang, Z.; Yumigeta, K.; Blei, M.; Carlström, J. D.; Watanabe, K.; Taniguchi, T.; Tongay, S.; Crommie, M.; Zettl, A.; Wang, F., Mott and Generalized Wigner Crystal States in $WSe_2/WS_2$ Moiré Superlattices. *Nature* **2020**, *579*, 359-363.

214. Ghiotto, A.; Shih, E.-M.; Pereira, G. S. S. G.; Rhodes, D. A.; Kim, B.; Zang, J.; Millis, A. J.; Watanabe, K.; Taniguchi, T.; Hone, J. C.; Wang, L.; Dean, C. R.; Pasupathy, A. N., Quantum Criticality in Twisted Transition Metal Dichalcogenides. *Nature* **2021**, *597*, 345-349.

215. Li, T.; Jiang, S.; Li, L.; Zhang, Y.; Kang, K.; Zhu, J.; Watanabe, K.; Taniguchi, T.; Chowdhury, D.; Fu, L.; Shan, J.; Mak, K. F., Continuous Mott Transition in Semiconductor Moiré Superlattices. *Nature* **2021**, *597*, 350-354.

216. Koppens, F. H. L.; Mueller, T.; Avouris, P.; Ferrari, A. C.; Vitiello, M. S.; Polini, M., Photodetectors Based on Graphene, Other Two-Dimensional Materials and Hybrid Systems. *Nat. Nanotechnol.* **2014**, *9*, 780-793.

217. Xie, C.; Mak, C.; Tao, X.; Yan, F., Photodetectors Based on Two-Dimensional Layered Materials Beyond Graphene. *Adv. Funct. Mater.* **2017**, *27*, 1603886.

218. Fang, H.; Hu, W., Photogating in Low Dimensional Photodetectors. *Adv. Sci.* **2017**, *4*, 1700323.

219. Furchi, M. M.; Polyushkin, D. K.; Pospischil, A.; Mueller, T., Mechanisms of Photoconductivity in Atomically Thin $MoS_2$. *Nano Lett.* **2014**, *14*, 6165-6170.

220. Island, J. O.; Blanter, S. I.; Buscema, M.; Van der Zant, H. S. J.; Castellanos-Gomez, A., Gate Controlled Photocurrent Generation Mechanisms in High-Gain $In_2Se_3$ Phototransistors. *Nano Lett.* **2015**, *15*, 7853-7858.

221. Zhang, W.; Chuu, C.-P.; Huang, J.-K.; Chen, C.-H.; Tsai, M.-L.; Chang, Y.-H.; Liang, C.-T.; Chen, Y.-Z.; Chueh, Y.-L.; He, J.-H.; Chou, M.-Y.; Li, L.-J., Ultrahigh-Gain Photodetectors Based on Atomically Thin Graphene-$MoS_2$ Heterostructures. *Sci. Rep.* **2014**, *4*, 3826.

222. Razeghi, M.; Rogalski, A., Semiconductor Ultraviolet Detectors. *J. Appl. Phys.* **1996**, *79*, 7433-7473.

223. Monroy, E.; Omnes, F.; Calle, F., Wide-Bandgap Semiconductor Ultraviolet Photodetectors. *Semicond. Sci. Technol.* **2003**, *18*, R33-R51.

224. Huang, H.; Wang, P.; Gao, Y. Q.; Wang, X. D.; Lin, T.; Wang, J. L.; Liao, L.; Sun, J. L.; Meng, X. J.; Huang, Z. M.; Chen, X. S.; Chu, J. H., Highly Sensitive Phototransistor Based on GaSe Nanosheets. *Appl. Phys. Lett.* **2015**, *107*, 143112.

225. Late, D. J.; Liu, B.; Luo, J.; Yan, A.; Matte, H. S. S. R.; Grayson, M.; Rao, C. N. R.; Dravid, V. P., Gas and GaSe Ultrathin Layer Transistors. *Adv. Mater.* **2012**, *24*, 3549-3554.

226. Hu, P. A.; Wang, L. F.; Yoon, M.; Zhang, J.; Feng, W.; Wang, X. N.; Wen, Z. Z.; Idrobo, J. C.; Miyamoto, Y.; Geohegan, D. B.; Xiao, K., Highly Responsive Ultrathin GaS Nanosheet Photodetectors on Rigid and Flexible Substrates. *Nano Lett.* **2013**, *13*, 1649-1654.

227. Carey, T.; Cacovich, S.; Divitini, G.; Ren, J.; Mansouri, A.; Kim, J. M.; Wang, C.; Ducati, C.; Sordan, R.; Torrisi, F., Fully Inkjet-Printed Two-Dimensional Material Field-Effect Heterojunctions for Wearable and Textile Electronics. *Nat. Comm.* **2017**, *8*, 1202.

228. Yang, D.; Li, B.; Hu, C.; Deng, H.; Dong, D. D.; Yang, X. K.; Qiao, K. K.; Yuan, S. J.; Song, H. S., Controllable Growth Orientation of $SnS_2$ Flakes for Low-Noise, High-Photoswitching Ratio, and Ultrafast Phototransistors. *Adv. Opt. Mater.* **2016**, *4*, 419-426.

229. Jia, X. S.; Tang, C. C.; Pan, R. H.; Long, Y. Z.; Gu, C. Z.; Li, J. J., Thickness-Dependently Enhanced Photodetection Performance of Vertically Grown $SnS_2$ Nanoflakes with Large Size and High Production. *ACS Appl. Mater. Interfaces* **2018**, *10*, 18073-18081.

230. Liu, J. Z.; Xia, C. X.; Li, H. L.; Pan, A. L., High On/Off Ratio Photosensitive Field Effect Transistors Based on Few Layer $SnS_2$. *Nanotechnology* **2016**, *27*, 34LT01.

231. Wan, X.; Xu, Y.; Guo, H.; Shehzad, K.; Ali, A.; Liu, Y.; Yang, J.; Dai, D.; Lin, C.-T.; Liu, L.; Cheng, H.-C.; Wang, F.; Wang, X.; Lu, H.; Hu, W.; Pi, X.; Dan, Y.; Luo, J.; Hasan, T.; Duan, X.; Li, X.; Xu, J.; Yang, D.; Ren, T.; Yu, B., A Self-Powered High-Performance Graphene/Silicon Ultraviolet Photodetector with Ultra-Shallow Junction: Breaking The Limit of Silicon? *npj 2D Mater. Appli.* **2017**, *1*, 4.

232. Arash, A.; Ahmed, T.; Rajan, A. G.; Walia, S.; Rahman, F. A.; Mazumder, A.; Ramanathan, R.; Sriram, S.; Bhaskaran, M.; Mayes, E.; Strano, M. S.; Balendhran, S., Large-Area Synthesis of 2D $MoO_{3-x}$ for Enhanced Optoelectronic Applications. *2D Mater.* **2019**, *6*, 035031.

233. Zhong, M. Z.; Zhou, K.; Wei, Z. M.; Li, Y.; Li, T.; Dong, H. L.; Jiang, L.; Li, J. B.; Hu, W. P., Highly Anisotropic Solar-Blind UV Photodetector Based on Large-Size Two-Dimensional Alpha-$MoO_3$ Atomic Crystals. *2D Mater.* **2018**, *5*, 035033.

234. Yu, W. J.; Liu, Y.; Zhou, H.; Yin, A.; Li, Z.; Huang, Y.; Duan, X., Highly Efficient Gate-Tunable Photocurrent Generation in Vertical Heterostructures of Layered Materials. *Nat. Nanotechnol.* **2013**, *8*, 952-958.

235. Massicotte, M.; Schmidt, P.; Vialla, F.; Schädler, K. G.; Reserbat-Plantey, A.; Watanabe, K.; Taniguchi, T.; Tielrooij, K. J.; Koppens, F. H. L., Picosecond Photoresponse in van der Waals Heterostructures. *Nat. Nanotechnol.* **2016**, *11*, 42-46.

236. Xue, Y.; Zhang, Y.; Liu, Y.; Liu, H.; Song, J.; Sophia, J.; Liu, J.; Xu, Z.; Xu, Q.; Wang, Z.; Zheng, J.; Liu, Y.; Li, S.; Bao, Q., Scalable Production of a Few-Layer $MoS_2/WS_2$ Vertical Heterojunction Array and Its Application for Photodetectors. *ACS Nano* **2016**, *10*, 573-580.

237. Pezeshki, A.; Shokouh, S. H. H.; Nazari, T.; Oh, K.; Im, S., Electric and Photovoltaic Behavior of a Few-Layer A-$MoTe_2/MoS_2$ Dichalcogenide Heterojunction. *Adv. Mater.* **2016**, *28*, 3216-3222.

238. Flöry, N.; Jain, A.; Bharadwaj, P.; Parzefall, M.; Taniguchi, T.; Watanabe, K.; Novotny, L., A $WSe_2/MoSe_2$ Heterostructure Photovoltaic Device. *Appl. Phys. Lett.* **2015**, *107*, 123106.

239. Wei, X.; Yan, F. G.; Lv, Q. S.; Shen, C.; Wang, K. Y., Fast Gate-Tunable Photodetection in The Graphene Sandwiched $WSe_2$/GaSe Heterojunctions. *Nanoscale* **2017**, *9*, 8388-8392.

240. Islam, A.; Lee, J.; Feng, P. X. L., Atomic Layer GaSe/$MoS_2$ Van der Waals Heterostructure Photodiodes with Low Noise and Large Dynamic Range. *ACS Photonics* **2018**, *5*, 2693-2700.

241. Long, M.; Liu, E.; Wang, P.; Gao, A.; Xia, H.; Luo, W.; Wang, B.; Zeng, J.; Fu, Y.; Xu, K.; Zhou, W.; Lv, Y.; Yao, S.; Lu, M.; Chen, Y.; Ni, Z.; You, Y.; Zhang, X.; Qin, S.; Shi, Y.; Hu, W.; Xing, D.; Miao, F., Broadband Photovoltaic Detectors Based on an Atomically Thin Heterostructure. *Nano Lett.* **2016**, *16*, 2254-2259.

242. Li, A.; Chen, Q.; Wang, P.; Gan, Y.; Qi, T.; Wang, P.; Tang, F.; Wu, J. Z.; Chen, R.; Zhang, L.; Gong, Y., Ultrahigh-Sensitive Broadband Photodetectors Based on Dielectric Shielded $MoTe_2$/Graphene/$SnS_2$ p-g-n Junctions. *Adv. Mater.* **2019**, *31*, e1805656.

243. Zhou, X.; Hu, X. Z.; Zhou, S. S.; Song, H. Y.; Zhang, Q.; Pi, L. J.; Li, L.; Li, H. Q.; Lu, J. T.; Zhai, T. Y., Tunneling Diode Based on $WSe_2/SnS_2$ Heterostructure Incorporating High Detectivity and Responsivity. *Adv. Mater.* **2018**, *30*, 1703286.

244. Pospischil, A.; Furchi, M. M.; Mueller, T., Solar-Energy Conversion and Light Emission in an Atomic Monolayer p–n Diode. *Nat. Nanotechnol.* **2014**, *9*, 257-261.

245. Baugher, B. W. H.; Churchill, H. O. H.; Yang, Y.; Jarillo-Herrero, P., Optoelectronic Devices Based on Electrically Tunable p–n Diodes in a Monolayer Dichalcogenide. *Nat. Nanotechnol.* **2014**, *9*, 262-267.

246. Ross, J. S.; Klement, P.; Jones, A. M.; Ghimire, N. J.; Yan, J.; Mandrus, D. G.; Taniguchi, T.; Watanabe, K.; Kitamura, K.; Yao, W.; Cobden, D. H.; Xu, X., Electrically Tunable Excitonic Light-Emitting Diodes Based on Monolayer $WSe_2$ p–n Junctions. *Nat. Nanotechnol.* **2014**, *9*, 268-272.

247. Cheng, R.; Li, D.; Zhou, H.; Wang, C.; Yin, A.; Jiang, S.; Liu, Y.; Chen, Y.; Huang, Y.; Duan, X., Electroluminescence and Photocurrent Generation from Atomically Sharp $WSe_2/MoS_2$ Heterojunction p-n Diodes. *Nano Lett.* **2014**, *14*, 5590-5597.

248. Withers, F.; Del Pozo-Zamudio, O.; Mishchenko, A.; Rooney, A. P.; Gholinia, A.; Watanabe, K.; Taniguchi, T.; Haigh, S. J.; Geim, A. K.; Tartakovskii, A. I.; Novoselov, K. S., Light-Emitting Diodes by Band-Structure Engineering in van der Waals Heterostructures. *Nat. Mater.* **2015**, *14*, 301-306.

249. Palacios-Berraquero, C.; Barbone, M.; Kara, D. M.; Chen, X.; Goykhman, I.; Yoon, D.; Ott, A. K.; Beitner, J.; Watanabe, K.; Taniguchi, T.; Ferrari, A. C.; Atatüre, M., Atomically Thin Quantum Light-Emitting Diodes. *Nat. Comm.* **2016**, *7*, 12978.

250. Sheng, Y.; Chen, T.; Lu, Y.; Chang, R.-J.; Sinha, S.; Warner, J. H., High-Performance $WS_2$ Monolayer Light-Emitting Tunneling Devices Using 2D Materials Grown by Chemical Vapor Deposition. *ACS Nano* **2019**, *13*, 4530-4537.

# Chapter 3

# Methodology

## 3.1 Introduction

This chapter aims to offer a brief introduction to the basic principles and experimental details for the synthesis and characterisation of 2D layered materials carried out in this project. The approaches described are based on both self-developed procedures as well as personal practice of previous work from other group members. This includes synthesis and transfer of 2D layered materials and fabrication of 2D layered semiconductor based VLHs. A series of microscopic and spectroscopic characterisation techniques for providing comprehensive information of 2D layered material properties are introduced. Finally, fabrication and measurement processes for nanoelectronics devices are provided. With the given details, it is expected that all experiments and characterisation results conducted in this thesis can be reproducible.

## 3.2 Vapour Phase Deposition Synthesis of 2D Materials

### 3.2.1 Synthesis of $MoS_2$

The synthesis of monolayer $MoS_2$ single crystals on glass was done by sulfurization of pre-deposited $MoO_3$ on glass. For preparation of the $MoO_3$/glass by spin-coating, molybdenum trioxide ($MoO_3$, powder, ≥99.5%, Sigma-Aldrich) was firstly dissolved in 28.0 % $NH_4OH$ solution with different concentrations. The substrate, soda lime silicate glass, was pre-cleaned by deionized water (DI water), acetone and isopropanol

alcohol (IPA). Then the solution was spin-coated onto the glass at 4500 rpm for 1 min for uniformity. After that, the glass was heated at 300 °C in air for 10 min to completely remove the water residue.

Sulfurization of $MoS_2$ was conducted in a two-furnace system to separately control two temperature zones with a 1-inch-diameter quartz tube, which is shown in Figure 3.1. The inlet carrier gas was controlled by digital mass flowmeter (Alicat, MC-500SCCM-D/5M) and the outlet contained mineral oil sealing to avoid reverse flow of air. Both furnaces were designed to be moved horizontally after the growth for a fast-cooling process. For a typical growth, the pre-deposited $MoO_3$/glass was placed in the centre of the furnace downstream (Furnace 2) supported by an alumina ceramic boat, and 300 mg sulfur (S, powder, ≥99.5%, Sigma-Aldrich) was loaded in the centre of the furnace upstream (Furnace 1) in another ceramic boat. After the precursors and substrate had been loaded, the system was flushed with 500 sccm argon for 30 min to form an inert atmosphere. Then the gas flow was maintained at 150 sccm and Furnace 2 was ramped up at 40 °C /min to 840 °C. 5 min after the target temperature was reached, the temperature of sulfur was increased to 180 °C at 40 °C /min. The sulfurization was complete in 5 min and finally a fast-cooling stage ended the synthesis.

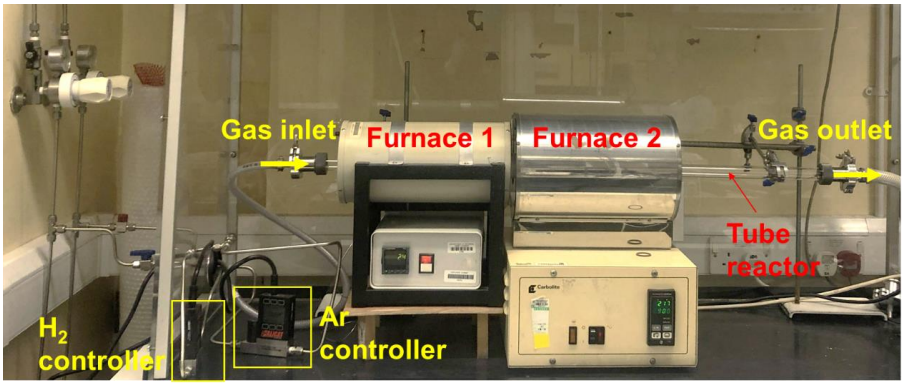



**Figure 3.1. Photograph of 1-inch CVD experimental setup for chalcogenide 2D semiconductor growth.**

### 3.2.2 Synthesis of GaS

Synthesis of ultrathin GaS films on $SiO_2$/Si was carried out in the same two-furnace system. For a typical synthesis of defective GaS, 10 mg gallium (III) sulfide ($Ga_2S_3$, powder, ≥99%, Sigma-Aldrich) was placed in the centre of Furnace 2. The 1*1 $cm^2$ $SiO_2$/Si substrate was cleaned in acetone and IPA for 15 min each, and placed 8 cm downstream of the $Ga_2S_3$ powder. After flushing the system with 500 sccm Ar for 30 min, 100 sccm 25% $H_2$/Ar was used as carrier gas. Furnace 2 was ramped up at 40 °C /min, so that the $Ga_2S_3$ powder reaches 810 °C and the substrate reaches 650 °C at the same time. The temperature zone was calibrated using a thermocouple put in between the furnace and the quartz tube, and the substrate temperature zone could be adjusted by changing the substrate position. After 20 min growth, the carrier gas was switched to 75 sccm Ar followed by a fast-cooling process to stop the reaction and protect the growth product. For synthesis of stoichiometric GaS crystals, the same growth procedure was applied, with additional 20 mg sulfur put in the centre of Furnace 1. Then Furnace 1 was ramped up at 20 °C /min after Furnace 2 had reached 570 °C, until reaching the target temperature of 120 °C simultaneously with Furnace 2 reaching 810 °C.

### 3.2.3 Synthesis of Graphene

Monolayer graphene growth was based on previous study from other group members.[1] As shown in Figure 3.2, a 4-inch CVD system was used for the purpose of monolayer graphene growth. 14*6 $cm^2$ copper foil (25 μm Cu foil, 99.8%, Goodfellow) was cleaned with diluted hydrochloric solution (HCl:$H_2O$ 1:3) for 5 min for removal of

surface oxides, then washed with DI water, acetone and IPA for 5 min each. Then the copper foil was kept flat on a ceramic boat which was loaded in the centre of the furnace. The system was first flushed with 2000 sccm Ar, 500 sccm $H_2$ and 50 sccm $CH_4$ for 30 min, followed by heating up the furnace at 60 °C/min ramping rate under 500 sccm Ar and 100 sccm $H_2$. The copper sheet was annealed at 1060 °C under the mixed gas for 1 h, then 10 sccm additional $CH_4$ was introduced to initiate the growth. After 1 h growth, the $CH_4$ supply was stopped and the furnace was moved towards downstream on a rail system to reveal the copper foil for fast-cooling.

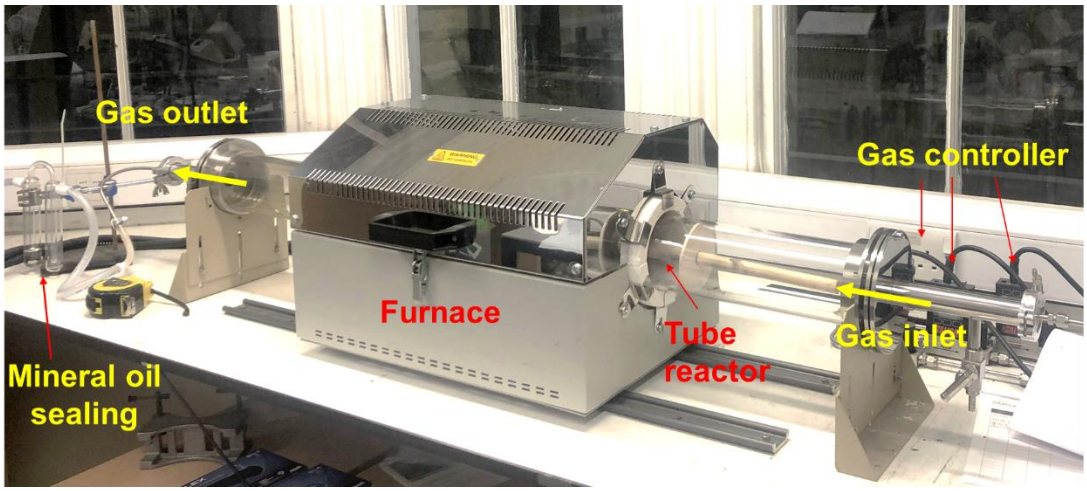



**Figure 3.2. Photograph of 4-inch tube CVD experimental setup for graphene growth.**

### 3.2.4 Synthesis of $WS_2$

Monolayer $WS_2$ growth was based on previous study from other group members.[2] The same two-furnace system used for $MoS_2$ and GaS growth was used. Before growth, 2*2 $cm^2$ $SiO_2$/Si substrates were cleaned in acetone and IPA similar to that in GaS growth. 300 mg sulfur and 200 mg tungsten trioxide ($WO_3$, powder, >99.5%, Sigma-Aldrich) were used as precursors. A smaller quartz tube (0.5 inch in diameter) was used to load the $WO_3$ power to avoid sulfurization of the solid precursor during growth. The sulfur

powder was placed in the centre of Furnace 1 and the $WO_3$ power was placed in the centre of the Furnace 2 in the inner tube. The $SiO_2$/Si substrate was placed 9 cm away from the $WO_3$ powder and 4 cm away from the open end of the small tube to allow sufficient mixing of gaseous precursors. After the system had been flushed with 500 sccm Ar for 30 min, the carrier gas was switched to 250 sccm Ar. Sulfur was first heated to 180 °C to create a S-rich environment, while $WO_3$ and substrate was heated to 1070 °C and 960 °C at ramping rate of 40 °C/min. The reaction was carried out for 4 min, and then Furnace 2 was set to 0 °C and the gas flow was reduced to 10 sccm Ar to stop the growth. After the temperature of Furnace 2 had dropped below 920 °C, sulfur was heated to 400 °C for blowing the remaining sulfur away from the reaction zone under 500 sccm Ar. Finally, both furnaces were fast cooled to room temperature.

### 3.2.5 Synthesis of GaS-Based VLHs

For growth of GaS/graphene heterostructures, monolayer graphene films grown on copper film was transferred onto TEM $Si_3N_4$ grid via the wet transfer method described in the next section. The growth conditions were similar to the growth procedures of stoichiometric GaS. The TEM SiN grid covered with graphene film was put in the centre of the 1*1 $cm^2$ $SiO_2$/Si substrate, and the precursor temperature was changed to 830 °C and grid temperature was set at 625 °C. The precursor amount and the growth time were kept the same. For the growth of GaS/graphene heterostructures, monolayer graphene film grown on copper film and monolayer $MoS_2$ single crystals grown on glass were subsequently transferred onto 1*1 $cm^2$ $SiO_2$/Si substrates, then the same growth conditions for GaS/graphene heterostructures were used.

## 3.3 Transfer of 2D Materials

### 3.3.1 Transfer of 2D Materials on Glass Substrates

After VPD growth, the as-grown $MoS_2$ was firstly spin-coated with a thin film of poly(methylmethacrylate) (PMMA, 8 wt % in anisole, 495k molecular weight) at 4500 rpm for 60 s to protect the 2D material from mechanical damage, followed by curing at 150 °C for 5 min. A diamond file was used to gently scratch the edge of the glass substrate to create a crack on the PMMA film so that water could penetrate between the PMMA and glass in the next step. Then the PMMA-coated glass was slowly immersed into deionized water where the PMMA film with $MoS_2$ detached from the glass and floated on the water due to the large surface tension between hydrophobic PMMA and hydrophilic glass. After that, the target substrate was used to fish out the PMMA/$MoS_2$ film. The sample was dried overnight at room temperature, then baked at 180 °C for 30 min for better adhesion. Finally, the PMMA layer was removed by acetone at 45 °C for 3 h.

### 3.3.2 Transfer of 2D Materials on $SiO_2$/Si Substrates

2D materials grown on $SiO_2$/Si substrates were firstly spin-coated with PMMA thin film at 4500 rpm for 60 s, followed by curing at 180 °C for 90 s. Then the edge of the $SiO_2$/Si substrate was scratched with a tungsten flat file to expose the 300 nm $SiO_2$ layer. The substrate was subsequently floated on 1 M potassium hydroxide aqueous solution for 4 h to etch the $SiO_2$ layer, which separated the floating PMMA/2D material film from the sunken bottom Si substrate. The floating PMMA/2D material film was rinsed by transferring it onto DI water three times. The target substrate was used to fish out the rinsed polymer/2D material stack and then dried overnight. After baking under

180 °C for 30 min for better adhesion, the PMMA layer was removed by acetone at 45 °C for 3 h.

### 3.3.3 Transfer of 2D Materials on Cu Substrates

After the CVD growth of 2D materials on Cu substrates, the sample was first spin-coated with PMMA thin film at 4500 rpm for 60 s, followed by curing at 180 °C for 90 s. The back of the copper substrate was further cleaned with cotton to remove the 2D materials and polymer residues. The copper substrate was then etched in 0.3 M ammonium persulfate aqueous solution. After that, the PMMA/2D material film was rinsed with DI water three times to remove etchant residues. The rinsed polymer/2D material stack was then fished out by the target substrate and dried overnight in air. Finally, the sample was baked under 180 °C for 30 min for better adhesion, followed by removal of the PMMA layer in acetone at 45 °C for 3 h.

## 3.4 Microscopy Characterisation

### 3.4.1 Optical Microscopy

Optical microscopy (OM) enables fast and non-destructive characterisation of the morphology, crystal size, crystal thickness and coverage of ultrathin 2D semiconductors in this project. Especially on $SiO_2$/Si substrates, depending on the thickness of the $SiO_2$ layer, the interference between light from two neighbouring paths results in significant colour and brightness contrast for 2D semiconductors with different number of layers (Fig. 3.3).[3] It also enables quick identification of micrometre-scale VLHs regions from its constituents, which is shown in Chapter 7. $MoS_2$ on glass

substrates also show significant contrast between monolayer and multilayer $MoS_2$, thus is used for demonstration of thickness uniformity in Chapter 4. Optical images were processed with the software of ImageJ to highlight contrast difference of region of interest by adjusting contrast/brightness.

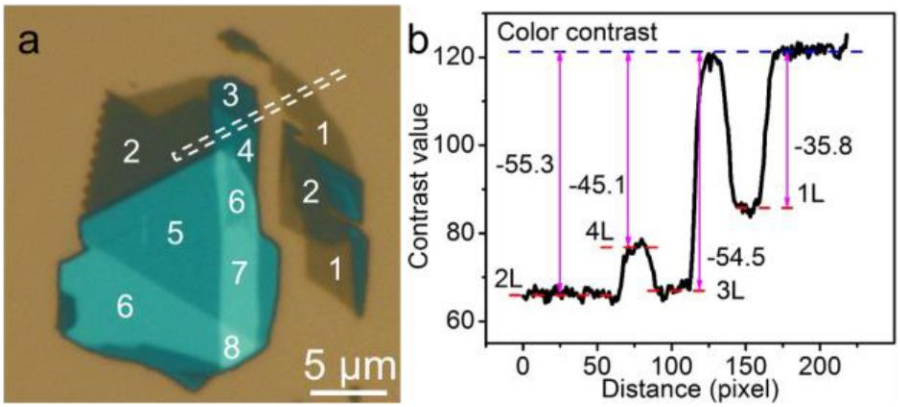



**Figure 3.3. Optical contrast between 2D $MoS_2$ with various thickness on 90 nm $SiO_2$/Si substrate.** (a) Optical image of exfoliated 2D $MoS_2$ crystal from 1L to 8L. (b) Contrast value plot profile from the dashed rectangular in (a). Reproduced with permission from ref. 4. Copyright 2013 American Chemical Society.

### 3.4.2 Scanning Electron Microscopy

While OM characterisation is facile and accurate, it's resolution is typically micrometre due to the diffraction limit of visible light. For more detailed morphology and surface topology study, scanning electron microscopy (SEM) offer similar benefits from OM but with higher resolution (down to nanometre) with an electron beam as probe. In SEM, the incident electron beam is emitted by a thermionic or field emission gun under ultrahigh vacuum. The imaging signal is from secondary electrons, which are low-energy electrons generated after the incident electrons enter the specimen surface. As only secondary electrons formed within a few nanometres below the surface can escape

and be collected, the contrast is very sensitive to the specimen's surface topography. In addition, contrast can also be generated by electronic variations. As a result, although topographical contrast between monolayer 2D semiconductor and underlying $SiO_2$/Si substrate is low, notable contrast from conducting properties reveals the morphology of the 2D materials.

In this project, Hitachi S-4300 and ZEISS EVO with field emission guns were used with an accelerating voltage of 3.0 kV. Such low accelerating voltage reduces the penetration depth of the primary electrons and allows more information on surface structure and components. During the SEM characterisation, the specimen was mounted onto the sample stub by conductive carbon sticky pads to reduce unwanted charging effects.

### 3.4.3 Annular Dark Field Scanning Transmission Electron Microscopy

Scanning Transmission Electron Microscopy (STEM) uses a very small electron beam probe to scan across region of interest in a similar manner as in SEM. The difference is that in STEM, the detectors are placed below the specimen to record signals from transmitted electrons. As a result, the thickness of specimen is usually within 10 nm and a higher-energy electron beam is used which allows atomic resolution imaging. By utilising an annular dark-field (ADF) detector, signals from scattered electrons collected at higher-angle show strong dependence on atomic number (approximately $Z^2$), where heavier atoms show brighter contrast than light atoms. Based on the above considerations, this technique is very useful for obtaining crystal lattice and atomic positions in ultrathin 2D semiconductors.

In this thesis, ADF-STEM imaging was conducted by Dr. Jun Chen (Chapter 5, 6) and Dr. Gyeong Hee Ryu (Chapter 4). ADF-STEM imaging for $MoS_2$, $GaS_{0.87}$ degradation study and GaS/$MoS_2$ was performed using Oxford's JEOL ARM-200 cold field emission gun transmission electron microscope with a spherical aberration (Cs) probe corrector at an accelerating voltage of 80 kV. ADF-STEM imaging for GaS/graphene heterostructures were obtained using an aberration corrected JEOL ARM300CF STEM equipped with a JEOL ETA corrector operating under an accelerating voltage of 60 kV. Dwell times of 10−20 μs and pixel sizes between 0.01−0.03 nm $px^{-1}$ were typically used for imaging. To reduce surface contamination from exposure in air, vacuum annealing of specimen at 150 °C was typically applied before characterisation to remove absorbates thoroughly.

Imaging processing was performed by ImageJ software. Atomic resolution images were typically applied with Gaussian blur filter of 2 pixels to highlight atom positions. The FFT images in Chapter 6 were further modified with blue-orange icb false colour to enhance visual contrast. For image simulations, atomic models were built by CrystalMaker and Accelrys Discovery Studio Visualizer software. The coordinates of atoms in the model were converted into a suitable format using python script written by Dr. Christopher S. Allen. Multislice image simulations of corresponding atomic models were conducted by JEMS software (programmed by Dr. P. A. Stadelmann), which operates by slicing the atomic model into multiple thin layers and then simulating the scattering of electrons propagating through the specimen. The image simulation was used in qualitative comparison with experimental images for information regarding stacking configurations (in Chapter 5) and Moiré superlattices (in Chapter 6).

### 3.4.4 Atomic Force Microscopy

Atomic Force Microscopy (AFM) provides direct information about the thickness and number of layers of 2D semiconductors as well as any surface contaminations. The technique determines surface topography by using a sharp tip on a cantilever to scan across the surface. Under the tapping mode (or AC mode), the vdWs force between the tip and specimen results in attractive or repulsive force depending on the distance between them. Output signal is recorded by deflection of the cantilever oscillating at its resonant frequency. The sensitivity of vdWs interactions with distance as well as the dangling-bond-free surface of 2D semiconductors allow accurate measurement of sub-nanometre step height. In this thesis, AFM measurements were conducted by Ms. Yu Shu and Dr. Nhlakanipho Mkhize on an Asylum Research MFP-3D in AC mode with silicon Tap300-G cantilever (BudgetSensors, spring constant ~40 N/m and resonant frequency ~300 kHz). The resultant AFM map and corresponding height profiles were processed by the Gwyddion software.

## 3.5 Spectroscopic Characterisation

### 3.5.1 Raman Spectroscopy

Raman spectroscopy is an efficient, non-invasive approach for probing vibrational modes in 2D materials that provides information about crystal structure, number of layers, strain, etc. In general, this technique uses a monochromic light source and collects signal from inelastic scattering with the specimen. For inelastic scattering processes generating phonons, the scattered light has an energy lower than the incident light (Stokes scattering). Such energy difference is recorded as frequency shift ($cm^{-1}$) in typical Raman spectra along with intensity of the scattered light.

The frequency shift is related to characteristic vibrational modes of the specimen. For 2D materials characterised in this thesis, the 2D $MoS_2$ has two characteristic vibration modes, $E^1_{2g}$ and $A_{1g}$ (Fig. 3.4a).[5] The $E^1_{2g}$ mode (around 385 $cm^{-1}$) corresponds to double-degenerate in-plane opposite vibration between the two S atoms and the middle Mo atom, while the $A_{1g}$ mode (around 410 $cm^{-1}$) corresponds to out-of-plane opposite vibration of S atoms. The out-of-plane vibration is more affected by interlayer vdWs interactions as well as Coulomb interactions, showing position shift with varying thickness or charge doping.[6-7] In contrast, the in-plane vibration is more affected by intralayer interactions, thus more sensitive to compression/tensile strain effects.[8] In practice, the difference between the two peak positions is commonly used as an indicator of number of layers. A frequency difference between 17.5−21 $cm^{-1}$ is expected for monolayer $MoS_2$, with bilayer $MoS_2$ showing around 22 $cm^{-1}$ and multilayer $MoS_2$ approaching its bulk value of 25 $cm^{-1}$ (Fig. 3.4b). $WS_2$ shows multiple characteristic peaks between 200−500 $cm^{-1}$ (Fig. 3.4c),[9] while the $E^1_{2g}$ (around 356 $cm^{-1}$) and $A_{1g}$ (around 416 $cm^{-1}$) peaks were used to probe layer number, doping and strain information similar to the case of $MoS_2$. For GaS, previous studies showed two strong characteristic peaks at $A^1_{1g}$ (188 $cm^{-1}$), $A^1_{2g}$ (360 $cm^{-1}$) (Fig. 3.4d).[10] In this thesis, as GaS has weak interaction with the incident visible light, the strongest $A^1_{1g}$ peak is used as indicator for layer numbers, which is further discussed in Chapter 5.

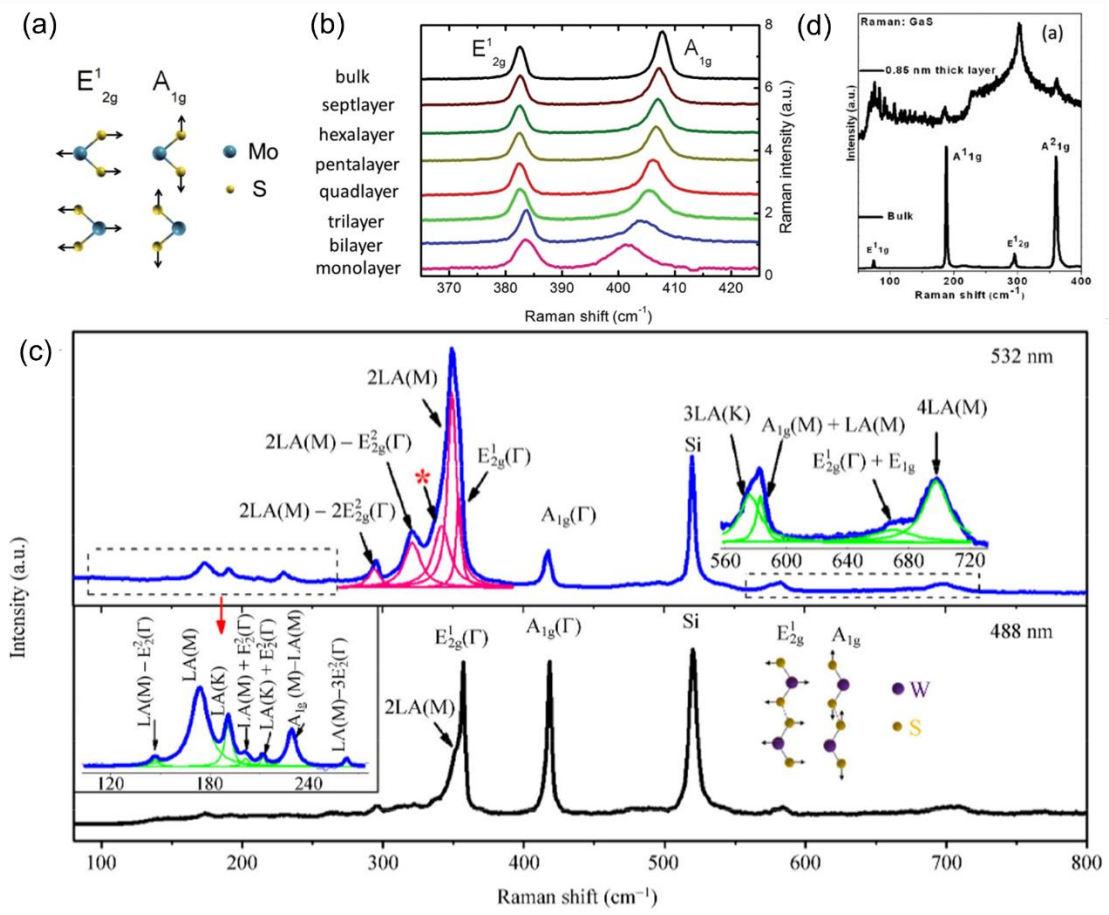



**Figure 3.4. Characteristic Raman spectra of $MoS_2$, $WS_2$ and GaS.** (a) $E^1_{2g}$ and $A_{1g}$ vibration modes in $MoS_2$. (b) Raman spectra of $MoS_2$ crystals from monolayer to few-layer. Reproduced with permission from ref. 11. Copyright 2012 American Physical Society. (c) Raman spectra of monolayer $WS_2$ crystals under different illumination wavelength. Reproduced with permission from ref. 9. Copyright 2014 Springer. (d) Raman spectra of monolayer and bulk GaS crystals. Reproduced with permission from ref. 10. Copyright 2012 Wiley-VCH.

The Raman spectroscopy characterisation was conducted in a LabRam Aramis Raman spectrometer system with confocal microscope, using a 532 nm laser as incident light with ×50 objective lens and spot size of ~1 μm. A motorised stage was included in the system which allows collection of spectra in fixed steps to show uniformity of the specimen. The excitation source has a maximum power of 7.76 mW but various filters

down to 0.01% can be applied according to signal intensity and sample robustness. A grating of 1800 $mm^{-1}$ (1800 grooves per mm grating) is used to resolve the peaks. Before the measurement, the system was calibrated using standard silicon chips (520.7 $cm^{-1}$). Measurements were typically done with 10 % filter, in the range of 100−500 $cm^{-1}$, with acquisition time of 5 s and an accumulation number of 2. For defective GaS with weak signal and laser degradation, multiple spectra at different positions were integrated to obtain a better signal-to-noise ratio.

### 3.5.2 Photoluminescence Spectroscopy

2D semiconductors with direct bandgaps show strong photoluminescence (PL) emission under excitation by a source with higher energy than their bandgaps, which originates from exciton recombination. A PL spectrum shows the band information as well as excitonic behaviours. For $MoS_2$ and $WS_2$, only the monolayer form has a direct bandgap and high PL quantum efficiency, thus PL spectroscopy is used for assessing its optical properties or interlayer interactions in VLHs. For monolayer $MoS_2$ excited under a 532 nm laser, two characteristic PL peaks at 1.83 eV (A peak) and 1.98 eV (B peak) exist, which result from strong valence band maximum splitting due to the strong spin-orbit effect of the Mo d orbital (Fig. 3.5a). In addition, as the synthesised $MoS_2$ is often negatively doped, another trion peak ($A^-$ peak) is often observed next to the A peak. Since the position, intensity and peak shape of the exciton peak reflects band structure, it is used to probe strain or alloying effect that would change the semiconductor's bandgap.[12-13] Furthermore, as formation of trions is dependent on the free electron concentration, the exciton-to-trion peak intensity ratio is affected by electrostatic gating or chemical doping, and can be further used to determine its carrier

density.[14] Monolayer $WS_2$ shows similar optical properties, with A peak at 2.00 eV (Fig. 3.5b). The B peak at 2.35 eV was not observed in this study due to the excitation energy at 532 nm (2.33 eV).[15]

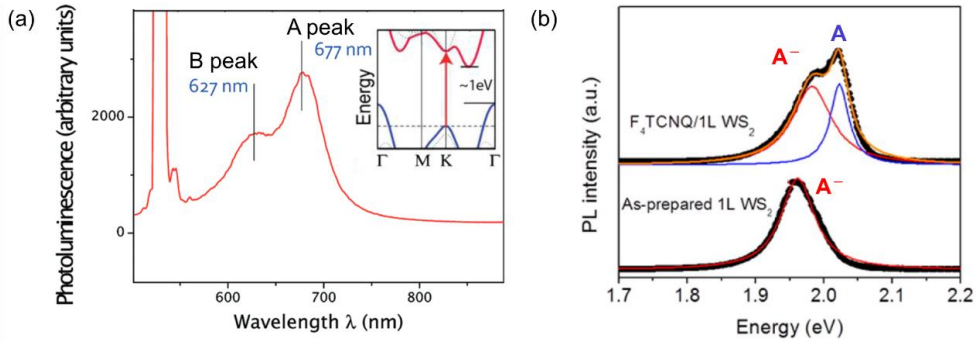



**Figure 3.5. PL spectra of $MoS_2$ and $WS_2$.** (a) A and B exciton peak in monolayer $MoS_2$. Reproduced with permission from ref. 16. Copyright 2010 American Chemical Society. (b) A exciton and $A^-$ trion peaks in monolayer $WS_2$. The coupling with $F_4TCNQ$ molecules introduces positive doping into the as-prepared $WS_2$ to enhance the exciton A peak. Reproduced with permission from ref. 17. Copyright 2014 American Chemical Society.

The PL spectroscopy measurements were conducted in the same instrument used for Raman spectroscopy, except that grating of 600 $mm^{-1}$ (600 grooves per mm grating) was used. Acquisition time of 2 s and an accumulation number of 2 was applied, and for monolayer $WS_2$ sample with very high PL quantum efficiency, a 0.1% filter was employed to avoid signal saturation. Multi-Lorentzian fitting was applied to differentiate overlapping peaks.

### 3.5.3 X-Ray Photoelectron Spectroscopy

X-ray photoelectron spectroscopy (XPS) is a surface sensitive technique utilising the photoelectric effect. In principle, an incident X-ray excites electrons in the valence band

which leaves the specimen surface with kinetic energy equalling to the energy of the incident photon minus the electron binding energy (the minimum energy required to remove an electron from an atom or ion) and the work function. XPS requires high vacuum or ultra-high vacuum conditions. During the measurement, the electron energy analyser's work function is corrected by the work function of the specimen, so that the measured electron kinetic energy equals to the electron binding energy. By plotting the number of collected electrons with electron binding energy, the XPS spectrum provides rich information for identification of chemical elements, determination of stoichiometry as well as their chemical states. When combined with ion etching techniques, the surface sensitive feature of XPS could further provide depth profile analysis into the specimen, which allows investigation of precursor dissolution into substrate shown in Chapter 4.

In this work, XPS characterisation was carried out by Dr. Philip Holdway in a Thermo K-alpha XPS instrument with monochromatic Al Kα radiation (12 kV, 3 mA). For depth profile measurements, argon ion (4 keV) etching with an area of 3×3 $mm^2$ was used during intervals of measurements. Typical spot size was between 400-600 μm. The obtained spectrum was further calibrated by the amorphous carbon peak at 284.8 eV to eliminate charging effects. Fitting and element analysis were done in the CasaXPS software.

### 3.5.4 Energy-Dispersive X-Ray Spectroscopy

Energy-Dispersive X-Ray (EDX) spectroscopy can be used in element analysis and their relative abundance and utilises the characteristic energy structure of the atomic structure of different elements. Typically, electrons in an inner shell of atoms are first

excited by high-energy electrons or X-rays, which leaves a hole at the original position. Then the hole is filled by another electron from higher-energy shell accompanied by emission of characteristic X-rays. While EDX and XPS are both used in chemical composition analysis, they are suitable for different tasks based on their mechanisms: XPS is surface sensitive while electron beam in EDX can penetrate further into the specimen, thus ultrathin 2D materials have stronger signal in XPS while thicker materials are suitable for EDX measurement. Spectra in XPS record energy of outer-shell electrons thus can reflect valence state of elements, while EDX involves inner electrons that are less affected by its surroundings. Certain elements have identical peak positions in EDX (such as W and Si, or Mo and S) but can be distinguished in XPS. As EDX signals could be generated with an electron beam, they can be acquired in SEM or STEM with micron-scale resolution, while normal XPS has beam spot size of >100 μm. Based on the above reasons, EDX was used less frequently for large-area ultrathin 2D semiconductors but for bulk or small-region characterisation.

EDX spectroscopy characterisation was carried out in the Zeiss Merlin field emission analytical SEM with Oxford instruments Xmax 150 EDX detector. The accelerating voltage was set at 5 keV and beam current was 200 pA. Deduction of background (mostly due to inelastic scattering of electrons with atom nucleus), peak fitting and composition analysis were done in the Aztec software.

### 3.5.5 Cathodoluminescence

Cathodoluminescence (CL) is similar to PL, only the specimen is not excited with photons but with high-energy electrons. In this way, semiconductors with large bandgaps such as GaS that cannot be excited by a 532 nm laser could show band-to-

band emission. More importantly, photon excitation emission in indirect semiconductors has low quantum efficiency as photons do not possess momentum and thus an additional phonon must participate in the process. However, in CL measurements, the incident electrons could transfer momentum to assist indirect band-to-band transition. In addition, as GaS is relatively less conductive, the high cross-section of the electron-hole creating process enables sufficient signal even for monolayer thickness. Thus, CL spectroscopy is applied in characterisation of the GaS bandgap.

The CL spectrum was obtained in a JEOL JSM-6500F SEM with a Gatan MonoCL3 system under an accelerating voltage of 5 kV in room temperature. Monolayer GaS (both defective and stoichiometric) continuous films on 300 nm $SiO_2$/Si substrates with size of 15*20 $\mu m^2$ were typically selected and scanned under fast scan mode for excitation. The emission spectrum signal was collected under a step size of 1 nm and a dwell time of 2 s. Spectrum on bare 300 nm $SiO_2$/Si substrate surface was also collected as background signal. The final GaS spectra were fitted with Lorentzian functions.

## 3.6 Device Measurement

### 3.6.1 Device Fabrication

To fabricate nano-optoelectronic devices based on 2D materials, electron-beam lithography (EBL, JEOL 5500 FS) is used for patterning over large area (Fig. 3.6a). A focused electron beam is employed to scan across the desired area for customised and high-resolution exposure of the photoresist. Both positive and negative photoresists could be used here. In the development process, the exposed positive photoresist undergoes bond weakening due to the electron-beam damage, thus the exposed

photoresist becomes more soluble under the presence of a developer. For negative photoresist, electron-beam radiation induces crosslinking of the photoresist, thus they appear less soluble during the development process. In this thesis, for the purpose of depositing metal contact pad onto 2D materials, positive photoresist is used. After revealing the pattern by the developer, an ultrathin metal film is deposited onto the sample in a slow and controlled way to avoid metal clustering or damage of the underlying 2D materials. Finally, the metal on remaining photoresist in the inverse pattern is lifted-off while metal contacts are left on the chip.

For a typical fabrication process, a bilayer PMMA positive photoresist is applied to form re-entrant sidewall for better lift-off process. 8 wt % PMMA-495K and 4 wt % PMMA-950K are spincoated subsequently onto the 2D material on a 300 nm $SiO_2/p^{++}$-Si substrate, both under 4500 rpm for 60 s and cured under 180 °C for 90 s, where the polymer with larger molecular weight is expected to be less soluble during the development process. After patterning using the EBL system, the sample is developed for 45 s using the conventional 1:3 MIBK/IPA developer. Subsequently, the samples are sent into a thermal evaporator (Edward 360; Fig. 3.6b) for metal deposition (10 nm Cr/50 nm Au), during which the required metal element is evaporated by Joule heating in high vacuum ($10^{-6}$ mbar) and slowly deposited onto the sample surface at 1 nm/s. Finally, the lift-off process is carried out by dipping the sample in acetone overnight at room temperature.

### 3.6.2 Electrical and Optoelectrical Measurements

Electrical and opto-electrical measurements of devices are performed using a home-built probe station (Fig. 3.6c) The device sample is placed on top of a movable stage

(in x, y, z directions), which controls the position of the nanodevice, assisted by a confocal microscope on top of it. Two tungsten tips (Signatone SE-T) are used to connect the source and drain electrodes of the device to a Keithley 2400 sourcemeter for conductance measurements. For field effect transistor (FET) characteristic measurements, the 300 nm $SiO_2$ layer is used as dielectric layer and the $p^{++}$-doped Si substrate is used as metal gate, which is connected to another Keithley 2400 sourcemeter through silver paste on the back side of the substrate. For optoelectronic measurements, various light sources are used in this study. Among them, the 532 nm diode-pumped solid-state laser (Thorlabs, DJ532-40) is coupled into the confocal microscope which is focused with a spot size of ~5 μm. LEDs with various wavelengths (Thorlabs, LED395L; RS components, C503B-BAN-CZ0A0451, C503B-GAN-CB0F0791, L-7113SYC-J3, C503D-WAN; Vishay, TLCR5800) are coupled into confocal microscope with a spot size of ~300 μm; 275 nm deep-UV LED (Thorlab M275L4) with independent lens systems focused into a spot size of ~200 μm. Power values of various light sources are recorded by a manually fixed power meter (Thorlab Optics PM100D, wavelength 200 nm–1000 nm) placed at the position of the device each time before measurement. All measurements are done in ambient atmosphere at room temperature.

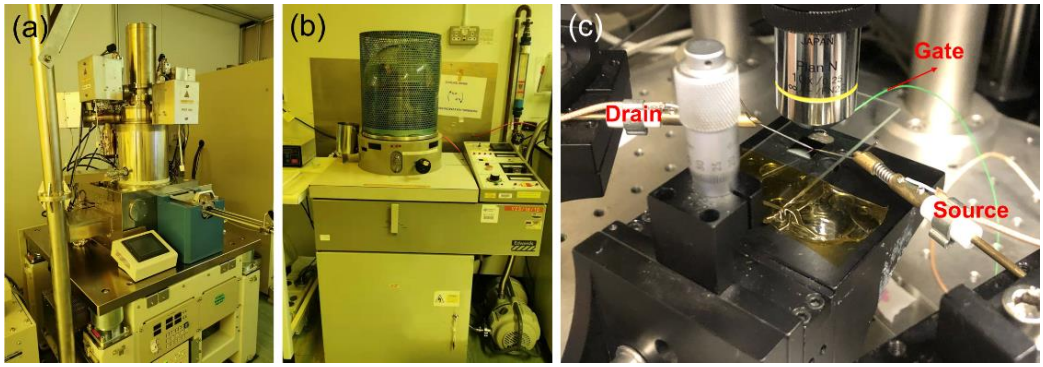



**Figure 3.6. Device fabrication and measurement setup.** (a) JEOL 5500 FS electron-beam lithography for patterning. (b) Edward 360 thermal evaporator system for metal deposition. (c) Probe station for device measurement.

## 3.7 References

1. Sheng, Y.; Xu, W.; Wang, X.; He, Z.; Rong, Y.; Warner, J. H., Mixed Multilayered Vertical Heterostructures Utilizing Strained Monolayer $WS_2$. *Nanoscale* **2016**, *8*, 2639-2647.

2. Rong, Y.; Fan, Y.; Leen Koh, A.; Robertson, A. W.; He, K.; Wang, S.; Tan, H.; Sinclair, R.; Warner, J. H., Controlling Sulphur Precursor Addition For Large Single Crystal Domains of $WS_2$. *Nanoscale* **2014**, *6*, 12096-13103.

3. Bing, D.; Wang, Y.; Bai, J.; Du, R.; Wu, G.; Liu, L., Optical Contrast for Identifying the Thickness of Two-Dimensional Materials. *Optics Communications* **2018**, *406*, 128-138.

4. Li, H.; Wu, J.; Huang, X.; Lu, G.; Yang, J.; Lu, X.; Xiong, Q.; Zhang, H., Rapid and Reliable Thickness Identification of Two-Dimensional Nanosheets Using Optical Microscopy. *ACS Nano* **2013**, *7*, 10344-10353.

5. Lee, C.; Yan, H.; Brus, L. E.; Heinz, T. F.; Hone, J.; Ryu, S., Anomalous Lattice Vibrations of Single- and Few-Layer $MoS_2$. *ACS Nano* **2010**, *4*, 2695-2700.

6. Zhou, K.-G.; Withers, F.; Cao, Y.; Hu, S.; Yu, G.; Casiraghi, C., Raman Modes of $MoS_2$ Used as Fingerprint of van der Waals Interactions in 2-D Crystal-Based Heterostructures. *ACS Nano* **2014**, *8*, 9914-9924.

7. Chakraborty, B.; Bera, A.; Muthu, D. V. S.; Bhowmick, S.; Waghmare, U. V.; Sood, A. K., Symmetry-Dependent Phonon Renormalization in Monolayer $MoS_2$ Transistor. *Phys. Rev. B* **2012**, *85*, 161403.

8. Ganatra, R.; Zhang, Q., Few-Layer $MoS_2$: A Promising Layered Semiconductor. *ACS Nano* **2014**, *8*, 4074-4099.

9. Peimyoo, N.; Shang, J.; Yang, W.; Wang, Y.; Cong, C.; Yu, T., Thermal Conductivity Determination of Suspended Mono- and Bilayer $WS_2$ by Raman Spectroscopy. *Nano Res.* **2014**, *8*, 1210-1221.

10. Late, D. J.; Liu, B.; Matte, H.; Rao, C. N. R.; Dravid, V. P., Rapid Characterization of Ultrathin Layers of Chalcogenides on $SiO_2$/Si Substrates. *Adv. Funct. Mater.* **2012**, *22*, 1894-1905.

11. Zeng, H.; Zhu, B.; Liu, K.; Fan, J.; Cui, X.; Zhang, Q. M., Low-Frequency Raman Modes and Electronic Excitations in Atomically Thin $MoS_2$ Films. *Phys. Rev. B* **2012**, *86*, 241301.

12. Conley, H. J.; Wang, B.; Ziegler, J. I.; Haglund, R. F., Jr.; Pantelides, S. T.; Bolotin, K. I., Bandgap Engineering of Strained Monolayer and Bilayer $MoS_2$. *Nano Lett.* **2013**, *13*, 3626-3630.

13. John, M.; Quan, M.; M., O. P.; Miguel, I.; Duy, L.; Edwin, P.; David, B.; Koichi, Y.; Gretel, v. S. P.; Andrew, N.; Tai, T.; Michelle, W.; Ariana, N.; Velveth, K.; Sarah, B.; Dezheng, S.; F., H. T.; S., R. T.; Roland, K.; Ludwig, B., 2-Dimensional Transition Metal Dichalcogenides with Tunable Direct Band Gaps: $MoS_{2(1-x)}Se_{2x}$ Monolayers. *Adv. Mater.* **2014**, *26*, 1399-1404.

14. Mouri, S.; Miyauchi, Y.; Matsuda, K., Tunable Photoluminescence of Monolayer $MoS_2$ via Chemical Doping. *Nano Lett.* **2013**, *13*, 5944-5948.

15. McCreary, K. M.; Hanbicki, A. T.; Sivaram, S. V.; Jonker, B. T., A- and B-Exciton Photoluminescence Intensity Ratio as A Measure of Sample Quality for Transition Metal Dichalcogenide Monolayers. *APL Mater.* **2018**, *6*, 111106.

16. Splendiani, A.; Sun, L.; Zhang, Y.; Li, T.; Kim, J.; Chim, C.-Y.; Galli, G.; Wang, F., Emerging Photoluminescence in Monolayer $MoS_2$. *Nano Lett.* **2010**, *10*, 1271-1275.

17. Peimyoo, N.; Yang, W.; Shang, J.; Shen, X.; Wang, Y.; Yu, T., Chemically Driven Tunable Light Emission of Charged and Neutral Excitons in Monolayer $WS_2$. *ACS Nano* **2014**, *8*, 11320-11329.

# Chapter 4

# Facile, Uniform and Low-Cost Growth of Large Monolayer $MoS_2$ Single Crystals

## 4.1 Introduction

As one of the most studied 2D semiconductors with small bandgaps, considerable efforts have been made to achieve large-scale synthesis of high-quality $MoS_2$ monolayers.[1-3] Chemical vapour deposition (CVD) and other similar methods have been known to produce high quality $MoS_2$ suitable for device fabrication.[4-8] However, in such systems where the nucleation and growth of 2D crystals is significantly affected by the transport of precursors in the vapour phase, it is challenging to achieve large-area uniformity due to the consumption of precursors along the gas flow direction or the geometric effect of chamber and substrate on flow rate.[9] While scalability can be improved by increasing the mean free path of gas molecules under vacuum or low-pressure environment,[10-13] the requirement of a low-pressure system and relatively long growth times hindered its application in mass production. On the other hand, the direct sulfurization method, where a thin layer of pre-deposited metal precursor undergoes in-situ sulfurization, possesses the potential to achieve large-scale uniformity.[14-18] However, the synthesised $MoS_2$ often suffers from poor quality. One challenge is that multilayer regions are almost inevitable,[19-21] because it is usually difficult to precisely control the thickness of pre-deposited precursor due to particle aggregation effects. A more severe problem is that the grain size is usually limited to the nanoscale due to

sudden burst of nucleation at the beginning of sulfurization,[22] which will result in poor device performance. Several improvements have been proposed, such as the deposition of uniform precursors via atomic layer deposition,[23] or the sulfurization of $MoO_2$ single crystals,[24] etc., but the grain size is still restricted to ~10 μm.

The key obstacles towards achieving monolayer growth and high crystallinity in the direct sulfurization method lie in a) the tendency to aggregate of pre-deposited metal precursors, and b) the excess amount of metal precursors on the substrate to the amount of sulfur from the vapour phase. To address these problems, the influence of the underlying substrate must be considered. Previous reports on direct sulfurization methods use inert substrates such as commercial $SiO_2$/Si or sapphire. These substrates are stable at high temperature, but make no contribution to the reaction.

I proposed that a substrate with certain solubility of pre-deposited precursors would solve these problems by forming uniform distributions of metal precursors on the substrate to eliminate the formation of aggregates and to avoid uncontrolled reaction between excess pre-deposited precursor and sulfur. Two requirements must be satisfied for such substrates: the precursor can dissolve into the substrate; and on encountering sulfur, the dissolved precursor near the surface of substrate can react to form the corresponding TMDs. Recently, Ju et al.[25] reported the synthesis of strictly monolayer $MoS_2$ crystals by using glass substrates in a CVD system to incorporate excess $MoO_3$ on the surface. They demonstrated that stable $MoO_4^{2-}$ is formed and it diffused gradually from the surface into the bulk glass. Very recently, it was also proved that liquid $Na_2MoO_4$/$Na_2Mo_2O_7$ droplets on NaCl crystals can form $MoS_2$ monolayer nanoribbons with sulfur vapour.[26] In addition, low-cost and transparent glass has been demonstrated as an excellent candidate for growing $MoS_2$ for photonic applications in recent years. For example, Chen et al.[27] presented the growth of millimetre scale $MoS_2$

on molten glass at 1050 °C as a result of low nucleation density and low migration barrier on a homogeneous liquid surface. The same group also studied the growth of highly organised TMD patterns on glass.[28] Yang et al.[29] also discovered that trace amounts of Na in the glass may act as growth catalysts. However, to my knowledge, no one has ever proposed the use of precursor-soluble substrates for the synthesis of $MoS_2$ before publication of this work in Dec 2018.

Herein, low-cost glass is used as precursor-soluble substrate for facile synthesis of large-area uniform monolayer $MoS_2$ crystals via a modified direct sulfurization method. Owing to the glass's unique ability to incorporate pre-deposited $MoO_3$ on the surface, large-size monolayer $MoS_2$ single crystals are obtained rather than nanoscale small particles. Raman and photoluminescence (PL) spectroscopy and scanning transmission electron microscopy (STEM) were further used to demonstrate its high quality. A series of experiments were designed to confirm the incorporation of $MoO_3$ into glass and a detailed discussion of the kinetics is presented to help understand the scalability of the method. A field effect transistor (FET) was fabricated based on the synthesised $MoS_2$ to demonstrate its potential application in electronics and optoelectronics. The first use of precursor-soluble substrate in this method combines the merits of both scalability and simplicity from direct sulfurization method and high-quality resultants from CVD method, and exhibits excellent tolerance to environmental fluctuations, therefore should be suitable for industrial mass production.

## 4.2 Results and Discussions

### 4.2.1 Self-Limiting Sulfurization at Vapour-Solid Interface

As illustrated in Figure 4.1a, the $MoS_2$ grown by direct sulfurization methods on inert substrates ($SiO_2$/Si) would form multilayer regions and small grain size due to the aggregation of precursors and the burst of nucleation. However, the use of substrates (glass) with certain solubilities of precursor can dramatically change the behaviour of pre-deposited precursors and allow for better control of the morphology of $MoS_2$. As shown in Figure 4.1b, an annealing stage is designed which allows the pre-deposited $MoO_3$ to fully dissolve into the glass substrate, forming small molecule-like Mo species such as $MoO_x$ (x=3,4). Since glass has a low viscosity under the annealing temperature, these small molecules can diffuse easily from Mo-rich regions to the surrounding Mo-deficient regions, resulting in a homogeneous distribution of Mo species across the substrate. In addition, the diffusion of Mo species from the surface into the bulk glass leads to a decrease in surface Mo concentration. Therefore, at a later stage when the S vapour is introduced and absorbed onto the surface, the homogeneous distribution and low concentration of Mo species on the surface results in a uniform and low nucleation density across the substrate, and the absence of large $MoO_3$ particles avoids the formation of multilayer $MoS_2$ nucleus. With the consumption of Mo species near the surface, the Mo species that have diffused into the bulk glass would gradually flow back onto the surface due to the concentration gradient, forming a continuous feeding of precursor from the inside of the glass substrate. In other words, the supply of Mo species for reaction is always kept at a slow rate and will facilitate the self-limiting growth of monolayer $MoS_2$ crystals with large grain size.

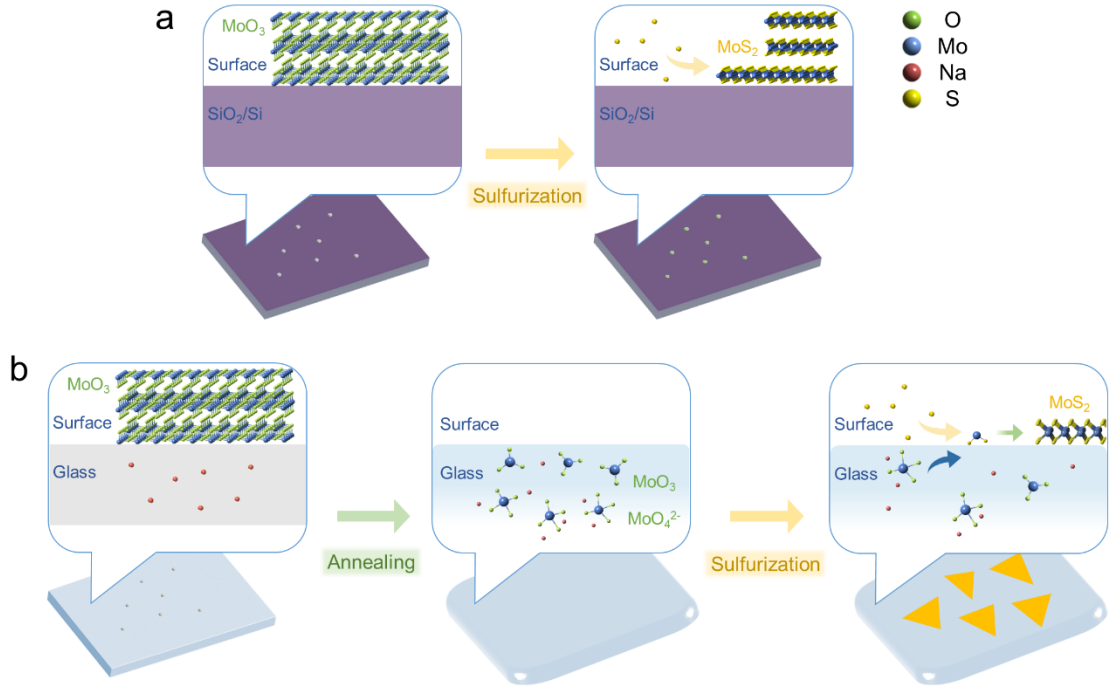



**Figure 4.1. Effect of substrate on direct sulfurization method.** (a) Schematic illustration of direct sulfurization of $MoO_3$ on $SiO_2$/Si with thick regions and small grains. (b) Schematic illustration of the incorporation of $MoO_3$ into glass and following sulfurization process.

To examine the proposed hypothesis, a modified direct sulfurization method was designed with an emphasis on simplicity and scalability. Figure 4.2a shows a schematic illustration of the processes for the modified direct sulfurization method, which consisted of two parts: the pre-deposition of $MoO_3$ onto the substrate and the sulfurization of the $MoO_3$/substrate into $MoS_2$. Normally, the pre-deposition of $MoO_3$ is achieved by careful control of thermal evaporation in vacuum environment or other sophisticated methods, to precisely control the thickness of deposited films. Here, to demonstrate the advantage that no requirement of thickness uniformity is needed during pre-deposition in this modified direct sulfurization method, a simple spin-coating process with $MoO_3$/$NH_4OH$ solution at 4500 rpm for 1 min is employed. Ammonium

hydroxide ($NH_4OH$) has proven to be a very good solvent for $MoO_3$ by forming the highly soluble $(NH_4)_2MoO_4$, which is very helpful in adjusting the amount of $MoO_3$ spin-coated onto the surface.[8] In addition, it would fully decompose into $MoO_3$ and $NH_3$ at 500 °C before the reaction takes place, hence the precursor can be regarded as $MoO_3$. Then, the sulfurization is conducted in a home-built two-furnaces CVD system with a 1-inch quartz tube so that the temperature of the substrate and sulfur regions can be controlled separately. 300 mg S powder is placed in the centre of the furnace upstream to create abundant sulfur atmosphere while the pre-deposited $MoO_3$/substrate is placed in the centre of the furnace downstream, supported by a ceramic boat. The heating profile of a typical experiment is shown in Figure 4.2b. The tube is first flushed with 500 sccm argon gas for 30 min. Then pre-deposited $MoO_3$/substrate is heated up at 40 °C/min (Stage I) until it reached 840 °C. It stays at this temperature for 5 minutes, which is called as the annealing stage (Stage II). After that, sulfur is heated to 180 °C to be introduced into the system (Stage III). The sulfurization is complete in 5 minutes, which is consistent with the reported ultrafast growth speed of $MoS_2$ on glass. At the end of growth, both furnaces are cooled down to room temperature (Stage IV). 150 sccm Ar is used as the carrier gas throughout the whole four stages.

The experimental results on $SiO_2$/Si and glass substrates under exactly the same conditions agree well with the proposed hypotheses. SEM images (Fig. 4.2c, f) of pre-deposited $MoO_3$ on both substrates showed island-like uneven distribution of precursor. The sulfurization of these precursor islands on $SiO_2$/Si substrate demonstrated the disadvantages of traditional direct sulfurization method. As shown in SEM and optical images (Fig. 4.2d-e), the obtained multilayer $MoS_2$ crystals on $SiO_2$/Si substrate were mostly restricted to nanoscale, with small nanoparticles sitting in the middle of each domain. In comparison, the $MoO_3$ particles on glass disappeared after the annealing

process under SEM (Fig. 4.2g), leaving a very uniform surface. X-ray photoelectron spectroscopy (XPS) analysis was also performed on the annealed $MoO_3$/glass. Surface analysis of the binding energy showed two sets of Mo(VI) 3d peaks ($3d^{3/2}$ and $3d^{5/2}$), which corresponded to $Na_2MoO_4$ (with $3d^{5/2}$ peak at 232.04 eV) and $MoO_3$ (with $3d^{5/2}$ peak at 232.54 eV) respectively,[15, 30-31] demonstrating strong interactions between precursor and glass (Fig. 4.2h). Depth profile analysis of the glass also observed the existence of Mo-species inside the glass (Fig. 4.3), which confirmed that the precursor can be incorporated into the glass under the high annealing temperature. In addition, the XPS spectra show increasing ratio of Mo(IV) species with increasing etching time that are likely to be $MoO_2$ and $MoSi_2$. The Mo(IV) species is formed probably due to ion-induced reduction during the etching process, [32-34] as chemical reduction of $MoO_3$ to both $MoSi_2$ and $MoO_2$ are reported to require strong reduction agents such as Al, C powder or $H_2$, CO gases, which are not likely to occur in the glass.[47-48]

Hence, despite the uneven distribution of $MoO_3$ particles after spin-coating, the $MoS_2$ grown on glass showed large and perfect triangular domains with the size of over 80 μm (Fig. 4.2i-j). The strictly triangular shape of the crystals is attributed to the low migration barrier on molten glass that enables the active species to migrate and find the most energy-favourable sites. No contrast is observed in both images of the crystal, indicating the absence of multilayer regions. Figure 4.2k shows the low-magnified SEM image of $MoS_2$ grown on glass, demonstrating large-scale uniformity of this modified direct sulfurization method. In addition, statistical analysis of more than 100 triangles in a randomly selected region showed that the edge length is mostly in the range of 50−100 μm, with an average edge length of 75 μm and a standard deviation of only 17 μm, indicating the obtained $MoS_2$ crystals are highly uniform in size (Fig. 4.2l).

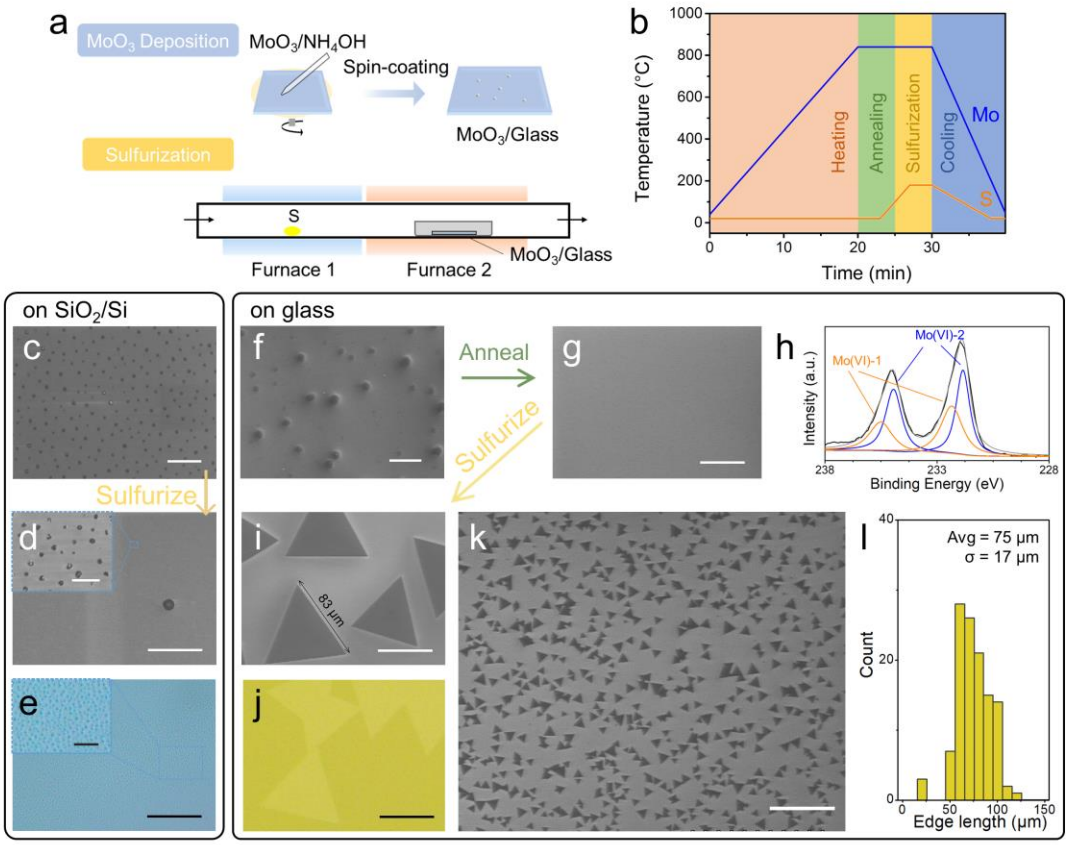



**Figure 4.2. Synthesis of $MoS_2$ on $SiO_2$/Si substrate and glass.** (a) Schematics of pre-deposition of $MoO_3$ on glass and sulfurization of $MoO_3$. (b) Heating profile for a typical sulfurization process. (Stage I: Heating; Stage II: annealing; Stage III: Sulfurization; Stage IV: Cooling.) (c) SEM image of pre-deposited precursor on $SiO_2$/Si substrate; scale bar 2 μm. (d-e) SEM and optical images of $MoS_2$ on $SiO_2$/Si substrate by sulfurization; scale bars: 50 μm. The insets show zoomed-in pictures of selected regions; scale bars represent 2 μm for (d) inset and 10 μm for (e) inset, respectively. (f) SEM image of pre-deposited precursor on glass substrate; scale bar 20 μm. (g) SEM image of precursor/glass after annealing at 840 °C. (h) XPS spectrum of annealed $MoO_3$/glass showing Mo(VI) species. The two sets of Mo 3d peaks are fitted and assigned to $MoO_3$ (orange) and $Na_2MoO_4$ (blue), respectively. (i-j) SEM and optical images of $MoS_2$ grown on glass substrate by the modified direct sulfurization method; scale bar: 50 μm. (k) Low-magnitude SEM image of $MoS_2$ grown on glass substrate; scale bar: 500 μm. (l) Histogram of edge length of 117 triangles in a randomly selected area from (k).

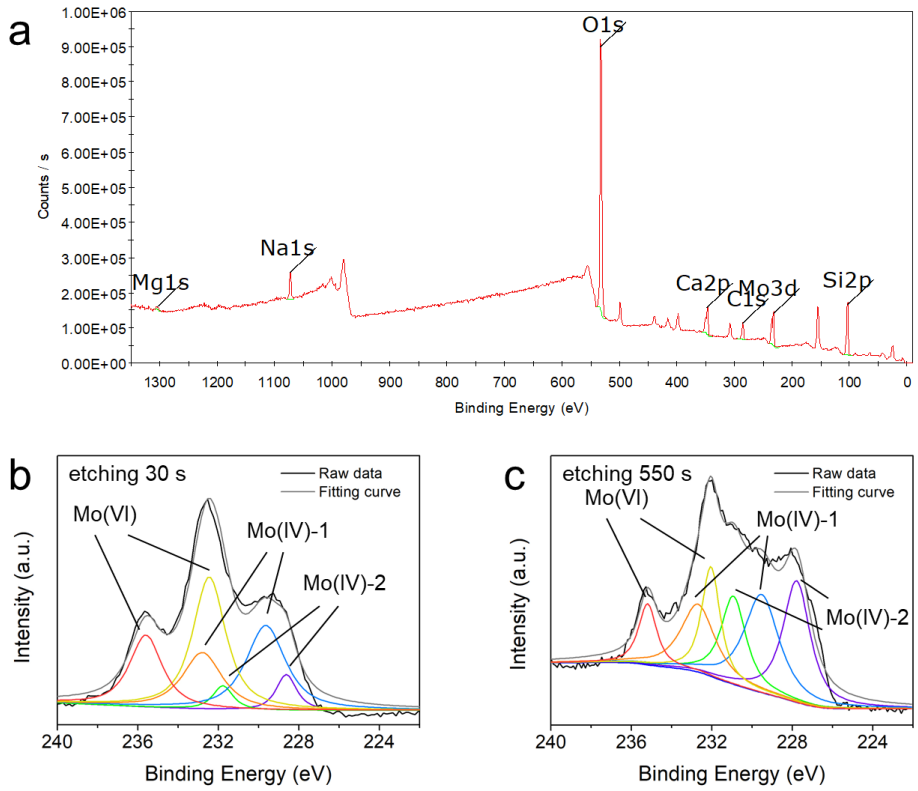



**Figure 4.3. XPS characterisation of glass substrate after annealing with Mo-precursors.** (a) XPS survey spectrum of glass surface. (b, c) XPS spectra and fitting of Mo 3d binding energy during different etching stages. Due to ion-induced reduction, two Mo(IV) peaks emerge which are assigned to $MoO_2$ (with $3d^{5/2}$ peak at 229.53 eV) and $MoSi_2$ (with $3d^{5/2}$ peak at 227.79 eV), and they increase with etching time,[32-34] while the percentage of Mo(VI) species decreased from 52% (t = 30 s) to 23% (t = 550 s).

The synthesis of $MoS_2$ crystals with such large-scale uniformity is rarely reported in atmospheric pressure VPD synthesis. Normally, in horizontal-flow CVD methods, the size and coverage of $MoS_2$ crystals vary significantly from centre to side, and from upstream to downstream areas. It is generally considered that there are five steps involved in the CVD reaction: (a) sublimation of precursor in the upstream; (b) diffusion of precursor in the bulk vapour phase across the boundary layer and absorption onto surface; (c) surface reaction and diffusion of active species; (d)

attachment of active species to growth sites; (e) desorption of excess active species and diffusion across the boundary layer into bulk vapour phase. Usually, in systems with a high reaction temperature under atmospheric pressure, the surface diffusion step is fast, and the mass transport of precursor steps is considered as the rate-limiting step due to short mean free path of precursor molecules. The diffusion of precursor from bulk vapour phase to surface is governed by Fick's first law,

$$F_{mass\ transport} = D_{gas} \times \frac{C_{gas} - C_{surface}}{\delta} \tag{4.1}$$

where $D_{gas}$ is the diffusivity of the precursor in gas, $C_{gas}$ and $C_{surface}$ is the concentration of precursor in the gas phase and on the surface, and $\delta$ is the thickness of the boundary layer. In the CVD system, the thickness of boundary layer is very sensitive to the local gas flow rate, which is closely related to the geometry of gas flow, chamber and substrate. Furthermore, the concentration of precursor in the gas phase continues to decrease from upstream to downstream due to the consumption along the gas flow. Hence, the growth kinetics in different areas of the substrate differ from each other, leading to inevitable variations in the morphology of obtained 2D crystals. In this modified direct sulfurization method, however, the kinetics are quite different. Since the sulfur supply is generally considered as sufficient in this condition, and the diffusion and reaction rate on glass surface is reported to be much faster than on common insulating substrate, the slow supply of Mo species from inside the glass can be reckoned as the rate-limiting step. Inside the glass, Fick's first law can be expressed as follow:

$$F_{mass\ transport} = D_{glass} \times \frac{C_{bulk} - C_{surface}}{\Delta x} \tag{4.2}$$

where $D_{glass}$ is the diffusivity of precursor in glass, $\frac{C_{bulk} - C_{surface}}{\Delta x}$ represents the concentration gradient of Mo species near the surface of the glass during reaction.

Intriguingly, the rate limiting step of the reaction is no longer influenced by factors related to gas flow, but only to the local concentration gradient of Mo in glass, which is homogeneous across the substrate after the annealing stage. In other words, the scalability of this 'substrate-supply' method can only be limited by the size of the substrate. As a demonstration, the synthesis of uniform $MoS_2$ in the 1-inch system has already been achieved on a 2*5.5 $cm^2$ substrate (Fig. 4.4), and larger-area uniformity could be achieved with larger reaction system and substrate.

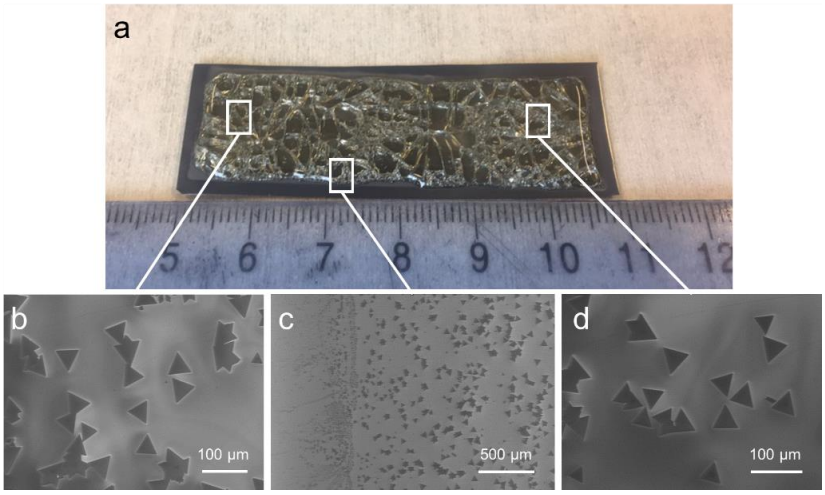



**Figure 4.4. Growth of uniform $MoS_2$ on a 2*5.5 $cm^2$ substrate.** (a) Photograph of the as-synthesised $MoS_2$ on glass supported by a Mo foil. The glass cracked during cooling due to difference in thermal expansion coefficient between glass and the Mo foil. A more suitable supporting layer would solve the problem. (b-d) SEM images from different areas of substrate, showing a large-area uniformity.

### 4.2.2 Morphological Control of $MoS_2$ Crystals

To further examine the proposed growth kinetics in this modified direct sulfurization method, a series of controlled experiments was conducted aiming to optimise the dissolution and precipitation behaviour of precursor in the glass. The results are presented in Figure 4.5a-f, with accompanying statistics of average nucleation density

(assuming no grain boundaries in each perfect triangle), average crystal size and average coverage to show the trends. Schematics were also drawn to illustrate the influence of these parameters on the distribution of the Mo-species in the glass, which is supported by XPS depth profile results (Fig. 4.5g-j). By varying the temperature for annealing and sulfurization from 760 °C to 840 °C, an increase in crystal size and a decrease in nucleation density was observed. One speculated reason for this phenomenon is the formation of a more homogeneous surface under higher temperature, which reduces the nucleation density. In addition, a higher temperature would decrease the viscosity of glass (μ). According to Stokes-Einstein equation ($D \propto T/\mu$), a higher temperature leads to a higher $D_{glass}$. As a result, the diffusion of precursors into the glass during the annealing stage is accelerated and the remaining $MoO_3$ on the surface is reduced (Fig. 4.5i), which further decreased the nucleation density at the beginning stage. Further increasing the temperature would continue to decrease the $MoO_3$ concentration on the surface, but the high diffusivity could also lead to a higher back-flow rate of Mo species, which may extend the nucleation stage and increase the nucleation density. This explains why the nucleation density of $MoS_2$ grown at 880 °C is very similar to that at 840 °C. At all growth temperatures, the surface coverage is nearly unaffected, which indicates that almost all the $MoO_3$ deposited on the glass is absorbed into the glass and is almost depleted by the sulfurization process. This was also confirmed by reacting the glass after transfer with sulfur again, and very few $MoS_2$ domains were seen after this second sulfurization. Another parameter that affects the distribution of Mo precursor in glass is the annealing time. As shown in Figure 4.5c-d, a similar trend of decrease in nucleation density and increase in crystal size is observed with the extension of annealing time. Without the annealing stage, many $MoO_3$ particles stay on the surface, hence a burst of nucleation appears and multilayer regions form.

By extending the annealing time, a more homogeneous distribution of $MoO_3$ is achieved inside the glass and the surface Mo concentration is decreased (Fig. 4.5i). Therefore, the nucleation density is reduced by more than 3 orders of magnitude, thus increasing the average crystal size from several μm to over 80 μm. However, prolonging the annealing time also leads to decrease in coverage, possibly due to the escape of $MoO_3$ into the gas phase at high temperature. Finally, the surface coverage of $MoS_2$ can be easily adjusted by the pre-deposited amount of $MoO_3$, which is represented by the concentration of $MoO_3/NH_4OH$ solution used for spin-coating (Fig. 4.5e). It can be seen from Figure 4.5f that the nucleation density slowly increases along with the $MoO_3$ concentration due to higher amount of $MoO_3$ present at the surface. It is interesting to see that the crystal size remains about 50 μm at a coverage of 53%, and the average crystal size can reach more than 100 μm at a smaller coverage. These results are not only the highest reported by direct sulfurization, but also comparable to most CVD-based results. These findings and analysis were also supported by depth profiles of annealed $MoO_3$/glass. As shown in Figure 4.5g, the $MoO_3$/glass pre-deposited with 15 mM solution and annealed for 2 min showed a steep decrease in concentration of Mo-species from surface to bulk. In comparison, the $MoO_3$/glass pre-deposited with 200 mM solution and annealed for 15 min showed a much higher amount of Mo-species dissolved in glass, and a stable Mo concentration near surface followed a steadier decrease into bulk glass. The two depth profile curves are in good accordance with the schematics in Figure 4.5i, and also indicate that the solubility of Mo-species in molten glass is about ~22 % at the annealing temperature.

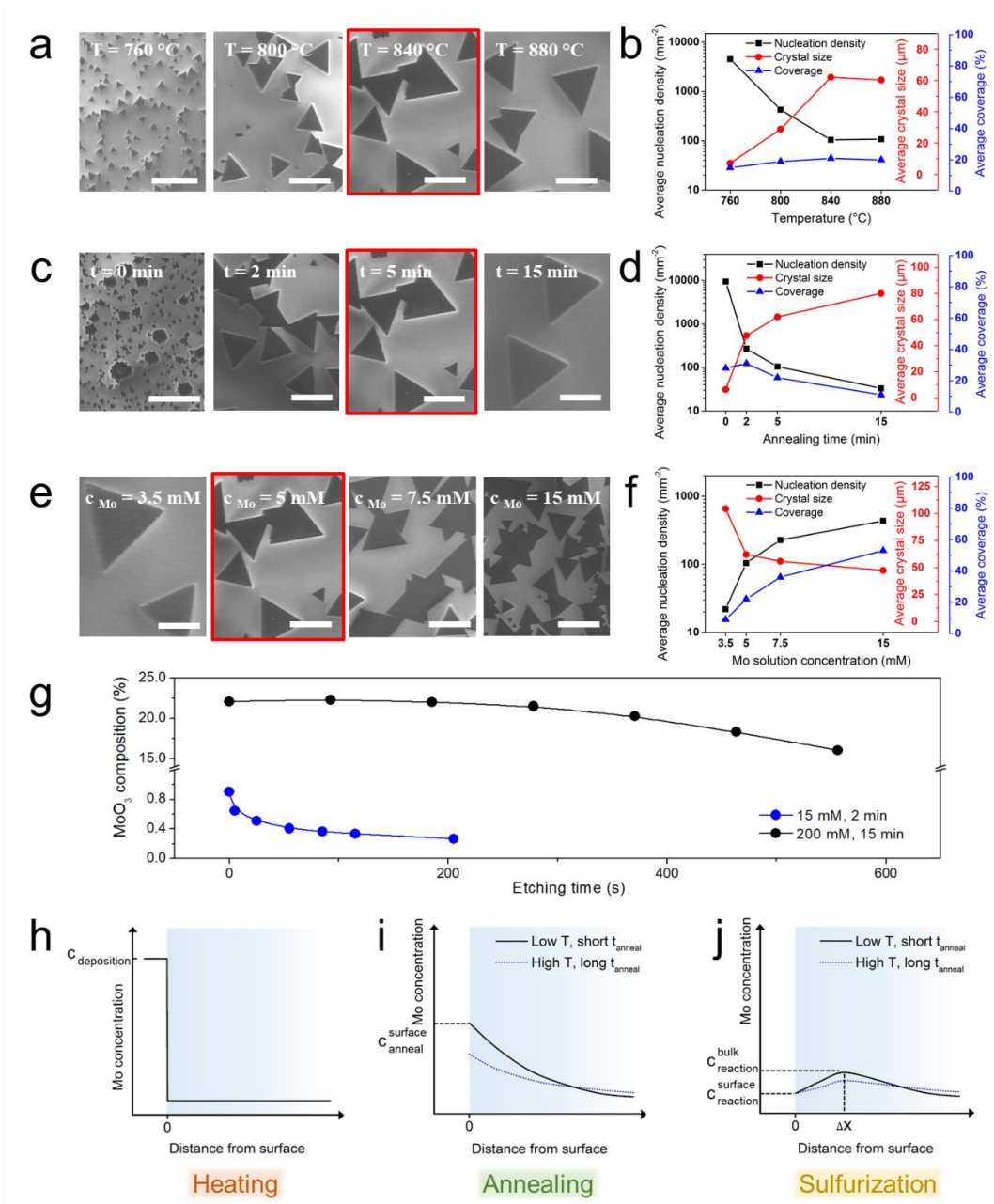



**Figure 4.5. SEM images of $MoS_2$ grown under various conditions.** (a) $MoS_2$ grown under different annealing and growth temperature form 760 °C to 880 °C. (c) $MoS_2$ grown under different annealing time from 0 min to 15 min. (e) $MoS_2$ grown spin-coated with different $MoO_3$ solution concentrations from 3.5 mM to 15 mM. Scale bars: 50 μm. (b, d, f) Accompanied extracted average nucleation density, average coverage, and average crystal size as a function of the corresponding conditions on the right. (g) XPS depth profile of $MoO_3$ composition in glass after annealing at 840 °C. (h-j) Hypothetical Mo species concentration in glass during heating, annealing and sulfurization processes, respectively.

Besides tuning the substrate-related properties, growth of ultralarge $MoS_2$ single crystals is achieved by further optimising the reaction process with thesulfur precursor. Successful growth of ultralarge single crystals demands very low nucleation density, which is analysed to be greatly reduced by a low concentration of Mo species at the surface when sulfur is introduced. Consequently, the concentration of sulfur species can also affect the nucleation rate in such a sulfurization reaction. According to the LaMer burst nucleation theory,[35] nucleation occurs only at the initial stage when precursor concentrations are high. After the precursor concentration drops below a critical value, nucleation stops and the remaining precursors attach to existing nuclei to enlarge the crystals. Thus, adjustment to the following parameters is proposed: First, a higher Mo concentration (50−60 mM) is required for sufficient precursor supply for growth of large single crystals. Second, with higher Mo concentration, a longer annealing time (>10 min) is applied to guarantee complete dissolution. Most importantly, the sulfur temperature profile is divided into two stages: nucleation and growth (Fig. 4.6a). In the first stage, sulfur is heated to 120 °C (just beyond its melting point at 115 °C) for a well-controlled slow nucleation process. After 10 min, the Mo concentration at the glass surface is expected to drop to the growth regime, when the sulfur temperature is raised to 150 °C to complete the growth. The results are shown in Figure 4.6b-c, where millimetre-sized monolayer $MoS_2$ single crystals are obtained. For crystals with average edge length of ~400 μm, the morphology remains perfect triangular. In comparison, crystals with average edge length of ~600 μm shows three-point star shape. According to study on edge terminations,[36] the perfect triangular shape is associated with Mo:S precursors ratio of 1:2, while the three-point star shape suggest Mo:S ratio of over 1:2, which agrees with the observation here that less sulfur precursor leads to

smaller nucleation density and larger crystals size. Such large $MoS_2$ single crystals are challenging to grow even through careful controlled CVD processes. In addition, the surface coverage is over 76%. Further tuning of nucleation density and Mo concentration could lead to growth of continuous monolayer films, but a different glass substrate with low thermal expansion is required to avoid crack of $MoS_2$ at its grain boundaries during the cooling process.

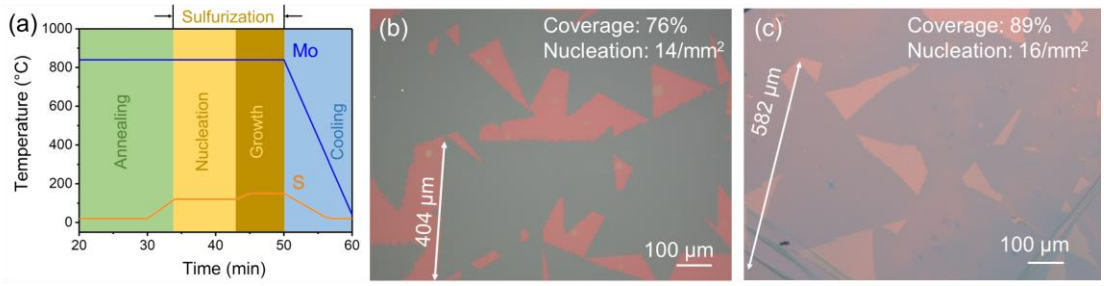



**Figure 4.6. Growth of ultralarge $MoS_2$ single crystals.** (a) Heating profile for growth of ultralarge $MoS_2$ single crystals. (b) Optical image of 400 μm size $MoS_2$ single crystals by increasing Mo concentration and decreasing sulfur temperature. (c) Optical image of 600 μm size $MoS_2$ single crystals by further increasing Mo concentration and decreasing sulfur temperature.

### 4.2.3 Characterisation and Properties of $MoS_2$ Crystals

To assess the quality of $MoS_2$ synthesised by this method, annular dark field scanning transmission electron microscopy (ADF-STEM) was used to directly reveal the crystal structure of the material. The ADF-STEM image (Fig. 4.7a) shows the monolayer $MoS_2$ sheet is well-synthesised and hexagonal lattices of $MoS_2$ with bright spots representing Mo atoms and dim spots representing two stacked S atoms can be seen. The diffractogram in the inset of Figure 4.7a also represents perfect hexagonal lattice of $MoS_2$. No grain boundary was observed in the observed region. Figure 4.7b shows a

lower magnification image with a small hole in the lattice, revealing the $MoS_2$ is a monolayer. These results confirm the high crystalline quality of the synthesised $MoS_2$.

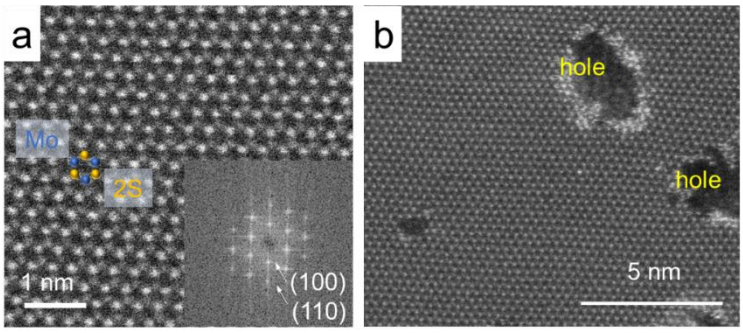



**Figure 4.7. STEM characterisation of $MoS_2$.** (a) Atomic resolution ADF-STEM images of the structure of monolayer $MoS_2$ with corresponding FFT pattern as inset. The bright spots are Mo atoms, and the dim spots are two S atoms. (b) ADF-STEM image of $MoS_2$ with holes showing its monolayer nature.

Raman and PL spectroscopies with a 532 nm laser were further performed to determine the layer thickness, the crystal quality and uniformity of the $MoS_2$ crystals on glass. Figure 4.8a shows the typical Raman spectrum of $MoS_2$, with two characteristic Raman modes of $MoS_2$, $E^1_{2g}$ and $A_{1g}$, respectively. A statistical analysis of the Raman signals from 46 different $MoS_2$ triangles over the glass substrate is presented in Figure 4.8b, with an average $E^1_{2g}$ peak position at 384.39 $cm^{-1}$ and average $A_{1g}$ peak position at 403.60 $cm^{-1}$. These results with a small deviation of less than 0.2 % indicate that the quality of $MoS_2$ at different places of the substrate is identical. An average frequency difference of 19.21 $cm^{-1}$ indicates the monolayer nature of the $MoS_2$ crystal. This is further confirmed by the PL spectrum of the $MoS_2$ crystal with a direct bandgap shown in Figure 4.8c. It is known that the PL spectrum of intrinsic monolayer $MoS_2$ has a strong A peak at 1.85 eV and a moderately strong B peak at 2.00 eV,[37] which corresponds to exciton emission from two different direct transitions within the

bandgap, and also a third $A^-$ peak, which has a slightly lower energy than the A peak and can be associated with the recombination of trions (an electron bounded with A exciton).[38] Multiple Lorentzian fitting of a typical PL spectrum of $MoS_2$ on glass showed three peaks with red-shifted positions which are assigned to $A^-$ (1.75 eV), A (1.80 eV), B (1.94 eV), respectively. It is believed that the peak position is easily affected by various factors including strain, temperature and doping level. Here, the red shift of all three peaks could be attributed to the strain effect by the difference in thermal expansion coefficient between glass and the as-grown $MoS_2$.[39] In addition, a small $A^-$ peak indicated low doping level from the substrate.[40] Mapping of the Raman frequency difference and PL peak intensity of a $MoS_2$ crystal with an edge length over 100 μm (Fig. 4.8d-f) further confirms the homogeneous uniformity of the crystal's quality within a large monolayer domain.

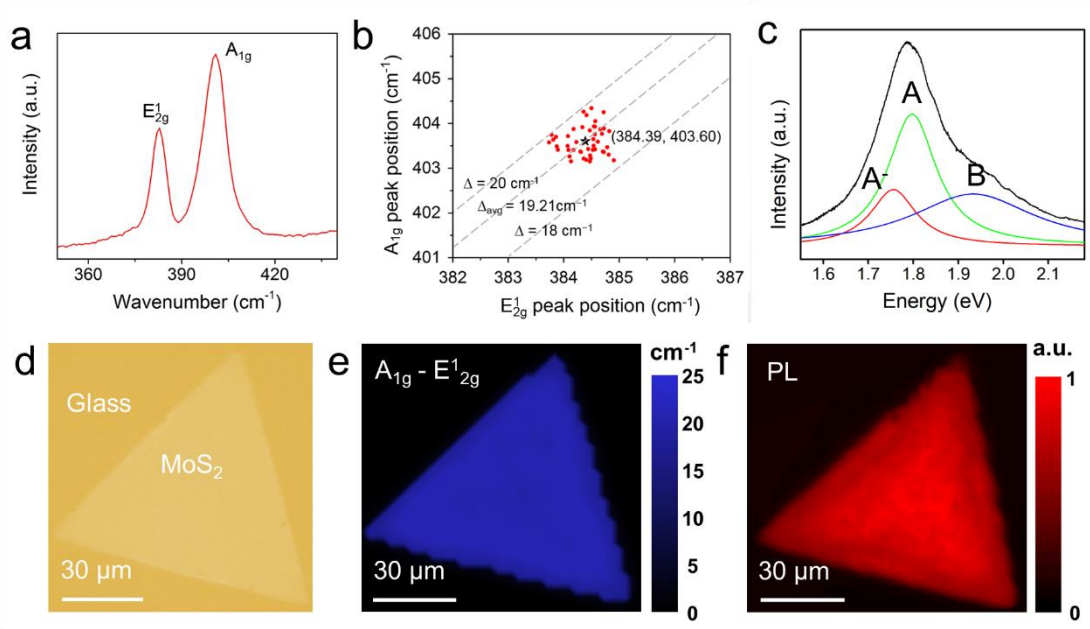



**Figure 4.8. Optical characterisation of $MoS_2$.** (a) Raman spectrum of a typical crystal. (b) Raman $E^1_{2g}$ and $A_{1g}$ peak positions from 46 randomly selected $MoS_2$ crystals, which confirms it is monolayer. (c) PL spectrum of $MoS_2$ with multipeak Lorentzian fitting. (d-f) Optical image,

corresponding Raman peak difference and PL intensity mapping of a typical $MoS_2$ crystal with edge length over 100 μm.

In order to further evaluate the quality of the $MoS_2$ and its potential applications in electronics and optoelectronics, a field effect transistor (FET) device was fabricated by transferring the as-grown $MoS_2$ onto a $SiO_2$/Si substrate prepatterned with Au electrodes via an easy polymer-assisted etchant-free method reported by Yang et al.[29] Figure 4.9a shows the schematic structure of the back-gated device with a channel length of 1 μm and width of 20 μm. OM and SEM images of a typical device are shown in Figure 4.9b-c. The transfer curve of the device under a $V_{ds}$ of 2 V is shown in Figure 4.9d, demonstrating the behaviour of a typical n-type transistor with a threshold voltage of ~+30 V. The field-effect electron mobility is expressed by the following formula:

$$\mu_{FE} = \frac{dI_{ds}}{dV_g} \times \frac{L}{W \times C_{ox} \times V_{ds}} \tag{4.3}$$

where $\frac{dI_{ds}}{dV_g}$ is the transconductance, L is the channel length, W is the channel width, $C_{ox}$ is the gate capacitance, and $V_{ds}$ is the applied drain-source bias. The mobility and on-off ratio of a typical $MoS_2$ FET device is 1.1 $cm^2V^{-1}s^{-1}$ and $10^5$–$10^6$, which is among the best for $MoS_2$ grown by the direct sulfurization, and comparable with CVD-grown $MoS_2$ FET devices with gold contacts (see Table 4.1&4.2). In addition, the optoelectronic properties of the $MoS_2$ FET device were measured under 532 nm green laser. As shown in Figure 4.9e, the current is measured under four different illumination conditions. A large gain in photocurrent is observed under various illumination powers compared to dark current, with a photoresponsivity R ($R = \frac{I_{photo}}{P_{laser}}$) of 9.9 A/W measured under 0.08 $W/cm^2$ at a bias of 5 V (Fig. 4.9f). Under higher illumination power, the

photocurrent reaches a saturation and photoresponsivity drops to 0.9 A/W under 98 W/cm$^2$ at a bias of 5 V. These results combined with the easiness of production demonstrate the method's potential for applications in large-scale fabrication of nano-devices.

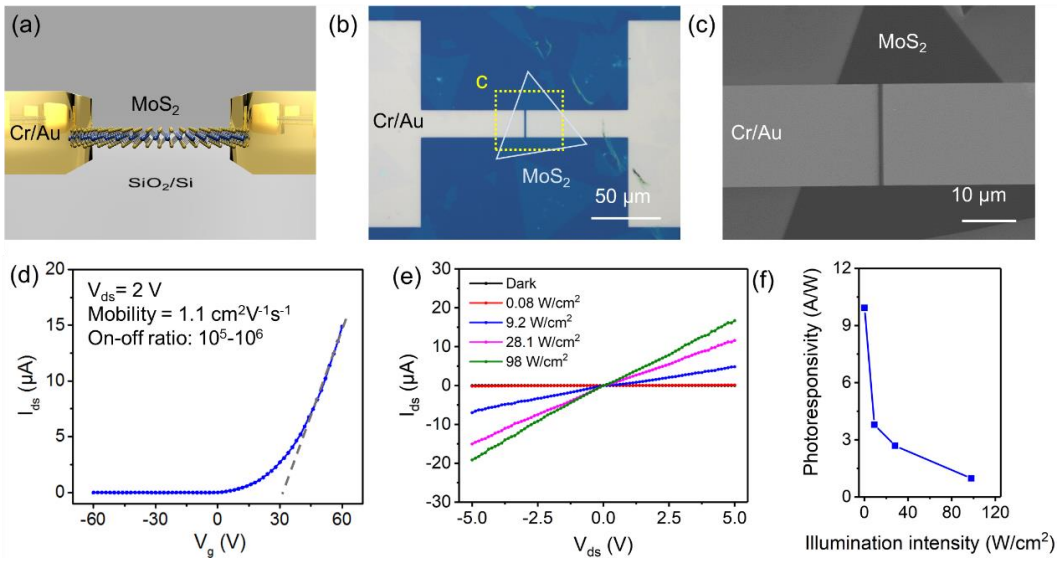



**Figure 4.9. Measurement of $MoS_2$ FET device.** (a) Schematic illustration of a fabricated $MoS_2$ FET device with Cr/Au as source, drain electrodes. (b) Optical image of a typical $MoS_2$ FET device. (c) SEM image of fabricated device in b showing the gap between two electrodes. (d) Transfer curve for a typical device ($V_{ds}$ = 2 V). (e) I−V curve of the device under different illumination powers (532 nm). (f) Photoresponsivity ($V_{ds}$ = 5 V) under different illumination powers.

**Table 4.1. Electrical properties of $MoS_2$ FET devices grown by direct sulfurization**

| Precursor | Device structure | Morphology | Device performance | Ref. |
|---|---|---|---|---|
| **Mo** | $SiO_2$ back-gated; 5 nm Ti/30 nm Au | Few layer | Mobility: 0.004–0.04 cm$^2$ V$^{-1}$ s$^{-1}$ | 15 |
| **Mo** | 20 nm $Al_2O_3$ top-gated; 5 nm Cr/200 nm Au | Monolayer | Mobility: 0.005−0.01 cm$^2$ V$^{-1}$ s$^{-1}$<br>On-off ratio: $10^4$–$10^6$ | 22 |
| **Mo** | 30 nm $HfO_2$ top-gated; Au electrode | 4 layered | Mobility: 0.07 cm$^2$ V$^{-1}$ s$^{-1}$<br>On-off ratio: $10^5$ | 41 |
| **$MoO_3$** | $SiO_2$ back-gated; Ti/Au | 2−3 layered | Mobility: 0.8 cm$^2$ V$^{-1}$ s$^{-1}$<br>On-off ratio: $10^5$ | 42 |

| | | | | |
|---|---|---|---|---|
| **$MoO_3$** | $SiO_2$ back-gated; Au | Monolayer | Mobility: 1.1 $cm^2 V^{-1} s^{-1}$<br>On-off ratio: $10^5$–$10^6$ | This work |

**Table 4.2. Electrical properties of other back-gated $MoS_2$ FET devices**

| Method | Electrode | Morphology | Device performance | Ref. |
|---|---|---|---|---|
| **Exfoliated** | Au | Monolayer | Mobility: 0.1–10 $cm^2 V^{-1} s^{-1}$ | 43 |
| **Exfoliated** | Au | Bilayer | Mobility: 0.5–3 $cm^2 V^{-1} s^{-1}$ | 44 |
| **CVD** | Au | Monolayer with thick regions | Mobility: 0.09 $cm^2 V^{-1} s^{-1}$<br>On-off ratio: $10^3$ | 45 |
| **CVD** | Au | Monolayer | Mobility: 0.02 $cm^2 V^{-1} s^{-1}$<br>On-off ratio: $10^4$ | 5 |
| **CVD** | 5 nm Ti/50 nm Au | Monolayer | Mobility: 0.2−3 $cm^2 V^{-1} s^{-1}$<br>On-off ratio: $10^4$–$10^6$ | 46 |
| **CVD** | 10 nm Ti/50 nm Au | Monolayer | Mobility: 6.3−11.4 $cm^2 V^{-1} s^{-1}$<br>On-off ratio: $10^5$–$10^7$ | 29 |
| **CVD** | 3 nm Ti/50 nm Au | Monolayer | Mobility: 4.3±0.8 $cm^2 V^{-1} s^{-1}$<br>On-off ratio: $6\times10^6$ | 4 |
| **CVD** | Au | Monolayer | Mobility: 1.1 $cm^2 V^{-1} s^{-1}$<br>On-off ratio: $10^5$–$10^6$ | This work |

## 4.3 Conclusions

In summary, by employing low-cost glass as substrate, this chapter presents a facile method for growing monolayer $MoS_2$ via a modified direct sulfurization method. This chapter demonstrates that the ability to incorporate pre-deposited precursors into molten glass substrate facilitates the growth of high-quality and monolayer $MoS_2$ crystals with large-area uniformity which is only limited by the size of the substrate. The results from optical microscopy, SEM, Raman and PL spectroscopy, STEM and the measurement of FETs confirmed the high quality and uniformity, with comparable electrical performance and largest crystal size (~600 μm) ever reported for $MoS_2$ grown by the direct sulfurization method. A combination of low-cost, uniformity, scalability, simplicity and high-quality is achieved in this method, which is superior to conventional CVD methods in scalability and reproducibility. It is believed that this method should

facilitate the development of wafer scale electronic devices based on 2D materials. This work also shows that precursor-soluble substrate can be an excellent supplier of precursors, which provides a new look at the role substrates could play in the synthesis and the possibilities of using other glass or liquid substrates for the growth of high-quality 2D materials.

## 4.4 References


1. Shi, Y. M.; Li, H. N.; Li, L. J., Recent Advances in Controlled Synthesis of Two-Dimensional Transition Metal Dichalcogenides via Vapour Deposition Techniques. *Chem. Soc. Rev.* **2015,** *44*, 2744-2756.
2. Cai, Z.; Liu, B.; Zou, X.; Cheng, H. M., Chemical Vapour Deposition Growth and Applications of Two-Dimensional Materials and Their Heterostructures. *Chem. Rev.* **2018,** *118*, 6091-6133.
3. Chhowalla, M.; Shin, H. S.; Eda, G.; Li, L. J.; Loh, K. P.; Zhang, H., The Chemistry Of Two-Dimensional Layered Transition Metal Dichalcogenide Nanosheets. *Nat. Chem.* **2013,** *5*, 263-275.
4. Najmaei, S.; Liu, Z.; Zhou, W.; Zou, X.; Shi, G.; Lei, S.; Yakobson, B. I.; Idrobo, J.-C.; Ajayan, P. M.; Lou, J., Vapour Phase Growth and Grain Boundary Structure of Molybdenum Disulphide Atomic Layers. *Nat. Mater.* **2013,** *12*, 754-759.
5. Lee, Y. H.; Zhang, X. Q.; Zhang, W.; Chang, M. T.; Lin, C. T.; Chang, K. D.; Yu, Y. C.; Wang, J. T. W.; Chang, C. S.; Li, L. J.; Lin, T. W., Synthesis of Large-Area $MoS_2$ Atomic Layers with Chemical Vapour Deposition. *Adv. Mater.* **2012,** *24*, 2320-2325.
6. Zhang, J.; Yu, H.; Chen, W.; Tian, X.; Liu, D.; Cheng, M.; Xie, G.; Yang, W.; Yang, R.; Bai, X.; Shi, D.; Zhang, G., Scalable Growth of High-Quality Polycrystalline $MoS_2$ Monolayers on $SiO_2$ with Tunable Grain Sizes. *ACS Nano* **2014,** *8*, 6024-6030.
7. Rong, Y.; Fan, Y.; Leen Koh, A.; Robertson, A. W.; He, K.; Wang, S.; Tan, H.; Sinclair, R.; Warner, J. H., Controlling Sulphur Precursor Addition for Large Single Crystal Domains of $WS_2$. *Nanoscale* **2014,** *6*, 12096-103.
8. Lee, J.; Pak, S.; Giraud, P.; Lee, Y. W.; Cho, Y.; Hong, J.; Jang, A. R.; Chung, H. S.; Hong, W. K.; Jeong, H. Y.; Shin, H. S.; Occhipinti, L. G.; Morris, S. M.; Cha, S.; Sohn, J. I.; Kim, J. M., Thermodynamically Stable Synthesis of Large-Scale and Highly Crystalline Transition Metal Dichalcogenide Monolayers and their Unipolar n–n Heterojunction Devices. *Adv. Mater.* **2017,** *29*, 1702206
9. Rajan, A. G.; Warner, J. H.; Blankschtein, D.; Strano, M. S., Generalized Mechanistic Model for the Chemical Vapour Deposition of 2D Transition Metal Dichalcogenide Monolayers. *ACS Nano* **2016,** *10*, 4330-4344.

10. Huang, J. K.; Pu, J.; Hsu, C. L.; Chiu, M. H.; Juang, Z. Y.; Chang, Y. H.; Chang, W. H.; Iwasa, Y.; Takenobu, T.; Li, L. J., Large-Area Synthesis of Highly Crystalline $WSe_2$ Monolayers and Device Applications. *ACS Nano* **2014,** *8*, 923-930.

11. Lu, X.; Utama, M. I. B.; Lin, J.; Gong, X.; Zhang, J.; Zhao, Y.; Pantelides, S. T.; Wang, J.; Dong, Z.; Liu, Z.; Zhou, W.; Xiong, Q., Large-Area Synthesis of Monolayer and Few-Layer $MoSe_2$ Films on $SiO_2$ Substrates. *Nano Lett.* **2014,** *14*, 2419-2425.

12. Kang, K.; Xie, S.; Huang, L.; Han, Y.; Huang, P. Y.; Mak, K. F.; Kim, C. J.; Muller, D.; Park, J., High-Mobility Three-Atom-Thick Semiconducting Films with Wafer-Scale Homogeneity. *Nature* **2015,** *520*, 656-660.

13. Lin, Y. C.; Jariwala, B.; Bersch, B. M.; Xu, K.; Nie, Y.; Wang, B.; Eichfeld, S. M.; Zhang, X.; Choudhury, T. H.; Pan, Y.; Addou, R.; Smyth, C. M.; Li, J.; Zhang, K.; Haque, M. A.; Fölsch, S.; Feenstra, R. M.; Wallace, R. M.; Cho, K.; Fullerton-Shirey, S. K.; Redwing, J. M.; Robinson, J. A., Realizing Large-Scale, Electronic-Grade Two-Dimensional Semiconductors. *ACS Nano* **2018,** *12*, 965-975.

14. Choi, S. H.; Boandoh, S.; Lee, Y. H.; Lee, J. S.; Park, J. H.; Kim, S. M.; Yang, W.; Kim, K. K., Synthesis of Large-Area Tungsten Disulfide Films on Pre-Reduced Tungsten Suboxide Substrates. *ACS Appl. Mater. Interfaces* **2017,** *9*, 43021-43029.

15. Zhan, Y.; Liu, Z.; Najmaei, S.; Ajayan, P. M.; Lou, J., Large-Area Vapour-Phase Growth and Characterization of $MoS_2$ Atomic Layers on a $SiO_2$ Substrate. *Small* **2012,** *8*, 966-971.

16. Wu, C. R.; Chang, X. R.; Chu, T. W.; Chen, H. A.; Wu, C. H.; Lin, S. Y., Establishment of 2D Crystal Heterostructures by Sulfurization of Sequential Transition Metal Depositions: Preparation, Characterization, and Selective Growth. *Nano Lett.* **2016,** *16*, 7093-7097.

17. Wu, Z.; Tai, G.; Wang, X.; Hu, T.; Wang, R.; Guo, W., Large-Area Synthesis and Photoelectric Properties of Few-Layer $MoSe_2$ on Molybdenum Foils. *Nanotechnology* **2018,** *29*, 125605.

18. Hu, T.; Bian, K.; Tai, G.; Zeng, T.; Wang, X.; Huang, X.; Xiong, K.; Zhu, K., Oxidation-Sulfidation Approach for Vertically Growing $MoS_2$ Nanofilms Catalysts on Molybdenum Foils as Efficient HER Catalysts. *J. Phys. Chem. C* **2016,** *120*, 25843-25850.

19. Boandoh, S.; Choi, S. H.; Park, J. H.; Park, S. Y.; Bang, S.; Jeong, M. S.; Lee, J. S.; Kim, H. J.; Yang, W.; Choi, J.-Y.; Kim, S. M.; Kim, K. K., A Novel and Facile Route to Synthesise Atomic-Layered $MoS_2$ Film for Large-Area Electronics. *Small* **2017,** *13*, 1701306.

20. Wu, C. R.; Chang, X. R.; Wu, C. H.; Lin, S. Y., The Growth Mechanism of Transition Metal Dichalcogenides by using Sulfurization of Pre-deposited Transition Metals and the 2D Crystal Hetero-structure Establishment. *Sci. Rep.* **2017,** *7*, 42146.

21. Thangaraja, A.; Shinde, S. M.; Kalita, G.; Tanemura, M., Effect of $WO_3$ Precursor and Sulfurization Process on $WS_2$ Crystals Growth by Atmospheric Pressure CVD. *Mater. Lett.* **2015,** *156*, 156-160.

22. Orofeo, C. M.; Suzuki, S.; Sekine, Y.; Hibino, H., Scalable synthesis of Layer-Controlled $WS_2$ and $MoS_2$ Sheets by Sulfurization of Thin Metal Films. *Appl. Phys. Lett.* **2014,** *105*, 083112.

23. Song, J. G.; Park, J.; Lee, W.; Choi, T.; Jung, H.; Lee, C. W.; Hwang, S. H.; Myoung, J. M.; Jung, J. H.; Kim, S. H.; Lansalot-Matras, C.; Kim, H., Layer-Controlled, Wafer-Scale,

and Conformal Synthesis of Tungsten Disulfide Nanosheets Using Atomic Layer Deposition. *ACS Nano* **2013,** *7*, 11333-11340.

24. Wang, X.; Feng, H.; Wu, Y.; Jiao, L., Controlled Synthesis of Highly Crystalline $MoS_2$ Flakes by Chemical Vapour Deposition. *J. Am. Chem. Soc.* **2013,** *135*, 5304-5307.

25. Ju, M.; Liang, X. Y.; Liu, J. X.; Zhou, L.; Liu, Z.; Mendes, R. G.; Rummeli, M. H.; Fu, L., Universal Substrate Trapping Strategy To Grow Strictly Monolayer Transition Metal Dichalcogenides Crystals. *Chem. Mater.* **2017,** *29*, 6095-6103.

26. Li, S.; Lin, Y. C.; Zhao, W.; Wu, J.; Wang, Z.; Hu, Z.; Shen, Y.; Tang, D. M.; Wang, J.; Zhang, Q.; Zhu, H.; Chu, L.; Zhao, W.; Liu, C.; Sun, Z.; Taniguchi, T.; Osada, M.; Chen, W.; Xu, Q. H.; Wee, A. T. S.; Suenaga, K.; Ding, F.; Eda, G., Vapour-Liquid-Solid Growth of Monolayer $MoS_2$ Nanoribbons. *Nat. Mater.* **2018,** *17*, 535-542.

27. Chen, J.; Zhao, X.; Tan, S. J. R.; Xu, H.; Wu, B.; Liu, B.; Fu, D.; Fu, W.; Geng, D.; Liu, Y.; Liu, W.; Tang, W.; Li, L.; Zhou, W.; Sum, T. C.; Loh, K. P., Chemical Vapour Deposition of Large-Size Monolayer $MoSe_2$ Crystals on Molten Glass. *J. Am. Chem. Soc.* **2017,** *139*, 1073-1076.

28. Chen, J.; Zhao, X.; Grinblat, G.; Chen, Z.; Tan, S. J. R.; Fu, W.; Ding Z.; Abdelwahab, I.; Li, Y.; Geng, D.; Liu, Y.; Leng, K.; Liu, B.; Liu, W.; Tang, W.; Maier, S. A.; Pennycook, S. J.; Loh, K. P. Homoepitaxial Growth of Large-Scale Highly Organized Transition Metal Dichalcogenide Patterns. *Adv. Mater.* **2018,** *30*, 1704674.

29. Yang, P.; Zou, X.; Zhang, Z.; Hong, M.; Shi, J.; Chen, S.; Shu, J.; Zhao, L.; Jiang, S.; Zhou, X.; Huan, Y.; Xie, C.; Gao, P.; Chen, Q.; Zhang, Q.; Liu, Z.; Zhang, Y., Batch Production of 6-Inch Uniform Monolayer Molybdenum Disulfide Catalyzed by Sodium in Glass. *Nat. Commun.* **2018,** *9*, 979.

30. Jin, Y. S.; Yan, Q. J.; Yin, Z. R.; Chen, Y., Secondary Ion Mass Spectrometry and X-Ray Photoelectron Spectroscopy of $Na_2MoO_4/SiO_2$ Catalysts for Methane Oxidative Coupling. *J. Chem. Soc., Faraday Trans.* **1995,** *91*, 381-384.

31. Spevack, P. A.; McIntyre, N. S., Thermal Reduction of Molybdenum Trioxide. *J. Phys. Chem.* **1992,** *96*, 9029-9035.

32. Storp, S., Radiation Damage During Surface Analysis. *Spectrochim. Acta, Part B* **1985,** *40*, 745-756.

33. Spevack, P. A.; McIntyre, N. S., Thermal Reduction of Molybdenum Trioxide. *J. Phys. Chem.* **1992,** *96*, 9029-9035.

34. Shaw, L.; Abbaschian, R., Chemical States of the Molybdenum Disilicide ($MoSi_2$) Surface. *J. Mater. Sci.* **1995,** *30*, 5272-5280.

35. LaMer, V. K.; Dinegar, R. H., Theory, Production and Mechanism of Formation of Monodispersed Hydrosols. *J. Am. Chem. Soc.* **1950**, *72*, 4847-4854.

36. Wang, S.; Rong, Y.; Fan, Y.; Pacios, M.; Bhaskaran, H.; He, K.; Warner, J. H., Shape Evolution of Monolayer $MoS_2$ Crystals Grown by Chemical Vapour Deposition. *Chem. Mater.* **2014**, *26*, 6371-6379.

37. Conley, H. J.; Wang, B.; Ziegler, J. I.; Haglund, R. F., Jr.; Pantelides, S. T.; Bolotin, K. I., Bandgap Engineering of Strained Monolayer and Bilayer $MoS_2$. *Nano Lett.* **2013,** *13*, 3626-3630.

38. Mak, K. F.; He, K.; Lee, C.; Lee, G. H.; Hone, J.; Heinz, T. F.; Shan, J., Tightly Bound Trions in Monolayer $MoS_2$. *Nat. Mater.* **2012,** *12*, 207.

39. Zhang, X.; Qiao, X. F.; Shi, W.; Wu, J. B.; Jiang, D. S.; Tan, P. H., Phonon and Raman Scattering of Two-Dimensional Transition Metal Dichalcogenides from Monolayer, Multilayer to Bulk Material. *Chem. Soc. Rev.* **2015,** *44*, 2757-2785.

40. Buscema, M.; Steele, G. A.; van der Zant, H. S. J.; Castellanos-Gomez, A., The Effect of the Substrate on the Raman and Photoluminescence Emission of Single-Layer $MoS_2$. *Nano Res.* **2014,** *7*, 561-571.

41. Lee, Y.; Lee, J.; Bark, H.; Oh, I. K.; Ryu, G. H.; Lee, Z.; Kim, H.; Cho, J. H.; Ahn, J. H.; Lee, C., Synthesis of Wafer-Scale Uniform Molybdenum Disulfide Films with Control over the Layer Number Using a Gas Phase Sulfur Precursor. *Nanoscale* **2014,** *6*, 2821-2826.

42. Lin, Y. C.; Zhang, W. J.; Huang, J. K.; Liu, K. K.; Lee, Y. H.; Liang, C. T.; Chu, C. W.; Li, L. J., Wafer-Scale $MoS_2$ Thin Layers Prepared by $MoO_3$ Sulfurization. *Nanoscale* **2012,** *4*, 6637-6641.

43. Radisavljevic, B.; Radenovic, A.; Brivio, J.; Giacometti, V.; Kis, A., Single-Layer $MoS_2$ Transistors. *Nat. Nanotechnol.* **2011,** *6*, 147-150.

44. Novoselov, K. S.; Jiang, D.; Schedin, F.; Booth, T. J.; Khotkevich, V. V.; Morozov, S. V.; Geim, A. K., Two-Dimensional Atomic Crystals. *Proc. Natl. Acad. Sci. U. S. A.* **2005,** *102*, 10451-10453.

45. Senthilkumar, V.; Tam, L. C.; Kim, Y. S.; Sim, Y.; Seong, M. J.; Jang, J. I., Direct vapour phase growth process and robust photo-luminescence properties of large area $MoS_2$ layers. *Nano Res.* **2014,** *7*, 1759-1768.

46. Liu, B.; Chen, L.; Liu, G.; Abbas, A. N.; Fathi, M.; Zhou, C., High-Performance Chemical Sensing Using Schottky-Contacted Chemical Vapour Deposition Grown Monolayer $MoS_2$ Transistors. *ACS Nano* **2014,** *8*, 5304-5314.

47. Zakeri, M.; Yazdani-Rad, R.; Enayati, M. H.; Rahimipour, M. R.; Mobasherpour, I., Mechanochemical reduction of $MoO_3/SiO_2$ powder mixtures by Al and carbon for the synthesis of nanocrystalline $MoSi_2$. *J. Alloys Compd.* **2007**, *430*, 170-174.

48. Wang, L.; Xue, Z.-L.; Huang A.; Wang, F.-F., Mechanism and Kinetic Study of Reducing $MoO_3$ to $MoO_2$ with CO−15 vol % $CO_2$ Mixed Gases. *ACS Omega* **2019**, *4*, 20036-20047.

# Chapter 5

# Synthesis of High-Quality Continuous 2D GaS Films

## 5.1 Introduction

Most 2D semiconductors that have been studied possess small bandgaps, while the applications for 2D LEDs with blue or ultraviolet (UV) light emission, formation of vdWs type-I heterojunctions and quantum wells call for materials with a larger bandgap.[1-3] Gallium (II) sulfide (GaS), a member of the group-III monochalcogenide layered materials, is one such semiconductor with a wide bandgap semiconductor but scarcely explored.[4-5] Bulk GaS has a bandgap of ~2.5 eV, and its bandgap increases with decreasing thickness due to quantum confinement effects, which gives wide tunability that could fill the space between 2D small bandgap semiconductors and insulators.[6-7] Previous reports of mechanically-exfoliated few-layer GaS devices have demonstrated high photoresponsivity up to 64.43 A/W, large on/off ratios ($10^4$–$10^5$) and short response time of < 10 ms, properties suitable for many applications including photodetector, photoswitching and flexible devices.[8-9]

Although there have been a few studies on thin GaS crystals, the stability of GaS is still in question, which greatly hindered its further studies. On one hand, GaS shows no obvious morphology changes in ambient environment for months. On the other hand, many researches have noticed that few-layer GaS devices suffered from poor long-term performance and optical signals were very weak in some studies,[8, 10] which impedes further application of the material in optics or optoelectronics. In addition, due to difficulties in exfoliation and lack of thickness-controlled synthesis methods, previous

reports were unable to study layered-dependent properties of the 2D layered material, and to my knowledge, characterisation or properties of GaS thinner than 3 layers are missing. Furthermore, although other members in the group-III monochalcogenide layered materials with similar structures (GaSe, GaTe, InSe) have attracted intense attention as they have demonstrated superior optical properties including ultra-high second-harmonic generation,[11-12] giant piezo-phototronic response,[13] polarisation-dependent absorption,[14] etc.,[15-16] the properties of GaS with wide potential remain unexplored as a result of unanswered stability issues and unsatisfying samples. In 2018, Dr. Xiaochen Wang, a previous group member, developed a simple and atmospheric-pressure chemical vapour deposition (CVD) method for growth of 2D GaS crystals,[10] which paved way for further study of the material's stability and layer-dependent properties.

In this chapter, large-area synthesis of thickness-controlled continuous films (1–4L) of defective $GaS_{0.87}$ and stoichiometric GaS crystals is achieved with an optimised CVD synthesis method. The elemental composition was determined by energy-dispersive X-ray spectroscopy (EDX) and X-ray photoelectron spectroscopy (XPS). A comprehensive characterisation of the defective $GaS_{0.87}$ and stoichiometric GaS crystals was conducted by means of Raman spectrometry, atomic force microscopy (AFM) and scanning electron microscopy (SEM). To answer the question of GaS stability, the degradation behaviour of the two crystals under laser and UV light were compared and the unique degradation mechanism was studied by valence state changes with XPS, atomic structure changes with high angle annular dark field scanning transmission electron microscopy (HAADF-STEM) and further linked with device performance, and it is found that the poor stability and weak optical signal from GaS is strongly related to defects. Finally, GaS-based photodetectors showed excellent UV

detection ability (with highest R=10.2 A/W, D*=$1.6\times10^{12}$ Jones, EQE=2364% and photoresponse time < 66 ms), and by tuning defects in GaS, the photoresponse range could be changed from vis-to-UV to UV-discriminating.

## 5.2 Results and Discussion

### 5.2.1 Controlling Stoichiometry in Continuous 2D GaS Films

The defects in GaS material were tuned in the two-furnace CVD system for further study of their influence on material properties and device performance. Figure 5.1a-d shows the schematic illustration of the synthesis of two GaS crystals, defective $GaS_{0.87}$ and stoichiometric GaS (the stoichiometry was determined in later discussion), with the detailed method described in Chapter 3.2.2.

The relations between morphology and synthesis parameters are first studied for both defective $GaS_{0.87}$ and stoichiometric GaS, which have many aspects in common. As the deposited amount increases, the morphology of both materials changes from isolated monolayer triangles with rounded corners, to monolayer continuous films, to bilayer continuous films, further to trilayer films with adlayers (small bulk crystals) on top of the film, and for $GaS_{0.87}$ films the thickness can reach 4 layers (Fig. 5.1e-f). With fine control of the growth conditions, large-area and uniform all-monolayer continuous films throughout almost the substrate can be obtained. As can be seen in Figure 5.1g, the two edges of the substrate show isolated monolayer GaS domains due to smaller flow rate near the side of the system, but the major area (almost the whole substrate) is covered with continuous monolayer film. The film thicknesses are determined by AFM results and Raman peak positions, which will be discussed later. Besides, the growth behaviour is self-limiting in nature as the film thickness is highly uniform for very large

areas. The lack of contrast variation in SEM and AFM images (Fig. 5.1e-g, Fig. 5.5a, c) indicates that there are no adlayers on any of the monolayer and bilayer regions. AFM results also show that even for the 3 and 4 layer films, the film roughness of regions between small bulk crystals is only 0.22 nm (Fig. 5.2), hence the morphology can be described as "some small islands of GaS crystals sitting epitaxially on top of a large area continuous 3–4 layer GaS 2D films". This layer-controlled synthesis is essential for studying its layer-dependent properties. Moreover, the deposition rate (which can be estimated by film thickness given the same deposition time) increases as the substrate temperature decreases. The deposition rate also increases with increasing temperature of precursor (i.e. the sublimation rate of precursor) (Fig. 5.3). Taking the growth of defective $GaS_{0.87}$ as an example, growing at 650 °C for 20 min resulted in isolated domains of monolayer defective $GaS_{0.87}$, and as the reaction time extends, it would continue to merge into monolayer continuous films. At a lower reaction temperature of 637 °C, the deposition amount increases and the film is mostly bilayer, followed by 3–4 layer film at 625 °C. This suggests that the growth kinetics are controlled by the deposition stage. Finally, the addition of sulfur could greatly increase the deposition rate for stoichiometric GaS compared with defective $GaS_{0.87}$. At 650 °C with the addition of sulfur, stoichiometric trilayer GaS films form instead of monolayer defective $GaS_{0.87}$, and monolayer stoichiometric GaS is obtained at a growth temperature of 675 °C.

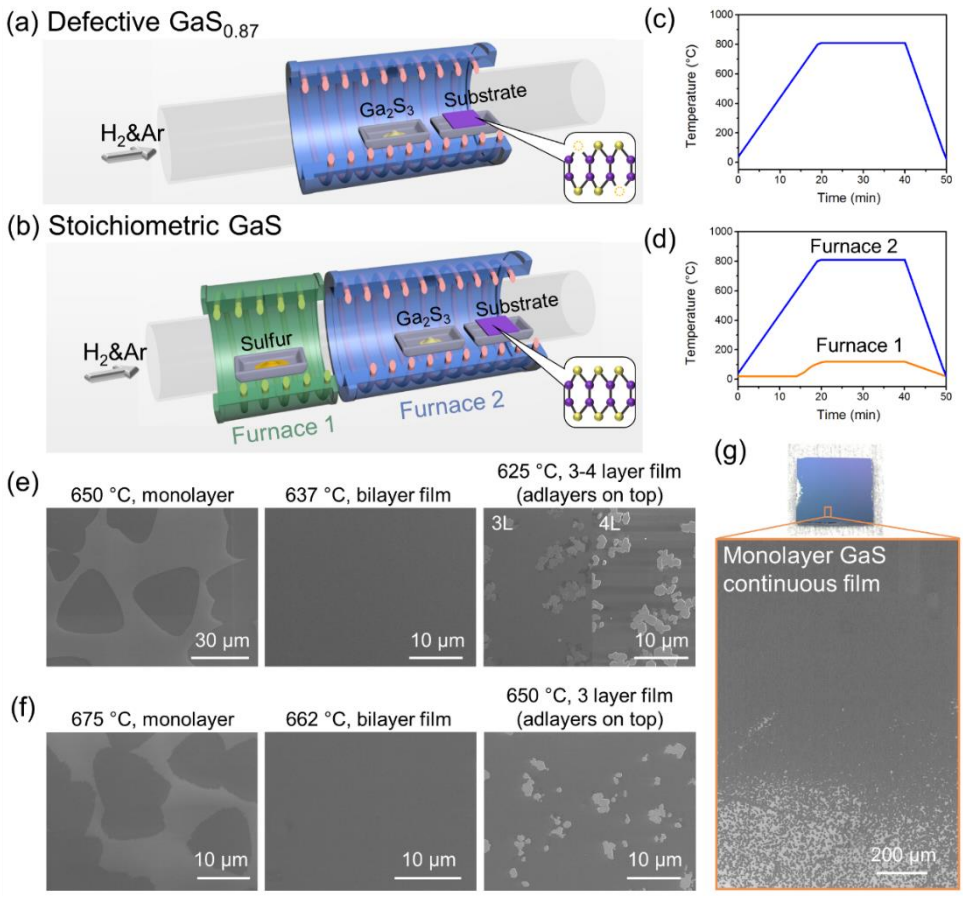



**Figure 5.1. Synthesis and SEM images of gallium (II) sulfide.** (a, b) Schematic of synthesis of defective $GaS_{0.87}$ and stoichiometric GaS, respectively. (c, d) Temperature profile for the process of $GaS_{0.87}$ and GaS growth, respectively. (e) SEM images of defective $GaS_{0.87}$ from monolayer to 4 layer films. (f) SEM images of stoichiometric GaS from monolayer to 3 layer films. (g) Photograph and SEM images of synthesised large-area uniform monolayer stoichiometric GaS continuous films.

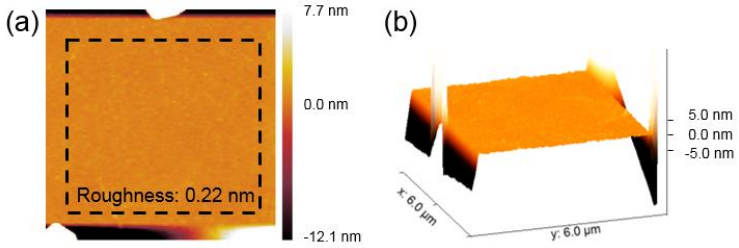



**Figure 5.2. Roughness of GaS trilayer films by AFM.** (a) AFM height scan of GaS trilayer films between thick crystals. (b) 3D landscape of (a).

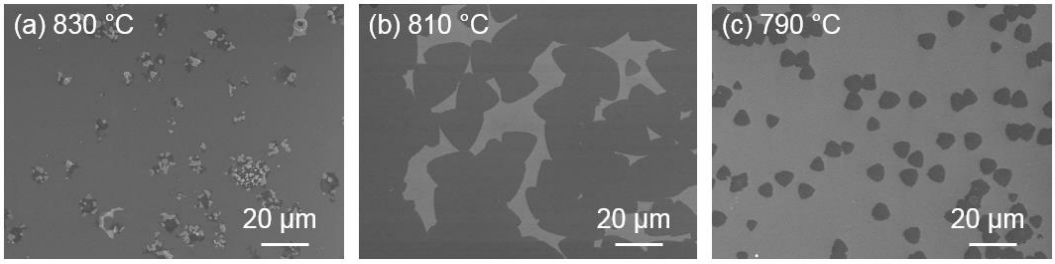



**Figure 5.3. Influence of precursor temperature on final product.** (a-c) SEM images of $GaS_{0.87}$ deposited at 675 °C with precursor temperature at (a) 830 °C, monolayer with adlayers, (b) 810 °C, monolayer domains, (c) 790 °C, smaller and more sparse monolayer domains, respectively.

Next, to further check the stoichiometry information on the materials, both EDX and XPS were employed to characterise the gallium (II) sulfide films. As shown in Figure 5.4a, the Ga and S element peaks can be clearly identified in EDX. The two peaks are fitted and statistical results for the samples are summarised in Table 5.1. The values are narrowly distributed and consistent for crystals from bulk to monolayer, indicating that it is not related to surface effects or caused by byproducts, but intrinsic stoichiometry of the material. A S:Ga ratio of 0.87±0.03 was obtained for defective GaS films, and the stoichiometric GaS shows the pristine stoichiometry of 1.00±0.01. XPS was further conducted as a supplementary to EDX, which is shown in Figure 5.4b-c. The Ga 3d peak at 20.43±0.05 eV was used for quantification of Ga elements, and the other two fitted peaks located at 162.7 eV (S $2p_{3/2}$) and 163.8 eV (S $2p_{1/2}$) were used for quantification of S elements. The obtained results from XPS were in great agreement with EDX, with a S:Ga ratio of 0.88 for defective GaS and 1.01 for stoichiometric GaS. Hence, according to the well-agreed EDX and XPS results, the defective and stoichiometric 2D crystals are denoted as $GaS_{0.87}$ and GaS, respectively.

The structural nature of the deficiency in sulfur in the $GaS_{0.87}$ compound might be classified into two cases. In the first case, the sulfur vacancies distributed randomly in the GaS crystal structure, while in the second case, ordered structure of sulfur vacancies or new phases of Ga-S compounds appear. In this study, the weak Raman signal in section 5.5.2 and the electron beam-induced GaS degradation under STEM in section 5.5.3 impeded further exclusion of one of the possibilities. Further X-ray diffraction characterisations are needed to resolve this question.

**Table 5.1. Ga:S ratio in final product under different growth conditions by EDX**

| No. | T_Sulfur | T_Ga | S:Ga | Result |
|---|---|---|---|---|
| 1 | / | 810 °C | 0.87±0.03 | $GaS_{0.87}$ |
| 2 | 120 °C | 810 °C | 1.00±0.01 | GaS |
| 3 | 135 °C | 810 °C | 1.48±0.01 | $Ga_2S_3$ |

These results showed that the addition of sulfur have significant influence on the composition of the final crystal. Unlike many well-studied TMD materials where the product has only one stoichiometry, the cases with III(A) group metals (Ga, In) are more complicated based on my experiments. Several conclusions based on a series of comparative experiments is introduced as the basis for understanding the growth mechanism as well as how the growth affects stoichiometry. First, the precursor is confirmed to be $Ga_2S_3$ only. Although the composition of the residue powder after the synthesis is studied by Raman to contain both GaS and $Ga_2S_3$, no deposition was found using GaS powder alone as precursor, excluding the possibility of physical vapour deposition. The observed GaS in precursor powder is merely a byproduct of hydrogen reduction that slightly decreases the amount of $Ga_2S_3$. Second, the reactive species are identified. As the addition of sulfur powder (converted into $H_2S$ by $H_2$ carrier gas)

significantly increased the deposition rate, $H_2S$ is assumed as one of the reactive species. Hence, $Ga_2S_3$ is believed to be transformed into $H_2S$ and a gallium-containing species (denoted as Ga*) under hydrogen. The importance of hydrogen is supported by the experiment where no deposition was found even with $Ga_2S_3$ heated up to 970 °C in Ar. Third, the deposition rate increases dramatically with decreasing substrate temperature, which implies that within this temperature region, the growth is different from the mass-transport-limited case discussed in Chapter 4.

Based on the above observations, the reaction mechanism is illustrated in Figure 5.4d following the five-step CVD growth mechanism described in Chapter 4: Step 1. $Ga_2S_3$ is decomposed into volatile Ga* (a gallium-containing species) and $H_2S$, catalysed by hydrogen; Step 2. The sublimated Ga* and $H_2S$ in gas phase (labelled with (g)) are transported to the substrate; Step 3. A balance of adsorption and desorption of Ga*(g) and $H_2S$(g) is established on the surface, with the adsorbed amount of Ga* and $H_2S$ (labeled with (a)) determined by substrate temperature and gas phase concentration. Step 4. Ga*(a) and $H_2S$(a) react to form $GaS_x$ with various stoichiometries. Step 5. Detachment of excess active species. Among these steps, step 3 is considered as the rate-limiting step, and thus the relative ratio of the adsorbed species Ga*(a) and $H_2S$(a) determines the stoichiometry in the final product. As $H_2S$ molecules are lighter (indicating smaller vdWs interaction) and have no special binding with the substrate, there should be less $H_2S$(a) absorbed than Ga*(a) given the same gaseous concentration. Hence, even though the S:Ga stoichiometry from the precursor is 1.5, the actual absorbed species on the substrate have a much smaller S:Ga ratio. The influence from this is illustrated in Figure 5.4f-h. When growing under insufficient $H_2S$ coming only from the $Ga_2S_3$, a defective yet thermally stable 2D crystal $GaS_{0.87}$ is formed, which has the same crystal structure of GaS but with ~13% sulfur vacancies. When a suitable

amount of $H_2S$ is added to the system, the ratio of S:Ga in reactive species becomes larger and stoichiometric GaS is formed. If more $H_2S$ is continuously added to the gas phase, extra sulfur on the substrate resulted in the formation of 2D $Ga_2S_3$ (Fig. 5.4e). The role of hydrogen is usually considered as creating reduction atmosphere, but the above results suggest that $Ga_2S_3$ could form under such high hydrogen environment, and thus the real contribution of hydrogen is to facilitate the transformation of the precursors into active species ($H_2S$ and Ga*). These findings suggest that extra care must be taken for 2D materials with other possible forms of stoichiometry, and especially in cases where it is not the stoichiometry in the precursor, but in the absorbed reactive species, which determines that in the final product.

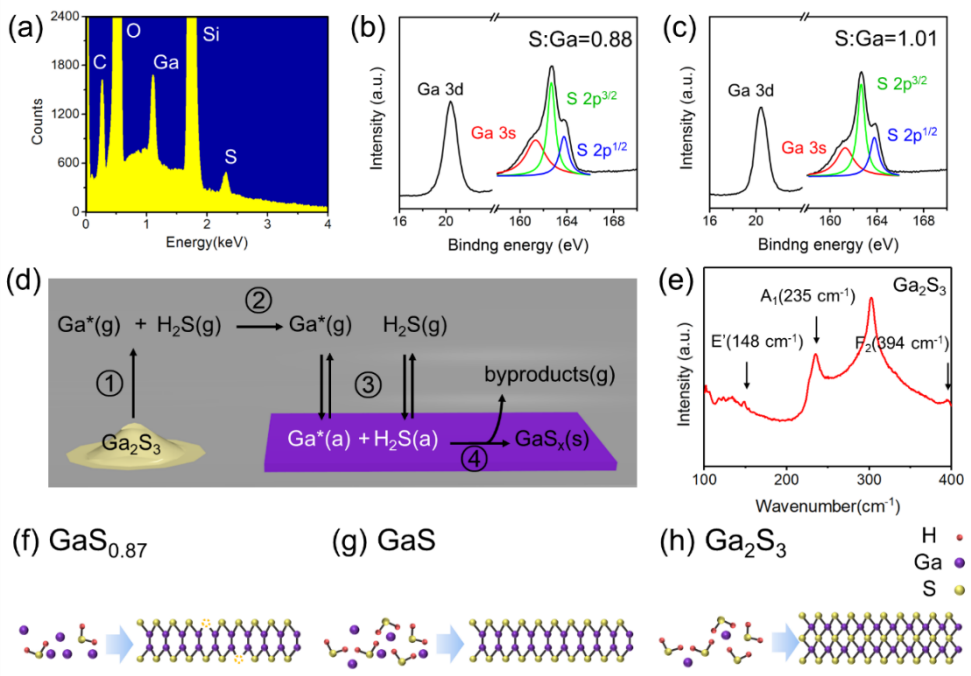



**Figure 5.4. Stoichiometry and growth mechanisms for 2D layered gallium sulfide crystals.** (a) EDX spectrum of a typical gallium sulfide thin films. (b, c) XPS spectrum of monolayer $GaS_{0.87}$ and GaS, respectively. (d) Schematic illustration of the reaction mechanisms. (e) Raman spectrum of $Ga_2S_3$ thin films showing typical peaks at 148 $cm^{-1}$(E'), 235 $cm^{-1}$($A_1$), 394 $cm^{-1}$($A_2$). (f-h) The effect of relative ratio of absorbed species on the stoichiometry in the final product ($GaS_{0.87}$, GaS, $Ga_2S_3$).

### 5.2.2 Thickness- and Stoichiometry-Dependent Properties of GaS

For the first time, a fast and easy approach for determining the number of layers of GaS by Raman spectroscopy is established as the starting point of a layer-dependent property study in GaS. Bulk GaS has three Raman peaks, which are located at 187.3 $cm^{-1}$($A^1_{1g}$), 294.1 $cm^{-1}$($E^1_{2g}$), 360.2 $cm^{-1}$($A^1_{2g}$).[17] The signals of the peaks weakened with the decrease of number of layers, and in few-layered GaS, the $E^1_{2g}$ peak can hardly be distinguished from the signal from the Si substrate. No other signals are observed from these samples. The peak position of $A^1_{1g}$ was found as a trusty indicator for simple and fast identification of the GaS thickness between 1~4 layers. AFM was first employed which confirmed the thickness for 1~4L $GaS_{0.87}$ to be 0.85 nm (1L), 1.6 nm (2L), 2.5 nm (3L), 3.4 nm (4L) (Fig. 5.5a-b); and 1~3L GaS to be 0.85 nm (1L), 1.6 nm (2L), 2.6 nm (3L) (Fig. 5.5c-d), which is in accordance with previous reports from mechanically exfoliated GaS.[17] Raman spectra of the samples are then correlated with AFM results, and $A^1_{1g}$ peak position of both samples decreased with decreasing number of layers due to reduced interaction between layers, as is also observed in GaSe with similar structure.[17] As shown in Figure 5.5e, the $A^1_{1g}$ peak position of $GaS_{0.87}$ is at 182.3 $cm^{-1}$ (1L), 184.2 $cm^{-1}$ (2L), 185.3 $cm^{-1}$ (3L), 186.3 $cm^{-1}$ (4L); and for GaS the peak position is at 183.5 $cm^{-1}$ (1L), 184.3 $cm^{-1}$ (2L), 185.4 $cm^{-1}$ (3L). The Raman signal intensities of GaS are significantly stronger than their counterparts of $GaS_{0.87}$ (Fig. 5.5f). For example, monolayer GaS $A^1_{1g}$ peaks are more than three times stronger than that of monolayer $GaS_{0.87}$, even slightly stronger than that of 3L $GaS_{0.87}$. The stronger Raman signals indicate better crystallinity and fewer defects, and as will be discussed next, the difference in stability also accounts for the difference in Raman signal intensities.

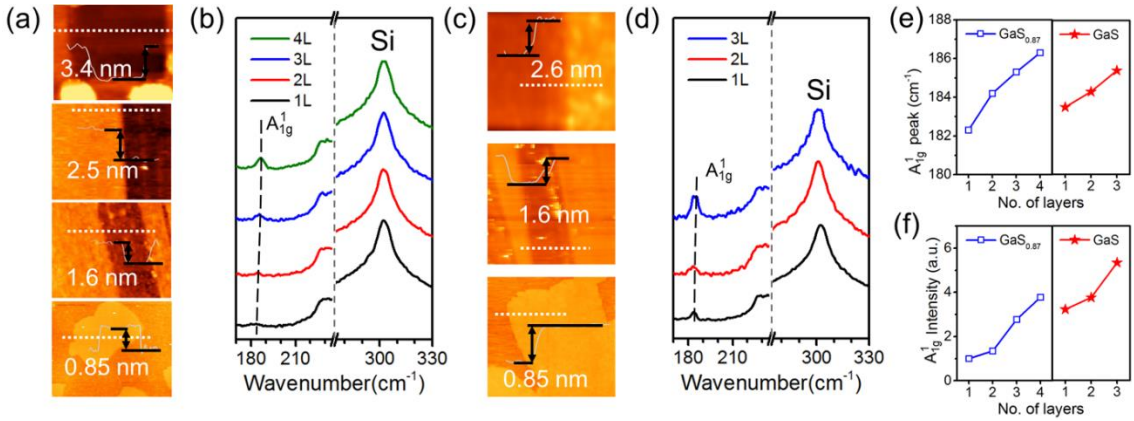



**Figure 5.5. AFM image and Raman spectra of gallium sulfide crystals.** (a) AFM images of $GaS_{0.87}$ films from monolayer to 4 layer and (b) corresponding Raman spectra. (c) AFM images of GaS films from monolayer to 3 layer and (d) corresponding Raman spectra. (e) Relation of $A^1_{1g}$ peak position and film thickness. (f) Relation of $A^1_{1g}$ peak intensity and film thickness.

As mentioned before, the two gallium(II) sulfide samples ($GaS_{0.87}$ and GaS) are significantly different in stability under laser or UV light. Since Raman signals are related to the crystal's structure, the level of degradation from laser can be detected from the weakening of Raman peak signals due to loss of crystallinity or formation of new substances. Thus, the $A^1_{1g}$ peak intensity can be used as an indicator of level of degradation, and here the sample quality was always checked by Raman to be fresh before any further characterisation was conducted. To study the effect of laser on the material, the evolution of Raman signal intensity from trilayer $GaS_{0.87}$ and GaS films with time were recorded every 3 seconds under 7.76 mW of 532 nm laser (spot size ~1 μm). As shown in Figure 5.6a, the Raman peak intensity in trilayer $GaS_{0.87}$ films started to decrease immediately and continuously until it dropped to only 20% of its starting value within 30 s. No peak shifting was observed, excluding the possibility of layer-by-layer laser-thinning. As a comparison, the trilayer GaS films showed more stable Raman signal intensities and after 30 s the signal was still above 80% of its original

value. It is therefore believed that the lower Raman signals from $GaS_{0.87}$ films are also resulted from its instability under high-energy laser beam. Interestingly, unlike many other reports on the study of 2D materials degradation, here apart from the changes in Raman signal intensities, little change was observed for the degraded gallium(II) sulfide. As can be seen from Figure 5.5c-e, AFM was used to acquire the topography of a region where the underlying 3L $GaS_{0.87}$ film had been annealed under 7.76 mW 532 nm laser for 60 s and no longer showed any signals from GaS or other substances (Fig. 5.7a, d). Such condition would usually generate a hole with the depth of the original film, whereas AFM height profile only showed a small 0.75 nm difference in height, even less than the thickness of monolayer GaS, indicating that the film was transformed into a non-volatile species without aggregation. The sample was also characterised by SEM but no difference was shown (Fig. 5.7c). Raman mapping was used at the end of the series of characterisations to confirm the annealed region (Fig. 5.7b).

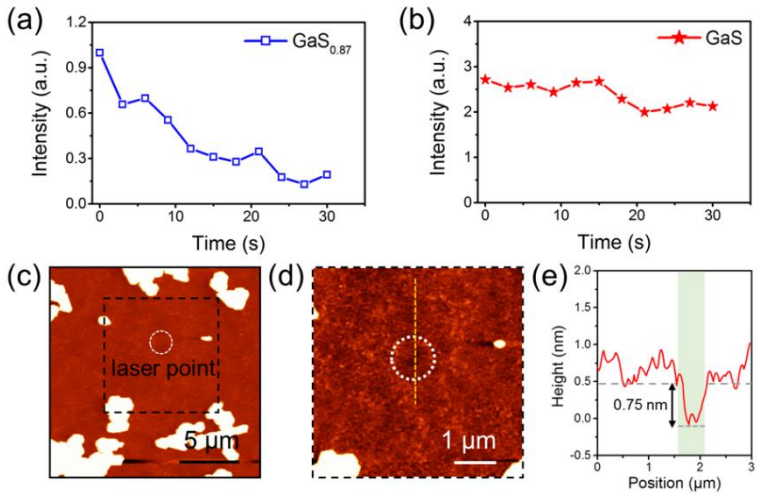



**Figure 5.6. Laser-induced degradation of trilayer thin films of $GaS_{0.87}$.** (a, b) Evolution in time of the $A^1_{1g}$ peak intensity in trilayer $GaS_{0.87}$ and trilayer GaS under 7.76 mW of 532 nm laser. (c, d) AFM image of trilayer $GaS_{0.87}$ films after annealed under 7.76 mW laser for 60 s. (e) AFM line profile of the annealed spot.

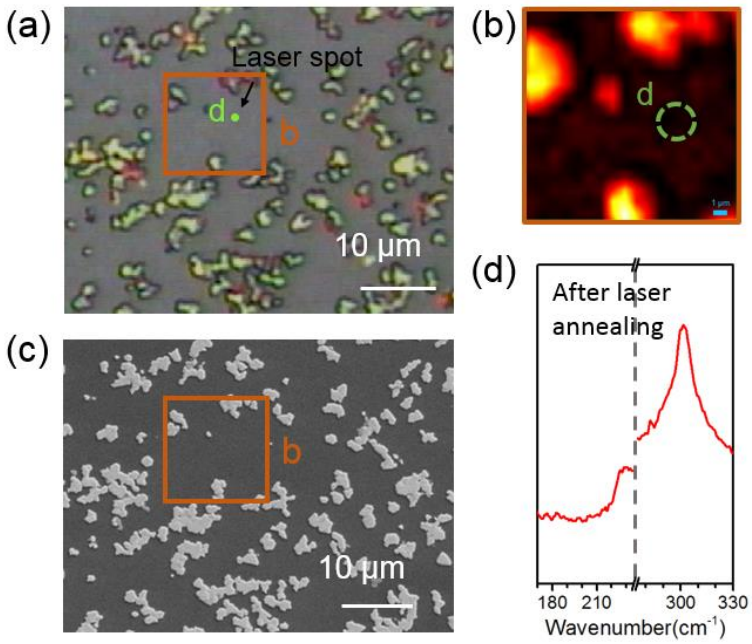



**Figure 5.7. Further characterisation of laser-annealed $GaS_{0.87}$ film.** (a) Optical zoom-out image of annealed region. (b) Raman mapping of GaS $A^1_{1g}$ peak intensity. The dim region (green circle) corresponds to the annealed and degraded $GaS_{0.87}$ film region. (c) SEM image of the annealed region showing no obvious difference with surrounding areas. (d) Raman spectrum of the degraded region showing no GaS Raman signals.

Then, the optoelectronic properties of the crystals with different stoichiometry are compared and the degradation of $GaS_{0.87}$ films is studied under strong UV light. E-beam lithography is used for patterning with 80 nm gold as electrodes. As a large bandgap semiconductor, the off-state current of GaS is quite small. Therefore, the channel for 1L and 2L GaS (and $GaS_{0.87}$) films are designed to be 200 μm in width for larger current with 1 μm channel length, while the channel for the 3L and 4L GaS (and $GaS_{0.87}$) films are designed to be 20 μm in width, and the devices with thick crystals sitting between the gaps are excluded by SEM so that the measurement results are related to the exact number of layers. To excite electrons from valence band into the conduction band, a 275 nm UV LED was used as the light source with intensities as high as 1.25 $mW/cm^2$.

Figure 5.8a-f shows the photocurrent of devices with different light intensities under a bias of 0–20V. Note that the photocurrent of 1L $GaS_{0.87}$ was below the equipment's detection limit, which indicates that the channel might have broken down during device fabrication or measurement. The 1–3 layer GaS and 2–4 layer $GaS_{0.87}$ all showed good and sensitive photoresponse to the UV light. Besides photoresponsivity, another critical parameter used is external quantum efficiency (EQE= $hcR_\lambda/e\lambda$), which shows the number of electrons per incident photon, where h is the Planck's constant, c is the velocity of light, $R_\lambda$ as the photoresponsivity at exciting photon wavelength λ. Based on these results, the photoresponsivity are plotted in Figure 5.8i. It is clearly shown that the photoresponsivity increases with the number of layers of the crystals due to increased absorption with thickness. The 4 layer $GaS_{0.87}$ films achieved a high photoresponsivity of 10.2 A/W and high EQE of 2364% (@9.8 μW/cm$^2$), and 3 layer GaS film had a photoresponsivity of 4.7 A/W and EQE of 1312%, which is comparable to mechanically exfoliated GaS thin crystals, demonstrating the good quality of the as-synthesised GaS. In addition, the photoresponsivity of GaS crystals less than 3L is measured for the first time, with 1.1 A/W for 2L GaS at 9.8 μW/cm$^2$ (EQE=291%), and 0.05 A/W for monolayer GaS at 102 μW/cm$^2$ (EQE=23%). Due to the small dark current, gallium sulfide also showed good detectivity (D*), which is used to describe the smallest detectable light signal:

$$D* = \frac{\mathrm{R} \times \sqrt{A}}{\sqrt{2eI_{dark}}} \tag{5.1}$$

where R is the photoresponsivity, A is the area of device channel, e as the electronic charge and $I_{dark}$ as the dark current. A high D* is measured for all devices, with $1.6\times10^{12}$ Jones for 4-layer $GaS_{0.87}$, $1.4\times10^{12}$ Jones for 3-layer GaS and $GaS_{0.87}$, $5\times10^{11}$ Jones for bilayer GaS, $6\times10^{11}$ Jones for bilayer $GaS_{0.87}$ and $1.2\times10^{11}$ Jones for monolayer GaS.

A comparative study of the photoresponse of bilayer and trilayer defective $GaS_{0.87}$ and stoichiometric GaS was also conducted as shown in Figure 5.8g, where defective $GaS_{0.87}$ shows smaller photocurrent compared with stoichiometric GaS. Also, under weak light, the difference between two crystals was only 20-30%, but the gap increased with stronger light, and at a power density of 102 $\mu W/cm^2$, the photoresponsivity of defective $GaS_{0.87}$ was less than half of the stoichiometric GaS, suggesting a larger concentration of trap states in defective $GaS_{0.87}$. Another important difference lies in their behaviour under strong UV light. As shown in Figure 5.8h-i, the I–t (current–time) curve, with the UV light of 1.25 $mW/cm^2$ switching on and off every 10 seconds, the stoichiometric GaS shows very stable and consistent performance with a sharp edge indicating instant response. The response time is less than 66 ms (Fig. 5.9), which is 2 to 3 orders less than other visible-light blind UV photodetectors (Table 5.2).[18-24] However, the photocurrent of $GaS_{0.87}$ decreased drastically as soon as the light was on, and continued with every switching on of the light, dropping to only half of the starting values after only a total of 110 s exposure. Examination of the $GaS_{0.87}$ material after device measurements under strong UV exposure showed very weak Raman signals. Note that at lower power density (102 $\mu W/cm^2$) the $GaS_{0.87}$ devices showed stable performance (Fig. 5.10). Although the degradation of the $GaS_{0.87}$ devices were observed when bias was applied, it was not the result of large current flow or combined effect from current and light. As shown in Figure 5.8j, the device was first measured under weak UV light with stable performance, then excited with strong UV lights for 120 s with no bias applied. A clear drop in current was shown which demonstrated that UV strong light alone can cause degradation in defective $GaS_{0.87}$. In comparison, a stoichiometric GaS device was excited with strong UV light for 15 min, and the photocurrent measured after that was still > 90% of its original value (Fig. 5.8k),

demonstrating that the stoichiometric GaS was much more robust than the defective material.

The wavelength dependent photoresponse of the two crystals was also studied by using a series of LEDs with different wavelengths from UV to visible red light at the same power density of 100 $\mu W/cm^2$. Both trilayer and bilayer GaS shows exclusive response to UV light, with no detectable photocurrent in the visible light range. However, the defective trilayer $GaS_{0.87}$ showed response to blue light (470 nm), possibly from sub-bandgap states absorption arising from defects; and the bilayer $GaS_{0.87}$ has rather weak photoresponse to 275 nm deep-UV light and its response to 370 nm or 470 nm is possibly below the detection limit. Based on the above results, the robust and UV-discriminating stoichiometric GaS crystals are very suitable for UV-sensitive applications.

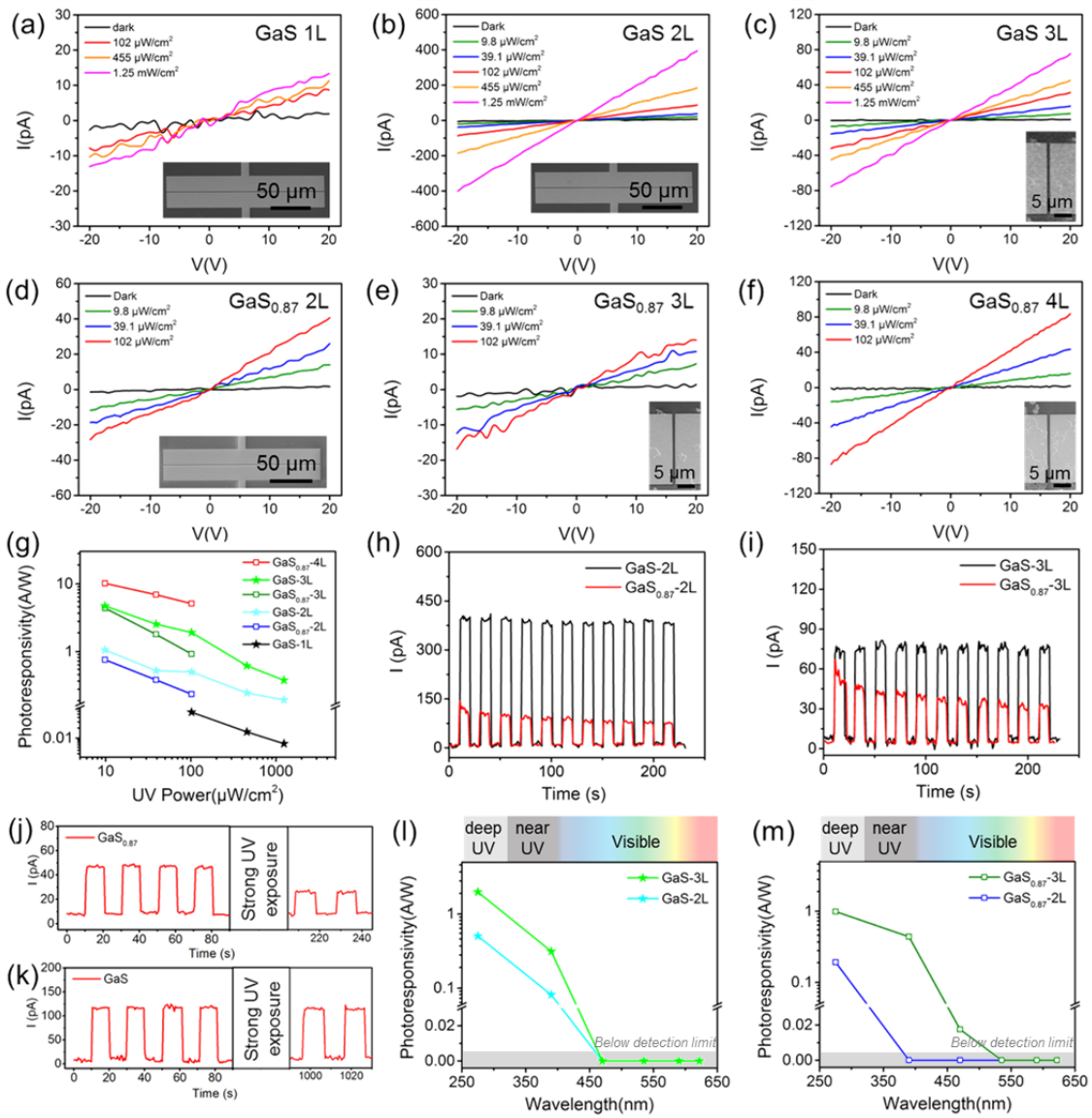



**Figure 5.8. Optoelectronic performance of gallium sulfide thin films and UV-induced degradation behaviour of $GaS_{0.87}$ films.** (a-c) I–V curve of 1–3L stoichiometric GaS thin film devices under dark and different power densities of 275 nm UV light. Inset: SEM images of fabricated Au–GaS–Au devices. (d-f) I–V curve of 2–4L defective $GaS_{0.87}$ thin film devices under dark and different power densities of 275 nm UV light. Inset: SEM images of fabricated Au–$GaS_{0.87}$–Au devices. (g) Power density dependence of photoresponsivity of CVD-grown large-scale GaS and $GaS_{0.87}$ thin film devices under UV light with a bias of 20 V. (h) I–t curves of bilayer $GaS_{0.87}$ and GaS thin film devices under 1.25 mW/cm$^{-2}$ strong 275 nm UV light. (i) I–t curves of trilayer $GaS_{0.87}$ and GaS thin film devices under 1.25 mW/cm$^{-2}$ strong 275 nm UV light. (j) I–t curve of bilayer $GaS_{0.87}$ thin film device's photoresponse to 102 μW/cm$^2$ 275 nm

UV light before and after exposure to 1.25 mW/cm$^{-2}$ strong 275 nm UV light for 120 s. (k) I–t curve of bilayer GaS thin film device's photoresponse to 102 μW/cm$^2$ 275 nm UV light before and after exposure to 1.25 mW/cm$^{-2}$ strong 275 nm UV light for 900 s. (l) Wavelength dependence of photoresponsivity of 2–3L stoichiometric GaS thin film devices (100 μW/cm$^2$, 20V). (m) Wavelength dependence of photoresponsivity of 2–3L defective $GaS_{0.87}$ thin film devices (100 μW/cm$^2$, 20V).

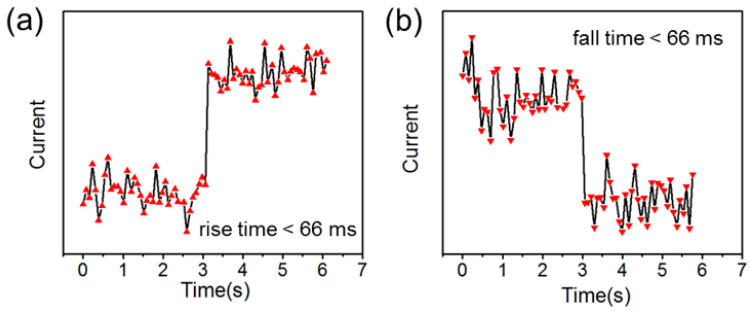



**Figure 5.9. Response time of GaS photodetectors under 275 nm illumination.** As shown in the figures, the current rise and drop is instant, indicating very short rise time and fall time below the detection limit.

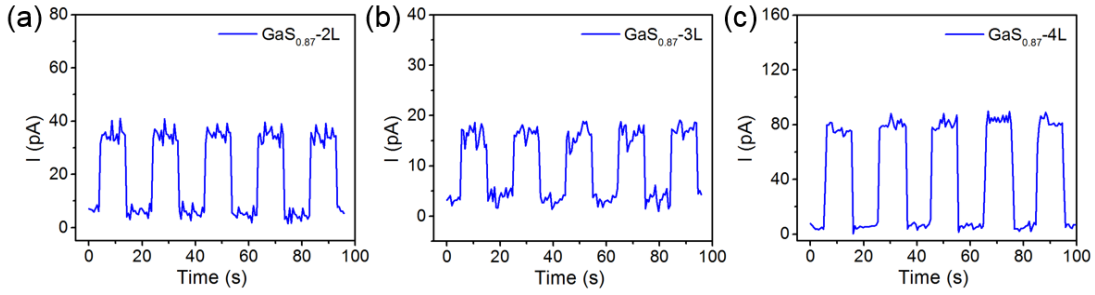



**Figure 5.10. Stable performance of $GaS_{0.87}$ devices under weak UV light (102 μW/cm$^2$).** (a-c) I–t curve of $GaS_{0.87}$ (a) bilayer, (b) trilayer, (c) 4-layer crystals with steady photocurrent.

**Table 5.2. Device performance of other UV-discriminating photodetectors**

| Material | Photoresponsivity (A/W) | Rise time/Fall time (s) | Wavelength(nm) | Ref |
|---|---|---|---|---|
| SiC thin film | 0.18 | 18/>100 | 250 | 18 |
| GaN-based p–i–n | 0.23 | -/- | 356 | 19 |
| ZnO nanoparticles | 13 | 250/150 | 370 | 20 |
| ZnO nanowires/graphene | 13.8 | 0.3/6.5 | - | 21 |
| $TiO_2$ nanorods | 0.01 | 1.4/6.1 | 365 | 22 |
| B-$Ga_2O_3$/graphene | 39.3 | 94.83/219.19 | 254 | 23 |
| InGaZnO Superlattice | $1.95 \times 10^5$ | 0.93/0.2 | 261 | 24 |
| 2D GaS | 0.05−10.2 | < 0.066 | 275 | This work |

### 5.2.3 Degradation Mechanism of 2D GaS

A series of experiments with the assistance of Dr. Philip Holdway and Dr. Jun Chen were further conducted to better understand the degradation behaviour and mechanisms of the defective $GaS_{0.87}$ under both high-intensity laser beam and high-energy UV light using XPS and HAADF-STEM, respectively.

As shown in Figure 5.11a-b, a 532 nm laser and a motorised stage were used to write a laser-annealed 200*200 matrix with a step size of 1 μm on monolayer $GaS_{0.87}$ continuous film, with each spot being annealed for 1 s. XPS was then conducted on the region with a spot size of ~150*150 $\mu m^2$ which suggested loss of sulfur from the film as the S:Ga ratio reduced from 0.88 to 0.69 (Fig. 5.11c). In addition, the Ga 3d peak position also shifted from 20.3 eV to 20.89 eV, very close to the Ga 3d peak in $Ga_2O_3$, indicating possible oxidation reaction.[25-26] However, the Raman spectrum of the annealed region showed no signals from $Ga_2O_3$ crystals.

HAADF-STEM was further employed to look directly at the structure changes during degradation. The sample was prepared by direct growth of $GaS_{0.87}$ crystals epitaxially on monolayer graphene films that had been first transferred onto SiN TEM grids with 2 μm windows (methods described in Chapter 3.2.5), similar to previous reports on

GaSe.[27] The monolayer $GaS_{0.87}$ crystals are very sensitive to beam irradiation thus bilayer and trilayer crystals were studied which are stable under the imaging environment. Figure 5.11d shows bilayer $GaS_{0.87}$ crystals with AA' stacking similar to the simulated results (Fig. 5.11f, Fig. 5.12). The graphene with low atomic number underneath the $GaS_{0.87}$ film could not be seen. Due to contaminations from CVD-grown graphene and polymer residues during the transfer process, it was difficult to resolve every sulfur vacancy, however, certain sulfur vacancies in the lattice can be clearly seen in Figure 5.11e. Then the TEM grid was put under 1.25 $mW/cm^{-2}$ strong 275 nm UV light for 15 min and put back to check for structure changes. Figure 5.11h is the enlarged image corresponding to the area shown in the bilayer $GaS_{0.87}$ region in Figure 5.11g. As can be seen, in most areas the lattice was undamaged, and fast Fourier transform (FFT) image showed similar 6-fold symmetry patterns. However, disorder appeared in many nano-sized regions indicating degradation, and unlike the degradation in TMDs, there were no clusters. The formation of these nanoholes was instantly reflected by the impairment of optoelectronic properties shown in Figure 5.8h-j. In contrast, degradation in trilayer $GaS_{0.87}$ crystals are less obvious (Fig. 5.11i). After another 45 min of UV light illumination, the crystal disorder was much more serious. No hexagonal lattice can be observed from the original bilayer region shown in Figure 5.11k, and the broad ring-shaped FFT patterns suggest that the $GaS_{0.87}$ crystals have been transformed into an amorphous phase. EDX was performed in the degraded region and no signal from S element was detected (Fig. 5.11k). Based on the elemental composition, the degraded substance is most likely to be amorphous $Ga_2O_3$. In addition, Figure 5.11l showed that the trilayer $GaS_{0.87}$ crystals have not completely degraded yet. The 6-fold symmetry spots in FFT patterns became weaker and the same ring-shaped as in Figure 5.11k also appeared.

It appears that the final products from laser and UV light damage are very similar to each other, as they both showed loss in sulfur, lack of crystallinity and absence of clusters. The degradation behaviour of the defective $GaS_{0.87}$ can be summarised as follows. First, photo-induced degradation should start from the absorption of $O_2$ molecules at exposed S vacancy sites. Yang et al.[9] showed that physisorbed $O_2$ molecules on monolayer GaS serve as acceptors of electrons, which favours oxidation of GaS. With the assistance of either thermal energy from the laser beam or being energised into an excited state by UV light, the Ga atoms could be oxidised into Ga (III) to form $GaS_xO_y$, where the oxidisation and loss of sulfur continue until it was transformed completely into amorphous $Ga_2O_3$. As a conjecture, the degradation could be greatly suppressed by encapsulation or inert gas protection, as have been shown to be effective in GaSe and GaTe.[10, 28] Second, the $GaS_{0.87}$ crystals degradation rate varies with thickness. After 1 hour exposure to strong UV light, the bilayer $GaS_{0.87}$ layers are completely destroyed while some lattice can still be observed in trilayer $GaS_{0.87}$. Similar degradation behaviour is also noticed in laser-related experiments, where trilayer $GaS_{0.87}$ requires 30 s of annealing for the signals to disappear but monolayer $GaS_{0.87}$ requires less than 5 s, and degradation in bulk GaS crystals was not noticed. Amorphous $Ga_2O_3$ has been observed on the surface of gallium metals, where a less than 3 nm native oxide layer skin can prevent further oxidation of the inner metal.[29-30] This suggests that the degraded amorphous $Ga_2O_3$ could slow down further degradation underneath. Third, the defective $GaS_{0.87}$ crystals, although having a large amount of sulfur vacancies (13%), are surprisingly stable in ambient conditions. Samples after 8 months of storage in air showed little difference to fresh samples from every aspect, including optoelectronic properties. It should be investigated in the future whether these stable defects can be of use in optics, magnetics or other fields after proper protection

from degradation. In summary, the degradation behaviour of $GaS_{0.87}$ is quite unique in comparison with other 2D materials, and this could provide valuable information for other degradation studies.

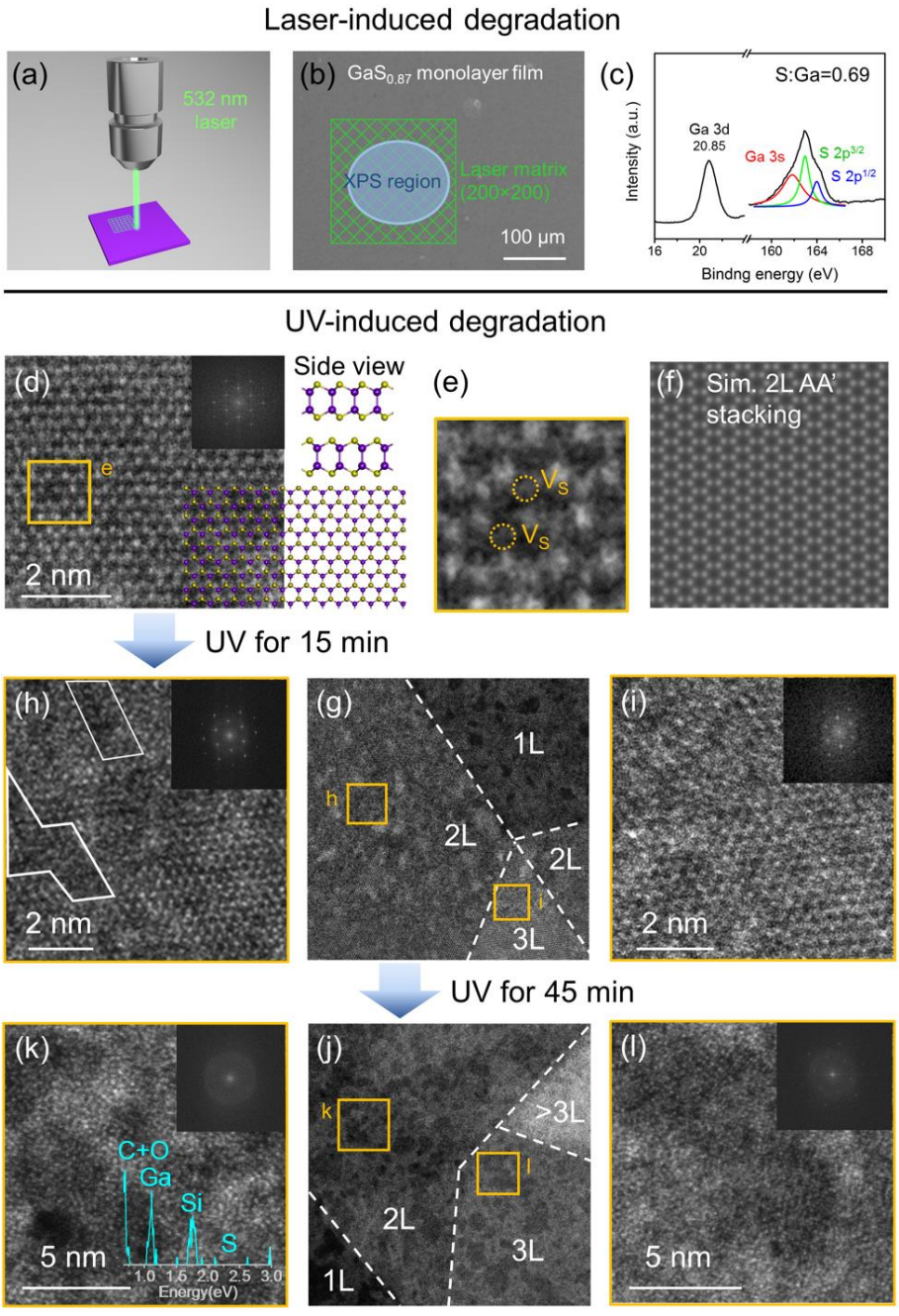



**Figure 5.11. Degradation mechanisms of $GaS_{0.87}$ films.** (a) Schematics of matrix written by laser using motorised stage. (b) SEM image of monolayer $GaS_{0.87}$ film after laser annealing and the position of XPS characterisation. (c) XPS spectrum of monolayer $GaS_{0.87}$ film after laser annealing. (d) HAADF-STEM image of bilayer AA' stacking $GaS_{0.87}$ crystal. Inset:

Corresponding FFT images of the figure. (e) Enlarged image of selected region showing sulfur vacancies. (f) Simulated bilayer AA' stacking GaS crystal. (g) HAADF-STEM image of $GaS_{0.87}$ crystal after 15 min exposure to strong UV light. (h-i) Enlarged image from (g) of bilayer and trilayer $GaS_{0.87}$ crystal after 15 min exposure to strong UV light. Inset: Corresponding FFT images of the area. (j) HAADF-STEM image of $GaS_{0.87}$ crystal after another 45 min exposure to strong UV light. (k) Enlarged image from (j) of bilayer $GaS_{0.87}$ crystal after 45 min exposure to strong UV light and EDX spectrum of the region showing no existence of S. Inset: Corresponding FFT images of the area. (l) Enlarged image from (j) of trilayer $GaS_{0.87}$ crystal after 45 min exposure to strong UV light. Inset: Corresponding FFT images of the area.

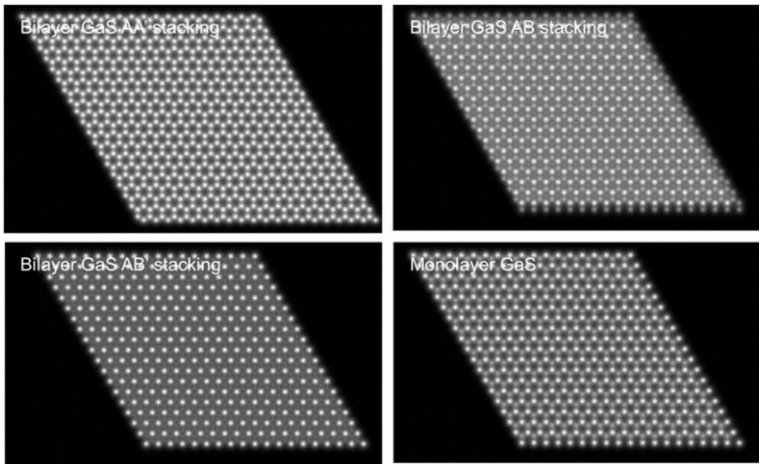



**Figure 5.12. Simulations of possible stackings of bilayer GaS and monolayer GaS under HAADF-STEM.**

Finally, owing to the unique UV-discriminating photoresponse, ultrashort response time, large on/off ratio, robustness and stable performance of the stoichiometric 2D GaS crystals, the device arrays are used for information encoding with UV lights, with the simplest design of 'on' state being '1' and 'off' state being '0'. As illustrated in Figure 5.13a, unlike most 2D crystals with small bandgap which would respond to both

visible light and UV light, the large bandgap ensures that GaS crystals only shows large photocurrent when excited with UV light, while no signal is detected when excited with visible light. The non-detectable photoresponse to strong and broadband white light LEDs (1.35 mW/cm$^2$, 400-700 nm) is shown in Figure 5.13b. Therefore, it is suitable for information encoding under noise of visible light/room light background, or be employed as a separate information receiving channel in addition to another broadband 2D semiconductor photodetector. Figure 5.13c shows the performance of bilayer GaS device's response to weak 65 μW/cm$^2$ 275 nm UV light under simultaneous excitation with a strong 9.2 μW 532 nm green light laser (with a laser spot diameter of 5 μm). When there was green light only, the current was 5.8 pA. It increased to 66 pA under both green and UV light, hence gives a signal to noise ratio of 10.4. In comparison, the same condition was applied to monolayer $MoS_2$ synthesised in Chapter 4. It generated a large photocurrent of 0.95 μA with strong green light alone, and 1.35 μA under both green and UV light (Fig. 5.13d). The signal generated by UV light was immersed in the background signal from green light, giving a very low signal to noise ratio of 0.4. Therefore, by using large bandgap semiconductors, a 26-times increase of sensitivity was achieved for information encoding by UV light under large green light background. In addition, the response time of $MoS_2$ for UV light is ~41 s (due to photogating mechanism where minority carriers gradually transferred to interfaces or nearby molecules until saturation), while the response time of GaS is beyond the detection limit (<66 ms), which is a critical advantage in high-speed information storage. The distinctive response to two different lights in these two materials also makes them a good candidate for dual-channel information encoding, with GaS responding only to deep-UV light while $MoS_2$ responds mainly to green light.

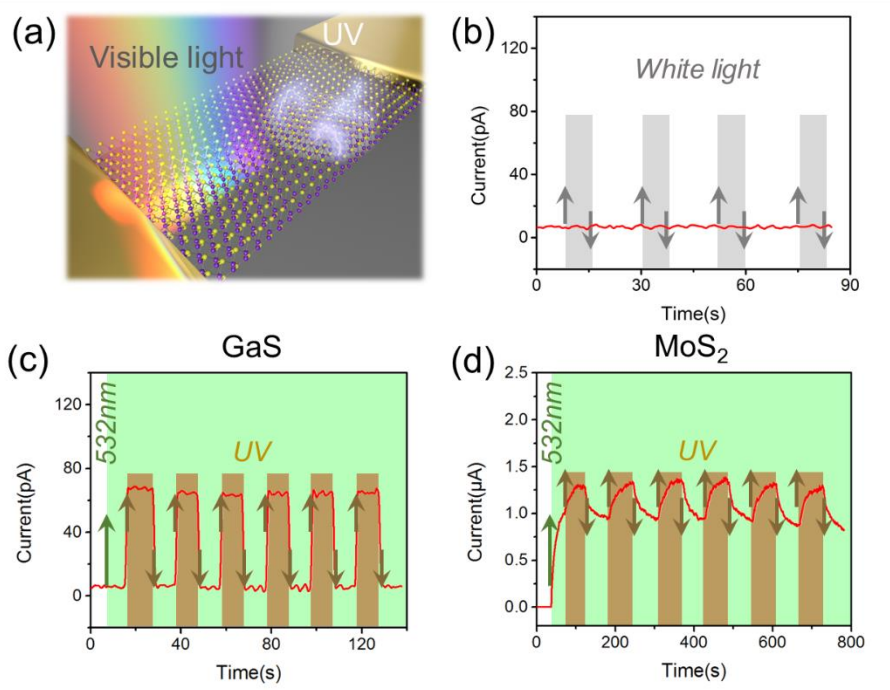



**Figure 5.13. Application of GaS devices in information encoding by UV light.** (a) Schematic illustration of UV-discriminating response in GaS optoelectronic devices. (b) I–t curve of GaS devices response to white light LED (1.35 mW/cm$^2$, 400-700 nm). (c) I–t curve of GaS thin film devices response to UV light (65 μW/cm$^2$) under green laser background (9.2 μW). (d) I–t curve of $MoS_2$ thin film devices response to UV light under green laser background.

## 5.3 Conclusion

In this chapter, a detailed study of the layer-dependent synthesis, characterisation, degradation behaviour and device performance of the defective $GaS_{0.87}$ and stoichiometric GaS is presented. Large area and uniform films of 1–4 layer thickness are synthesised by CVD and the stoichiometry is controlled by the ratio of absorbed reactive species. Stoichiometric GaS shows much stronger light-matter interactions. Enhanced stability and UV-discriminating photoresponse was observed in stoichiometric GaS while the defective $GaS_{0.87}$ showed photoresponse to certain visible

wavelengths. Using XPS and ADF-STEM, photo-induced degradation of defective $GaS_{0.87}$ is related to sulfur vacancies and absorbed $O_2$. Degradation product, the amorphous $Ga_2O_3$, serves as encapsulation for protecting further degradation. The defective $GaS_{0.87}$ is stable without exposure to strong light, which provides a good platform to study the effect of defects in Chapter 7. Finally, the stoichiometric GaS was used in fabrication of large-scale high-performance device arrays for information encoding with UV-discriminating sensitivity, showing a 26-times increase of signal-to-noise ratio under visible light background than $MoS_2$ devices. These findings provide a thorough study (from atomic-scale structures to large-scale device performances) of the stability of GaS crystals, and demonstrate that pristine 2D GaS crystals are stable in ambient conditions and could be used in high performance sensors, photodetectors, photoswitches and short-wavelength LEDs.

## 5.4 References


1. Özçelik, V. O.; Azadani, J. G.; Yang, C.; Koester, S. J.; Low, T., Band Alignment of Two-Dimensional Semiconductors for Designing Heterostructures with Momentum Space Matching. *Phys. Rev. B.* **2016**, *94*, 035125.
2. Castellanos-Gomez, A., Why all the fuss about 2D semiconductors? *Nat. Photonics* **2016**, *10*, 202.
3. Xia, F.; Wang, H.; Xiao, D.; Dubey, M.; Ramasubramaniam, A., Two-Dimensional Material Nanophotonics. *Nat. Photonics* **2014**, *8*, 899.
4. Late, D. J.; Liu, B.; Luo, J.; Yan, A.; Matte, H. S. S. R.; Grayson, M.; Rao, C. N. R.; Dravid, V. P., GaS and GaSe Ultrathin Layer Transistors. *Adv. Mater.* **2012**, *24*, 3549-3554.
5. Luxa, J.; Wang, Y.; Sofer, Z.; Pumera, M., Layered Post-Transition-Metal Dichalcogenides (X−M−M−X) and Their Properties. *Chem. Eur. J.* **2016**, *22*, 18810.
6. Jung, C. S.; Shojaei, F.; Park, K.; Oh, J. Y.; Im, H. S.; Jang, D. M.; Park, J.; Kang, H. S., Red-to-Ultraviolet Emission Tuning of Two-Dimensional Gallium Sulfide/Selenide. *ACS Nano* **2015**, *9*, 9585-9593

7. Li, X.; Tao, L.; Chen, Z.; Fang, H.; Li, X.; Wang, X.; Xu, J.-B.; Zhu, H., Graphene and Related Two-Dimensional Materials: Structure-Property Relationships for Electronics and Optoelectronics. *Appl. Phys. Lett.* **2017**, *4*, 021306.

8. Hu, P.; Wang, L.; Yoon, M.; Zhang, J.; Feng, W.; Wang, X.; Wen, Z.; Idrobo, J. C.; Miyamoto, Y.; Geohegan, D. B.; Xiao, K.; Highly Responsive Ultrathin GaS Nanosheet Photodetectors on Rigid and Flexible Substrates. *Nano Lett.* **2013**, *13*, 1649-1654.

9. Yang, S.; Li, Y.; Wang, X.; Huo, N.; Xia, J.-B.; Li, S.-S.; Li, J., High Performance Few-Layer GaS Photodetector and its Unique Photo-Response in Different Gas Environments. *Nanoscale* **2014**, *6*, 2582-2587.

10. Wang, X.; Sheng, Y.; Chang, R.-J.; Lee, J. K.; Zhou, Y.; Li, S.; Chen, T.; Huang, H.; Porter, B. F.; Bhaskaran, H.; Warner, J. H., Chemical Vapour Deposition Growth of Two-Dimensional Monolayer Gallium Sulfide Crystals Using Hydrogen Reduction of $Ga_2S_3$. *ACS Omega* **2018**, *3*, 7897-7903.

11. Zhou, J.; Shi, J.; Zeng, Q.; Chen, Y.; Niu, L.; Liu, F.; Yu, T.; Suenaga, K.; Liu, X.; Lin, J., InSe Monolayer: Synthesis, Structure and Ultra-High Second-Harmonic Generation. *2D Mater.* **2018**, *5*, 025019.

12. Gan, X.; Zhao, C.; Hu, S.; Wang, T.; Song, Y.; Li, J.; Zhao, Q.-H.; Jie, W.-Q.; Zhao, J.-L., Microwatts Continuous-Wave Pumped Second Harmonic Generation in Few- and Mono-layer GaSe. *Light Sci. Appl.* **2018**, *7*, 17126.

13. Jia, T.; Fuh, H.; Chen, D.; Abid, M.; Abid, M.; Zhang, D.; Sarker, A. B.; Cho, J.; Choi, M.; Chun, B. S.; Xu, H.; Coileain, C. O.; Liu, H.; Chang, C.-R.; Wu, H.-C. Giant and Linear Piezo-Phototronic Response in Layered GaSe Nanosheets. *Adv. Electron. Mater.* **2018**, *4*, 1700447.

14. Antonius, G.; Qiu, D. Y.; Louie, S. G. Orbital Symmetry and the Optical Response of Single-Layer MX Monochalcogenides. *Nano Lett.* **2018**, *18*,1925-1929.

15. Yang, Z.; Jie, W.; Mak, C.-H.; Lin, S.; Lin, H.; Yang, X, Yan, F.; Lau, S. P.; Hao, J., Wafer-Scale Synthesis of High-Quality Semiconducting Two-Dimensional Layered InSe with Broadband Photoresponse. *ACS Nano* **2017**, *11*, 4225-4236.

16. Yan, F.; Zhao, L.; Patane, A.; Hu, P, Wei, X.; Luo, W.; Zhang, D.; Lv, Q.; Feng, Q.; Shen, C.; Chang, K.; Eaves, L.; Wang, K., Fast, Multicolor Photodetection with Graphene-Contacted p-GaSe/n-InSe van der Waals Heterostructures. *Nanotechnology* **2017**, *28*, 27LT01.

17. Late, D. J.; Liu, B.; Matte, H.; Rao, C. N. R.; Dravid, V. P., Rapid Characterization of Ultrathin Layers of Chalcogenides on $SiO_2$/Si Substrates. *Adv. Funct. Mater.* **2012**, *22*, 1894-1905.

18. Aldalbahi, A.; Li, E.; Rivera, M.; Velazquez R.; Altalhi T.; Peng X.; Feng P., A New Approach for Fabrications of SiC Based Photodetectors. *Sci. Rep.* **2016**, 6, 23457.

19. Butun, B.; Tut T.; Ulker, E.; Yelboga, T.; Ozbay, E., High-Performance Visible-Blind GaN-Based p-i-n Photodetectors. *Appl. Phys. Lett.* **2008**, *92*, 033507.

20. Nasiri, N.; Bo, R.; Wang, F.; Fu, L.; Tricoli, A., Ultraporous Electron-Depleted ZnO Nanoparticle Networks for Highly Sensitive Portable Visible-Blind UV Photodetectors. *Adv. Mater.* **2015**, *27*, 4336-4343.

21. Liu, J.; Lu, R.; Xu, G.; Wu, J.; Thapa, P.; Moore, D., Development of a Seedless Floating Growth Process in Solution for Synthesis of Crystalline ZnO Micro/Nanowire Arrays on Graphene: Towards High-Performance Nanohybrid Ultraviolet Photodetectors. *Adv. Funct. Mater.* **2013**, *23*, 4941-4948.

22. Wang, Z.; Wang, H.; Liu, B.; Qiu, W.; Zhang, J.; Ran, S.; Huang, H.; Xu, J.; Han, H.; Chen, D.; Shen, G., Transferable and Flexible Nanorod-Assembled $TiO_2$ Cloths for Dye-Sensitized Solar Cells, Photodetectors, and Photocatalysts. *ACS Nano* **2011**, *5*, 8412-8419.

23. Kong, W.-Y.; Wu, G.-A.; Wang, K.-Y.; Zhang, T.-F.; Zou, Y.-F.; Wang, D.-D.; Luo, L.-B., Graphene-β-$Ga_2O_3$ Heterojunction for Highly Sensitive Deep UV Photodetector Application. *Adv. Mater.* **2016**, *28*, 10725-10731.

24. Li, F.; Meng, Y.; Dong, R.; Yip, S.; Lan, C.; Kang, X.; Wang, F.; Chan, K.S. Ho, J.C., High-Performance Transparent Ultraviolet Photodetectors Based on InGaZnO Superlattice Nanowire Arrays. *ACS Nano* **2019**, *13*, 12042-12051.

25. Ishikawa, T.; Ikoma, H., X-Ray Photoelectron Spectroscopic Analysis of the Oxide of GaAs. *Jpn. J. Appl. Phys.* **1992**, *31*, 3981.

26. Catalán-Gómez, S.; Briones, M.; Redondo-Cubero, A.; Palomares, F. J.; Nucciarelli, F.; Lorenzo, E.; Pau, J. L., The Role of the Oxide Shell in the Chemical Functionalization of Plasmonic Gallium Nanoparticles. *Proc. of SPIE* **2017**, *10231*, 102310D-1.

27. Li, X.; Basile, L.; Huang, B.; Ma, C.; Lee, J. W.; Vlassiouk, I. V.; Puretzky, A. A.; Lin, M.-W.; Yoon, M.; Chi, M.; Idrobo, J. C.; Rouleau, C. M.; Sumpter, B. G.; Geohegan, D. B.; Xiao, K. Van der Waals Epitaxial Growth of Two-Dimensional Single-Crystalline GaSe Domains on Graphene. *ACS Nano* **2015**, *9*, 8078-8088.

28. Zhao, Q.; Frisenda, R.; Gant, P.; Perez de Lara, D.; Munuera, C.; Garcia-Hernandez, M.; Niu, Y.; Wang, T.; Jie, W.; Castellanos-Gomez, A., Toward Air Stability of Thin GaSe Devices: Avoiding Environmental and Laser-Induced Degradation by Encapsulation. *Adv. Funct. Mater.* **2018**, *28*, 1805304.

29. Dickey, M. D., Emerging Applications of Liquid Metals Featuring Surface Oxides. *ACS Appl. Mater. Interfaces* **2014**, *6*, 18369-18379.

30. Scharmann, F.; Cherkashinin, G.; Breternitz, V.; Knedlik, C.; Hartung, G.; Weber, T, Schaefer, J. A., Viscosity effect on GaInSn studied by XPS. *Surf. Interface Anal.* **2004**, *36*, 981-985.

# Chapter 6

# Commensurability of van der Waals Epitaxy in High-Mismatched Systems

## 6.1 Introduction

The high bonding anisotropicity of two-dimensional (2D) layered materials, with chemical bonds between intralayer atoms and van der Waals (vdWs) interactions between layers, opens two degrees of freedom compared with conventional 3D heterostructures: lattice mismatch and crystal orientation.[1] The freedom in lattice mismatch allows fabrication of arbitrary VLH with unlimited possibilities; and the freedom in crystal orientation has recently served as convenient platform for emerging quantum phenomena such as interlayer Moiré excitons and strongly-correlated electronic states.[2-6] However, tuning of the crystal orientation in bilayer systems has mainly been achieved by mechanical reassembly of individual layers in a low-output manner, thus it is desired to develop new approaches for precise and efficient control of orientation.

Epitaxy, the oriented overgrowth, has been frequently used for large-scale production of VLHs.[7-10] While conventional epitaxy is characterised by small lattice mismatch, identical crystal structure and 0°-orientation originated from the strong, directional and saturated covalent bonds (40-300 kcal/mol), vdWs epitaxy from relatively weak, non-directional and non-specific vdWs interactions (0-1 kcal/mol) is unique in relaxation of the lattice mismatch limit,[11-12] and that the growth orientation is ruled by alignment

between high-symmetry directions (0°-orientation) from two layers that can possess different in-plane symmetries.[13] Nevertheless, small-angle-misorientation is often noticed to accompany dominant 0°-orientation when significant lattice mismatch exists. While some attribute this to wrinkles or surface contamination, others believe these small misorientations have similar energy to the 0°-orientation.[14-16] In the above analysis and simulations, it is assumed that both crystal planes are perfect lattices without distortions. An alternative picture provided by the Frenkel-Kontorova (F-K) model proposes that atoms are affected simultaneously by harmonic interactions from intralayer neighbouring atoms as well as periodic potential wells from the other layer.[17-19] As a result, local atomic displacements and topological domain walls appear in Moiré patterns when every atom finds its energy-minimum position, which has been experimentally observed.[20-28] Still, previous studies are restricted to manual-stacked twisting VLHs with very small lattice mismatch (<1.8%), while its implications for epitaxy in high-mismatched vdWs heterostructures are poorly understood.

In this chapter, the concept of vdWs epitaxy from the F-K model and commensurability is revisited to demonstrate its potential in creating and tuning small-angle epitaxy in high-mismatch hexagonal VLHs. Commensurate multilevel maps were proposed which allow one to predict possible twist angles in any epitaxially-grown hexagonal VLHs. The theory is experimentally evidenced in two epitaxial high-mismatch (15%, 47%) systems under HAADF-STEM, with observation of discrete small angles (separated by ~1°).

## 6.2 Results and Discussion

### 6.2.1 Commensurate Multilevel Maps

In the 1D F-K model, the periodic potential tends to lock the system into low-order commensurate phases (C-phases) that constitute the ground state (Fig. 6.1).[29] Here commensurability indicates the formed heterostructure has translational symmetry (and incommensurability for lack of translational symmetry), and the order of C-phase is understood as the C-phase periodicity.[30]

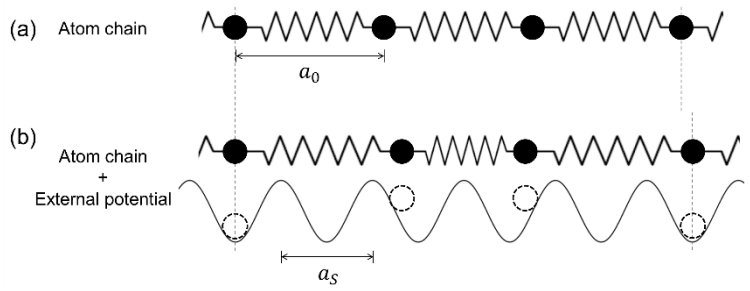



**Figure 6.1. Schematic presentation of the 1D Frenkel-Kontorova model.** (a) A chain of atoms interacting via harmonic springs with equilibrium distance $a_0$ in the absence of external potentials. (b) A chain of interacting atoms subject to external sinusoidal ($a_S$) substrate potential in a commensurate phase.

However, little progress has been made on the commensurate phase locking in 2D systems. Figure 6.2a shows a C-phase supercell formed by H-type stacking of $MX_2$-M'$X'_2$ bilayers with lattice mismatch η ($\eta \equiv a_B/a_A - 1, a_A < a_B$) of 15.13% and twist angle α of 1.00°. The interlayer potential at various positions could be approximated by the stacking energy of a homogenous bilayer heterostructure (i.e., without mismatch or misorientation) with a phase shift,[26, 28] where the variation in stacking energy from small twist angle is neglected.[17] The vdWs interaction at red points can be approximated by MX-type stacking energy (MX stacking indicates that metal[M] of layer A is right on top of chalcogen[X] of layer B), while interactions at green and blue points can be approximated by MM- and XX-type stacking (Fig. 6.2b). The position corresponding

to configuration with the lowest stacking energy is defined as the ideal stacking point (ISP), and the distance between adjacent ISP is the C-phase period. The ISP should satisfy symmetry rules, i.e., when high-symmetry points (3-fold rotational center) of the two layers overlap. As various experiment and simulation results have suggested the interlayer distance d(XX)>d(MM)>d(MX), the red spots in Figure 6.2b are marked as ISP.[26, 28] From the system energy viewpoint, atom displacements in the F-K model tend to increase the area of the low-energy regions around ISP and decrease high-energy regions between ISPs.[26, 31] Especially for high-mismatch systems, around each ISP, the area of region shifting to lower energy is limited in size due to large bond length difference. Thus, the low-order C-phase with high density of ISPs that can lower the total energy is the ground state.[32]

The locking behaviour in 1D F-K chains is described by the relationship between the ground state's average mismatch $\eta$ and the natural mismatch $\eta_0$ (when the atom-atom coupling is at the balanced position) in the 'devil's staircase' diagram: as $\eta_0$ increases, the value of $\eta$ after atom relaxation rises through an infinite number of stairs, each stair corresponding to one C-phase.[19, 29] The length of each stair increases with larger amplitude of the substrate potential and smaller period of the C-phase. From here on, this project proposes a 'commensurate multilevel map' of low-order C-phases with lattice mismatch and twist angle as *x*- and *y*-axis for describing the similar locking-in in 2D case. As the energy cost of small misorientations is trivial compared with that in lattice mismatch (Fig. 6.2c), each C-phase point is accompanied with a level (similar to the stair in Devil's staircase) in the *x*-direction referred as 'C-phase level'. The boundary of the level is when the energy cost in intralayer elastic potential is balanced with energy gain from interlayer potential. For any hexagonal VLHs with natural mismatch $\eta_0$, a vertical line at $x = \eta_0$ is drawn, and those C-phase levels crossing it are

low-energy configurations. Among these selected levels, those with smallest C-phase period comprise the ground states of the heterostructure, which determines the vdWs epitaxy. The map is named as the 'commensurate multilevel' in the following discussion as $\eta_0$ could be associated with multiple C-phases with similar stability (versus the 1D Devil's staircase).

To offer quantitative insights, the commensurate multilevel map for epitaxial hexagonal VLHs with $\eta_0$<25% is shown (Fig. 6.2f). According to the rigid Moiré theory, the Moiré superlattice formed by two hexagonal lattices is still hexagonal, and that it is unaffected by the number of layers or the phase shift of the crystals.[33] The plotted C-phases are derived from geometric relations (Fig. 6.2d-e). In reciprocal space, the Moiré pattern formed by (κ, 0) lattice point in crystal A ($\vec{k}_{A(\kappa,o)}$) and ($\lambda$, 0) lattice point in crystal B ($\vec{k}_{B(\lambda,0)}$) is described by

$$\vec{k}_{Moiré} = \vec{k}_{A(\kappa,o)} - \vec{k}_{B(\lambda,0)}. \tag{6.1}$$

Also in real space, the Moiré superlattice vector $\vec{a}_{Moiré}$ with length of *l* (in units of $a_A$) and orientation of γ (γ>0) to crystal A is expressed using base vectors from the hexagonal lattices (Fig. 6.2e):

$$\vec{a}_{Moiré} = \frac{\lambda}{\kappa}(m\overrightarrow{a_1} + n\overrightarrow{a_2}) = u\overrightarrow{b_1} + v\overrightarrow{b_2}. \tag{6.2}$$

If the unified form of mismatch η' is used ($\eta' \equiv \kappa \cdot a_B/\lambda \cdot a_A - 1$), then a unified expression for both first-order (κ=λ=1) and high-order (κ, λ≠1) Moiré lattice is obtained. For η', α>0:[33]

$$\begin{cases} l = \dfrac{a_{Moiré}}{a_A} = \dfrac{1+\eta'}{\sqrt{1+(1+\eta')^2 - 2(1+\eta')\cos\alpha}} \\ \cos\gamma = \dfrac{\cos\alpha - 1 - \eta'}{\sqrt{1+(1+\eta')^2 - 2(1+\eta')\cos\alpha}} \end{cases} \tag{6.3}$$

From the above relations, the coordinates (*m*, *n*) and (*u*, *v*) is determined by η', α through:

$$\begin{cases} m = 2l * \sin(90 - \gamma) \\ n = 2l * \sin(\gamma + 30) \\ u = 2\dfrac{l}{1+\eta'}\sin(90 - \alpha - \gamma) = m - 2 \\ v = 2\dfrac{l}{1+\eta'}\sin(\alpha + \gamma + 30) = n - 1. \end{cases} \tag{6.4}$$

Thus, the superlattice parameter η, α is converted into coordinate (*m*, *n*) in equation 6.3 and 6.4. As commensurability requires that the Moiré superlattice period is a rational fraction of the lattice period, a factor *Q* is defined:

$$\begin{cases} \dfrac{\lambda}{\kappa} \cdot m = M/Q \\ \dfrac{\lambda}{\kappa} \cdot n = N/Q \end{cases} \tag{6.5}$$

where either (*M*, *Q*) or (*N*, *Q*) are co-prime integers. The plotted C-phases in Figure 6.2f are simple C-phases (κ=λ=1, *Q*=1) with period $d = \sqrt{M^2 + N^2 - MN}$ (in units of $a_1$). The C-phase period is characterised by periodic changes in stacking energy, thus it is different from but still closely related to the heterostructure's Moiré supercell. Since the area density of ISPs of unplotted C-phases (*Q*>1) is at most 25% of that of plotted ones, simple C-phases are much more energy-favourable than others. Also, the neighbouring simple C-phases should be similarly energy-favourable as variance in *d* value is within 10%. Consequently, simple C-phases are ground states in this mapping.

Next, the two-chain F-K model was applied to estimate the half-length of the C-phase level ($\Delta\eta_C$). The model considers structural relaxation of both layers and has been successfully applied in study of topological defects in vdWs systems such as double-walled carbon nanotubes, bilayer graphene, and graphene/boron nitride heterostructures.[34-36] By applying a few modifications, the model can be used to

describe high-mismatch bilayer vdWs systems. To continue our assumption that the energy cost from small misorientation can be neglected compared to that from universal strain, the stacking energy under small misorientation is approximated by that under 0°-orientation and only biaxial strain is allowed. In fact, it was pointed out that under small twist angles the dislocation energy of the domain wall is very similar to that under 0°-orientation.[17] The topological change of such system under lattice mismatch or twist angle can be described by hexagonal networks of domain wall, whose length is the C-phase period *d*. According to Lebedeva and Popov, the dislocation energy per unit length of a single domain wall is described by the F-K soliton solution:[35-36]

$$W_{DW} = \left(\frac{3\sqrt{3}}{\pi} - 1\right) a \sqrt{\frac{2 g_0 \varepsilon_{inter}}{1 - \nu^2}} \tag{6.6}$$

In the equation, $g_0$ is the reduced elastic constant (Young's modulus) of both layers, $\nu$ is the Possion ratio, $\varepsilon_{inter} = \varepsilon_0/2$, where $\varepsilon_0$ is the stacking energy difference between the highest and lowest stacking configurations. Subsequently, they obtain the critical mismatch value for formation of networks of domain walls from coincident lattice (0%-mismatch):

$$\eta_C = (1 - \nu) \frac{W_{DW}}{g_0 a} \tag{6.7}$$

which can be interpreted as the relative value between the intralayer elastic energy (related to $\eta_C g a/(1-\nu)$) and the interlayer potential energy $W_{DW}$.

To obtain the critical mismatch value for any C-phase, the critical mismatch value $\eta_C$ from coincident lattice is generalised as the half-length of the C-phase level $\Delta\eta_C(d)$. For a given C-phase with mismatch value P, the C-phase corresponds to the ground state of the system with $\eta_0$ between:

$$P - \Delta\eta_C(d) < \eta_0 < P + \Delta\eta_C(d) \tag{6.8}$$

In addition, equation 6.7 is used where the reference structure is a coincident lattice. For domain wall configurations on the background of other referenced commensurate structures with domain wall networks, the elastic constant in $W_{DW}$ is no longer the elastic constant between atoms, but the elastic constant between domain walls $g(p) = \frac{g_0}{d}$.[19] After taking the above considerations, the general critical mismatch value becomes

$$\Delta\eta_C(d) = \left(\frac{3\sqrt{3}}{\pi} - 1\right)\sqrt{\frac{1-\nu}{1+\nu}}\sqrt{\frac{\varepsilon_{inter}}{dg_0}}. \tag{6.9}$$

Similar to the 1D devil's staircase, the half-length increases with smaller C-phase period.

By adding results from equation 6.9 into Figure 6.2f, the complete picture of the commensurate multilevel is shown. The following parameters are used for purpose of general discussions: $\nu$=0.2, $\varepsilon_{inter}$=40 meV/nm$^2$≈0.064 J/m$^2$, $g_0$=100 J/m$^2$. Various epitaxial behaviours exhibit at different $\eta_0$ as simple C-phases become sparser at higher $\eta$. For example, in small-mismatch vdWs systems (0−5%), 205 C-phase levels cross with $\eta_0$=4.5% that are nearly undistinguishable between 0−5° (Fig. 6.2g), therefore vdWs epitaxy appears as predominantly 0°-orientation, in accordance with previous findings. After a transition period in the medium-mismatch range (5−15%), in high-mismatch systems (15−25%), only five simple C-phase levels cross with $\eta_0$=15.5%. The orientation might no longer occur at 0° and are separated by more than 1°, thus vdWs epitaxy appears as several discrete orientations. For $\eta_0$>25%, the vertical line may not cross with simple C-phase levels, thus different commensurate multilevel maps showing other C-phases (Q>1 or $\kappa$, $\lambda \neq 1$) were drawn for discussion. Figure 6.2h further shows the total number of stable simple C-phase levels under different natural

mismatch values. Limited by the ability to resolve very small angles, it is difficult to differentiate low-order C-phases and others in small-mismatch vdWs systems. Alternatively, high-mismatch vdWs systems with $\eta_0 \geq 15\%$ that are previously less explored could help examine the map.

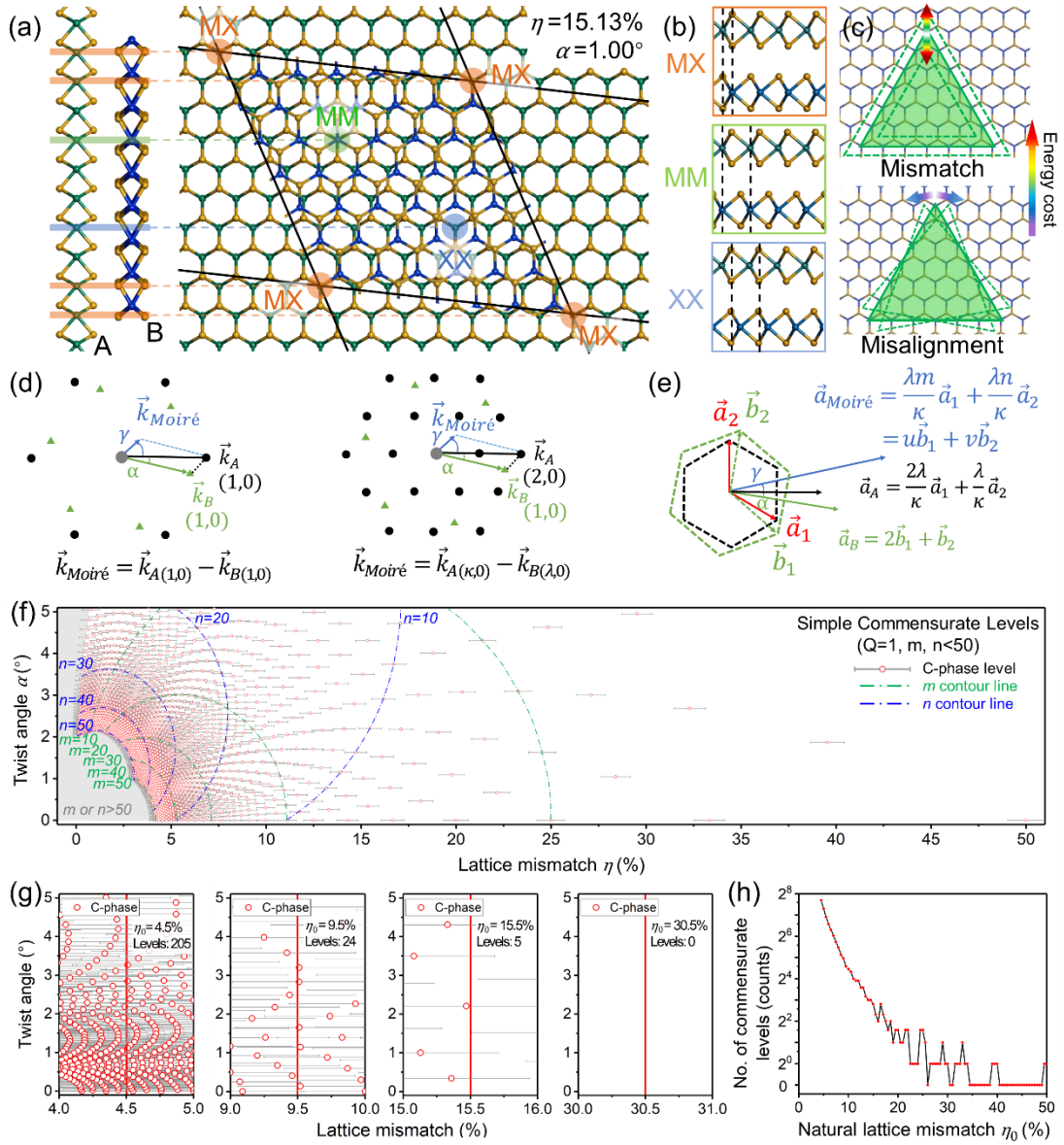



**Figure 6.2. Commensurability in vdWs epitaxy between hexagonal crystals.** (a) Side-view and top-view of the unit cell of a commensurate hexagonal VLH of $MX_2$-M'$X'_2$ ($\eta$=15.13%, $\alpha$=1.00°). (b) Side-view of three symmetric types of stacking in hexagonal $MX_2$-M'$X'_2$ VLH. (c) Relative energy cost for transition in freedom of mismatch and freedom of misorientation

for VLH. (d) Illustration of rigid Moiré model in reciprocal space. Left: basic Moiré superlattice from (1,0) lattice points; Right: high-order Moiré superlattice from (κ,0) and (λ,0) lattice points. (e) Schematic of selected base vectors for describing hexagonal Moiré superlattice vector in real space. (f) Commensurate multilevel map consisting of simple C-phase levels, which are C-phases from basic Moiré superlattice (κ=λ=1) with $Q$=1. To reduce data size, only $m$, $n$ under 50 is plotted. These simple C-phases possess lower system energy compared with nearby complex C-phases or incommensurate phases. (g) Number of simple C-phase levels when the natural lattice mismatch is 4.5%, 9.5%, 15.5%, 30.5%, respectively. (h) Relationship between the number of simple C-phase levels with natural lattice mismatch from 4.5% to 50%.

In the absence of simple C-phases, the C-phase multilevel diagram for >25% mismatch needs to be analysed case by case when more complex C-phases become ground states. Below one example is given whose results will be examined against experiment results from GaS/graphene. Measurement results of GaS/graphene show an average lattice mismatch around 46.5%. As the average lattice mismatch could derive from multiple C-phases, the commensurate multilevel map in the range of 45.5-47.5% is drawn. In addition, considering an average level length of 0.5%, C-phases in the range of 45.0-48.0% is included in Figure 6.3a-c to find out the ground states. Since the total number of C-phases are unlimited, candidates of low-order C-phases are first shortlisted, which are plotted in Figure 6.3a-c where each diagram corresponding to a different set of κ, λ, then these candidates are compared with each other to generate Figure 6.3d. In Figure 6.3a, the smallest $Q$ value of C-phases from basic Moiré superlattice (κ=λ=1) is 3 (labelled D1), thus C-phases with $Q$≤6 were listed in Figure 6.3a and C-phases from high-order Moiré superlattices until λ>3 in Figure 6.3b-c for finding all C-phases with similar or shorter period to C-phase D1. In Figure 6.3b-c, the κ, λ of high-order Moiré

superlattices is selected based on the Moiré vectors in reciprocal space (Fig. 6.4), and the (*m*, *n*) coordinates of those C-phases are determined by modifying the *x*-axis η in Fig. 6.2f into $[(\eta+1)\frac{\lambda}{\kappa}-1]$. Note that if $[(\eta+1)\frac{\lambda}{\kappa}-1]<0$, then the *x*-axis η should be changed into $[1/(\eta+1)\frac{\lambda}{\kappa}-1]$, and the map shows the (*u*, *v*) coordinates. After plotting all candidates in Figure 6.3a-c, the C-phases with five shortest period are chosen as D1-D5 and plotted in Figure 6.3d, where the five C-phase levels split the map into several regions: D1 ($45.54<\eta_0<45.64$), D1+D4 ($45.64<\eta_0<45.86$), D1+D5 ($45.86<\eta_0<46.62$), D5 ($46.62<\eta_0<47.02$), D2+D3 ($47.02<\eta_0<47.12$), D2 ($47.12<\eta_0<47.48$), and other high-order C-phases ($45.5<\eta_0<45.54$, $47.48<\eta_0<47.5$). The half-length of the C-phase level is estimated using equation 6.4 with the same parameters used for Figure 6.2f. Each region corresponds to one result of epitaxial orientations when the $\eta_0$ value is in the region. Note that compared with the simple C-phase levels where neighboring ones have similar period, these C-phases differ in ISP area densities and are different in system energy, thus vdWs epitaxy should preferably adopt small period C-phases. As a result, despite that D2, D3 and D5 levels meet at $\eta_0$=47.0%, the ISP area density of D2, D3 is only 45% of that of D5, which implies vdWs epitaxy mainly adopts D5.

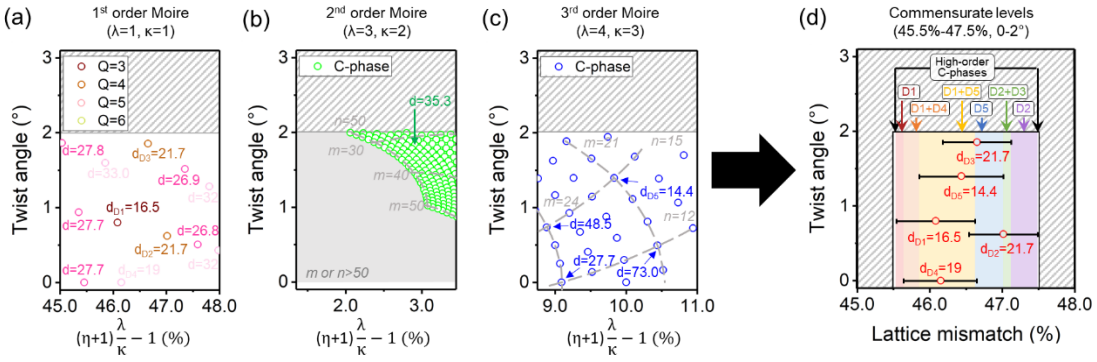



**Figure 6.3. Construction of complex commensurate multilevel diagram examples in ultrahigh-mismatch systems.** (a) Low-order commensurate phases from first-order Moiré

lattices ($\kappa$=$\lambda$=1 and 3≤$Q$≤6) and their periodicity with lattice mismatch between 45.0-48.0%. (b-c) Low-order commensurate phases from second and third-order Moiré lattices ($\kappa$>1, $\lambda$>1 and $Q$=1) and their periodicity with lattice mismatch between 45.0-48.0%. Searching for potential candidates with small period could be assisted by the same map of Figure 6.2f. By changing the $x$-axis $\eta$ into $[(\eta+1)\frac{\lambda}{\kappa}-1]$, the (m, n) coordinates, especially those containing factor of $\kappa$, is selected, followed by calculating their period. (d) Commensurate multilevel diagram for lattice mismatch between 45.5-47.5%, consisting of five C-phases analysed in (a-c) with the shortest periods.

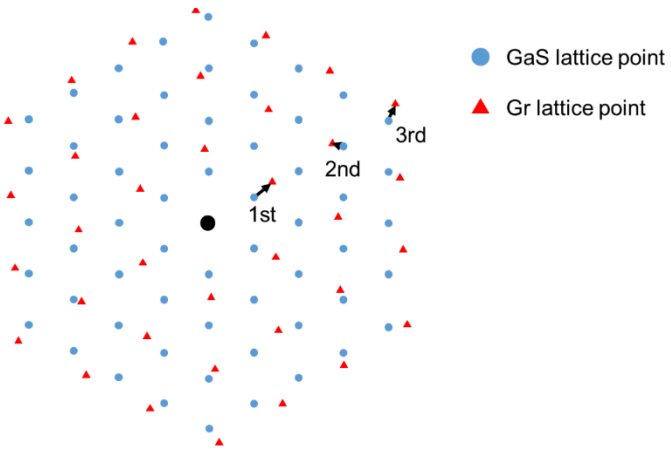



**Figure 6.4. Schematic presentation of GaS/graphene high-order Moiré patterns from rigid Moiré theory in reciprocal space.** The 1st order Moiré patterns are formed by (1, 0) lattice points of GaS and graphene; The 2nd order Moiré patterns are formed by (2, 0) lattice points of graphene and (3, 0) lattice points of GaS; And the 3rd order Moiré patterns are formed by (3, 0) lattice points of graphene and (4, 0) lattice points of GaS.

### 6.2.2 Growth and Characterisation of High-Mismatched Epitaxial Systems

Two high-mismatch vdWs systems, GaS/$MoS_2$ and GaS/graphene, with lattice mismatch values of 15% and 47%, were chosen to test the universality of the above

theory. Note that a complete study further investigates an additional 20 regions from $PtSe_2/WS_2$, $SnS_2/WS_2$ and $PbI_2$/graphene heterostructures whose results also concur with this study, but were not included here since they were synthesised and characterised by other people. The accurate lattice information was captured under atomic resolution HAADF-STEM with the assistance of Dr. Jun Chen. In most cases, the synthesised heterostructure is bilayer so that lattice information from both crystals can be clearly seen (Fig. 6.5). The region size is typically between 10-20 nm to capture both short-range lattice and long-range superlattice features.

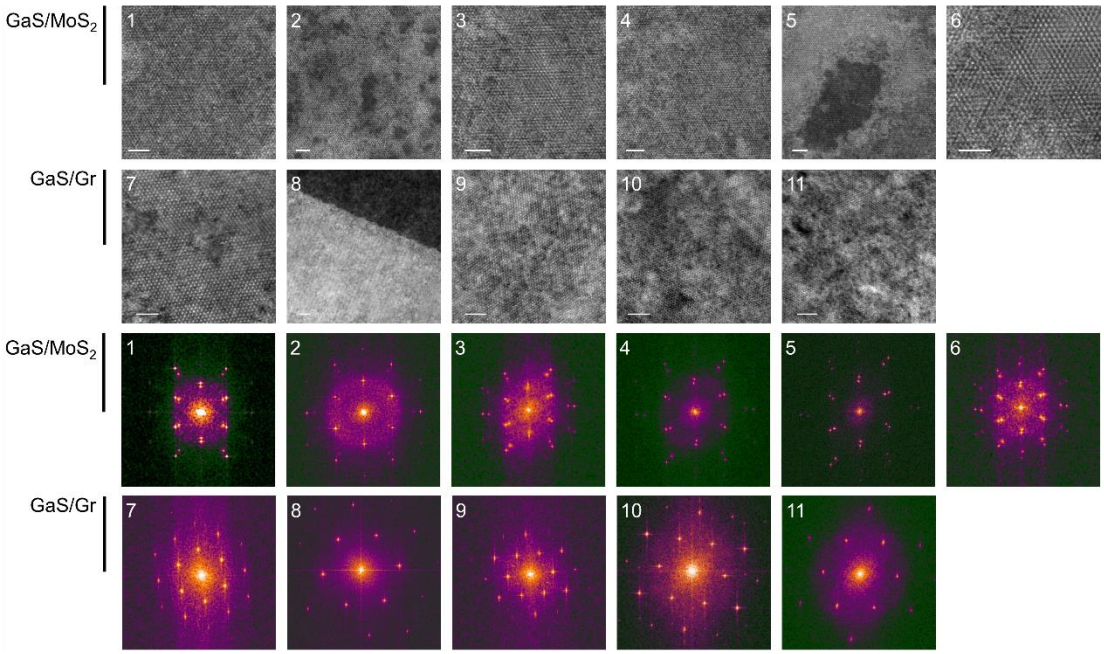



**Figure 6.5. ADF-STEM and corresponding FFT images of 11 different regions of 2D hexagonal VLHs.** (Scale bar: No.1-6: 2 nm; No. 7-11: 5 nm).

Then, fast-Fourier transition (FFT) was applied to reveal two groups of lattices points in reciprocal space (Fig. 6.6a). A semi-automatic fitting process using 2D Gaussian functions is developed to acquire accurate lattice mismatch η and twist angle θ values. Briefly, the FFT image was polar transformed to obtain a reciprocal radius-angle (R-θ)

image. Then, six regions of the polar transformed image showing the six groups of lattice points were selected and fitted with 2D Gaussian functions with manually acquired initial fitting parameters. To further enhance the result's reliability, the raw image was cropped into multiple slices, each was fitted for lattice mismatch and twist angle values. The final lattice mismatch and twist angle values of the raw image was obtained from statistical analysis of results from the cropped images with small error of 0.25% for mismatch and 0.20° for misorientation, which is between 1/5-1/4 of the interval of those between stable C-phases, thus enabling successful and reliable distinction between commensurate and incommensurate phases. Statistical results of 11 independent heterostructures show significant C-phase locking-in behaviour within measurement error (Table 6.1, Fig. 6.6b-c). The observed C-phases are labelled as A1-A3, D1 and D5. Details of these observed C-phases are summarised in Table 6.2 and Figure 6.7, Figure 6.8. All C-phases have twist angles below 2° which validates our small-angle approximation. The maximum twist angle is therefore suspected to be related to crystal size due to the scaling of the rotational energy barrier.[37] More than one C-phase is observed, which agrees with the 'commensurate multilevel' picture. The observed C-phases further offer information on the natural mismatch. In practice, highly-accurate $\eta_0$ is unknown due to varying values from different simulation approaches and thermal effects. $\eta_0$ should fall into the overlapping range of the observed C-phase levels, which is approximately 14.78-15.29% for GaS/$MoS_2$. In the case of GaS/graphene, all results belong to two commensurate Moiré patterns D1 and D5, which implies that $\eta_0$ is between 45.86-46.62%. The agreement of observed commensurate Moiré patterns with cases of complex commensurate multilevel analysed in Figure 6.3 clearly demonstrate the key role of small commensurate period in stabilising the system energy of the VLH. It is worth noting that the absence of 0°-

orientation suggests previous understanding of vdWs epitaxy as 0°-orientation between high-symmetry directions is inaccurate. In summary, statistical results from high-quality ADF-STEM images strongly confirm the commensurate multilevel map, where VLHs exhibit particular small twists dependent on their natural mismatch.

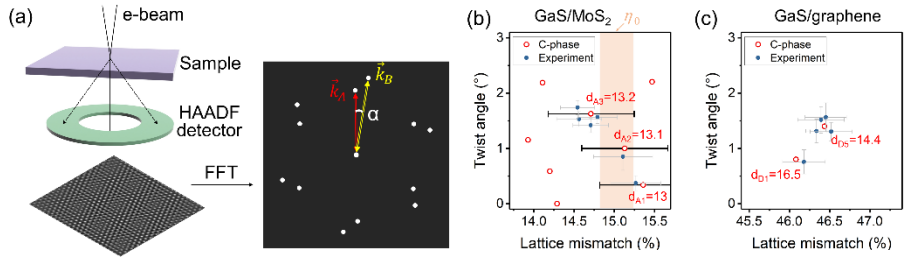



**Figure 6.6. Measurement of twist angle in 2D VLHs.** (a) Schematic illustration of STEM characterisation, as well as example of HAADF-STEM Moiré images and measurement of corresponding FFT image. (b-c) Statistical measurement results of lattice mismatch and misorientation in high-mismatch heterostructures plotted in blue dots, in comparison to red circles from the commensurate multilevel map. The gray error bars of blue dots indicate the uncertainty of fitting results. The orange region in (b) indicates possible range of natural mismatch.

**Table 6.1. Statistical measurements of synthesised VLHs**

| Heterostructure | No. | η (%) | STDEV (%) | α (°) | STDEV (°) | Moiré pattern |
|---|---|---|---|---|---|---|
| $GaS/MoS_2$ | 1 | 15.27 | 0.31 | 0.37 | 0.13 | A1 |
| | 2 | 15.07 | 0.40 | 0.90 | 0.33 | A2 |
| | 3 | 14.79 | 0.25 | 1.57 | 0.12 | A3 |
| | 4 | 14.56 | 0.28 | 1.53 | 0.14 | A3 |
| | 5 | 14.54 | 0.21 | 1.74 | 0.13 | A3 |
| | 6 | 14.71 | 0.22 | 1.42 | 0.13 | A3 |
| GaS/Gr | 7 | 46.18 | 0.27 | 0.76 | 0.22 | D1 |
| | 8 | 46.33 | 0.13 | 1.31 | 0.22 | D5 |
| | 9 | 46.52 | 0.26 | 1.30 | 0.17 | D5 |
| | 10 | 46.45 | 0.26 | 1.56 | 0.26 | D5 |
| | 11 | 46.39 | 0.29 | 1.52 | 0.24 | D5 |

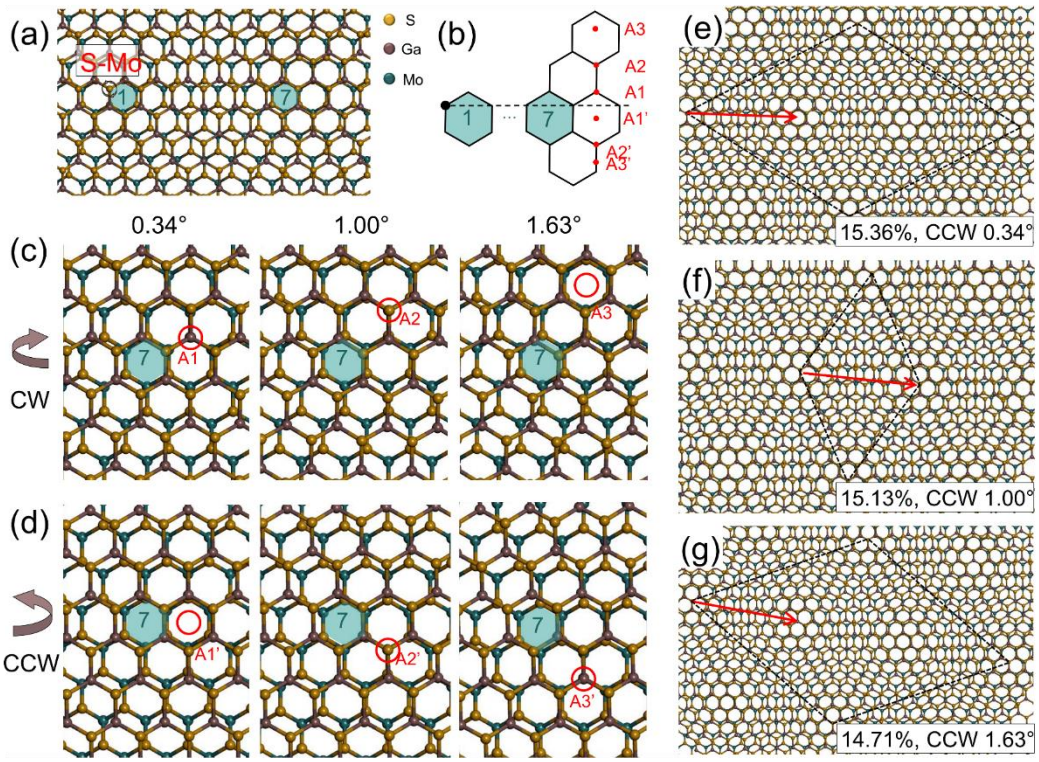



**Figure 6.7. Atomic models for commensurate Moiré patterns A1-A3 of GaS/$MoS_2$ heterostructures.** (a) Top-view of aligned GaS/$MoS_2$ heterostructure. The number 7 marks the seventh parallel Mo-S hexagonal ring for reference in other pictures. (b) Simplified schematics of $MoS_2$ lattice showing ISPs for Moiré patterns A1-A3 and A1'-A3' (the inverted comma symbol indicates contraclockwise rotation). (c-d) Atomic model showing ISPs region for Moiré patterns A1-A3 and A1'-A3'. The S(GaS)-Mo($MoS_2$) atom pairs in hexagonal ring 1 is fixed during rotation and strain relaxation. (e-g) Overview of Moiré superlattice of Moiré patterns A1'-A3'. The black dashed lines indicate the heterostructure supercell (considering atomic difference), and the red arrow indicates the commensurate phase (considering stacking energy) periodicity.

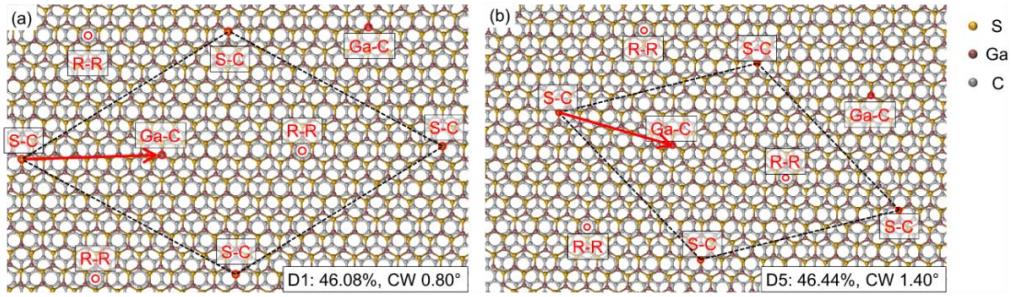



**Figure 6.8. Atomic models for commensurate Moiré patterns D1, D5 of GaS/graphene heterostructures.** (a) Commensurate Moiré patterns D1. Red circles are three kinds of overlapping atom pairs that are identified as the ideal stacking points: S-C, Ga-C and R-R (R for hexagonal ring centre). The red arrow indicates commensurate phase periodicity, which is 1/3 smaller than the longer diagonal of the heterostructure supercell. (b) Commensurate Moiré patterns D5. The red arrow indicating commensurate phase periodicity is 30° to, and $1/\sqrt{3}$ smaller than the Moiré vector, which is the edge of the heterostructure supercell.

**Table 6.2. Summary of commensurate Moiré information**

| Hetero-structure | $\lambda$ | $\kappa$ | Commensurate Moiré | Lattice mismatch (%) | Twist angle (°) | $\frac{\lambda}{\kappa}m$ | $\frac{\lambda}{\kappa}n$ | d |
|---|---|---|---|---|---|---|---|---|
| $GaS/MoS_2$ | 1 | 1 | A1 | 15.36 | 0.34 | 15 | 8 | 13.0 |
| | | | A2 | 15.13 | 1.00 | 15 | 9 | 13.1 |
| | | | A3 | 14.71 | 1.63 | 15 | 10 | 13.2 |
| GaS/Gr | 1 | 1 | D1 | 46.08 | 0.80 | 19/3 | 10/3 | 16.5 |
| | | | D2 | 47.01 | 0.62 | 25/4 | 13/4 | 21.7 |
| | | | D3 | 46.65 | 1.85 | 25/4 | 14/4 | 21.7 |
| | | | D4 | 46.15 | 0.00 | 38/6 | 19/6 | 19.0 |
| | 4 | 3 | D5 | 46.44 | 1.40 | 28 | 20 | 14.4 |

### 6.2.3 Visualisation of Moiré Patterns

The bilayer $GaS/MoS_2$ superlattice could be clearly visualised in HAADF-STEM as both layers have similar contrast, which revealed long-range ordering. Below the A3 C-phases are examined with simulations to show the orientations. Simulated ADF-STEM images and atomic models of incommensurate phases with the C-phases' lattice

mismatch but 0°-orientation lack periodicity, with slight misplacements of atom pairs at the Moiré superlattice vertexes (Fig. 6.9a, d). Also, the Moiré supercell is in 0°-alignment to the $MoS_2$ lattice. In contrast, simulated images and models of the C-phase superlattice show periodicity 3-times that of the Moiré supercell (Fig. 6.9b, e). In addition, despite twist angles smaller than 2°, the supercells display significant tilt angle (>10°) to the horizontal $MoS_2$ lattice. Experimental images in Figure 6.9c exhibit identical supercell and periodicity to A3 simulations. It should be noted that the slight difference in atom contrast with the simulated image is due to local degradation of monolayer GaS under the e-beam (see Chapter 5) or small area of uncovered $MoS_2$, which does not affect long-range ordering. The enlarged image in Figure 6.9f further presents a Moiré period of 2.43 nm for $GaS/MoS_2$, which exactly agrees with theoretical values. Finally, the corresponding FFT image of Figure 6.9c is shown in Figure 6.9g-h to illustrate the 1.63° twist angle between the two groups of hexagonal lattices.

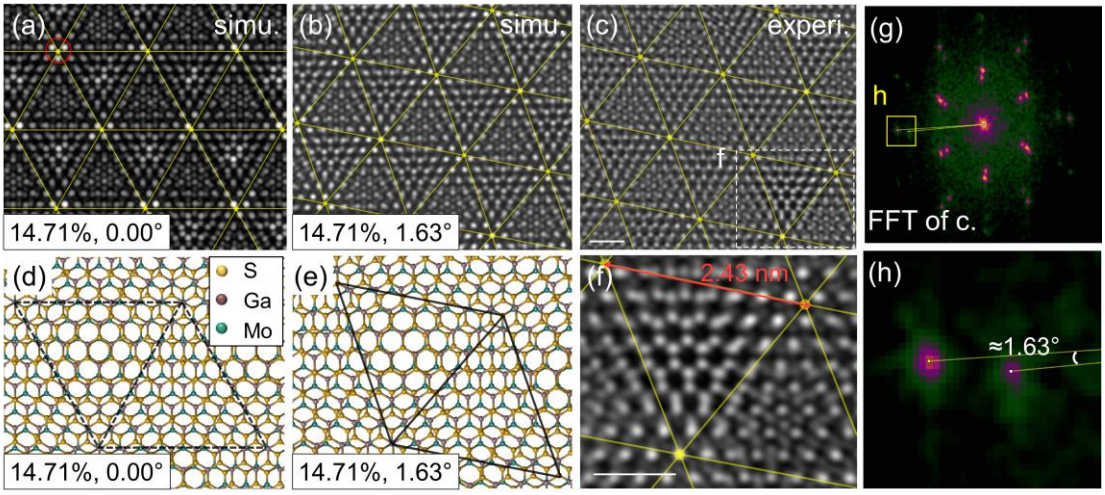



**Figure 6.9. Direct visualisation of commensurate Moiré lattices.** (a) Simulated image of incommensurate $GaS/MoS_2$ heterostructure (η=14.71%, α=0.00°) without translational symmetry. (b) Simulated and (c) experimental ADF-STEM image of commensurate $GaS/MoS_2$ heterostructure (Moiré pattern A3: η=14.71%, α=1.63°) with translational symmetry. (d) Atomic models of incommensurate $GaS/MoS_2$ heterostructure (η=14.71%, α=0.00°); Black

dotted lines indicate Moiré vectors. (e) Atomic models of commensurate GaS/$MoS_2$ heterostructure (Moiré pattern A3: η=14.71%, α=1.63°); Black solid lines indicate unit cell of commensurate phase. (f) Enlarged atomic-resolution ADF-STEM image of commensurate GaS/$MoS_2$ heterostructure in (c). Scale bars: 1 nm. (g) FFT image of (c). (h) Enlarged region of one set of GaS and $MoS_2$ (1,1) lattice points in (g) showing twist angle ≈1.63°.

## 6.3 Conclusion

In this chapter, commensurate multilevel maps were proposed to reinterpret vdWs epitaxy in VLHs based on the F-K model. Low-order C-phases with periodic ISPs result in lower energy than 0°-orientation. As a result, small twist angles form according to the natural lattice mismatch, especially in high-mismatch systems. The predicted small angles and their relation to lattice mismatch were observed in two epitaxial VLHs under HAADF-STEM. Although currently the boundary of small twist angles or the distribution ratio between neighbouring C-phases cannot be quantitively determined, it grants people accurate prediction of possible configurations of epitaxial VLHs without using DFT simulations which demand enormous calculating resources for Moiré systems. This study opens a potential approach for precise and efficient control of crystal orientation by tuning the natural mismatch. It also calls for close examination of C-phases in stacked VLHs, as the observed overall twist angle might be composed by several local low-order C-phases,[38] leading to local variation of its properties.

## 6.4 References

1. Geim, A. K.; Grigorieva, I. V., Van der Waals Heterostructures. *Nature* **2013**, 499, 419-425.

2. Tran, K.; Choi, J.; Singh, A., Moiré and Beyond in Transition Metal Dichalcogenide Twisted Bilayers. *2D Materials* **2020**, *8*, 022002.

3. Novoselov, K. S.; Mishchenko, A.; Carvalho, A.; Castro Neto, A. H., 2D Materials and van der Waals Heterostructures. *Science* **2016**, *353*, aac9439.

4. Seyler, K. L.; Rivera, P.; Yu, H. Y.; Wilson, N. P.; Ray, E. L.; Mandrus, D. G.; Yan, J. Q.; Yao, W.; Xu, X. D., Signatures of Moire-Trapped Valley Excitons in $MoSe_2/WSe_2$ Heterobilayers. *Nature* **2019**, *567*, 66-70.

5. Shabani, S.; Halbertal, D.; Wu, W.; Chen, M.; Liu, S.; Hone, J.; Yao, W.; Basov, D. N.; Zhu, X.; Pasupathy, A. N., Deep Moiré Potentials in Twisted Transition Metal Dichalcogenide Bilayers. *Nat. Phys.* **2021**, *17*, 720-725.

6. Cao, Y.; Fatemi, V.; Demir, A.; Fang, S.; Tomarken, S. L.; Luo, J. Y.; Sanchez-Yamagishi, J. D.; Watanabe, K.; Taniguchi, T.; Kaxiras, E.; Ashoori, R. C.; Jarillo-Herrero, P., Correlated Insulator Behaviour at Half-Filling in Magic-Angle Graphene Superlattices. *Nature* **2018**, *556*, 80-84.

7. Li, X. F.; Lin, M. W.; Lin, J. H.; Huang, B.; Puretzky, A. A.; Ma, C.; Wang, K.; Zhou, W.; Pantelides, S. T.; Chi, M. F.; Kravchenko, I.; Fowlkes, J.; Rouleau, C. M.; Geohegan, D. B.; Xiao, K., Two-Dimensional GaSe/$MoSe_2$ Misfit Bilayer Heterojunctions by van der Waals Epitaxy. *Sci. Adv.* **2016**, 2, e1501882.

8. Gong, Y.; Lin, J.; Wang, X.; Shi, G.; Lei, S.; Lin, Z.; Zou, X.; Ye, G.; Vajtai, R.; Yakobson, B. I.; Terrones, H.; Terrones, M.; Tay, B. K.; Lou, J.; Pantelides, S. T.; Liu, Z.; Zhou, W.; Ajayan, P. M., Vertical and In-Plane Heterostructures from $WS_2/MoS_2$ Monolayers. *Nat. Mater.* **2014**, *13*, 1135-1142.

9. Lin, Y.-C.; Ghosh, R. K.; Addou, R.; Lu, N.; Eichfeld, S. M.; Zhu, H.; Li, M.-Y.; Peng, X.; Kim, M. J.; Li, L.-J.; Wallace, R. M.; Datta, S.; Robinson, J. A., Atomically Thin Resonant Tunnel Diodes Built from Synthetic van der Waals Heterostructures. *Nat. Comm.* **2015**, *6*, 7311.

10. Wang, S.; Wang, X.; Warner, J. H., All Chemical Vapour Deposition Growth of $MoS_2$:h-BN Vertical van der Waals Heterostructures. *ACS Nano* **2015**, *9*, 5246-5254.

11. Koma, A., Van der Waals epitaxy—A New Epitaxial Growth Method for a Highly Lattice-Mismatched System. *Thin Solid Films* **1992**, *216*, 72-76.

12. Tian, T.; Shih, C.-J., Molecular Epitaxy on Two-Dimensional Materials: The Interplay between Interactions. *Ind. Eng. Chem. Res.* **2017**, *56*, 10552-10581.

13. Dong, J.; Zhang, L.; Dai, X.; Ding, F., The Epitaxy of 2D Materials Growth. *Nat. Comm.* **2020**, *11*, 5862.

14. Azizi, A.; Eichfeld, S.; Geschwind, G.; Zhang, K.; Jiang, B.; Mukherjee, D.; Hossain, L.; Piasecki, A. F.; Kabius, B.; Robinson, J. A.; Alem, N., Freestanding van der Waals Heterostructures of Graphene and Transition Metal Dichalcogenides. *ACS Nano* **2015**, *9*, 4882-4890.

15. Yan, A.; Velasco, J.; Kahn, S.; Watanabe, K.; Taniguchi, T.; Wang, F.; Crommie, M. F.; Zettl, A., Direct Growth of Single- and Few-Layer $MoS_2$ on h-BN with Preferred Relative Rotation Angles. *Nano Lett.* **2015**, *15*, 6324-6331.

16. Ji, Q.; Kan, M.; Zhang, Y.; Guo, Y.; Ma, D.; Shi, J.; Sun, Q.; Chen, Q.; Zhang, Y.; Liu, Z., Unravelling Orientation Distribution and Merging Behaviour of Monolayer $MoS_2$ Domains on Sapphire. *Nano Lett.* **2015**, *15*, 198-205.

17. Woods, C. R.; Britnell, L.; Eckmann, A.; Ma, R. S.; Lu, J. C.; Guo, H. M.; Lin, X.; Yu, G. L.; Cao, Y.; Gorbachev, R. V.; Kretinin, A. V.; Park, J.; Ponomarenko, L. A.; Katsnelson, M. I.; Gornostyrev, Y. N.; Watanabe, K.; Taniguchi, T.; Casiraghi, C.; Gao, H. J.; Geim, A. K.; Novoselov, K. S., Commensurate–Incommensurate Transition in Graphene on Hexagonal Boron Nitride. *Nat. Phys.* **2014**, *10*, 451-456.

18. Jin, C.; Olsen, B. C.; Luber, E. J.; Buriak, J. M., van der Waals Epitaxy of Soft Twisted Bilayers: Lattice Relaxation and Mass Density Waves. *ACS Nano* **2020**, *14*, 13441-13450.

19. Braun, O. M.; Kivshar, Y. S., *The Frenkel-Kontorova Model* (Springer, 2010).

20. Koren, E.; Leven, I.; Lortscher, E.; Knoll, A.; Hod, O.; Duerig, U., Coherent Commensurate Electronic States at the Interface Between Misoriented Graphene Layers. *Nat. Nanotechnol.* **2016**, *11*, 752-757.

21. Mele, E. J., Commensuration and Interlayer Coherence in Twisted Bilayer Graphene. *Phys. Rev. B* **2010**, *81*, 161405(R).

22. Carr, S.; Massatt, D.; Torrisi, S. B.; Cazeaux, P.; Luskin, M.; Kaxiras, E., Relaxation and Domain Formation in Incommensurate Two-Dimensional Heterostructures. *Phys. Rev. B* **2018**, *98*, 224102.

23. Dai, S.; Xiang, Y.; Srolovitz, D. J., Twisted Bilayer Graphene: Moiré with a Twist. *Nano Lett.* **2016**, *16*, 5923-5927.

24. Kim, N. Y.; Jeong, H. Y.; Kim, J. H.; Kim, G.; Shin, H. S.; Lee, Z., Evidence of Local Commensurate State with Lattice Match of Graphene on Hexagonal Boron Nitride. *ACS Nano* **2017**, *11*, 7084-7090.

25. Naik, M. H.; Maity, I.; Maiti, P. K.; Jain, M., Kolmogorov–Crespi Potential for Multilayer Transition-Metal Dichalcogenides: Capturing Structural Transformations in Moiré Superlattices. *J. Phys. Chem. C* **2019**, *123*, 9770-9778.

26. Weston, A.; Zou, Y.; Enaldiev, V.; Summerfield, A.; Clark, N.; Zólyomi, V.; Graham, A.; Yelgel, C.; Magorrian, S.; Zhou, M.; Zultak, J.; Hopkinson, D.; Barinov, A.; Bointon, T. H.; Kretinin, A.; Wilson, N. R.; Beton, P. H.; Fal'ko, V. I.; Haigh, S. J.; Gorbachev, R., Atomic Reconstruction in Twisted Bilayers of Transition Metal Dichalcogenides. *Nat. Nanotechnol.* **2020**, *15*, 592-597.

27. Wijk, M. M. v.; Schuring, A.; Katsnelson, M. I.; Fasolino, A., Relaxation of Moiré patterns for slightly misaligned identical lattices: graphene on graphite. *2D Materials* **2015**, *2*, 034010.

28. Rosenberger, M. R.; Chuang, H.-J.; Phillips, M.; Oleshko, V. P.; McCreary, K. M.; Sivaram, S. V.; Hellberg, C. S.; Jonker, B. T., Twist Angle-Dependent Atomic Reconstruction and Moiré Patterns in Transition Metal Dichalcogenide Heterostructures. *ACS Nano* **2020**, *14*, 4550-4558.

29. Bak, P., Commensurate Phases, Incommensurate Phases and the Devil's Staircase. *Rep. Prog. Phys.* **1982**, *45*, 587-629.

30. Van Smaalen, S., Incommensurate Crystal Structures. *Crystallogr. Rev.* **1995**, *4*, 79-202.

31. Kazmierczak, N. P.; Van Winkle, M.; Ophus, C.; Bustillo, K. C.; Carr, S.; Brown, H. G.; Ciston, J.; Taniguchi, T.; Watanabe, K.; Bediako, D. K., Strain Fields in Twisted Bilayer Graphene. *Nat. Mater.* **2021**, *20*, 956-963.

32. Filippov, A. E.; Dienwiebel, M.; Frenken, J. W. M.; Klafter, J.; Urbakh, M., Torque and Twist against Superlubricity. *Phys. Rev. Lett.* **2008**, *100*, 046102.

33. Hermann, K., Periodic Overlayers and Moiré Patterns: Theoretical Studies of Geometric Properties. *J. Phys. Condens. Matter* **2012**, *24*, 314210.

34. Lebedeva, I. V.; Popov, A. M., Energetics and Structure of Domain Wall Networks in Minimally Twisted Bilayer Graphene under Strain. *J. Phys. Chem. C* **2020**, *124*, 2120-2130.

35. Lebedeva, I. V.; Popov, A. M., Commensurate-Incommensurate Phase Transition and a Network of Domain Walls in Bilayer Graphene with a Biaxially Stretched Layer. *Phys. Rev. B* **2019**, *99*, 195448.

36. Lebedev, A. V.; Lebedeva, I. V.; Popov, A. M.; Knizhnik, A. A., Stacking in Incommensurate Graphene/Hexagonal-Boron-Nitride Heterostructures Based on ab initio Study of Interlayer Interaction. *Phys. Rev. B* **2017**, *96*, 085432.

37. Bagchi, S.; Johnson, H. T.; Chew, H. B., Rotational Stability of Twisted Bilayer Graphene. *Phys. Rev. B* **2020**, *101*, 054109.

38. Coppersmith, S. N.; Fisher, D. S.; Halperin, B. I.; Lee, P. A.; Brinkman, W. F., Dislocations and the Commensurate-Incommensurate Transition in Two Dimensions. *Phys. Rev. B* **1982**, *25*, 349-363.

# Chapter 7

# Understanding Interfacial Coupling in $GaS_{0.87}/WS_2$ VLH for High-Performance Photodetectors

## 7.1 Introduction

In practical photodetector applications such as for imaging systems, it is critical to have high and linear photoresponse over a large intensity range of incident light power to convert light signals into accurate electric signals.[1-3] Current 2D photodetectors, however, often find it difficult to satisfy both requirements at the same time. The problem lies in the fundamental photodetection mechanism. 2D photodetectors generating electron-hole pairs are commonly categorised into photodiodes and photoconductor/phototransistors that have been shown in Chapter 2.5 operate under two different mechanisms. In photodiodes under the photovoltaic effect (PVE), photocurrent is formed by separation of photogenerated electron-hole pairs under built-in fields from junction interfaces.[4-5] While good linearity is obtained due to stable carrier lifetime, they show small electric signals in the order of mA/W, limited by the absorbance of the ultrathin layer.[6-10] For example, exfoliated few-layer GaSe/$MoS_2$ p–n diodes show linear response (with linear dynamic range of 70 dB) and comparatively low photoresponsivity of 50 mA/W.[11] Alternatively, in phototransistors based on the photogating effect (PGE), photogenerated minority carriers are trapped at localised states, acting as a local gate.[5, 12] With a large surface ratio, 2D materials show high sensitivity up to $10^7$ A/W under low illumination power.[13] However, the responsivity

decays exponentially under higher illumination powers, primarily due to trap saturation. According to Equation 2.3, trap states promote photogain by introducing a long carrier lifetime τ. Further excitation creates more free carriers due to gradually filled trap states, resulting in decreased average τ. While trap states are helpful in promoting sensitivity for low signals, there lacks a solution to maintain high photogain under increasing illumination.

VLHs, with unique interfacial coupling between the atomically thin layers, could introduce new photodetecting behaviours to solve this problem. Here a conductive sensitizer strategy is proposed that could tune the photoresponse's power-dependent relations, especially to mitigate or even stop the decaying tendency while preserving the high-sensitivity benefits from trap states in PGE. To achieve stable photogain, the decrease in average carrier lifetime must be compensated by an increase in average mobility. This behaviour of varying mobility with illumination power has been found in conventional sensitizer-channel hybrid photodetectors. Incorporation of a photosensitive material to tune the absorption behaviour of the photodetector has been reported to enhance device performance,[14-15] such as in 0D-2D hybrid PbS-$MoS_2$ photodetectors.[16] Photocurrent is generated by electrons transferred into the $MoS_2$ channel after being excited in the PbS quantum dot sensitizer, in which holes are trapped and the remaining electrons have little direct contribution to conductivity. In these kinds of devices, a similar $10^3$-times decrease in photoresponse under higher illumination is attributed mainly to increasing the inverse electric field from growing numbers of transferred charge carriers, which reduces the charge transfer rate. As conventional sensitizers typically have low mobility, the average mobility (which is the linear combination of individual channel mobilities by carrier proportions) for majority carriers in the device reduces when more and more photogenerated new carriers stay in

the sensitizer. In contrast, in a conductive sensitizer strategy (Fig. 7.1), the sensitizer is even more conductive than the channel, thus a transition to higher-mobility carrier transport at higher illumination power is realised. The device configuration is shown in Figure 7.1a, where both the high-mobility sensitizer and a low-mobility channel are connected to the electrodes in parallel. The strategy also demands specific band alignment engineering (Fig. 7.1b). The sensitizer (smaller bandgap) and channel (larger bandgap) should form an isotype type-II heterojunction (the schematics show the n–n case), and the band offset should be large to enable efficient majority carrier transfer from sensitizer to channel as well as channel-dominated transport at the beginning. A transition from low-mobility to high-mobility transport under high illumination power is therefore achieved for photos that only excite the sensitizer. Under dark or low power illumination, a large conduction band offset indicates low carrier concentration in the sensitizer conduction band (S-CB), thus at steady regime most photogenerated electrons contribute to photocurrent from the channel conduction band (C-CB). Under high illumination power, the increasing reverse electric field from transferred carriers reduces the band offset and charge transfer rate, thus photocurrent contribution from the high-mobility sensitizer gradually becomes dominant. The efficeint change in band offset cannot be achieved by back gating or photons that excite both channels. The photogain decay (and subsequently the photoresponsivity) can therefore be mitigated as long as the mobility rise compensates for the carrier lifetime fall.

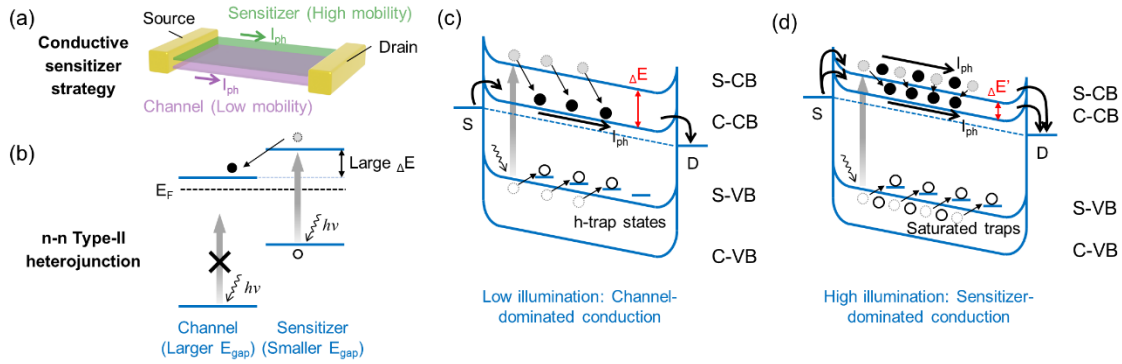



**Figure 7.1. Conductive sensitizer strategy for realizing 2D photodetectors with high sensitivity and linearity response.** (a) Device configuration of the proposed 2D photodetector where both channel and sensitizer are in contact with electrodes in parallel. (b) Band alignment engineering of the channel-sensitizer isotype type-II heterojunction (n–n type-II heterojunction is drawn as an example). The sensitizer should have a smaller bandgap so that only the sensitizer generates excitons upon illumination. In addition, the conduction band offset ΔE between the sensitizer and channel should be large to enable efficient charge transfer and guarantee small carrier concentration in the sensitizer conduction band. (c) Band schematic of device under weak irradiation. The sensitizer absorbs light, generates excitons and electrons are transferred into the channel conduction band (C−CB) while holes are trapped in trap states, a photogating effect known to promote sensitivity. Due to large ΔE, the sensitizer conduction band (S−CB) with small carrier concentration contributes little to the photocurrent, which is dominated by the low-mobility channel. (d) Band schematic of device under intense irradiation. Carrier lifetime in both sensitizer and channel decrease due to trap saturation. At the same time, the increasing inverse electric field from transferred carriers results in a smaller ΔE', leading to increasing participation in the photocurrent from the high-mobility sensitizer. This shift to high-mobility-sensitizer-dominated conduction slows the decreasing trend in photogain from saturated trap states.

Experimentally, 2D bilayer $WS_2/GaS_{0.87}$ photodetectors have been fabricated with the aim of achieving both high sensitivity and large linear range. $WS_2$ with high absorbance

is selected as sensitizer and non-stoichiometric $GaS_{0.87}$ with wide bandgap and low mobility is chosen as channel which could form the isotype type-II heterojunction.[17-19] The band alignment was examined to match the conductive sensitizer strategy using combined technique of X-ray photoelectron spectroscopy (XPS), cathodoluminescence (CL) and photoluminescence (PL) spectroscopy. Efficient charge carrier transfer from $WS_2$ to $GaS_{0.87}$ was probed by Kelvin probe force microscope (KPFM) and Raman, PL spectroscopy. Finally, electronic and optoelectronic characterisation confirmed the transition from $GaS_{0.87}$ dominated low-mobility transport to $WS_2$ dominated high-mobility transport behaviour predicted by the conductive sensitizer strategy. With wide bandgap in the visible spectrum and a large bandgap difference, for photons from red to blue (470−622 nm), the bilayer $WS_2/GaS_{0.87}$ heterostructure photodetectors successfully demonstrated stable photoresponsivity with illumination power, and achieved both a large linear dynamic range (LDR) of 73 dB and high photoresponsivity of 13 A/W under green light.

## 7.2 Results and Discussion

### 7.2.1 Band Alignment of Bilayer $GaS_{0.87}/WS_2$ VLH

Figure 7.2a shows the atomic structure of the $WS_2/GaS_{0.87}$ heterostructure, which is stacked according to the schematic diagrams in Figure 7.2b: First, monolayer $GaS_{0.87}$ and $WS_2$ crystals are synthesised by CVD on 300 nm $SiO_2/Si$ substrates via methods described in Chapter 3.2. The synthesised monolayer $WS_2$ domains show triangular shape with an edge length of ~100 μm, while monolayer $GaS_{0.87}$ has morphology in continuous monolayer films or rounded-corner triangular shaped domains with an edge length of ~35 μm. Then the $WS_2$ crystals are transferred onto the $GaS_{0.87}$ crystals by the

wet-transfer method described in Chapter 3.3.2. The fabricated structure is further annealed in a sulfur environment at 200 °C for better interlayer interactions. After transfer and annealing, Raman or PL of individual $GaS_{0.87}$ and $WS_2$ is examined and no sign of material degradation is found. Most importantly, $GaS_{0.87}$ did not turn into stoichiometric GaS after sulfur annealing. AFM height scans provide accurate information on sample thickness. As shown in Figure 7.3a-b, the $GaS_{0.87}$ crystals show a height of 0.85 nm and the $WS_2$ layer on top is 0.75 nm in thickness, which are in accordance with previous reports and indicate that polymer residues could be ignored.[20-21]

The band alignment of the $WS_2/GaS_{0.87}$ heterostructure is then determined from band offset and bandgap information. First, the valence band offset (VBO) is obtained using the core levels energy and the valence band maximum extracted from XPS results. According the Kraut's method, the VBO of $WS_2$ and $GaS_{0.87}$ could be determined using the following equation:[22]

$$VBO = \left(E_{W4f\frac{7}{2}} - VBM\right)_{WS_2} - (E_{Ga3d} - VBM)_{GaS} - \left(E_{W4f\frac{7}{2}} - E_{Ga3d}\right)_{W/G} \quad (7.1)$$

As shown in Figure 7.2d, the VBO of $WS_2/GaS_{0.87}$ is calculated as 32.01−19.16−11.93=0.92 eV. The uncertainty in determining peak positions is 0.03 eV and for fitting VBM position is 0.07 eV. Note that the measured region is continuous monolayer $GaS_{0.87}$ film covered with some isolated $WS_2$ domains. Therefore, Ga signals from two origins would co-exist: one corresponding to uncovered $GaS_{0.87}$ and the other arising from the heterojunction (noted as Ga*). They were separated during curve fitting according to W:Ga atom ratio (the ratio $x$ is derived from relative signal from XPS, which gives Ga*:$Ga_{total}$ ratio as $2x/(1-2x)$ given the monolayer thickness). Then, the bandgap of each material is measured. The bandgap of $WS_2$ is determined as

2.00 eV from the PL spectrum (see PL analysis in Section 7.2.2). Monolayer $GaS_{0.87}$ shows no signal under the 532 nm laser due to a large bandgap, thus cathodoluminescence (CL) spectroscopy is used where electrons are excited across the gap by the electron beam in a SEM. Fitting of the $GaS_{0.87}$ CL spectrum in Figure 7.2e shows two emission peaks. The high energy emission at 3.35 eV corresponds to recombination from the monolayer GaS conduction band (Fig. 7.4b).[17] The other one at 2.73 eV is attributed to a new defect-induced band (DB). The resulted band alignment schematic is drawn in Figure 7.2f. As the defect-induced band in $GaS_{0.87}$ is 0.19 eV lower than the conduction band minimum of $WS_2$, an n–n isotype type-II heterojunction is formed. The defect-induced band is key to achieving the type-II heterojunction and the channel's low mobility required by the conductive sensitizer strategy. Without that, stoichiometric GaS would form a type-I heterojunction with $WS_2$ (Fig. 7.4c).

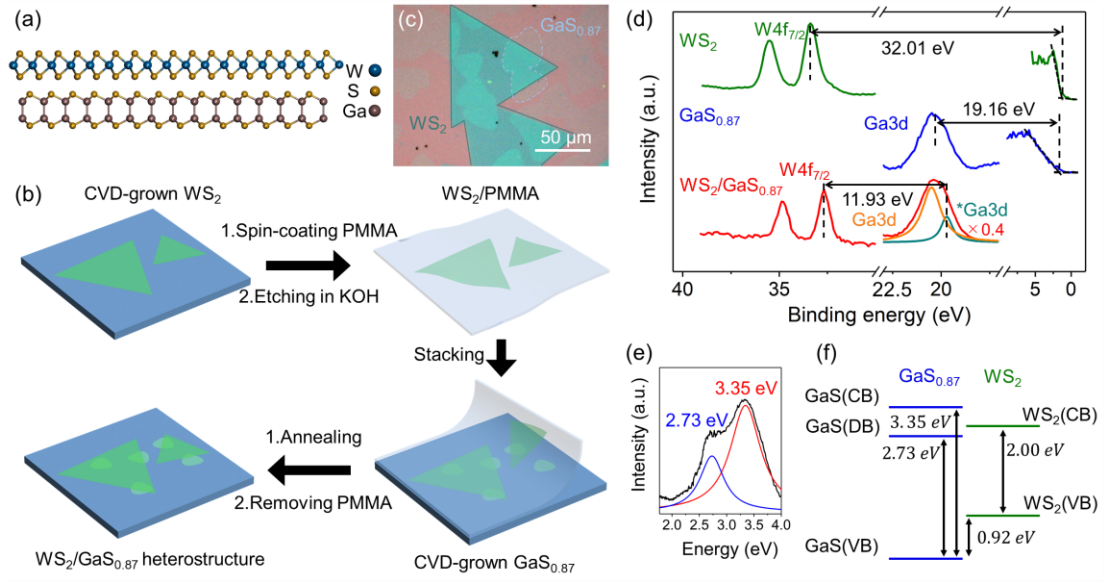



**Figure 7.2. Fabrication and band alignment of $WS_2/GaS_{0.87}$ heterostructure.** (a) Atomic structure of bilayer $WS_2/GaS_{0.87}$ heterostructure. (b) Schematic illustration for fabrication of bilayer $WS_2/GaS_{0.87}$ heterostructure. (c) Optical image of fabricated $WS_2$/GaS heterostructure. (d) XPS of $WS_2$, $GaS_{0.87}$ and $WS_2/GaS_{0.87}$ samples for calculating VBO from Kraut's method;

(e) CL of monolayer $GaS_{0.87}$ sample; (f) Schematic of $WS_2/GaS_{0.87}$ band alignment reconstructed from XPS and CL analysis.

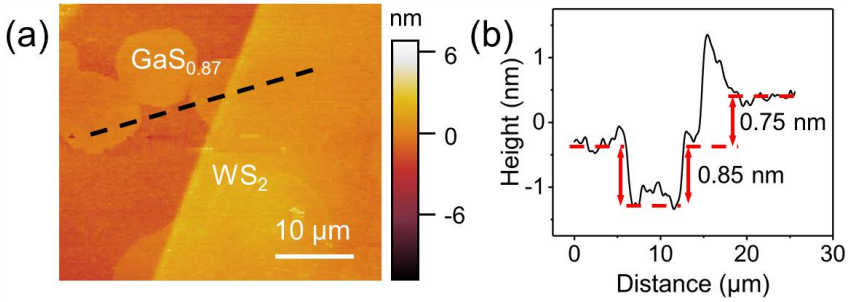



**Figure 7.3. Thickness of heterostructure and constituent materials.** (a) AFM height profile mapping of fabricated $WS_2/GaS_{0.87}$ heterostructure. (b) Line scan profile of $WS_2/GaS_{0.87}$ heterostructure.

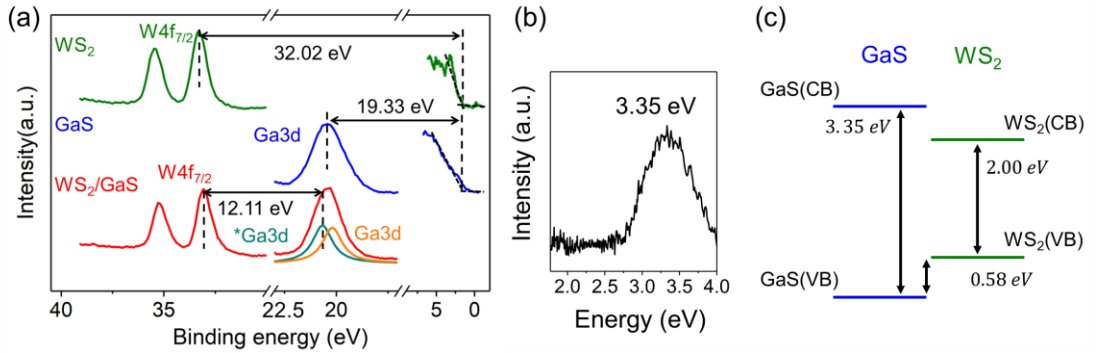



**Figure 7.4. Determination of band alignment of bilayer $WS_2$/GaS(stoichiometric) heterostructure.** (a) XPS of $WS_2$, GaS and $WS_2$/GaS samples. According to Kraut's method, the VBO of $WS_2$ and GaS is calculated as 32.02−19.33−12.11=0.58 eV. (b) Cathodoluminescence spectrum of monolayer GaS sample with emission peak at 3.35 eV. (c) Type-I heterojunction band diagram in bilayer $WS_2$/GaS(stoichiometric) heterostructure.

### 7.2.2 Characterisation of Charge Transfer Under Visible Light Excitation

Charge carrier transfer from the $WS_2$ conduction band to the $GaS_{0.87}$ defect-induced band is confirmed. KPFM mapping was used to determine the work function and band bending of the type-II heterojunction (Fig. 7.5a).[23] Figure 7.5b shows the contact potential differences (CPD) across the orange line in Figure 7.5a which contains all three different surfaces: $WS_2$, $GaS_{0.87}$ and $WS_2/GaS_{0.87}$ (W/G). The CPD is related to the work function ($\Phi$) difference between the material and tip surface by $\Phi_{sample} = \Phi_{tip} - e*CPD$. Therefore, the difference between the work function of $WS_2$ on top of $GaS_{0.87}$ or the substrate is obtained as $\Phi_{W/G} - \Phi_{WS2} = 0.04$ eV, and that between the work function of $GaS_{0.87}$ and $WS_2$ is obtained as $\Phi_{W/G} - \Phi_{GaS0.87} = -0.10$ eV. Since the Fermi level at the junction in equilibrium is constant, the energy levels of $WS_2$ bend 0.04 eV upwards at the junction, and the energy levels of $GaS_{0.87}$ bend 0.10 eV downwards at the junction, as shown in Figure 7.5c. The observation suggests that electrons are transferred from $WS_2$ to $GaS_{0.87}$ at the atomical sharp interface upon heterojunction formation.

To further understand charge transfer behaviour between the two semiconductors under illumination, Raman and PL spectroscopy with a 532 nm laser excitation source were used to probe the interlayer coupling. In all analysis, the measurement conditions were kept the same so that signal intensities can be directly compared. The Raman spectrum of monolayer defective $GaS_{0.87}$ shows the $A^1_{1g}$ peak at 182.6 $cm^{-1}$ (Fig. 7.5d). As the 532 nm (2.33 eV) photon energy is smaller than the bandgap of $GaS_{0.87}$, no PL signal was observed (Fig. 7.5g). Fitting of the Raman spectrum of pristine $WS_2$ shows the $E_{1g}$ peak at 356.1 $cm^{-1}$ and the $A_{1g}$ peak at 416.4 $cm^{-1}$ (Fig. 7.5e), while the PL spectrum shows an exciton peak (A) at 2.003 eV, a trion peak ($A^-$) at 1.980 eV, and a small but broad localised state (LS) peak at ~1.9 eV, indicating the inevitable presence of certain structural disorder or impurities introduced during the transfer process (Fig. 7.5h).[24-25]

The exciton-to-trion ratio ($I_A/I_{A^-}$) is determined to be 0.43±0.03 in $WS_2$ on $SiO_2$/Si substrates, due to n-type doping introduced by the $SiO_2$ interface or polymer/solvent residues.

Since Raman and PL signals from $GaS_{0.87}$ are very small (<1%) compared with $WS_2$, the signals from the heterostructure are regarded as generated by $WS_2$, therefore they are compared with monolayer $WS_2$ and show changes in various peak positions and intensities after forming the heterostructure. Previous studies have shown that the signals can be affected by many factors including strain effects, trap states from environment, free charge carriers, environmental dielectric screening effect, etc.[26-29] Impacts from trap states by molecular physisorption are first excluded as the transfer process should have the same impact on $WS_2$ on $SiO_2$ or on $GaS_{0.87}$. The $E_{1g}$ peak position of $WS_2$ could be used to probe the level of strain in the crystal.[30-31] As $WS_2$ in the heterostructure shows little variation (< 0.2 $cm^{-1}$) in $E_{1g}$ peak position, strain effects are also ruled out (Fig. 7.5f). A lower carrier density in $WS_2$ in the heterostructure is supported by a blue-shift of $A_{1g}$ peak position in $WS_2/GaS_{0.87}$ from 416.4 $cm^{-1}$ to 417.4 $cm^{-1}$ as well as an increasing $I_A/I_{A^-}$ in PL from 0.43 to 1.42.[30] The free electron carrier concentration in the $WS_2$ layer can be calculated from the $I_A/I_{A^-}$ ratio with the following relation:[30]

$$\frac{I_{A^-}}{I_A} = \frac{\gamma_{A^-}}{\gamma_A}\left(\frac{\pi\hbar^2 m_{A^-}}{4m_A m_e}\right)\frac{n_e}{k_B T}\mathrm{e}^{\frac{E_{trion}}{k_B T}} \tag{7.2}$$

where γ is the radiative decay rate of exciton and trion (assuming γ is constant in the doping level range and $\gamma_{A^-}$=0.02 $ps^{-1}$, $\gamma_A$=0.002 $ps^{-1}$); $m_A$ and $m_{A^-}$ are the effective mass of exciton and trion ($m_A=m_e+m_h$, and $m_{A^-}=2m_e+m_h$; in monolayer $WS_2$ $m_e=0.44m_0$, and $m_h=0.45m_0$); and $E_{trion}$ is the trion binding energy. The results (see Table 7.1) show that carrier densities of $WS_2$ in the $WS_2/GaS_{0.87}$ heterostructure

($1.6*10^{13}$ $cm^{-2}$) are only 25% of those in pristine $WS_2$ ($6.2*10^{13}$ $cm^{-2}$). This reduction in free electron carrier concentration is attributed to both reduced n-type doping and charge transfer. Reduction of n-type doping from the $SiO_2$ interface is commonly observed for $WS_2$ stacked on another 2D substrates.[32] However, a decreased doping level alone would result in higher PL intensity as quantum efficiency is greatly increased, which is contrary to an observed 52% quenching in total PL intensity.[33] Quenching in the heterostructure can originate from two principal mechanisms: energy transfer or charge transfer. However, energy transfer quenching must occur from a high energy transition to a low energy transition, which is impossible here because of the smaller bandgap of $WS_2$.[34] Thus, electron carrier transfer from $WS_2$ to $GaS_{0.87}$ under light illumination is likely. After the electron in $WS_2$ is excited to its conduction band, instead of forming intralayer bound exciton, the electron could undergo ultrafast transfer at the 2D interfaces into the $GaS_{0.87}$ lower band, leading to the formation of an interlayer bound exciton.[35] The interlayer exciton is suspected to be indirect as no extra PL peak was observed.

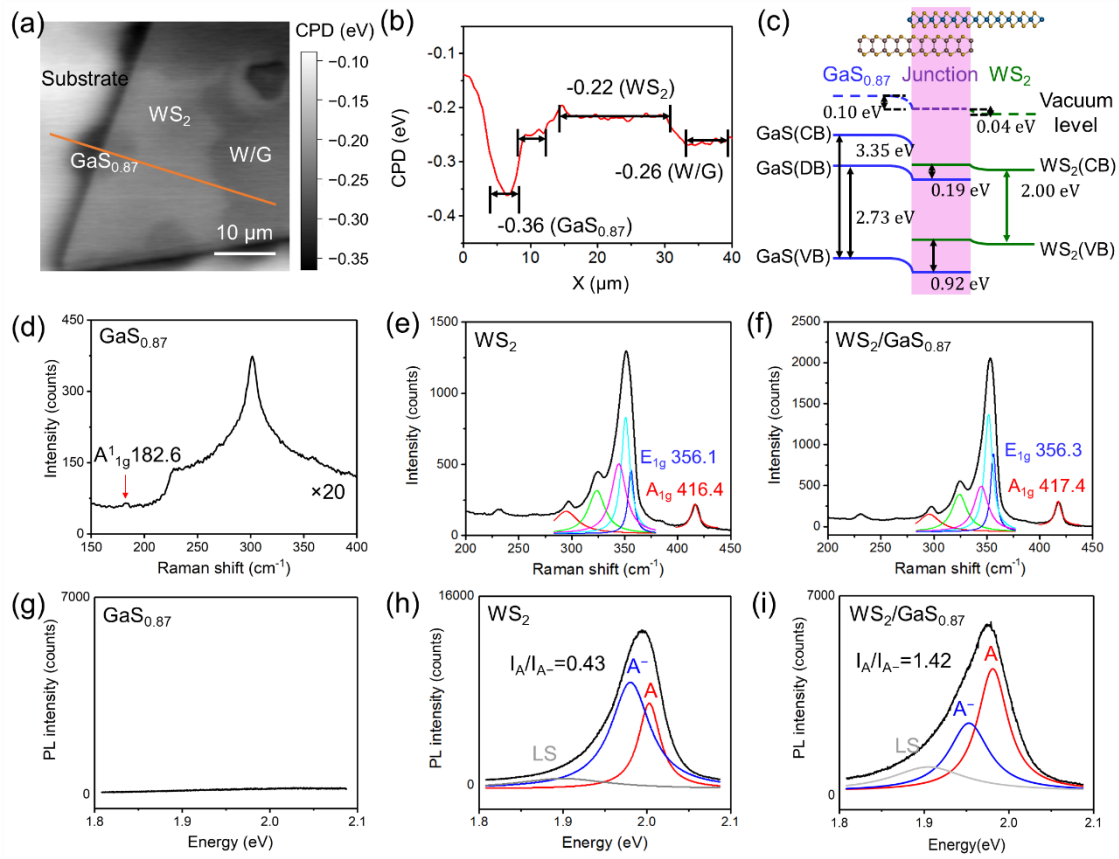



**Figure 7.5. Charge transfer in $WS_2/GaS_{0.87}$ heterostructures.** (a) KPFM scanning of $WS_2/GaS_{0.87}$ heterostructures. (b) CPD line profile in (a). (c) Schematic of band bending in $WS_2/GaS_{0.87}$ heterostructures in the lateral direction, suggesting charge transfer upon heterojunction formation. (d-f) Raman spectrum of (d) monolayer $GaS_{0.87}$, (e) monolayer $WS_2$ and (f) $WS_2/GaS_{0.87}$ heterostructure (532 nm, 620 μW). (g-i) PL spectrum of (g) monolayer $GaS_{0.87}$, (h) monolayer $WS_2$ and (i) $WS_2/GaS_{0.87}$ heterostructure (532 nm, 6 μW). The increasing $I_A/I_{A-}$ as well as strong quenching effect in the heterostructure suggest electron carrier transfer from $WS_2$ to $GaS_{0.87}$ and formation of interlayer excitons.

**Table 1. Average of extracted parameters from Raman and PL fitting**

| | $A_{1g}$ ($cm^{-1}$) | $E_{1g}$ ($cm^{-1}$) | A (eV) | $A^-$ (eV) | PL intensity | $I_A/I_{A-}$ | $n_e$ in $WS_2$ ($cm^{-2}$) | $E_{trion}$ (meV) |
|---|---|---|---|---|---|---|---|---|
| $WS_2$ | 416.4 | 356.1 | 2.003 | 1.980 | 1.00 | 0.43 | $6.2*10^{13}$ | 23 |
| $WS_2/GaS_{0.87}$ | 417.4 | 356.3 | 1.981 | 1.954 | 0.48 | 1.42 | $1.6*10^{13}$ | 27 |

In addition to quenching of the PL intensity and increase in $I_A/I_{A^-}$, it is noted that the A peak position for the type-II heterostructure has a red shift of ~22 meV, due to the combined effects from varied quasiparticle bandgap and exciton binding energy which are attributed to the screening effects from both free charge carrier and dielectric environment.[36-37] For additional comparison, spectral data from a type-I heterojunction of $WS_2$/GaS(stoichiometric) without charge transfer also support the above analysis (Fig. 7.6). Mapping results are also provided to present a clear distinction between pristine $WS_2$ and heterostructure regions as well as the spatial uniformity (Fig. 7.7).

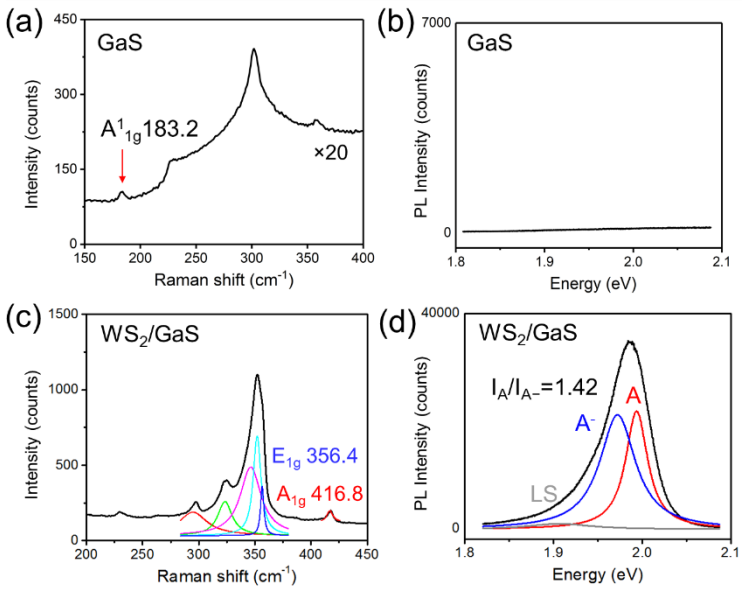



**Figure 7.6. Comparison study of Raman and PL spectrum of type-I $WS_2$/GaS(stoichiometric) bilayer heterostructure.** (a) Raman spectrum of monolayer stoichiometric GaS (532 nm, 620 μW). The GaS $A^1_{1g}$ peak at 183.2 cm$^{-1}$ corresponding to monolayer thickness. (b) PL spectrum of monolayer stoichiometric GaS (532 nm, 6 μW). (c) Raman spectrum of $WS_2$/GaS(stoichiometric) bilayer heterostructure (532 nm, 620 μW). Raman spectrum of the type-I $WS_2$/GaS heterostructure resembles that of pristine $WS_2$, indicating small or little change in both strain and carrier densities, similar to other type-I heterostructures such as $WS_2$/h-BN.[32, 38] (d) PL spectrum of $WS_2$/GaS(stoichiometric) bilayer

heterostructure (532 nm, 6 μW). Total PL intensity of $WS_2$/GaS is ~2.3 times of $WS_2$. The increased PL intensity in the $WS_2$/GaS heterostructure is possibly due to reduced trap states originated from substrate interface, which is replaced by the atomically flat GaS surface. A decrease in doping level is shown by the increased $I_A/I_{A-}$ ratio of 0.62±0.05 from fitting results, resulting in higher PL intensities as quantum efficiency is greatly increased.[30]

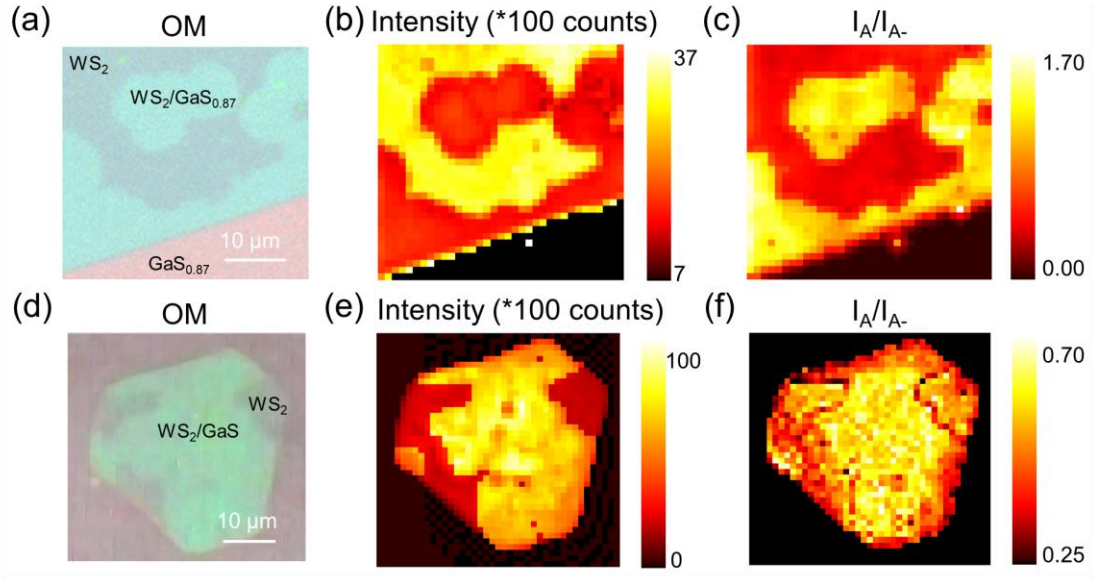



**Figure 7.7. Uniformity of PL spectral results of heterostructures.** (a) Optical image and (b) PL intensity mapping and (c) PL exciton-to-trion ratio mapping of $WS_2/GaS_{0.87}$ heterostructure. (d) Optical image and (e) PL intensity mapping and (f) PL exciton-to-trion ratio mapping of PL mapping $WS_2$/GaS heterostructure for comparison.

### 7.2.3 Mechanism for Achieving Large Linear Dynamic Range

As analysed above, the heterostructure's band alignment and charge transfer behaviours satisfy the requirements for the conductive sensitizer strategy. Therefore, photodetector devices based on the configurations shown in Figure 7.1a were fabricated by e-beam lithography with gold as electrodes on top of the 2D material. Figure 7.8c-d shows the

schematics and optical images of the Au−$WS_2$/$GaS_{0.87}$−Au FET device. To demonstrate the heterostructure properties, FET devices based on the individual components, Au−$WS_2$−Au and Au−$GaS_{0.87}$−Au, were also fabricated and studied as a reference (Fig. 7.8a-b). Measurements and observations were done on three devices for each type of devices which all showed consistent behaviours and photoresponse-power relations ($GaS_{0.87}$; $WS_2$; $WS_2$/$GaS_{0.87}$). Owing to the beginning of degradation of the top $WS_2$ layer under large current densities in a humid and oxygen measuring environment, devices with the most robust performance from each type of devices were reported in Figure 7.8-7.10.

A $GaS_{0.87}$-dominated conducting mode is suggested by measurements in the dark. Although the value of $GaS_{0.87}$ mobility was difficult to obtain from its low current (possibly due to both a low mobility and the large contact barrier with gold electrode), the mobilities of $WS_2$ and $WS_2$/$GaS_{0.87}$ heterostructure are calculated to be 0.13 $cm^2V^{-1}s^{-1}$ (similar to other CVD-grown $WS_2$) and 0.0013 $cm^2V^{-1}s^{-1}$, respectively, from transfer curves in Figure 7.8e-f.[20, 39] This 100-times smaller value in mobility cannot come from $WS_2$ layer even if screening effects from the bottom $GaS_{0.87}$ are considered, but instead should come directly from the defective $GaS_{0.87}$ channel. Because mobility is proportional to current density, the heterostructure's average mobility is the combination of contribution from the two layers. From the measured band offset ($\Delta E$=0.19 eV) the carrier density ratio is estimated as $n_{GaS0.87}$:$n_{WS2}\approx\exp(\Delta E/k_BT)\approx1.5*10^3$. Thus, the mobility contribution from the $WS_2$ monolayer in dark is less than 0.0001 $cm^2V^{-1}s^{-1}$, and the heterostructure's small mobility mainly comes from the $GaS_{0.87}$ channel. Measurement of the effective Schottky barrier also reveals $GaS_{0.87}$ as the main transport channel. Metal-2D material junctions are known to form Schottky barriers which are largely determined by defects

at the interface.[40] Applying a back-to-back model, the effective Schottky barrier height ($\Phi_{B_eff}$) in the monolayer $WS_2$ devices is determined to be 0.57 eV.[41] For the heterostructure devices, since the gold electrodes are deposited onto the top $WS_2$ under same conditions, the interface should be the same. Based on the band diagram in Figure 7.5c, the $WS_2$ conduction band should be positioned 0.61 eV above the Fermi level owing to the upward band bending, and subsequently the $GaS_{0.87}$ defect-induced band should be positioned 0.42 eV above the Fermi level (Fig. 7.8g-h). The measured $\Phi_{B_eff}$ of $WS_2/GaS_{0.87}$ FET devices is 0.43 eV, very close to the $GaS_{0.87}$ band position. The relative value of $\Phi_{B_eff}$ can also be reflected in the heterostructure devices' lower threshold voltage (Fig. 7.8e-f). These results further confirm that under dark conditions, the dominant pathway for electron carrier transport is $GaS_{0.87}$.

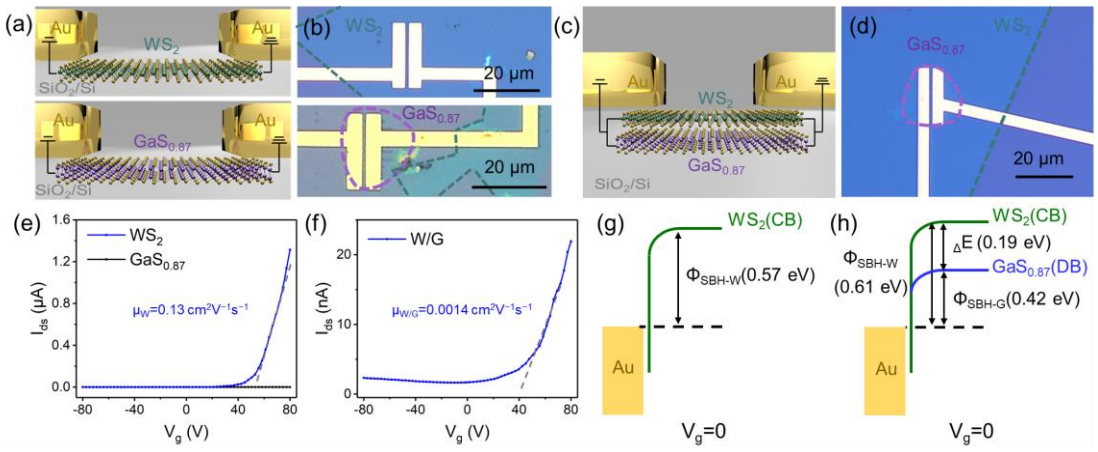



**Figure 7.8. Electronic properties of $GaS_{0.87}$, $WS_2$ and $WS_2/GaS_{0.87}$ devices**. (a) Schematic and (b) optical image of Au−$WS_2$−Au (Up) and Au−$GaS_{0.87}$−Au (Bottom) FET device. (c) Schematic and (d) optical image of Au−$WS_2/GaS_{0.87}$−Au FET device. (e) Transfer curves of $WS_2$ and $GaS_{0.87}$ FET devices (Dark, $V_{ds}$=2 V). (f) Transfer curve of $WS_2/GaS_{0.87}$ FET device (Dark, $V_{ds}$=2 V). (g) Schematic of measured Schottky barrier in Au−$WS_2$−Au FET device. (h) Schematic of estimated Schottky barriers in Au−$WS_2/GaS_{0.87}$−Au FET device.

Finally, the optoelectronic properties of the individual and heterostructure devices were studied. The photoresponse of these devices were measured under various wavelengths (395 nm, 470 nm, 535 nm, 590 nm, 622 nm) across a wide power range. As an example, photocurrent−voltage curves of devices under 535 nm are shown in Figure 7.9a-b. Photoresponsivity ($R_\lambda \equiv I_{photo}/P$) is used to demonstrate the sensitivity of these photodetectors to incident light, where $I_{photo}$ is the photocurrent and P is the illumination power. The $R_\lambda$ is in accordance with the $WS_2$ absorption spectrum which in the visible range is weakest at yellow (590 nm) and strongest at red (622 nm), and is slightly stronger at near UV (395 nm).[37] In comparison, for the heterostructure devices, the $R_\lambda$ is in accordance with the $WS_2$ absorption spectrum for photon energy below 2.73 eV, but shows unproportionally higher $R_\lambda$ for 395 nm. This is consistent with the $WS_2$-sensitized photodetector behaviour for photons within 2.00~2.73 eV range, which takes up most of the visible spectrum. Above this energy, carriers in $GaS_{0.87}$ valence band could be excited and contribute to the photocurrent. Such differences indicate that the heterostructure would operate under C(conductive)-Sensitizer mode within 2.00~2.73 eV, but turn to PGE mode for photon energy higher than 2.73 eV.

The power-related change in photocurrent can be characterised by the power dependence parameter α, defined by the relation $I_{photo} \propto P^{\alpha}$. For ideal linear response, the α value should be 1, while a small α value indicates severe photoresponse decay. For monolayer $WS_2$ devices, $R_\lambda$ shown in Figure 7.9c is in the range of 30−700 A/W under various visible light and power conditions. A smaller α value of 0.5~0.7 was measured for different wavelengths, which is typical for the PGE mechanism (Fig. 7.9c). In addition, both defective and stoichiometric gallium sulfide photodetectors under 275 nm UV light excitation show similar small α values as previously shown in Chapter 5. However, the heterostructure devices based on the conductive sensitizer strategy show

greatly reduced photorepsonse decay and exhibit a nearly ideal α value of 0.97~1.03 for photons between 2.00~2.73 eV, with a moderate photoresponsivity of 10−25 A/W compared to other PGE devices and a detectivity of $1.5\times10^9$ for red light (Fig. 7.9d). The significant difference in decay behaviour from individual components implies that it originates from coupling effects. At near-UV wavelengths, the photodetector operates under the PGE mechanism, thus leading to 20% decay in photoresponsivity with increasing power from 50 to 164 $\mu W/cm^2$, similar to other PGE photodetectors (Fig. 7.9d).

The $WS_2/GaS_{0.87}$ heterostructure should share some strong characteristics of the trap-based PGE, such as large photogain and long response time, as the sensitizer has trap states. The photogain (calculated by $G=h\nu R_\lambda/e\eta$, where η is the absorbance) is estimated to be in the range of 480−1070 in the visible spectrum range, demonstrating a highly efficient process in absorption, charge transfer and photocarrier transport. A long response time of 5 s is also similar to that of pristine $WS_2$ photodetectors (12 s) and other PGE photodetectors (Fig. 7.10).[12, 42] Still, a major difference between PGE or conductive sensitizer strategy is the change in mobility, which is revealed by the transfer curves under illumination. As shown in Figure 7.10e, transfer curve of the heterostructure under UV light show significant threshold voltage shift but little change in transconductance (defined as $gm \equiv \partial Ids/\partial V_{OG}$, where $V_{OG}$ is the overdrive gate voltage from the threshold voltage point), which is typical for conventional PGE mechanism where traps act as local gates.[43] However, transfer curve of the heterostructure under green light with the same illumination power show totally different behaviours, with significant increase in transconductance and little shift in threshold voltage. Such increased transconductance indicates larger mobility that originates from additional contribution from $WS_2$ sensitizer.

As charge transport is in the parallel mode, the transfer curves under visible illumination show both threshold voltage shift and change in interlayer charge transfer, whose effect can be separated by fitting the ON-state transfer curve using the photogating photocurrent equation for the two channels in ref. 54. This enables quantitively extracting the change in heterojunction's mobility. In Figure 7.9f, the heterojunction's mobility is directly evidenced to increase by a factor of 2 when the visible photon flux (photons absorbed per second, to exclude the influence of photon energy difference on illumination power) increased by a factor of 10, showing increasing participation from the $WS_2$ layer. In comparison, under UV illumination of similar photon flux, the device exhibits almost unvaried mobility of 0.002 $cm^2V^{-1}s^{-2}$ (GaS-dominated).

Such a difference between the PGE mode and the C-sensitizer mode for different photon energies is further illustrated in Figure 7.9g. Under the C-sensitizer mode, light is only absorbed by the sensitizer. The excited electrons then tunnel into the underlying channel, contributing to photocurrent but also creating a reverse electrical field. At higher illumination power, the newly excited electrons have a lower possibility of tunnelling and thus a higher possibility to contribute to photocurrent from the high-mobility sensitizer. Under the PGE mode, photons are absorbed both by the sensitizer and the channel. Light absorbed by underlying $GaS_{0.87}$ populates its own band with electrons, leaving fewer available states for charge to tunnel from the $WS_2$. Thus, with fewer transferred electrons, the reverse electrical field is comparably smaller than that in the C-sensitizer mode, and is not enough to hinder the decaying tendency in photoresponse from decreased photocarrier lifetime.

Finally, the near-ideal power dependence of this structure is further demonstrated over a larger power range. A 532 nm laser source is employed to provide a large power

density that LEDs cannot offer, while the small difference to 535 nm LEDs in wavelength-dependent absorbance can be neglected. Figure 7.9h shows that the photoresponsivity of the $WS_2/GaS_{0.87}$ heterostructure remains near 13 A/W in the range of power density from ~0.01 to 232 mW/cm$^2$, while the photoresponsivity of monolayer $WS_2$ drops steeply from ~200 to <1 A/W in the same range. In other words, the heterostructure outperforms its individual components. LDR describes the range of linear response of photodetectors with light intensity, which can be calculated by:

$$LDR = 10\log\left(\frac{P_{sat}R}{\sqrt{2eBI_{dark}}}\right) \quad (7.3)$$

where $P_{sat}$ is the saturated light power when it deviates from linear response (which is larger than the light power at the density of 232 mW/cm$^2$), $R_{532nm}$ is the photoresponsivity, B is the bandwidth (~0.1 Hz, see Figure 7.10b). The obtained LDR for the $WS_2/GaS_{0.87}$ heterostructure photodetector is larger than 73 dB, which surpasses many other 2D heterostructure photodetectors and commercial photodetectors such as GaN (50 dB) and InGaAs (66 dB).[8, 11, 44-46] It should be noted that higher irradiance power might induce subtle damage to the $WS_2$ layer exposed to air, as monolayer $WS_2$ devices also exhibit weakened performance after that, therefore the measured LDR can be further improved with inert atmosphere protection. In Figure 7.9i, the figures of merit of photodetectors based on type-II heterostructures are summarised with photoresponsivity in the x-axis and LDR in the y-axis.[3, 6-8, 11, 16, 47-53] While devices based on PVE show high LDR of 53−132 dB, the photoresponsivity values are less than 0.5 A/W. Other devices based on PGE or conventional sensitizers do not show linearity, and the photoresponsivity values often decay to under 10 A/W at high-power irradiance. In comparison, this work shows both a high LDR value of 73 dB and high photoresponsivity value of 13 A/W. With its advantageous band structure, the simple

bilayer $WS_2/GaS_{0.87}$ heterostructure proves that it can maintain a high photoresponsivity even at high-power irradiance and is promising for practical applications requiring a wide linear working range such as in imaging systems.

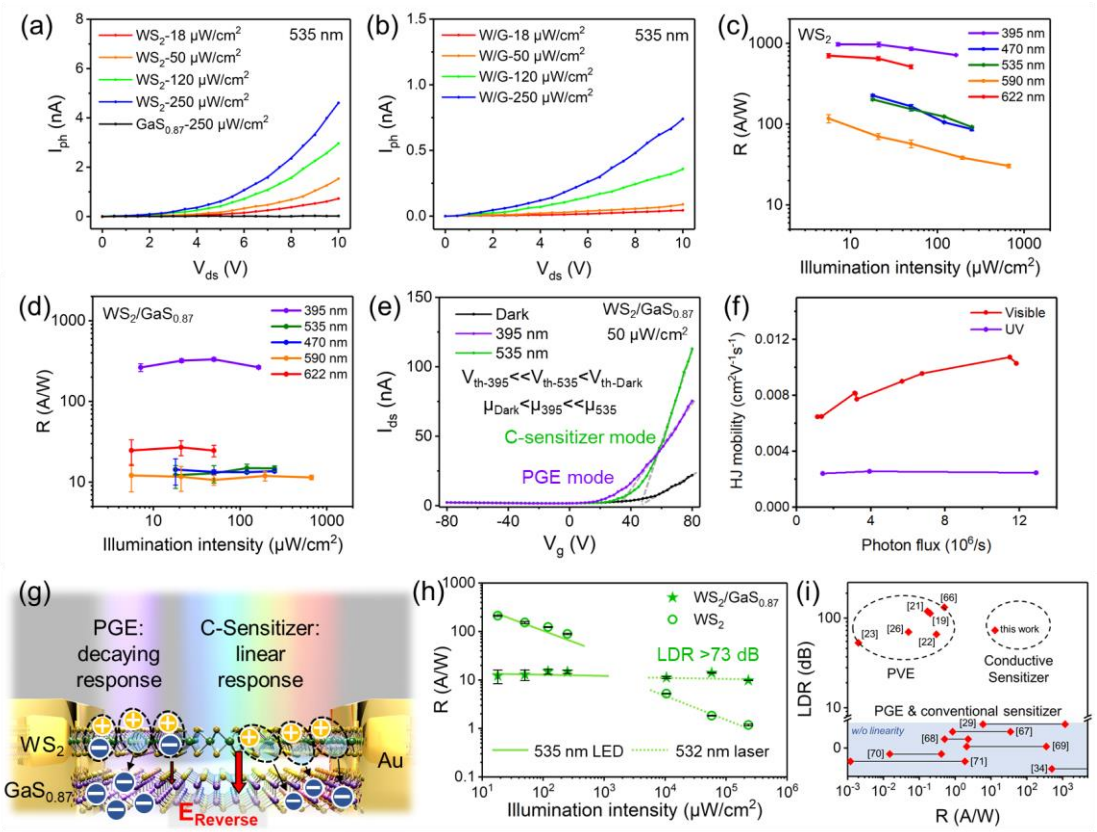



**Figure 7.9. Optoelectronic properties of $WS_2/GaS_{0.87}$ heterostructure.** (a) Photocurrent curves of $WS_2$ and $GaS_{0.87}$ FET devices under 535 nm illumination. (b) Photocurrent curves of $WS_2/GaS_{0.87}$ heterostructure FET device under 535 nm illumination. (c) Photoresponsivity of $WS_2$ photodetectors under different illumination intensity and wavelength. (d) Photoresponsivity of $WS_2/GaS_{0.87}$ photodetectors under different illumination intensity and wavelength. (e) I−$V_g$ curves of $WS_2/GaS_{0.87}$ heterostructure under dark and illumination ($V_{ds}$=2V). Under UV light (PGE mode) the transistor shows a major change in threshold voltage, while under visible light (Conductive-sensitizer mode) it mainly shows a change in transconductance and mobility. (f) Heterojunction mobility value versus photon flux under UV or visible illumination. (g) Schematic of carrier transfer and formation of reverse electric field in $WS_2/GaS_{0.87}$ heterostructure under visible light (Conductive-sensitizer mode) and UV light

(PGE mode) photodetection. (h) Photoresponsivity of $WS_2$ and $WS_2/GaS_{0.87}$ photodetectors under 535 nm LED and 532 nm laser light source. (i) Comparison of response sensitivity and linearity of reported photodetectors based on type-II 2D or 2D hybrid heterostructures.

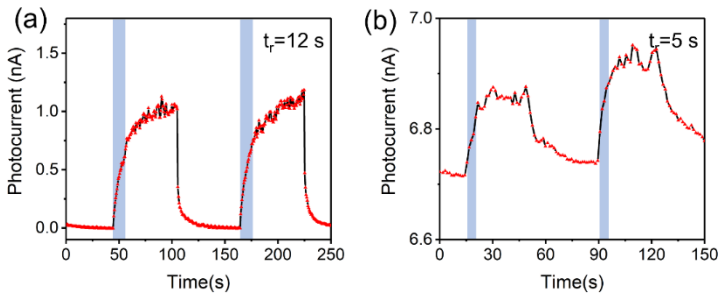



**Figure 7.10. Response time of the photodetectors.** (a) Photoresponse time measurement of $WS_2$ photodetector showing average response time of 12 s (under 120 μW/cm$^2$, V=10 V). (b) Photoresponse time measurement of $WS_2/GaS_{0.87}$ heterostructure photodetector showing average response time of 5 s (under 120 and 250 μW/cm$^2$, V=5 V).

## 7.3 Conclusion

In this chapter, a conductive sensitizer strategy is proposed for achieving both high photoresponsivity and small photoresponsivity decay under high illumination power and is demonstrated on bilayer $WS_2/GaS_{0.87}$ VLH. XPS, CL and PL were used to show that intrinsic defects in the $GaS_{0.87}$ form a defect-induced band within the bandgap that alters the relative band offsets and consequently forms an isotype type-II heterojunction, resulting in efficient electron transfer from $WS_2$ to $GaS_{0.87}$. The defect-induced type-II heterojunction displays strong interlayer coupling and quenching behaviour in the $WS_2$ PL. The transport characteristics of the bilayer $WS_2/GaS_{0.87}$ heterostructure deliver solid evidence of a $GaS_{0.87}$-dominated low-mobility carrier transport behaviour under dark conditions, and a transition to higher-mobility transport with increasing

illumination power. As a result, the photoresponsivity decay due to reduced carrier lifetime was compensated by the increase in channel mobility, leading to a power dependence parameter value of nearly 1. Thanks to the bandgap values selection, the linear photoresponse-power relation is demonstrated across broad visible wavelength spectrum. A large linear dynamic range of 73 dB at a high photoresponsivity of 13 A/W is achieved for green light, with a large photogain between 480−1070, which is suitable for high performance photodetectors with a large working range. The excellent optoelectronic properties of this simple bilayer heterostructure can be further improved with enhancement in mobilities of both layers as well as contact engineering. These results provide insights into the important role of band and interface modulation in offering heterostructures with outstanding properties and functions, and could be valuable in the future designing of more complex sets of heterojunctions to accomplish various tasks in next generation nano-electronic and -optoelectronics devices.

## 7.4 References

1. Li, L.; Ye, S.; Qu, J.; Zhou, F.; Song, J.; Shen, G., Recent Advances in Perovskite Photodetectors for Image Sensing. *Small* **2021,** *17*, 2005606.

2. García de Arquer, F. P.; Armin, A.; Meredith, P.; Sargent, E. H., Solution-Processed Semiconductors for Next-Generation Photodetectors. *Nat. Rev. Mater.* **2017,** *2*, 16100.

3. Ahn, J.; Kang, J. H.; Park, M. C.; Hwang, D. K., All 2D $WSe_2/MoS_2$ Heterojunction Photodiode and Its Image Sensor Application. *Opt. Lett.* **2020,** *45*, 4531-4534.

4. Frisenda, R.; Molina-Mendoza, A. J.; Mueller, T.; Castellanos-Gomez, A.; van der Zant, H. S. J., Atomically Thin p-n Junctions Based on Two-Dimensional Materials. *Chem. Soc. Rev.* **2018**, *47*, 3339-3358.

5. Buscema, M.; Island, J. O.; Groenendijk, D. J.; Blanter, S. I.; Steele, G. A.; van der Zant, H. S. J.; Castellanos-Gomez, A., Photocurrent Generation with Two-Dimensional van der Waals Semiconductors. *Chem. Soc. Rev.* **2015,** *44*, 3691-3718.

6. Lee, H. S.; Ahn, J.; Shim, W.; Im, S.; Hwang, D. K., 2D $WSe_2/MoS_2$ van der Waals Heterojunction Photodiode for Visible-Near Infrared Broadband Detection. *Appl. Phys. Lett.* **2018,** *113*, 163102.

7. Wu, F.; Li, Q.; Wang, P.; Xia, H.; Wang, Z.; Wang, Y.; Luo, M.; Chen, L.; Chen, F.; Miao, J.; Chen, X.; Lu, W.; Shan, C.; Pan, A.; Wu, X.; Ren, W.; Jariwala, D.; Hu, W., High Efficiency and Fast van der Waals Hetero-Photodiodes with a Unilateral Depletion Region. *Nat. Comm.* **2019,** *10*, 4663.

8. Lee, C.-H.; Lee, G.-H.; van der Zande, A. M.; Chen, W.; Li, Y.; Han, M.; Cui, X.; Arefe, G.; Nuckolls, C.; Heinz, T. F.; Guo, J.; Hone, J.; Kim, P., Atomically Thin p–n Junctions with van der Waals Heterointerfaces. *Nat. Nanotechnol.* **2014**, *9*, 676-681.

9. Deng, Y.; Luo, Z.; Conrad, N. J.; Liu, H.; Gong, Y.; Najmaei, S.; Ajayan, P. M.; Lou, J.; Xu, X.; Ye, P. D., Black Phosphorus–Monolayer $MoS_2$ van der Waals Heterojunction p–n Diode. *ACS Nano* **2014**, *8*, 8292-8299.

10. Li, X. F.; Lin, M. W.; Lin, J. H.; Huang, B.; Puretzky, A. A.; Ma, C.; Wang, K.; Zhou, W.; Pantelides, S. T.; Chi, M. F.; Kravchenko, I.; Fowlkes, J.; Rouleau, C. M.; Geohegan, D. B.; Xiao, K., Two-Dimensional GaSe/$MoSe_2$ Misfit Bilayer Heterojunctions by van der Waals Epitaxy. *Sci. Adv.* **2016**, *2*, e1501882.

11. Islam, A.; Lee, J.; Feng, P. X. L., Atomic Layer GaSe/$MoS_2$ van der Waals Heterostructure Photodiodes with Low Noise and Large Dynamic Range. *ACS Photonics* **2018**, *5*, 2693-2700.

12. Fang, H.; Hu, W., Photogating in Low Dimensional Photodetectors. *Adv. Sci.* **2017**, *4*, 1700323.

13. Zhang, W.; Chuu, C.-P.; Huang, J.-K.; Chen, C.-H.; Tsai, M.-L.; Chang, Y.-H.; Liang, C.-T.; Chen, Y.-Z.; Chueh, Y.-L.; He, J.-H.; Chou, M.-Y.; Li, L.-J., Ultrahigh-Gain Photodetectors Based on Atomically Thin Graphene-$MoS_2$ Heterostructures. *Sci. Rep.* **2014**, *4*, 3826.

14. Wang, J.; Han, J.; Chen, X.; Wang, X., Design Strategies for Two-Dimensional Material Photodetectors to Enhance Device Performance. *InfoMat* **2019,** *1*, 33-53.

15. Kufer, D.; Konstantatos, G., Photo-FETs: Phototransistors Enabled by 2D and 0D Nanomaterials. *ACS Photonics* **2016,** *3*, 2197-2210.

16. Kufer, D.; Nikitskiy, I.; Lasanta, T.; Navickaite, G.; Koppens, F. H. L.; Konstantatos, G., Hybrid 2D–0D $MoS_2$–PbS Quantum Dot Photodetectors. *Advanced Materials* **2015,** *27* (1), 176-180.

17. Jung, C. S.; Shojaei, F.; Park, K.; Oh, J. Y.; Im, H. S.; Jang, D. M.; Park, J.; Kang, H. S., Red-to-Ultraviolet Emission Tuning of Two-Dimensional Gallium Sulfide/Selenide. *ACS Nano* **2015**, *9* (10), 9585-9593.

18. Wang, X.; Sheng, Y.; Chang, R.-J.; Lee, J. K.; Zhou, Y.; Li, S.; Chen, T.; Huang, H.; Porter, B. F.; Bhaskaran, H.; Warner, J. H., Chemical Vapour Deposition Growth of Two-Dimensional Monolayer Gallium Sulfide Crystals Using Hydrogen Reduction of $Ga_2S_3$. *ACS Omega* **2018**, *3* (7), 7897-7903.

19. Luxa, J.; Wang, Y.; Sofer, Z.; Pumera, M., Layered Post-Transition-Metal Dichalcogenides (X−M−M−X) and Their Properties. *Chem. Eur. J.* **2016**, *22*, 18810-18816.

20. Lan, C.; Li, C.; Yin, Y.; Liu, Y., Large-Area Synthesis of Monolayer $WS_2$ and Its Ambient-Sensitive Photo-Detecting Performance. *Nanoscale* **2015**, *7*, 5974-5980.

21. Late, D. J.; Liu, B.; Matte, H.; Rao, C. N. R.; Dravid, V. P., Rapid Characterization of Ultrathin Layers of Chalcogenides on $SiO_2$/Si Substrates. *Adv. Funct. Mater.* **2012**, *22*, 1894-1905.

22. Aretouli, K. E.; Tsoutsou, D.; Tsipas, P.; Marquez-Velasco, J.; Aminalragia Giamini, S.; Kelaidis, N.; Psycharis, V.; Dimoulas, A., Epitaxial 2D $SnSe_2$/ 2D $WSe_2$ van der Waals Heterostructures. *ACS Appl. Mater. Interfaces* **2016**, *8*, 23222-23229.

23. Tosun, M.; Fu, D.; Desai, S. B.; Ko, C.; Seuk Kang, J.; Lien, D.-H.; Najmzadeh, M.; Tongay, S.; Wu, J.; Javey, A., $MoS_2$ Heterojunctions by Thickness Modulation. *Sci. Rep.* **2015**, *5*, 10990.

24. He, Z.; Wang, X.; Xu, W.; Zhou, Y.; Sheng, Y.; Rong, Y.; Smith, J. M.; Warner, J. H., Revealing Defect-State Photoluminescence in Monolayer $WS_2$ by Cryogenic Laser Processing. *ACS Nano* **2016,** *10*, 5847-5855.

25. Chow, P. K.; Jacobs-Gedrim, R. B.; Gao, J.; Lu, T.-M.; Yu, B.; Terrones, H.; Koratkar, N., Defect-Induced Photoluminescence in Monolayer Semiconducting Transition Metal Dichalcogenides. *ACS Nano* **2015**, *9*, 1520-1527.

26. Conley, H. J.; Wang, B.; Ziegler, J. I.; Haglund, R. F.; Pantelides, S. T.; Bolotin, K. I., Bandgap Engineering of Strained Monolayer and Bilayer $MoS_2$. *Nano Letters* **2013**, *13*, 3626-3630.

27. Tongay, S.; Zhou, J.; Ataca, C.; Liu, J.; Kang, J. S.; Matthews, T. S.; You, L.; Li, J.; Grossman, J. C.; Wu, J., Broad-Range Modulation of Light Emission in Two-Dimensional Semiconductors by Molecular Physisorption Gating. *Nano Lett.* **2013**, *13*, 2831-2836.

28. Chernikov, A.; van der Zande, A. M.; Hill, H. M.; Rigosi, A. F.; Velauthapillai, A.; Hone, J.; Heinz, T. F., Electrical Tuning of Exciton Binding Energies in Monolayer $WS_2$. *Phys. Rev. Lett.* **2015**, *115*, 126802.

29. Wang, Y.; Zhang, S.; Di, H.; Cheng, J.; Li, Y.; Wu, S., Screening Effect of Graphite and Bilayer Graphene on Excitons in $MoSe_2$ Monolayer. *2D Mater.* **2016**, *4*, 015021.

30. Peimyoo, N.; Yang, W.; Shang, J.; Shen, X.; Wang, Y.; Yu, T., Chemically Driven Tunable Light Emission of Charged and Neutral Excitons in Monolayer $WS_2$. *ACS Nano* **2014**, *8*, 11320-11329.

31. Wang, Y.; Cong, C.; Yang, W.; Shang, J.; Peimyoo, N.; Chen, Y.; Kang, J.; Wang, J.; Huang, W.; Yu, T., Strain-Induced Direct–Indirect Bandgap Transition and Phonon Modulation in Monolayer $WS_2$. *Nano Res.* **2015**, *8*, 2562-2572.

32. Ding, L.; Ukhtary, M. S.; Chubarov, M.; Choudhury, T. H.; Zhang, F.; Yang, R.; Zhang, A.; Fan, J. A.; Terrones, M.; Redwing, J. M.; Yang, T.; Li, M.; Saito, R.; Huang, S., Understanding Interlayer Coupling in TMD-hBN Heterostructure by Raman Spectroscopy. *IEEE Trans. Electron Devices* **2018,** *65*, 4059-4067.

33. Cong, C.; Shang, J.; Wang, Y.; Yu, T., Optical Properties of 2D Semiconductor $WS_2$. *Adv. Opt. Mater.* **2018**, *6*, 1700767.

34. Prasai, D.; Klots, A. R.; Newaz, A. K. M.; Niezgoda, J. S.; Orfield, N. J.; Escobar, C. A.; Wynn, A.; Efimov, A.; Jennings, G. K.; Rosenthal, S. J.; Bolotin, K. I., Electrical Control of near-Field Energy Transfer between Quantum Dots and Two-Dimensional Semiconductors. *Nano Lett.* **2015,** *15*, 4374-4380.

35. Hong, X.; Kim, J.; Shi, S.-F.; Zhang, Y.; Jin, C.; Sun, Y.; Tongay, S.; Wu, J.; Zhang, Y.; Wang, F., Ultrafast Charge Transfer in Atomically Thin $MoS_2/WS_2$ Heterostructures. *Nat. Nanotechnol.* **2014**, *9*, 682-686.

36. Kumar, R.; Verzhbitskiy, I.; Giustiniano, F.; Sidiropoulos, T. P. H.; Oulton, R. F.; Eda, G., Interlayer Screening Effects in $WS_2/WSe_2$ van der Waals Hetero-Bilayer. *2D Mater.* **2018**, *5*, 041003.

37. Zhu, B.; Chen, X.; Cui, X., Exciton Binding Energy of Monolayer $WS_2$. *Sci. Rep.* **2015**, *5*, 9218.

38. Sheng, Y.; Xu, W.; Wang, X.; He, Z.; Rong, Y.; Warner, J. H., Mixed Multilayered Vertical Heterostructures Utilizing Strained Monolayer $WS_2$. *Nanoscale* **2016**, *8*, 2639-2647.

39. Lee, Y.-H.; Yu, L.; Wang, H.; Fang, W.; Ling, X.; Shi, Y.; Lin, C.-T.; Huang, J.-K.; Chang, M.-T.; Chang, C.-S.; Dresselhaus, M.; Palacios, T.; Li, L.-J.; Kong, J., Synthesis and Transfer of Single-Layer Transition Metal Disulfides on Diverse Surfaces. *Nano Lett.* **2013**, *13*, 1852-1857.

40. Schulman, D. S.; Arnold, A. J.; Das, S., Contact Engineering for 2D Materials and Devices. *Chem. Soc. Rev.* **2018,** *47*, 3037-3058.

41. Fan, Y.; Zhou, Y.; Wang, X.; Tan, H.; Rong, Y.; Warner, J. H., Photoinduced Schottky Barrier Lowering in 2D Monolayer $WS_2$ Photodetectors. *Adv. Opt. Mater.* **2016**, *4*, 1573-1581.

42. Pak, J.; Min, M.; Cho, K.; Lien, D.-H.; Ahn, G. H.; Jang, J.; Yoo, D.; Chung, S.; Javey, A.; Lee, T., Improved Photoswitching Response Times of $MoS_2$ Field-Effect Transistors by Stacking *p*-Type Copper Phthalocyanine Layer. *Appl. Phys. Lett.* **2016,** *109*, 183502.

43. Mitta, S. B.; Choi, M. S.; Nipane, A.; Ali, F.; Kim, C.; Teherani, J. T.; Hone, J.; Yoo, W. J., Electrical Characterization of 2D Materials-Based Field-Effect Transistors. *2D Mater.* **2020,** *8*, 012002.

44. Roy, K.; Ahmed, T.; Dubey, H.; Sai, T. P.; Kashid, R.; Maliakal, S.; Hsieh, K.; Shamim, S.; Ghosh, A., Number-Resolved Single-Photon Detection with Ultralow Noise van der Waals Hybrid. *Adv. Mater.* **2018**, *30*, 1704412.

45. Khan, M. A.; Kuznia, J. N.; Olson, D. T.; Hove, J. M. V.; Blasingame, M.; Reitz, L. F., High-Responsivity Photoconductive Ultraviolet Sensors Based on Insulating Single-Crystal GaN Epilayers. *Appl. Phys. Lett.* **1992**, *60*, 2917-2919.

46. Gong, X.; Tong, M.; Xia, Y.; Cai, W.; Moon, J. S.; Cao, Y.; Yu, G.; Shieh, C.-L.; Nilsson, B.; Heeger, A. J., High-Detectivity Polymer Photodetectors with Spectral Response from 300 nm to 1450 nm. *Science* **2009**, *325*, 1665-1667.

47. Tan, H.; Xu, W.; Sheng, Y.; Lau, C. S.; Fan, Y.; Chen, Q.; Tweedie, M.; Wang, X.; Zhou, Y.; Warner, J. H., Lateral Graphene-Contacted Vertically Stacked $WS_2/MoS_2$ Hybrid Photodetectors with Large Gain. *Adv. Mater.* **2017**, *29*, 1702917.

48. Ahn, J.; Kang, J. H.; Kyhm, J.; Choi, H. T.; Kim, M.; Ahn, D. H.; Kim, D. Y.; Ahn, I. H.; Park, J. B.; Park, S.; Yi, Y.; Song, J. D.; Park, M. C.; Im, S.; Hwang, D. K., Self-Powered Visible-Invisible Multiband Detection and Imaging Achieved Using High-Performance 2D $MoTe_2/MoS_2$ Semivertical Heterojunction Photodiodes. *ACS Appl. Mater. Interfaces* **2020,** *12*, 10858-10866.

49. Luo, P.; Zhuge, F.; Wang, F.; Lian, L.; Liu, K.; Zhang, J.; Zhai, T., PbSe Quantum Dots Sensitized High-Mobility $Bi_2O_2Se$ Nanosheets for High-Performance and Broadband Photodetection Beyond 2 μm. *ACS Nano* **2019,** *13*, 9028-9037.

50. Xue, Y.; Zhang, Y.; Liu, Y.; Liu, H.; Song, J.; Sophia, J.; Liu, J.; Xu, Z.; Xu, Q.; Wang, Z.; Zheng, J.; Liu, Y.; Li, S.; Bao, Q., Scalable Production of a Few-Layer $MoS_2/WS_2$ Vertical Heterojunction Array and Its Application for Photodetectors. *ACS Nano* **2016,** *10*, 573-580.

51. Yang, Y.; Huo, N.; Li, J., Gate Modulated and Enhanced Optoelectronic Performance of $MoSe_2$ and CVD-Grown $MoS_2$ Heterojunctions. *RSC Adv.* **2017,** *7*, 41052-41056.

52. Yang, T.; Li, X.; Wang, L.; Liu, Y.; Chen, K.; Yang, X.; Liao, L.; Dong, L.; Shan, C.-X., Broadband Photodetection of 2D $Bi_2O_2Se$–$MoSe_2$ Heterostructure. *J. Mater. Sci.* **2019,** *54*, 14742-14751.

53. Sar, H.; Taghipour, N.; Lisheshar, I. W.; Delikanli, S.; Demirtas, M.; Demir, H. V.; Ay, F.; Perkgoz, N. K., $MoS_2$ Phototransistor Sensitized by Colloidal Semiconductor Quantum Wells. *Adv. Opt. Mater.* **2020,** *8*, 2001198.

54. Furchi, M. M.; Polyushkin, D. K.; Pospischil, A.; Mueller, T., Mechanisms of Photoconductivity in Atomically Thin $MoS_2$. *Nano Lett.* **2014**, *14*, 6165-6170.

# Chapter 8

# Conclusions

## 8.1 Thesis summary

The aim of this doctoral thesis is to contribute to the synthesis of 2D layered semiconductors and VLHs via vapour phase deposition, and also in the subsequent characterisation of the properties of those novel materials for optoelectronic applications. The goal is achieved through three main aspects: (a) Establishing new vapour phase deposition approaches for large-scale synthesis of high-quality 2D layered semiconductors, $MoS_2$ and GaS, with detailed understanding of the growth mechanisms (Chapter 4-5); (b) Developing a universal framework for predicting small twist angles in high-mismatch epitaxially-grown VLHs (Chapter 6); (c) Investigating the band alignment and charge transfer behaviour in stacked $GaS_{0.87}/WS_2$ VLH for optoelectronic applications (Chapter 7).

In Chapter 4, the use of precursor-soluble substrate is introduced in a simple and facile direct sulfurization process for large-scale growth of high-quality monolayer $MoS_2$. This chapter shows that by introducing an additional annealing stage before sulfurization which allows Mo-precursors to dissolve into the molten glass, the subsequent interfacial sulfurization reaction generates large monolayer $MoS_2$ single crystals. The size of monolayer $MoS_2$ single crystals could be increased to around 600 μm with over 89% coverage, which is the largest ones ever reported by direct sulfurization. A series of controlled experiments indicate that the nucleation process is associated with the interfacial Mo and S precursor concentrations, the former being

controlled by diffusion of Mo in the glass described by the Fick's first law. As a result, this approach demonstrates excellent scalability on 2*5.5 $cm^2$ glass with large-scale homogeneity from simple spin-coating process. In addition, the synthesised monolayer $MoS_2$ exhibits high mobility of 1.1 $cm^2V^{-1}s^{-1}$ and photoresponsivity of 9.9 A/W that is comparable to mechanically exfoliated material. Thus, this approach utilising low-cost glass substrates should be beneficial for industrial production of 2D semiconductors that require scalable, simple and stable processing routes.

In Chapter 5, high-quality ultrathin 2D GaS continuous films are obtained by a CVD process. This approach shows good controllability over film thickness as well as product stoichiometry through deposition temperature and the ratio of absorbed reactive species, respectively. The synthesised GaS films exhibit optical and vibrational properties that are layer- and stoichiometry-dependent, thus the $A_{1g}$ Raman vibration mode is found as a quick indicator of film layer number. In terms of optoelectronic properties, the photoresponsivity increases with the number of layers. Also, stoichiometric GaS generally shows higher photoresponsivity than its defective counterparts, and stoichiometric GaS shows a UV-discriminating photoresponse that is suitable for UV-sensor applications. Finally, stability study by XPS and ADF-STEM characterisation suggests that intrinsic GaS is stable in ambient conditions, while defective $GaS_{0.87}$ exhibits photo-induced oxidation degradation into amorphous $Ga_2O_3$ that starts at sulfur vacancies.

In Chapter 6, the concept of vdWs epitaxy for synthesising high-mismatch VLHs is revisited. Although vdWs epitaxy is commonly described as 0°-orientation between high-symmetry axes in two layers, by considering effects from atomic relaxation based on the Frenkel-Kontorova model, it was found that low-order commensurate phases with periodic ideal stacking points might result in lower energy than the 0°-orientation.

According to this, commensurate multilevel maps were proposed for predicting potential twist angles in hexagonal VLHs of any given lattice mismatch. Especially for high-mismatch (>15%) systems, the ground states of the system would exhibit discrete twist angles separated by ~1° that are easy to observe. Statistical results of lattice mismatch and twist angles by ADF-STEM in two epitaxially grown VLHs, GaS/$MoS_2$ and GaS/graphene, agree with the commensurate multilevel maps. The commensurate Moiré patterns can also be directly visualised under ADF-STEM. This study shows how vdWs epitaxy could bring in precise and scalable control of twist angles in VLHs.

In Chapter 7, stacked bilayer $WS_2$/$GaS_{0.87}$ heterostructure demonstrated a conductive sensitizer strategy which achieves both high photoresponsivity and small photoresponsivity decay under high illumination power. XPS, CL and PL characterisation show that intrinsic defects in the $GaS_{0.87}$ form a defect-induced band within the bandgap. An isotype type-II heterojunction with efficient electron transfer from $WS_2$ to $GaS_{0.87}$ is demonstrated by the PL quenching behaviour. Such interlayer coupling between the two layers, along with the difference in channel mobility, leads to a $GaS_{0.87}$-dominated low-mobility carrier transport behaviour under dark, and a transition to the $WS_2$ higher-mobility transport under visible light. Consequently, the photoresponsivity decay due to reduced carrier lifetime is compensated for increased mobility, leading to a nearly power-independent photoresponse across a broad visible wavelength spectrum. A large linear dynamic range of 73 dB at a high photoresponsivity of 13 A/W is achieved for green light, with a large photogain between 480−1070, which is suitable for high performance photodetectors with a large working range. This study shows that interlayer coupling in VLHs could bring outstanding properties and functions for next-generation nano-optoelectronic devices.

## 8.2 Outlook

The study of this thesis could be further developed in the following three directions. First, the concept of the precursor-soluble substrate approach could be further extended to other 2D layered semiconductors, especially those with wide bandgaps with suitable choices of precursor and liquid substrates. Also, current synthesis is restricted by the 1-inch tube, while successful demonstration of wafer-scale growth could further prove its applications in industrial production. In addition, apart from facile and self-limiting growth of one 2D semiconductors, this approach has great potential in precisely controlling the metal percentage in alloyed 2D semiconductors such as $Mo_xW_{1-x}S_2$, which is difficult to achieve in current CVD growth methods. Second, while this study on epitaxially-grown VLHs demonstrates the existence of natural non-zero twist angles, study of the electronic or optical properties of these small twist angle VLHs is another currently active field which requires further investigations into these high-mismatch VLHs. This also requires further advancement in epitaxial overgrowth techniques to create large-area top-layers with uniform thickness. Third, non-stoichiometric GaS has been proven as an interesting platform for stability as well as band modulation studies. It is worth further understanding whether the concentration of sulfur vacancies could be tuned in the non-stoichiometric GaS, which could further enhance our understanding of the role of defects in tuning the band structure and functionality of wide bandgap 2D semiconductors through DFT simulations or a series of *in-situ* and *ex-situ* characterisation methods. The development of knowledge in the above three directions is essential in application for 2D semiconductor-based nano-electronic and -optoelectronics.